

Passive Scalar Mixing in Chaotic Flows with Boundaries

Submitted by Fatma Altuhami Zaggout to the University of Exeter as a thesis for the degree of Doctor of Philosophy in Mathematics in April 2012.

This thesis is available for Library use on the understanding that it is copyright material and that no quotation from the thesis may be published without proper acknowledgement.

I certify that all material in this thesis which is not my own work has been identified and that no material has previously been submitted and approved for the award of a degree by this or any other University.

Fatma Altuhami Zaggout

Abstract

We are interested in examining the long-time decay rate of a passive scalar in two-dimensional flows. The focus is on the effect of boundary conditions for kinematically prescribed velocity fields with random or periodic time dependence. Scalar evolution is followed numerically in a periodic geometry for families of flows that have either a slip or a no-slip boundary condition on a square or plane layer subdomain \mathcal{D} . The boundary conditions on the passive scalar are imposed on the boundary \mathcal{C} of the domain \mathcal{D} by restricting to a subclass invariant under certain symmetry transformations. The scalar field obeys constant (Dirichlet) or no-flux (Neumann) conditions exactly for a flow with the slip boundary condition and approximately in the no-slip case.

At late times the decay of a passive scalar, for example temperature, is exponential in time with a decay rate $\gamma(\kappa)$, where κ is the molecular diffusivity. Scaling laws of the form $\gamma(\kappa) \simeq C\kappa^\alpha$ for small κ are obtained numerically for a variety of boundary conditions on flow and scalar, and supporting theoretical arguments are presented. In particular when the scalar field satisfies a Neumann condition on all boundaries, $\alpha \simeq 0$ for a slip flow condition; for a no-slip condition we confirm results in the literature that $\alpha \simeq 1/2$ for a plane layer, but find $\alpha \simeq 2/3$ in a square subdomain \mathcal{D} where the decay is controlled by stagnant flow in the corners. For cases where there is a Dirichlet boundary condition on one or more sides of the subdomain \mathcal{D} , the exponent measuring the decay of the scalar field is $\alpha \simeq 1/2$ for a

slip flow condition and $\alpha \simeq 3/4$ for a no-slip condition. The scaling law exponents α for chaotic time-periodic flows are compared with those for similarly constructed random flows.

Motivated by the theory of passive scalar field, in Part II of this work we extend the investigation of the evolution of passive scalar for the flows addressed specifically in Part I. Based on an ensemble averaging over random velocity fields, the theoretical results obtained confirm the scaling laws computed numerically for a single, long realisation of random flows. In analogy with Lebedev & Turitsyn (2004) and Salman & Haynes (2007) our results show very good agreement between such an ensemble theory and applications.

In part III of our study, we expand upon the work set out in the previous parts of this thesis in terms of the polar-co-ordinate system. We analyse the structures of flows driven near to a corner with a link to Moffatt corner eddies. A long-time exponential decay rate $\gamma(\kappa) = C\kappa^\alpha$ has been obtained confirming our numerical and theoretical results predicted in Part I and Part II in this work. The exponent α is determined in a structure of Moffatt corner eddies.

0.1 ACKNOWLEDGEMENTS

I thank the Almighty God, without whose blessings none of this would have been possible. The successful completion of this research would also not have been possible without the invaluable contribution and support of many people. I especially would like to express my gratitude to my supervisor Prof. Andrew Gilbert for the opportunity to conduct this research under his tutelage. I thank him for his support, guidance and patience. His broad scientific knowledge and passion for research inspired me to face many challenges in a scientific work and made it a pleasure to work with him. I am grateful for the freedom and encouragement he has given me.

I am also grateful to Dr. Stephen Cox and Prof. Mitchell Berger for accepting to serve on my thesis, and thank them for their insights and recommendations for the improvement of this work.

Many thanks for Prof. John Thuburn and Dr. Matthew Turner, their useful discussions have certainly helped me.

I received help and support in various other forms from the academic, administrative and technical staff at the college of Engineering, Mathematics and Physical Sciences, University of Exeter and I thank all the people that helped and supported me, particularly Dr. Mustafa Aziz, Peter Leget and Liz Roberts.

I would also like to thank Dr. Aisha Bello-Dambatta for her support and friendship throughout my PhD. She has always been incredibly helpful and I have particularly appreciated her support over the last three months.

I have had the pleasure of sharing an office with some wonderful people, some of whom have now left, but all of whom deserve thanks. In particular, I would like

to thank Nicholas Blackbeard and Ozkan Karabacak for their support and helpful discussions on this project.

Thanks are certainly due to the whole Geophysical and Astrophysical Fluid Dynamics group, GAFD, University of Exeter.

My deepest gratitude to my loving parents for their prayers, generosity, encouragement and support, especially in the final months of the thesis; and my siblings - you all continue to inspire me in your own ways. I would like to thank my extended family for all their prayers and support.

Last but not the least, I would like to thank my husband, Ramadan. Ramadan's constant love, unlimited support and his great sacrifices have sustained me throughout my PhD, and I would be lost without him.

Contents

Title	3
0.1 ACKNOWLEDGEMENTS	3
1 INTRODUCTION AND MOTIVATION	24
1.1 History of chaotic mixing	24
1.2 Examples of Aref and Ottino	26
1.3 Applications	35
1.4 Ideas from dynamical systems	36
1.4.1 Fluid flow	37
1.4.2 Motion of particles in a given flow	40
1.4.3 Poincaré section	42
1.4.4 Kinematics of chaos	43
1.5 Advection-diffusion equation	44
1.6 Mixing in global chaotic flows	45
1.7 Mixing in flows with boundaries	46
1.8 Mixing in open flows	52
1.9 Thesis outline	54
2 MAIN FUNCTIONS AND TRANSFORMATIONS	57
2.1 Outline	57
2.2 Main stream functions	59
2.3 General stream functions	60
2.4 Governing equations	64
2.5 Symmetry group and transformations	65

2.6	Some transformations of the stream functions	71
2.7	Numerical scheme	77
2.8	Summary	82
I	Numerical simulations	83
3	NUMERICAL SIMULATIONS	84
3.1	Outline	84
3.2	Simulations of random flows in the square domain	85
3.2.1	Numerical simulations for the flow ψ_{slip}	86
3.2.2	Numerical simulations for the flow $\psi_{\text{no-slip}}$	102
3.3	Summary and discussion	111
4	LARGE SCALES AND BLOCH WAVENUMBERS	113
4.1	Outline	113
4.2	Simulations in a plane layer and Bloch wavenumbers	114
4.2.1	Numerical simulations for random flow $\psi_{\text{slip},pl}$	116
4.2.2	Numerical simulations for random flow $\psi_{\text{no-slip},pl}$	126
4.3	Summary of results in the plane layer	128
4.4	Mixed Dirichlet/Neumann boundary conditions for flow in a square domain	129
4.5	Numerical simulations for time-periodic flows in a square domain	134
4.6	Summary	138
II	Theory and developments	143
5	THEORETICAL FOUNDATIONS	144

5.1	Outline	144
5.2	General foundations	145
5.3	Structure of the effective diffusivity tensor	147
5.4	Calculations of boundary layers	154
5.5	Decay of the scalar in a plane layer	159
6	THEORETICAL DEVELOPMENTS	163
6.1	Outline	163
6.2	Scaling laws	163
6.2.1	Theory for decay of no-slip flow with Neumann boundary conditions in a plane layer	164
6.2.2	Theory for decay in other configurations	166
6.3	Transfer of heat between cells of the flow	176
6.3.1	Approximating scalar decay in large-scale fields	177
6.3.2	Approximating scalar decay in a square cell	181
6.3.3	Extending Bloch wavenumbers	185
6.4	A cross section of the boundary layer	188
6.5	Summary and discussion	193
III	Approximating passive scalar evolution in polar co-ordinate system	196
7	PASSIVE SCALAR EVOLUTION IN POLAR CO-ORDINATE SYSTEM	197
7.1	Outline	197
7.2	Governing equations for no-slip flow near a corner	198

7.3	Approximating passive scalar evolution near to the corners	202
7.4	Simplifying the equation of averaged scalar field evolution	209
7.5	Numerical framework	219
7.5.1	Methodology	219
7.5.2	Identifying the mathematical problem	220
7.5.3	Numerical solutions and results	221
7.6	Decay rate near a sharp corner with $\alpha = \pi/4$	223
7.7	Transforming the polar co-ordinate results into the Cartesian co-ordinates	229
7.8	Summary	231
8	CONNECTION TO MOFFATT EDDIES	233
8.1	Outline	233
8.2	Background framework	234
8.2.1	Motion of fluid	234
8.2.2	Two-dimensional flow near a sharp corner	236
8.2.3	Viscous and resistive eddies near a sharp corner	237
8.2.4	Structure of Moffatt eddies near a sharp corner	239
8.2.5	Fourier series	241
8.3	Connection to Moffatt eddies	242
8.3.1	Specifying the flow	242
8.3.2	Specifying the components of diffusivity tensor and full mathematical problem	244
8.4	Numerical solutions and results	259
8.4.1	Decay of the scalar in the Moffatt problem	261
8.5	Summary	266

9 CONCLUSION	272
9.1 Summary and conclusion	272
9.2 Directions for future work	275

List of Tables

2.1	Group G of the symmetries	72
2.2	Test for simulation of the slip flow with the Dirichlet initial condition.	81
2.3	Suggested values for <code>npt</code> and <code>dt</code> for different values of κ related to both random and time-periodic flows.	82
3.1	Computed values for the decay rate of the scalar variance for the slip flow with Dirichlet boundary condition.	95
3.2	Computed values for the decay rate of the scalar variance for the slip flow with Neumann boundary condition.	100
3.3	Computed values for the decay rate of the scalar variance for the no-slip flow with Dirichlet boundary condition.	107
3.4	Computed values for the decay rate of the scalar variance for the no-slip flow with Neumann boundary condition.	109
4.1	Computed values for the decay rate of the scalar variance for the slip flow $\psi_{slip,pl}$ with Bloch wavenumbers: $M = N = 0.5$	123
4.2	Computed values for the decay rate of the scalar variance for the slip flow $\psi_{slip,pl}$ with Neumann boundary condition.	124
4.3	Computed values for the decay rate of the scalar variance for the slip flow with Bloch wavenumbers: $M = N = 0.5$	131
4.4	Summary of results: periodic flows.	140
4.5	Computed values for the decay rate of the scalar variance for the slip flow with Dirichlet boundary condition: periodic flow with $\omega = 1.141$	

4.6 Computed values for the decay rate of the scalar variance for the slip flow with Neumann boundary condition: periodic flow with $\omega = 1.142$

6.1 Summary of results: random flows. 164

8.1 The principal eigenvalue λ corresponding to a corner semi-angle α . . 241

8.2 Corresponding values for the corner angles (2α) based on the three-mode truncation (8.3.12): decay rate slopes C_D , scaling laws α_D and ζ for theoretical decay rate γ given by (8.4.12). 264

8.3 Corresponding values for the corner angles (2α) based on the six-mode truncation (8.3.13): decay rate slopes C_D , scaling laws α_D and ζ for theoretical decay rate γ given by (8.4.12). 265

List of Figures

1.1	Sample particle trajectories for the model stirring device of Aref (1984). Parameters are $\beta = 0.5$ and $\mu = 1.5$ (a-d) or 0.5 (e,f). Crosses indicate agitator positions (Aref, 1984).	27
1.2	Poincarè sections of particle positions showing changing motion from regular to chaotic. Parameters are $\beta = 0.5$ and (a) $\mu = 0.05$, (b) 0.10, (c) 0.125, (d) 0.15, (e) 0.20, (f) 0.35, (g) 0.50, (h) 1.0, (i) 1.5. Crosses indicate agitator positions (Aref, 1984).	28
1.3	Phases in the stirring of an initially square array of particles. Parameters are $\beta = 0.5$, $\mu = 1.0$. Panels shown are at times (a) $t = 0$, (b) 1, (c) 2, (d) 3, (e) 4, (f) 5, (g) 6, (h) 9, (i) 12 (Aref, 1984). . . .	30
1.4	Flow region. The dimensions of the cavity are width $W = 10.3\text{ cm}$ and height $H = 6.2\text{ cm}$ (Ottino, 1989).	31
1.5	Stretching of a line placed vertically, as shown in (a), in steady flows (b-d). The fluid is glycerine and the tracer is a fluorescent dye. The velocities of the top and bottom walls are $v_{top} = v_{bot} = 1.58\text{ cm/s}$ and $Re = 1.0$. In (b) both walls move in the same direction, in (c) both walls move in opposite directions, and (d) only the top wall moves. The total time of the experiment is 5 min. (Ottino, 1989). . .	33
1.6	Mixing of fluorescent dye in glycerine. The top and the bottom walls of the region move with $U = 2.69\text{ cm/s}$ ($Re = 1.7$). The pictures correspond to time perides $T = 15\text{ s}$ in (a) and 20 s in (b) (Ottino, 1989).	34

1.7	Stretching and folding of clouds in the wake of Guadalupe island. From the NASA archive.	36
1.8	Sea -ice distribution close to Kamchatka. From the NASA archive (http://images.jsc.nasa.gov/iams/images/earth/STS045/html/10068879.htm).	37
1.9	Particle trajectories in ABC flow. (Aref, 2002).	39
1.10	Poincaré section of a flow in three-dimensional showing islands through the mixer (Ottino, 1989).	42
1.11	Diagram showing the wall region of the flow with respect to Dirichlet boundary condition.	47
1.12	Scalar distribution of a random flow in a plane layer with slip bound- aries (left column) and no-slip boundaries (right column) with Neu- mann boundary conditions at $t =$ (a) 50, (b,c) 125, (d,e) 250, (f,g) 375, (h,i) 750 and (j) 1750 (Salman & Haynes, 2007).	49
1.13	(a) Chaotic mixing experiment in a closed vessel. The figure-eight stirring protocol. (b) Poincaré section obtained numerically for the corresponding flow (Gouillart <i>et al.</i> , 2007).	50
1.14	Successive stages of homogenisation for a blob of dye stirred by the figure-8 protocol (Gouillart <i>et al.</i> , 2008).	51
1.15	Numerical simulations of a flow in an open channel with a figure- eight rod stirring protocol. (Thiffeault <i>et al.</i> , 2008).	53
2.1	Within \mathbb{T}^2 are depicted (a) the square \mathcal{C} and the domain \mathcal{D} , together with the functions (b) $\phi_{1,1}$, (c) $\phi_{1,3}$ and (d) $\phi_{3,1}$	58
2.2	Stream functions (a) $\phi_{1,3}^2$, (b) $\phi_{3,1}^2$	60
2.3	Stream functions (a) $\phi_{1,3} \sin t + \phi_{3,1} \cos t$, (b) $\phi_{1,3}^2 \sin t + \phi_{3,1}^2 \cos t$; $t = \pi/2$	63

2.4	Stream functions (a) $\phi_{1,3} \sin t + \phi_{3,1} \cos t$, (b) $\phi_{1,3}^2 \sin t + \phi_{3,1}^2 \cos t$; $t = \pi/4$	63
2.5	Stream functions (a) $\phi_{1,3} \sin t + \phi_{3,1} \cos t$, (b) $\phi_{1,3}^2 \sin t + \phi_{3,1}^2 \cos t$; $t = \pi/6$	63
2.6	Stream functions (a) $\phi_{1,3} \sin t + \phi_{3,1} \cos t$, (b) $\phi_{1,3}^2 \sin t + \phi_{3,1}^2 \cos t$; $t = 3\pi/4$	64
3.1	Initial scalar field $\sigma_N = \phi_{1,1}^2 - 1$	87
3.2	Scalar field for $(\psi_{\text{slip}}, \sigma_D)$ with $\kappa = 0.001$ with times at (a) $t =$ 250, (b) 500 and (c) 750. In the colour scale values go from black (minimum) to red (maximum) with zero green.	88
3.3	Scalar field for $(\psi_{\text{slip}}, \sigma_D)$ with $\kappa = 0.001$ with times at (a-c) $t = 1,$ 2, 3, (d-f) $t = 5, 10, 15$, (g-i) $t = 10, 20, 30$ and (j-l) $t = 20, 40$ and 60.	89
3.4	Plots for $(\psi_{\text{slip}}, \sigma_D)$ against time t of (a) $V(t)$, (b) $\tilde{\gamma}(t)$, and (c) $\bar{\gamma}(t)$ (solid), $\bar{\gamma}_{\min}(t)$ and $\bar{\gamma}_{\max}(t)$ (dashed).	91
3.5	Plots (a) for $(\psi_{\text{slip}}, \sigma_D)$ showing $\bar{\gamma}$ (circles) and $\bar{\gamma} \pm \Delta\gamma$ (plus signs) against κ , and (b) for $(\psi_{\text{slip}}, \sigma_N)$ showing $\bar{\gamma}$ (circles), and $\bar{\gamma} \pm \Delta\gamma$ (plus signs) against $\sqrt{\kappa}$. In (a) the solid line is a fit with slope 0.546 while the dashed line has slope 0.5; in (b) the solid line has slope 1.6. 93	93
3.6	Scalar field for $(\psi_{\text{slip}}, \sigma_N)$ with $\kappa = 0.001$ with (a-c) losing symmetry and (d-f) imposing symmetry at (a,d) $t = 100$, (b,e) 200 and (c,f) 300.	96
3.7	Plots for $(\psi_{\text{slip}}, \sigma_N)$ against time t of (a,d) $\log V(t)$, (b,e) $\tilde{\gamma}(t)$, and (c,f) $\bar{\gamma}(t)$. Panels of the flow show (a-c) losing symmetry and (d-f) imposing symmetry.	96

3.8 Scalar field for $(\psi_{\text{slip}}, \sigma_N)$ with $\kappa = 0.001$ with time at (a-c) $t = 1, 2, 3$, (d-f) $t = 5, 10, 15$, (g-i) $t = 10, 20, 30$ and (j-l) $t = 20, 40$ and 60. 97

3.9 Scalar field for (a-c) $(\psi_{\text{no-slip}}, \sigma_D)$ with $\kappa = 0.001$. With time (a-c) $t = 1, 2, 3$, (d-f) $t = 4, 8, 12$, (g-i) $t = 5, 10, 15$ and (j-l) $t = 20, 40$, and 60. 103

3.10 Scalar field for $(\psi_{\text{no-slip}}, \sigma_N)$ with $\kappa = 0.001$. With time (a-c) $t = 1, 2, 3$, (d-f) $t = 4, 8, 12$, (g-i) $t = 5, 10, 15$ and (j-l) $t = 20, 40$ and 60. 104

3.11 Plots for (a-c) $(\psi_{\text{no-slip}}, \sigma_D)$ and (d-f) $(\psi_{\text{no-slip}}, \sigma_N)$ against time t of (a,d) $\log V(t)$, (b,e) $\tilde{\gamma}(t)$, and (c,f) $\bar{\gamma}(t)$ 106

3.12 Plot for (a) $(\psi_{\text{no-slip}}, \sigma_D)$ and (b) $(\psi_{\text{no-slip}}, \sigma_N)$ of $\bar{\gamma}$ (circles) and $\bar{\gamma} \pm \Delta\gamma$ (plus signs) against κ . The solid lines are fits with slope (a) 0.765 and (b) 0.625. The dashed lines have slope 0.75 in (a) and 0.67 in (b). 108

4.1 Geometry of a plane layer embedded in 2π -periodic space. 114

4.2 Initial scalar field $\sigma_{\frac{1}{2}D} = \cos \frac{1}{2}(y - x)$ 115

4.3 Plots of the stream functions (a) $\phi_{1,3}(x - ct, y - ct)$ and (b) $\phi_{3,1}(x + ct, y + ct)$ at $t = \pi/4$ with $c = 1$ 116

4.4 Scalar field for $(\psi_{\text{slip,pl}}, \sigma_N)$ with (a-c) losing symmetry and (d-f) imposing symmetry at $t =$ (a,d) 75, (b,e) 150, and (c,f) 225. 117

4.5 Plots for $(\psi_{\text{slip,pl}}, \sigma_N)$ against time t of (a,d) $\log V(t)$, (b,e) $\tilde{\gamma}(t)$, and (c,f) $\bar{\gamma}(t)$. Panels (a-c) losing symmetry and (d-f) imposing symmetry. 118

4.6 Scalar field for (a-c) $(\psi_{\text{slip,pl}}, \sigma_N)$ with $\kappa = 0.001$ at (a-c) $t = 1, 2, 3$, (d-f) 5, 10, 15, (g-i) 10, 20, 30 and (j-l) 20, 40 and 60. 119

4.7 Scalar field for (a-c) $(\psi_{\text{slip,pl}}, \sigma_{\frac{1}{2}D})$ and (d-f) $(\psi_{\text{slip,pl}}, \sigma_N)$ with $\kappa = 0.001$ at (a,d) $t = 100$, (b,e) 200 and (c,f) 300. 120

4.8	Plots (a) for $(\psi_{slip,pl}, \sigma_{\frac{1}{2}D})$ showing $\bar{\gamma}$ (circles) and $\bar{\gamma} \pm \Delta\gamma$ (plus signs) against κ , and (b) for $(\psi_{slip,pl}, \sigma_N)$ showing $\bar{\gamma}$ (circles), and $\bar{\gamma} \pm \Delta\gamma$ (plus signs) against $\sqrt{\kappa}$. The solid lines are fits with slopes (a) 0.53 and (b) 1.27, while in (a) the dashed line has slope 0.5.	122
4.9	Stream functions: (a) $\phi_{1,3}(x - ct, y - ct)^2$ and (b) $\phi_{3,1}(x + ct, y + ct)^2$ at $t = \pi/4$ with $c = 1$	125
4.10	Scalar field for $(\psi_{no-slip,pl}, \sigma_N)$ with $\kappa = 0.001$ at (a-c) $t = 1, 2, 3$, (d-f) $t = 5, 10, 15$ and (g-i) $t = 10, 20$ and 30	126
4.11	Plots for $(\psi_{no-slip,pl}, \sigma_N)$ against time t of (a) $\log V(t)$, (b) $\tilde{\gamma}(t)$, and (c) $\bar{\gamma}(t)$	127
4.12	Scalar field for (a-c) $(\psi_{no-slip,pl}, \sigma_{\frac{1}{2}D})$ and (d-f) $(\psi_{no-slip,pl}, \sigma_N)$ with $\kappa = 0.001$ at (a,d) $t = 100$, (b,e) 200 and (c,f) 300	128
4.13	Plot for (a) $(\psi_{no-slip,pl}, \sigma_{\frac{1}{2}D})$ and (b) $(\psi_{no-slip,pl}, \sigma_N)$ of $\bar{\gamma}$ (circles) and $\bar{\gamma} \pm \Delta\gamma$ (plus signs) against κ for the case. The solid line is a fit with slope (a) 0.718, (b) 0.43 while the dashed line has slope 0.75 in (a) and 0.5 in (b).	129
4.14	Scalar field for (a-c) $(\psi_{slip}, \sigma_{\frac{1}{2}D})$, (d-f) $(\psi_{no-slip}, \sigma_{\frac{1}{2}D})$ with $\kappa = 0.001$ at (a) $t = 25$, (b) 50 , (c) 75 , (d) $t = 10$, (e) 20 and (f) 30	130
4.15	Plot for (a) $(\psi_{slip}, \sigma_{\frac{1}{2}D})$ and (b) $(\psi_{no-slip}, \sigma_{\frac{1}{2}D})$ of $\bar{\gamma}$ (circles) and $\bar{\gamma} \pm \Delta\gamma$ (plus signs) against κ . The solid line is a fit with slope (a) 0.553, (b) 0.762 and the dashed line has slope (a) 0.5, (b) 0.75.	132

4.16	Poincaré sections for the time-periodic flows (a) ψ_{slip} and (b) $\psi_{\text{no-slip}}$ with $\omega = 1$. Panel (c) shows a part of a section zoomed in on the boundary, using coordinates $2^{-1/2}(x + y + \pi)$ (horizontal) and $2^{-1/2}(-x + y + \pi)$ (vertical); note the small range of the vertical scale, from 0 to 0.1, compared with the horizontal scale, from 0 to $\pi\sqrt{2}$	135
4.17	Scalar field for (a–c) $(\psi_{\text{no-slip}}, \sigma_{\text{D}})$ and (d–f) $(\psi_{\text{slip}}, \sigma_{\text{N}})$ with $\kappa = 0.001$ at (a,d) $t = 2\pi$, (b,e) 4π and (c,f) 6π	136
4.18	Plots for $(\psi_{\text{slip}}, \sigma_{\text{N}})$ and $(\psi_{\text{slip}}, \sigma_{\text{D}})$ against time t of (a,d) $\log V(t)$, (b,e) $\tilde{\gamma}(t)$, and (c,f) $\bar{\gamma}(t)$	137
4.19	Scalar field for (a–c) $(\psi_{\text{slip}}, \sigma_{\text{D}})$ and (d–f) $(\psi_{\text{no-slip}}, \sigma_{\text{N}})$ with $\kappa = 0.001$ at (a,d) $t = 10$, (b,e) 20 and (c,f) 30	138
4.20	Plots of γ against κ for the time-periodic flows. We have the cases (a) $(\psi_{\text{slip}}, \sigma_{\text{D}})$, with solid and dashed lines of slopes 0.53 and 0.5, (b) $(\psi_{\text{slip}}, \sigma_{\text{N}})$, slope 0.126 (c) $(\psi_{\text{no-slip}}, \sigma_{\text{D}})$, slopes 0.765 and 0.75, and (d) $(\psi_{\text{no-slip}}, \sigma_{\text{N}})$, slope 0.784.	139
6.1	Log-linear plot for scalar decay rate (a) $\kappa^{-1/2}\gamma(\kappa)$ against κ for no-slip flow $\psi_{\text{no-slip,pl}}$ with Neumann boundary conditions. Panel (b) shows $\kappa^{-3/4}\gamma(\kappa)$ against κ for no-slip flow $\psi_{\text{no-slip,pl}}$ and (c) $\kappa^{-1/2}\gamma(\kappa)$ against κ for slip flow $\psi_{\text{slip,pl}}$, both with Dirichlet boundary conditions. In each case numerical results are given by markers (solid lines) and theoretical results from (6.2.1), (6.2.17) and (6.2.48) are dashed.	165
6.2	Diagram showing the x' and y' axes for a no-slip flow in a plane layer domain.	168

6.3	Diagram showing the x'' and y' axes for the no-slip flow in a square domain.	172
6.4	Diagram for the transfers of the scalar field between cells.	179
6.5	Diagram showing a heat transfers between cells.	182
6.6	Log-log plot for the numerical and theoretical decay rate $\gamma(\kappa)$ against κ for the no-slip flow $\psi_{\text{no-slip}}$ with Dirichlet boundary conditions, corresponding to the Bloch wavenumbers $M = 0$ and $N = 1/2, 3/8, 2/8, 1/8, 1/16,$ and $1/32$ for $\kappa = 0.1, 0.01$ and 0.001 . Numerical result for the flow (circles) is compared with theoretical results (solid) from (6.3.30). The factor C in (6.3.30) is determined from (6.3.16); $C = \kappa_{eff} = \gamma(\kappa)/N^2$ for each value of N	186
6.7	Log-log plot for the numerical and theoretical decay rate $\gamma(\kappa)$ against κ for the slip flow ψ_{slip} with Dirichlet boundary conditions, corresponding to the Bloch wavenumbers $M = 0$ and $N = 1/2, 3/8, 2/8, 1/8, 1/16, 1/32$ and $1/64$ for $\kappa = 0.1, 0.01, 0.001$ and 0.0001 . Numerical result for the flow (circles) is compared with theoretical results (solid) from (6.3.30). The factor C in (6.3.30) is determined from (6.3.16); $C = \kappa_{eff} = \gamma(\kappa)/N^2$ for each value of N	187
6.8	Plots of (a) D_{xx} , (b) D_{yy} and (c) D_{xy} for the slip flow in a square domain.	189
6.9	D_{xx} , (b) D_{yy} and (c) D_{xy} for the no-slip flow in a square domain.	190
6.10	Plots of (a) D_{xx} , (b) D_{yy} and (c) D_{xy} for the no-slip flow in a plane layer domain.	191

6.11	Averaging scalar field obtained numerically for the no-slip flow $\psi_{no-slip}$ with Dirichlet boundary condition in a plane layer with $M = N = 0.5$ and $\kappa = 0.001$ at $t = 250$	192
6.12	Plots of averaged $\bar{\sigma}_{theo}(Y)$ (solid) and $\bar{\sigma}_{num}(Y)$ (dashed), against Y ; $Y = y'(\mu/\kappa)^{1/4}$ corresponding to (a) $\kappa = 0.1$, (b) $\kappa = 0.02$, (c) $\kappa = 0.005$, (d) $\kappa = 0.001$, (e) $\kappa = 0.0002$ and (f) $\kappa = 0.0001$ for the no-slip flow with Dirichlet boundary condition. $\bar{\sigma}_{theo}$ and $\bar{\sigma}_{num}$ refers to the averaged scalar field obtained theoretically and numerically, respectively.	194
7.1	Velocity components with respect to (x, y) and (r, θ) axes.	199
7.2	Solution profiles computed for averaged scalar field $\bar{\sigma}_0(r, t)$ against r based on (7.3.29) and resulting from (7.7.1) at different times; $0 \leq t \leq 4$ with 201 r -meshpoints between 0 and 10.	222
7.3	Solution profile computed for the averaged scalar field $\bar{\sigma}_0(r, t)$ against r based on (7.3.29) with the three-mode truncation resulting from (7.7.1) at $t=0.3$ with 201 r -meshpoints between 0 and 10.	223
7.4	Plot of $\log \bar{\sigma}(r, t)$ at $r = 0.45$ against time t ; $0 \leq t \leq 5$ with 201 r -meshpoints between 0 and 10 for the no-slip flow $\psi_{no-slip}$ with Neumann boundary condition. The fit slope C_D is 3.1.	224
7.5	Solution profile based on (7.3.29) with the three-mode truncation resulting from (7.7.1) and computed for the averaged scalar field $\bar{\sigma}_4(r, t)$ against r ; panel (a) at different times $0 \leq t \leq t_{max}$; $t_{max}=4$ and (b) at $t=0.3$ with 201 r -meshpoints between 0 and 10.	225

- 7.6 Solution profile based on (7.3.29) with the three-mode truncation resulting from (7.7.1) and computed for the averaged scalar field $\bar{\sigma}_8(r, t)$ against r ; panel (a) at different times $0 \leq t \leq t_{max}$; $t_{max}=4$ and (b) at $t=0.3$ with 201 r -meshpoints between 0 and 10. The vertical axis is scaled by 10^{-3} in (b). 226
- 7.7 Solution profile based on (7.3.29) with the six-mode truncation resulting from (7.7.2) and computed for the averaged scalar field (a) $\bar{\sigma}_0(r, t)$ and (b) $\bar{\sigma}_4(r, t)$ against r at $t=0.9$ with 201 r -meshpoints between 0 and 10. The vertical axis is scaled by 10^{-3} in (b). . . . 227
- 7.8 Solution profile based on (7.3.29) with the six-mode truncation resulting from (7.7.2) and computed for the averaged scalar field (a) $\bar{\sigma}_8(r, t)$ and (b) $\bar{\sigma}_{12}(r, t)$ against r at $t=0.9$ with 201 r -meshpoints between 0 and 10. The vertical axis in both panels is scaled by 10^{-4} . 228
- 7.9 Solution profile based on (7.3.29) with the six-mode truncation resulting from (7.7.2) and computed for the averaged scalar field (a) $\bar{\sigma}_{16}(r, t)$ and (b) $\bar{\sigma}_{20}(r, t)$ against r at $t=0.9$ with 201 r -meshpoints between 0 and 10. The vertical axis in both panels is scaled by 10^{-5} . 229
- 7.10 Plot of $\log \gamma(\kappa)$ against κ for the no-slip flow $\psi_{no-slip}$ with Neumann boundary condition. Numerical result is given by markers (solid line with circles) and theoretical results from (7.6.12) approximated via three-mode truncation are solid and six-mode truncation (dashed). . 230

7.11	Plot of scaled decay rate $\kappa^{-\frac{2}{3}}\gamma(\kappa)$ against κ for the no-slip flow $\psi_{no-slip}$ with Neumann boundary condition. Numerical result is given by markers (solid line with circles) and approximations of theoretical results via six-mode truncation are solid and three-mode truncation (dashed).	231
7.12	Plots of the scalar distribution of the no-slip flow $\psi_{no-slip}$ with Neumann boundary condition near to the corners in the Cartesian coordinate system. Panel (a) shows the approximation of such distribution resulting from (7.7.1), while in (b) it is given by (7.7.2). . . .	232
8.1	Flow in a corner between rigid boundaries, induced by an arbitrary two-dimensional agitation at a large distance (Moffatt, 1964). . . .	236
8.2	Plots of (a) solution profiles of averaged scalar field $\bar{\sigma}(r, t)$ against r for $0 \leq t \leq 2$ for the flow near corner regions of a semi-angle $\alpha = \pi/4$ and $\lambda = 3.73959 + 1.1191i$ with a three-mode truncation resulting from (8.3.12). In (b) $\log \bar{\sigma}(r, t)$ is plotted at $r = 0.45$ against time t ; $0 \leq t \leq 10$ with 201 r -meshpoints between 0 and 10. The fit slope in (b) is 9.06.	258
8.3	Plots of (a) solution profiles of averaged scalar field $\bar{\sigma}(r, t)$ against r for $0 \leq t \leq 2$ for the flow near corner regions of a semi-angle $\alpha = \pi/6$ and $\lambda = 5.05933 + 1.95205i$ with a three-mode truncation resulting from (8.3.12). In (b) $\log \bar{\sigma}(r, t)$ is plotted at $r = 0.45$ against time t ; $0 \leq t \leq 10$ with 201 r -meshpoints between 0 and 10. The fit slope in (b) is 10.24.	259

8.4 Plots of (a) solution profiles of averaged scalar field $\bar{\sigma}(r, t)$ against r for $0 \leq t \leq 2$ for the flow near corner regions of a semi-angle $\alpha = \pi/3$ and corresponding $\lambda = 3.09414 + 0.60458i$ with a three-mode truncation resulting from (8.3.12). In (b) $\log \bar{\sigma}(r, t)$ is plotted at $r = 0.45$ against time t ; $0 \leq t \leq 10$ with 201 r -meshpoints between 0 and 10. The fit slope in (b) is 6.59. 260

8.5 Solution profiles based on (8.3.89) with a three-mode truncation resulting from (8.3.12) and computed for averaged scalar field (a) $\bar{\sigma}_0(r, t)$, (b) $\bar{\sigma}_4(r, t)$ and (c) $\bar{\sigma}_8(r, t)$ against r at $t = 0.1$ with $\alpha = \pi/4$ and $\lambda = 3.73959 + 1.1191i$ and 201 r -meshpoints between 0 and 10. The vertical axis is scaled by 10^{-3} in (c). 262

8.6 Solution profile based on (8.3.89) with a six-mode truncation resulting from (8.3.13) and computed for averaged scalar field (a) $\bar{\sigma}_0(r, t)$, (b) $\bar{\sigma}_4(r, t)$ and (c) $\bar{\sigma}_8(r, t)$ against r at $t = 0.9$ with $\alpha = \pi/4$ and $\lambda = 3.73959 + 1.1191i$ and 201 r -meshpoints between 0 and 10. The vertical axis is scaled by (a) 10^{-4} and (b,c) 10^{-5} 267

8.7 Solution profile based on (8.3.89) with a six-mode truncation resulting from (8.3.13) and computed for averaged scalar field (a) $\bar{\sigma}_{12}(r, t)$, (b) $\bar{\sigma}_{16}(r, t)$ and (c) $\bar{\sigma}_{20}(r, t)$ against r at $t = 0.9$ with $\alpha = \pi/4$ and $\lambda = 3.73959 + 1.1191i$ and 201 r -meshpoints between 0 and 10. The vertical axis is scaled by (a,b) 10^{-6} and (c) 10^{-7} 268

- 8.8 Plots of the scalar distribution of the flow near to the corner of a semi-angle $\alpha = \pi/3$ and $\lambda = 3.09414 + 0.60458i$ in the Cartesian co-ordinate system. Panel (a) shows the approximation of such distribution resulting from (8.3.12), while in (b) it is approximated by (8.3.13). 269
- 8.9 Plots of the scalar distribution of the flow near to the corner of a semi-angle $\alpha = \pi/4$ and $\lambda = 3.73959 + 1.1191i$ in the Cartesian co-ordinate system. Panel (a) shows the approximation of such distribution resulting from (8.3.12), while in (b) it is approximated by (8.3.13). 270
- 8.10 Plots of the scalar distribution of the flow near to the corner of a semi-angle $\alpha = \pi/6$ and $\lambda = 5.05933 + 1.95205i$ in the Cartesian co-ordinate system. Panel (a) shows the approximation of such distribution resulting from (8.3.12), while in (b) it is approximated by (8.3.13). 271

1

INTRODUCTION AND MOTIVATION

1.1 History of chaotic mixing

“When you stir your coffee, you don’t usually put the spoon down and spin it in place! Rather, you move it about in circular or figure-eight like motion.” (Aref, 2002).

The work on advection in two-dimensional time dependent flows and on advection in steady three-dimensional flows is related to the development of the novel phenomenon of the mixing process called *Chaotic Advection* by Hassan Aref in the early 1980s.

“The term ‘chaotic advection’ was first introduced in the title of an abstract for the 35th annual meeting of the American Physical Society (APS) Division of Fluid Dynamics (DFD) in 1982. The main reference, a Journal of Fluid Mechanics paper published in 1984, may be the true ‘birth date’ of the term.” (Aref, 2002).

Chapter 1. INTRODUCTION AND MOTIVATION

Furthermore, the combined NATO and European Geophysical Society workshop on *Chaotic Advection, Tracer Dynamics and Turbulent Dispersion* held in Italy in 1993 was the first major meeting to have “Chaotic Advection” in the title. In fact, the first appearance of the two words ‘Stirring’ and ‘Mixing’ was in a paper for Carl Eckart in journal of Marine Research to distinguish the “mechanical” and “molecular” physical processes that produce mixing (Aref, 2002). In that, Eckart wrote:

“the effect of advection is appropriately called stirring” and “the effect of conduction on or diffusion is to decrease the mean value of the gradients. This is appropriately called mixing. Ordinarily, the early stages of the process... will be dominated by the advective processes... These may so increase the mean gradient that the mixing process will ultimately dominate... Viscosity, if not counteracted by other factors, tends to stop the stirring... before an appreciable amount of mixing can be occurred”.

Today, the name of Carl Eckart is associated with the Wigner-Eckart theorem in quantum mechanics.

However, chaotic advection has also been named by different terms: ‘Lagrangian turbulence’ (Dombre *et al.*, 1986; Chaiken *et al.*, 1987), ‘Chaotic mixing’ (Chien *et al.*, 1986) and ‘Chaotic convection’ (Ott and Antonsen, 1988). In fact, earlier work on advection has been done early in the 1960s by Arnol’d and Hénon on steady three-dimensional flows. This work - unfortunately - had not been widely appreciated despite related ideas and results it had contained and consequently “Chaotic Advection” had to wait another twenty years to appear in Aref (1984). This was the first time that this term has been used as a scientific concept and one of the key words of papers and journals related to chaotic mixing.

We conclude this section with this sentence quoted from Aref (2002): “*Essentially what is being proposed is the existence of a new advective regime, intermediate between turbulent and laminar advection, which one might call ‘Chaotic Advection’.*”

1.2 Examples of Aref and Ottino

In this section we introduce numerical and experimental examples of mixing invented by Aref (1984), (Ottino *et al.*, 1986) and Ottino (1989) to illustrate ‘chaotic advection’.

1- Blinking vortex (BV) flow:

In his early work on advection by interacting point vortices, Aref (1984) introduced the blinking vortex **BV** flow. This model is mathematically described by a flow in a circular boundary of radius a . The system consists of two fixed point vortices separated by a fixed distance $2b$ shown in Fig. 1.1. The agitating vortex with the position $Z(t)$ is generally given as a function of time t ,

$$Z(t) = b f(t/T), \quad (1.2.1)$$

where b and T are constants with an amplitude $b < a$ and f is a real periodic function with period unity. The vortex strength of the agitator is given by Γ and in this case the strength of its image (outside the circular boundary) will be given by $-\Gamma$. Both, the agitator and its image provides a system of unsteady flow. This idealised model is completely parametrised by two quantities, β which gives the dimensionless amplitude for the location of the agitator,

$$\beta = \frac{b}{a}, \quad (1.2.2)$$

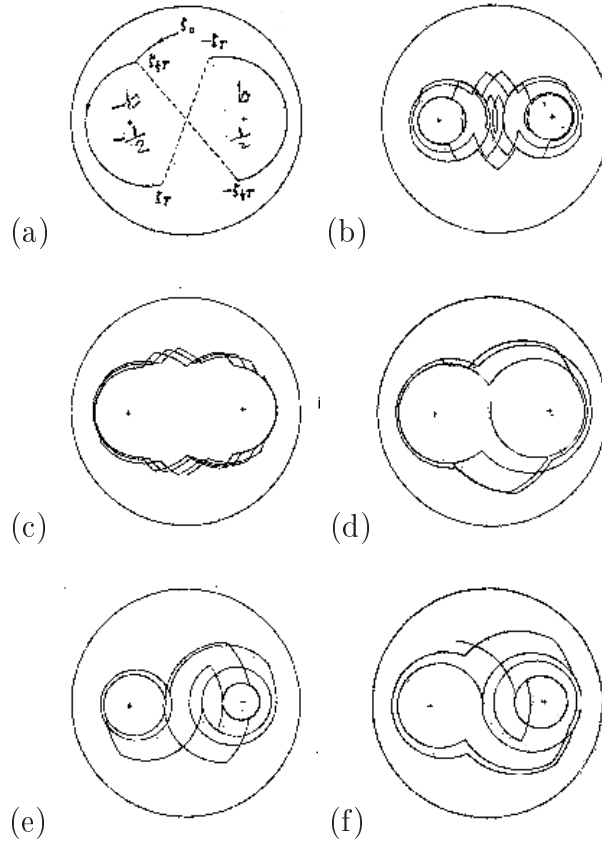


Figure 1.1: Sample particle trajectories for the model stirring device of Aref (1984). Parameters are $\beta = 0.5$ and $\mu = 1.5$ (a-d) or 0.5 (e,f). Crosses indicate agitator positions (Aref, 1984).

and μ which is the period of its motion,

$$\mu = \frac{\Gamma T}{2\pi a^2}. \quad (1.2.3)$$

Particularly, the motion of the stirrer has been considered by

$$Z(t) = \begin{cases} +b & ; nT \leq t < (n + 1/2)T, \\ -b & ; (n + 1/2)T \leq t < (n + 1)T, \end{cases}$$

for $n = 0, \pm 1, \pm 2, \dots$. This corresponds to a stirrer that jumps back and forth

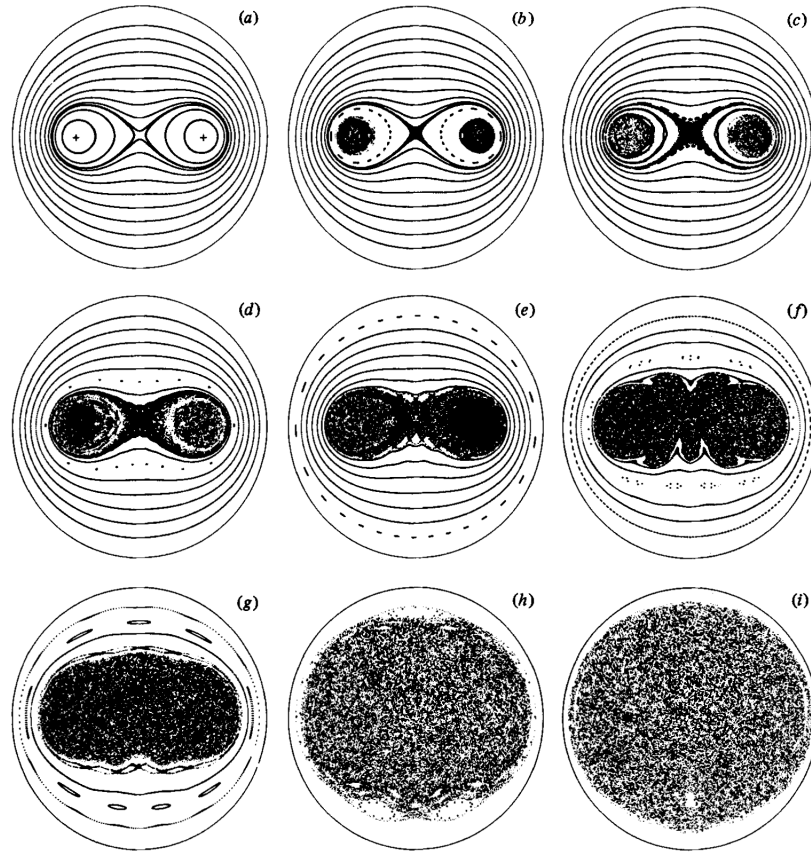


Figure 1.2: Poincaré sections of particle positions showing changing motion from regular to chaotic. Parameters are $\beta = 0.5$ and (a) $\mu = 0.05$, (b) 0.10, (c) 0.125, (d) 0.15, (e) 0.20, (f) 0.35, (g) 0.50, (h) 1.0, (i) 1.5. Crosses indicate agitator positions (Aref, 1984).

between the two fixed positions, $+b$ and $-b$ depending on the choice of f . The agitator is assumed to be ‘on’ when the corresponding point in the flow domain works as a point vortex. Under a single stirrer if a particle moves very close to one of the vortices, its motion draws a circle in the flow that dominates around the point. This flow is produced by this point vortex modulo the slip boundary

condition on the bounding circle. The flow stops immediately when the agitator is ‘turned off’. Through this system, an incompressible two-dimensional inviscid unsteady flow has been considered.

In order to demonstrate chaotic behaviour, this model of flows has been studied through several simulations. The parameters considered in this protocol are $\Gamma = 2\pi$ and $a = 1$ so that $\beta = b$ and $\mu = T$ in (1.2.2) and (1.2.3), respectively. These parameters, β and μ control the efficiency of the stirring protocol as shown in Fig. 1.2. The time interval was taken to equal the period of $Z(t)$ in (1.2.1).

Several sample particle trajectories according to the parameters $\beta = 0.5$ and $\mu = 1.5$ (a-d) or 0.5 (e,f) are shown in Fig. 1.1. As seen in this figure, the two point vortices blink ‘on’ and ‘off’ periodically. A length of circular arc is drawn around each agitator and when the agitator is ‘on’, the particle moves around it in a family of circles giving a description of its motion.

Figure 1.2 shows some numerical results obtained according to this model of flows. For all the cases shown in this figure $\beta = 0.5$ and the apparent results differ from each other by varying the time interval $\mu(= T)$. This figure shows regular formulations of curves presented by two vortex agitators fixed at $Z = 1/2$ and $Z = -1/2$. The streamlines of the particle motion can be seen in panel(a) of this figure where $\mu = T$ is short and so is approximately small as two agitators being ‘on’ simultaneously. The regular formations vanish gradually as μ is increased, turning the behaviour to a chaotic motion which sets in with $\mu = 0.1$ (panel (b)). This chaotic component of the phase space increases as μ increases to 1.5 as seen in panel (i) where no regularity of curves can appear except may be near the boundaries. This actually leads to an efficient stirring where particles may be found everywhere in the chaotic region of the flow.

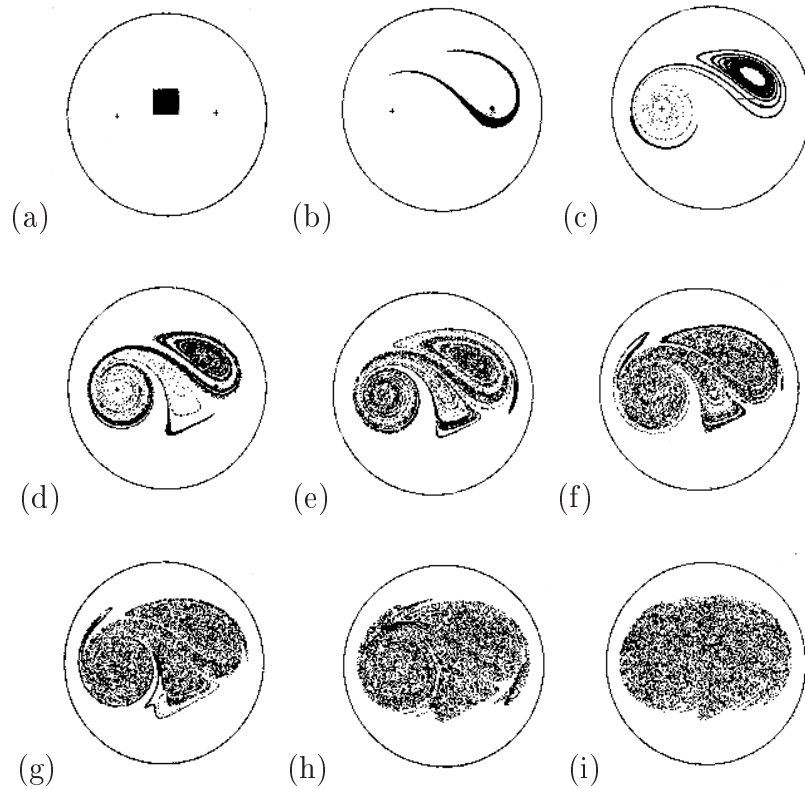


Figure 1.3: Phases in the stirring of an initially square array of particles. Parameters are $\beta = 0.5$, $\mu = 1.0$. Panels shown are at times (a) $t = 0$, (b) 1, (c) 2, (d) 3, (e) 4, (f) 5, (g) 6, (h) 9, (i) 12 (Aref, 1984).

Figure 1.3 shows different phases in the stirring of an initially square array marked by 10000 particles with parameters $\beta = 0.5$ and $\mu = 1.0$. These plots are obtained at times started with $t = 0$ as in panel(a) where mixing has been marked by dark and white flows. As we can see, a complicated behaviour of a scalar is observed through the phase spaces leading to a formulation of fine scales shown in this figure.

However, the blinking vortex flow is considered the simplest possible model of flow in which chaotic advection can be found. The motivation for this model relates to a study by Aref & Pomphrey (1980) on interacting point vortices, where four point

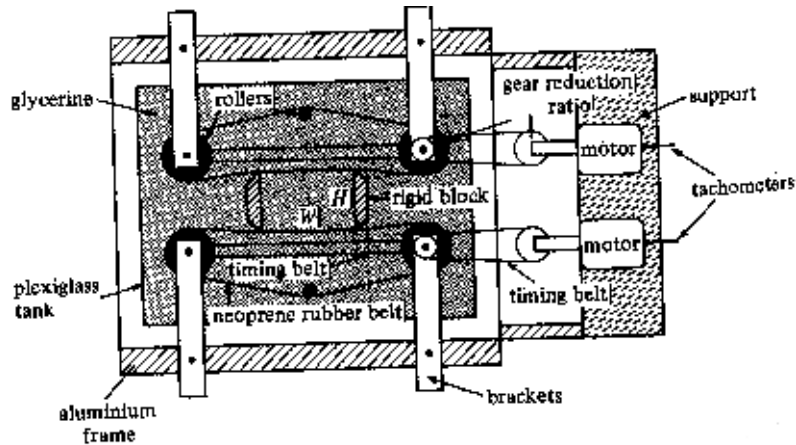


Figure 1.4: Flow region. The dimensions of the cavity are width $W = 10.3\text{ cm}$ and height $H = 6.2\text{ cm}$ (Ottino, 1989).

vortices were considered to produce chaotic advection. Furthermore, the ‘blinking-rotlet flow’ studied by Meleshko & Aref (1996) is considered as an extension to this flow.

2- Mixing of fluorescent dye in glycerine:

Most experiments on mixing in flows were carried out using cavity flows. These experiments are conducted to study several classes of steady (Fig. 1.5) and time-periodic flow (Fig. 1.6). Most interesting are experiments of mixing in two-dimensional flows conducted chemically by Ottino (1989) where mixing was displayed visually by a fluorescent dye dissolved in glycerine. This system consists of a rectangular region capable of producing a two-dimensional velocity field in the $x-y$ plane as shown in Fig. 1.5 and Fig. 1.6. This experimental system is based on an improved system (Fig. 1.4) described by Chien, Rising & Ottino (1986). This system consists (as shown in Fig. 1.4) of two sets of roller wheels connected by belts driven separately by motors and two bands acting as moving walls. Entirely,

this system is sunk in a tank of one foot depth filled with glycerine. This tank has been chosen suitably to visualise mixing. The size of the region of the flow can be changed to a maximum area 5×5.5 inches. In these experiments, the velocity of the top and bottom walls is denoted by v_{top} and v_{bot} , respectively. These velocities are generally functions in time and specified using a computer control system.

The first experiment was conducted using steady flows as shown in Fig. 1.5. Here, the velocities of the top and bottom walls are $v_{top} = v_{bot} = 1.58 \text{ cm/s}$ with Reynolds number $Re = 1$. This figure shows poor mixing resulting by a tracer (fluorescent dye) placed vertically (panel (a)) in a steady flow (glycerine) (b-d). The stretching of the flow clearly can be seen in panels (b-d) where the motion is considered to be integrable as the flow is steady. Both walls in (b) in this figure are moved in the same direction with velocities $v_{top} = v_{bot} = 1.58 \text{ cm/s}$, in (c) the walls are moved in opposite direction with $v_{top} = -v_{bot} = 1.58 \text{ cm/s}$ and in (d) just the top wall has been moved with $v_{top} = 1.58 \text{ cm/s}$ and $v_{bot} = 0$.

The second experiment (Fig. 1.6) was performed in a time-periodic cavity flow where mixing was displayed by injecting the fluorescent dye $2 - 5 \text{ mm}$ below the surface of the fluid. This system shows the evolution of a blob placed at the position $x = 2.2 \text{ cm}$ and $y = 3.1 \text{ cm}$ of the flow region using a higher Reynolds number $Re = 1.7$. In this experiment the top and the bottom walls have been moved at the same time with some time-dependence where the velocities of the walls were considered as

$$v_{top} = U \cos^2 \pi t/T, \quad (1.2.5)$$

$$v_{top} = -U \sin^2 \pi t/T. \quad (1.2.6)$$

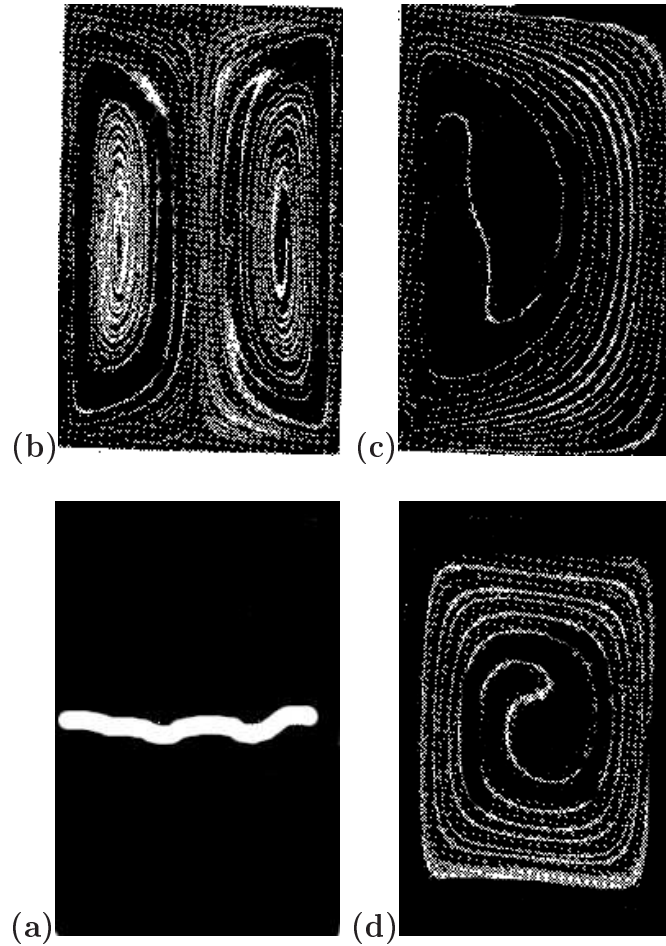


Figure 1.5: Stretching of a line placed vertically, as shown in (a), in steady flows (b-d). The fluid is glycerine and the tracer is a fluorescent dye. The velocities of the top and bottom walls are $v_{top} = v_{bot} = 1.58 \text{ cm/s}$ and $Re = 1.0$. In (b) both walls move in the same direction, in (c) both walls move in opposite directions, and (d) only the top wall moves. The total time of the experiment is 5 min. (Ottino, 1989).

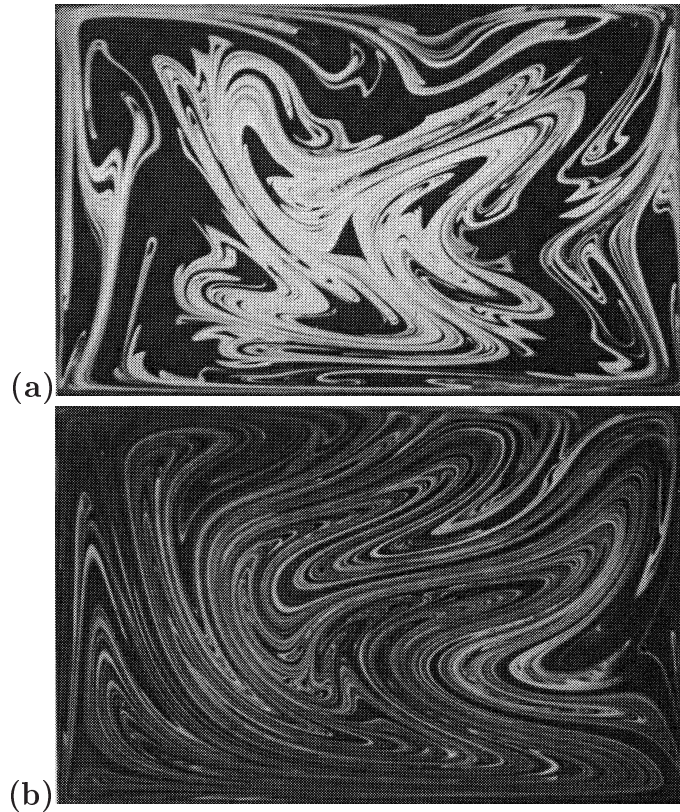


Figure 1.6: Mixing of fluorescent dye in glycerine. The top and the bottom walls of the region move with $U = 2.69 \text{ cm/s}$ ($Re = 1.7$). The pictures correspond to time periods $T = 15s$ in (a) and $20s$ in (b) (Ottino, 1989).

where the velocity $U = 2.69 \text{ cm/s}$ and time periods $T = 15s, 20s$ in panel (a) and (b), respectively in Fig. 1.6.

An important difference between the two experiments shown in Fig. 1.5 and Fig. 1.6 is that mixing appears very slow in Fig. 1.5. Here, the streamlines are trapped in constant levels as shown in panels (b-d). The fluid elements lie within the same streamlines for all time and do not distribute homogeneously throughout the flow domain. In Fig. 1.6 the flow mixes better with stretching and folding of the scalar appearing clearly through a wide area of the flow domain leading to efficient mixing.

1.3 Applications

Chaotic advection has been receiving an increasing interest not only because of its various application areas, but also because it presents an approach that can lead us to understand various kinds of dynamical phenomena occurring in different systems such as physical, biological and environmental flows. Furthermore, chaotic advection has been widely used by researchers in diverse areas of fluid mechanics to explain a variety of experimental or real world phenomena. Understanding such mixing and enhanced diffusion processes in deterministic, random and turbulent flows is key in many important applications such as:

- Stirring of fluids on geophysical or planetary scales. Due to the convective motions in the Earth's mantle, numerical simulations show signs of chaotic advection represented by folds and layers on smaller and smaller scales. This can be seen in individual rocks (Ottino, 1989; Aref, 2002).
- In the field of medicine where low Reynolds number mixing enabled human plasma mixing without damaging the cells.
- Enhanced heat transfer for heat exchanges (e.g., El Omari & Le Guer, 2010).
- Stirring and mixing devices in chemical engineering processes and combustion (e.g., Ottino, 1989).
- Transport in atmospheres and oceans (e.g., Pierrehumbert & Yang, 1993).
- Mixing and transport phenomena in biological systems (e.g., Pulsatile flow in corrugated channels and flow in twisted tubes).
- Acceleration of chemical reactions (e.g., Chertkov & Lebedev, 2003b).



Figure 1.7: Stretching and folding of clouds in the wake of Guadalupe island. From the NASA archive.

- In the atmosphere, where the flow is dominated by an azimuthal jet, such as might be encountered in the polar night jet surrounding the ozone hole in Antarctica (Aref, 2002).
- In environmental flows; in the atmosphere (Fig. 1.7) and in the ocean (Fig. 1.8) as plotted by NASA. The former shows a flow creating folds in cloud formations, formed by the wind in the wake of Guadalupe island. The latter shows the flow close to Kamchatka, where the stretching and folding of the flow that occur in the sea can be seen.

The list of applications continues to grow.

1.4 Ideas from dynamical systems

“The dynamical systems approaches based on flow kinematics have provided a first insight into chaotic mixing.” (Ottino, 1989).

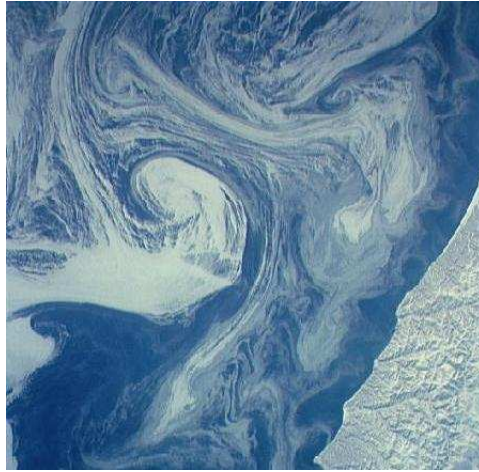


Figure 1.8: Sea -ice distribution close to Kamchatka. From the NASA archive (<http://images.jsc.nasa.gov/iams/images/earth/STS045/html/10068879.htm>).

1.4.1 Fluid flow

Mixing in fluid flow can be defined as the homogenisation of the scalar by the diffusion process. In general a flow can be one, two or three-dimensional and it may be steady (time-independent) or unsteady (time-dependent). Interestingly, all fluid flows naturally occur in full three-dimensional space. Much simpler are cases when one or two of the velocity field components vanish leading to two or one-dimensional flows, respectively. A more interesting case may be for the spherical Couette flow and regular duct flows in general, where one or more of the three velocity components are independent of one of the spatial co-ordinates. This set comes between two-dimensional flows where the third component is zero; $\mathbf{u} = (u(x, y), v(x, y), 0)$ and three-dimensional flows where all three components are independent of one co-ordinate; $\mathbf{u} = (u(x, y), v(x, y), w(x, y))$.

The flow can be visualised by different ways including streamlines, pathlines and streaklines. For example, a streamline is a purely theoretical line in space, defined

as being tangential to instantaneous velocity vectors.

Since the dynamics of one-dimensional incompressible flow at low Reynolds number (e.g., Poiseuille flow) are very simple, the case of two-dimensional incompressible flow is more interesting. Here the incompressibility of the flow implies that

$$\frac{\partial u}{\partial x} + \frac{\partial v}{\partial y} = 0. \quad (1.4.1)$$

and the existence of a stream function $\psi(x, y, t)$ such that

$$u = \frac{\partial \psi}{\partial y}, \quad v = -\frac{\partial \psi}{\partial x}. \quad (1.4.2)$$

where the stream function ψ plays the role of the Hamiltonian (see 1.4.12, 1.4.13). That is, two-dimensional steady incompressible flows are time-independent integrable systems while two-dimensional unsteady incompressible flows are time-dependent Hamiltonian systems, and so are generally non-integrable. However, numerous studies have been undertaken using two-dimensional chaotic advection (e.g., the ‘blinking-vortex flow’ discussed in Section §1.2, see Fig. 1.1). The ‘classical’ two-dimensional laminar mixing flow is found in the lid-driven cavity flow introduced by Ottino *et al.*, (1989) and discussed in Section §1.2 (see Fig. 1.5 and Fig. 1.6).

On the other hand, the first level of fully three-dimensional flows is steady three-dimensional incompressible flow, which is similar to unsteady flow in two dimensions. The first study of chaos in three dimensions was done by V. I Arnold (1965), who addressed the problem in steady incompressible inviscid fluid flow. It has been shown that for steady Euler flow $\mathbf{u} \times \boldsymbol{\omega} = \nabla p$ where \mathbf{u} and $\boldsymbol{\omega}$ refers to the ve-

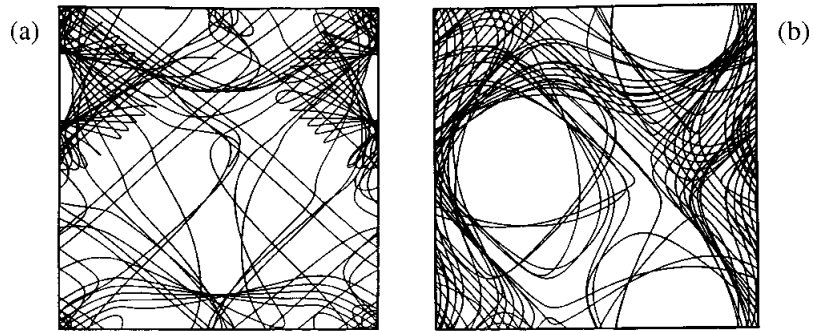


Figure 1.9: Particle trajectories in ABC flow. (Aref, 2002).

locity and the vorticity of the flow and p is the pressure. Arnol'd showed that for the Beltrami flows where the vorticity and the velocity are everywhere parallel; $\boldsymbol{\omega} = \lambda \mathbf{u}$ for a constant λ , the stream lines may be chaotic. In 1966 Hénon verified Arnold's suggestion by examining the value $\lambda = 1$, giving what is now known as the ABC (Arnold- Beltrami-Childress) flow of the velocity field $\mathbf{u} = (u, v, w)$ (Fig. 1.9),

$$u = A \sin z + C \cos y, \quad (1.4.3)$$

$$v = B \sin x + A \cos z, \quad (1.4.4)$$

$$w = C \sin y + B \cos x. \quad (1.4.5)$$

For any real values of the constants A , B , and C the incompressible flow on the right hand side of Eqs.(1.4.3), (1.4.4) and (1.4.5) is a steady solution of the three-dimensional Euler equation, which also has been studied by Dombre *et al.* (1986). The numerical results of Hénon (1966) indicate regions of chaotic behaviour for the advection which should translate into efficient stirring and mixing. Mathematically, this flow became the model for studying chaos in three-dimensional steady

incompressible laminar flow. Chaotic Beltrami flows in a sphere have been analysed by Zheligovsky (1993), that represent spherical analogues of ABC flow with vorticity $\boldsymbol{\omega}$ that is parallel to the velocity \mathbf{u} where $\boldsymbol{\omega} = \lambda\mathbf{u}$.

Other mathematical models of chaotic advection in three-dimensional steady Stokes flows within a spherical drop have been investigated by Bajer and Moffatt (1990).

1.4.2 Motion of particles in a given flow

The motion of a fluid is usually complex. The particle being moved may have inertia, or be subject to diffusion, or there are some physical characteristics such as differences of pressure or elevation that can cause its motion. In fluid mechanics, there are two distinct ways to specify the fluid; the Lagrangian method where individual particles are tracked and Eulerian method where fields are used rather than particles.

However, the basic idea of a passive scalar is a quite clear; when a particle moves in the fluid velocity field $\mathbf{v}(x, y, z, t)$, it is said it follows the flow at every point and at every instant. So, in this case it must be *passive* as it does nothing, just follows the flow and does not change the flow field. For such a particle, the Lagrangian position is represented by the agreement of its velocity with the fluid velocity,

$$\mathbf{v}_{particle} = \mathbf{v}_{fluid}, \quad (1.4.6)$$

This gives the formal statement of passive advection, where

$$\mathbf{v}_{particle} = \left(\frac{dx}{dt}, \frac{dy}{dt}, \frac{dz}{dt} \right), \quad (1.4.7)$$

is given as the rate of change of the particle position (x, y, z) and the fluid velocity is given as

$$\mathbf{v}_{fluid} = [u(x, y, z, t), v(x, y, z, t), w(x, y, z, t)]. \quad (1.4.8)$$

The condition (1.4.6) leads to a system of ordinary differential equations (ODEs) called *advection equations*,

$$\frac{dx}{dt} = u(x, y, z, t), \quad (1.4.9)$$

$$\frac{dy}{dt} = v(x, y, z, t), \quad (1.4.10)$$

$$\frac{dz}{dt} = w(x, y, z, t), \quad (1.4.11)$$

where, (u, v, w) are the Cartesian components of the fluid velocity field \mathbf{v} . A particle moving according to these equations is said to be subject to passive advection. In the sense of dynamical system theory, these equations (1.4.9), (1.4.10) and (1.4.11) are enough to produce non-integrable behaviour. In particular, this can occur for time dependent plane flow, when $w = 0$ and u and v depend only on x , y , and t , and for both steady and unsteady three-dimensional flows. In this case we have the phenomenon of *chaotic advection* and this is valid for both incompressible and compressible flow fields. If on the other hand, the advection equations (1.4.9), (1.4.10) and (1.4.11) are integrable, as they are in examples of a steady plane flow, then a system of *regular advection* is represented. Consequently, it has been demonstrated that the time dependence is not required for three-dimensional flow to produce chaotic particle motion, steady flow will do (e.g., ABC flows). In contrast, in two-dimensions, we do need time-dependent flow to have chaos, as steady two-dimensional flows are integrable (Aref, 2002).



Figure 1.10: Poincaré section of a flow in three-dimensional showing islands through the mixer (Ottino, 1989).

1.4.3 Poincaré section

A Poincaré or surface section is a method whereby the problems of dynamical systems can be simplified by reducing the number of the dimensions since it converts the periodic flow into a map. This method reveals how changing the flow and stream function leads to mixing in different regions of the flow as it displays the behaviour of the system for all possible initial conditions. Therefore, we can see how a passive particle moves over each period of the flow (see Fig. 1.10 and Fig. 1.2).

To obtain the Poincaré section, the flow field $\mathbf{u} = (u, v)$ is written as a system of two first order differential equations

$$\frac{dx}{dt} = u(x, y, t) = \frac{\partial \psi}{\partial y}, \quad (1.4.12)$$

$$\frac{dy}{dt} = v(x, y, t) = -\frac{\partial \psi}{\partial x}. \quad (1.4.13)$$

These equations are integrated from a set of initial conditions $(x(0), y(0))$ to give points on a trajectory $(x(nT), y(nT))$, $n = 0, 1, 2, \dots, N$ over a period T of the flow being studied. For each initial condition the position of the fluid particle is represented by a dot in real space after each period of the flow. Using this method, we may see islands, chaotic regions and boundaries and so find out about all the structures in the phase space, relevant to mixing. Later, in Chapter 4, by using this method we shall show how the flows with both slip and no-slip boundaries behave.

1.4.4 Kinematics of chaos

“Chaos is good, if you want to stir efficiently, you want as much chaotic advection as you can get.” (Aref, 2002).

Dynamical chaos is a phenomenon that can mathematically be described for many natural systems: physical, chemical, biological and others. Various definitions of chaos exist, but the most famous characteristic of these definitions is the sensitive dependence on the initial conditions (i.e., initially nearby trajectories of the particle motion diverge at an exponential rate). This concept can be encountered in the natural phenomena such as the flow of a river, the motion of clouds or planets as well as in games such as roulette, dice and billiards . However, chaotic mixing is the simplest possible case in which laminar flow is prescribed with complex streamlines and mixing is studied. It is an example of the complex irregular motion of particles in a regular periodic velocity field, like drops of cream in a cup of coffee. Here, we introduce some of the key definitions about chaotic flows and chaotic mixing:

- 1- Island: It is a region where a Poincaré section shows closed curves, and an

absence of chaos. Fluid in such regions shows slow mixing compared with that in a chaotic region (see Fig. 1.10).

- 2- Orbit(trajjectory): for a specific fluid particle $\mathbf{x}(t)$, gives its position at time t and the whole set $\{\mathbf{x}(t); t \geq 0\}$ is the orbit of the particle starting at $\mathbf{x}(0)$ (see Fig. 1.2(a-c)).
- 3- Lyapunov exponent: It is a number that is associated with an orbit and describes its stability in a linear approximation. Chaotic systems have orbits with at least one positive Lyapunov exponent, so that integrable systems can not be chaotic. Consequently, all steady bounded two-dimensional flows are poor mixing flows (see Fig. 1.5). Generally, Lyapunov exponent is used to provide a quantitative measure of chaotic mixing.

1.5 Advection-diffusion equation

The equation that is the focus of our interest is the *advection-diffusion equation*

$$\frac{\partial \sigma}{\partial t} + \mathbf{u} \cdot \nabla \sigma = \kappa \nabla^2 \sigma, \quad (1.5.1)$$

for a *passive* scalar field $\sigma(\mathbf{r}, t)$ (no feedback on the flow) being *advected* by a specified incompressible velocity field \mathbf{u} , so that $\nabla \cdot \mathbf{u} = 0$, and *diffused* with diffusivity $\kappa > 0$. We take a non-dimensional formulation with \mathbf{u} periodic in $(2\pi)^2$ space \mathbb{T}^2 , coordinates $\mathbf{r} = (x, y)$, and $\kappa \equiv \text{Pe}^{-1}$ as the inverse Péclet or Schmidt number. We consider flows \mathbf{u} defined by a stream function ψ

$$\mathbf{u} = (\partial_y \psi, -\partial_x \psi). \quad (1.5.2)$$

The second term on the left-hand side of (1.5.1) is called the advection term; it represents the transport of the scalar by the flow \mathbf{u} and generates fine spatial scales. The term on the right-hand side of (1.5.1) is called the diffusion term and it acts to smooth out the non-uniformity of the scalar.

The understanding of transport processes in chaotic flows is a central issue in many fields of applied and theoretical sciences. The dynamical approaches related to these flows can be broadly divided into three categories: experimental, numerical and theoretical. Many of them focus on the essential aspects of mixing in two-dimensional flows, as they provide a foundation for understanding the more complex cases of three-dimensional flows.

1.6 Mixing in global chaotic flows

Even though the first theoretical example of chaotic advection was a three dimensional flow (Hénon 1966), the theoretical studies addressing chaotic mixing in three dimensions are still few. However, mixing has been studied in idealised models: in deterministic or random flows. One of these studies includes the decay phase of a scalar field undergoing steady three-dimensional chaotic advection by Toussaint *et al.* (2000). This research showed that the spectral decay is found to be exponential and self-similar at large times, with the focus on the importance of the asymptotic decay-time as a measure of the efficiency of mixing. The power law variance spectrum in this study is found at scales intermediate between the large and the smallest ones, at which diffusion is effective. These flows exhibit global chaos, so that no integrable islands are present, the decay of a passive scalar is exponential, at a rate $\gamma(\kappa)$ that tends to a constant independent of the diffusivity as $\kappa \rightarrow 0$.

1.7 Mixing in flows with boundaries

Several predictions for the peripheral mixing have been recently made by Chertkov & Lebedev (2003a) and Lebedev & Turitsyn (2004) and checked with laboratory experiments in a chaotic microchannel by Simonnet *et al.*, (2005), in polymer solution by Burghilea *et al.* (2004) and in kinematic simulations by Salman & Haynes (2007) (Fig. 1.12). By ‘peripheral’ we mean the region of the flow near the wall boundaries where the slip ($\mathbf{n} \cdot \mathbf{u} = 0$) and no-slip ($\mathbf{u} = 0$) boundary conditions are considered together with a flow of poor mixing (see Fig. 1.11). Modern steps in the understanding of the passive scalar transport recently have been made by Chertkov & Lebedev (2003a), Lebedev & Turitsyn (2004), and Chernykh & Lebedev (2008). These authors made the key observation that near to a no-slip boundary the effective time scale of mixing becomes very long and the resulting boundary layer can control the mixing of passive scalar by acting as a reservoir, slowly releasing the scalar into the body of the flow, where mixing occurs more rapidly. If the flow is random, then near the boundary the effective correlation time of the flow becomes very short (as the turnover time increases). Approximation leads to a diffusion equation determining the boundary layer structure and giving predictions about decay rates and scalar field moments. This has been further explored by Salman & Haynes (2007) who use families of ‘renewing’ flows, in which the random flow is chosen to be independent and identically distributed on time intervals $[j\tau, (j+1)\tau]$. Specifically, the focus of the above studies for closed systems is the decay of passive scalar fluctuations for flows obeying a no-slip condition, where the scalar obeys a no-flux or Neumann condition, in a plane layer domain with periodic boundary conditions along the layer (see Fig. 1.12). In this case the long-time regime is

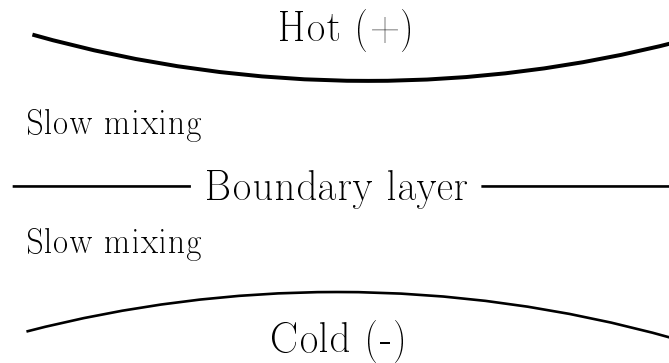


Figure 1.11: Diagram showing the wall region of the flow with respect to Dirichlet boundary condition.

exponential decay with a decay rate $\gamma(\kappa)$ proportional to $\kappa^{1/2}$. These authors identified several distinct regimes including a transient algebraic decay. Such a scenario was first identified theoretically by Chertkov & Lebedev (2003a) followed by Lebedev & Turitsyn (2004) and later examined by Salman & Haynes (2007). In particular, these theoretical predictions suggest four stages with an intermediate regime in which the scalar variance evolves according to a power law. The slip case in this scenario is described by two stages,

- First stage: the scalar variance remains constant producing thin structures of fluctuations (Fig 1.12(a,c)). Once the thickness of these structures decreases enough (Fig 1.12(e)), diffusion smears out high gradients in the scalar field.
- Second stage: followed rapid mixing in the interior of the flow, a long-time behaviour is observed leading to an exponential rapid decay of the scalar variance (Fig 1.12(g,i)).

In contrast, the no-slip case is characterised by four separate stages,

- First stage: the intense stirring of the scalar field is produced within the interior of the flow where diffusion is not important (Fig 1.12(b)).

- Second stage: after rapid mixing of the scalar in the bulk of the fluid, there is an intermediate regime of mixing where diffusion becomes important as seen in (Fig. 1.12(d,f)). The slow release of tongues (Fig. 1.12(f,j)) of relatively large scale scalar from the boundaries leads to a slow ‘algebraic’ decay of concentration variance in this stage discussed from the point of view of experiment and theory by Gouillart *et al.* (2007), Gouillart *et al.* (2008) and Gouillart, Thiffeault & Dauchot (2010).
- Third stage: the scalar becomes well-mixed in the body of the flow, but remains slower in a region near the boundaries that decreases with time (Fig. 1.12(h)).
- Fourth stage: once the boundary layer width becomes of the order of diffusion boundary layer width, the decreasing stops and the scalar trapped near the walls controls the decay rate, turning the ‘algebraic’ decay to an exponential one; $V \simeq \exp(-2\gamma t)$ (Fig. 1.12(j)).

The theory of Lebedev & Turitsyn (2004) has been supported by numerical simulations of scalar transport in three-dimensional Couette flow by Boffetta, De Lillo & Mazzino (2009) and extended to the case of turbulent flow, where the wall layer has a more complex structure (Garcia-Ybarra, 2009; Skvortsov & Yee, 2011). This is for flows in closed systems, bounded regions of the plane or a plane layer with periodic boundary conditions. In their study, Salman & Haynes (2007) emphasised the importance of the existence of the no-slip boundaries on the decay rate. Close to such boundaries the velocity field of the flow tends to zero and the advection slows down in the peripheral regions while mixing continues to be efficient in the bulk of the flow away from the boundary.

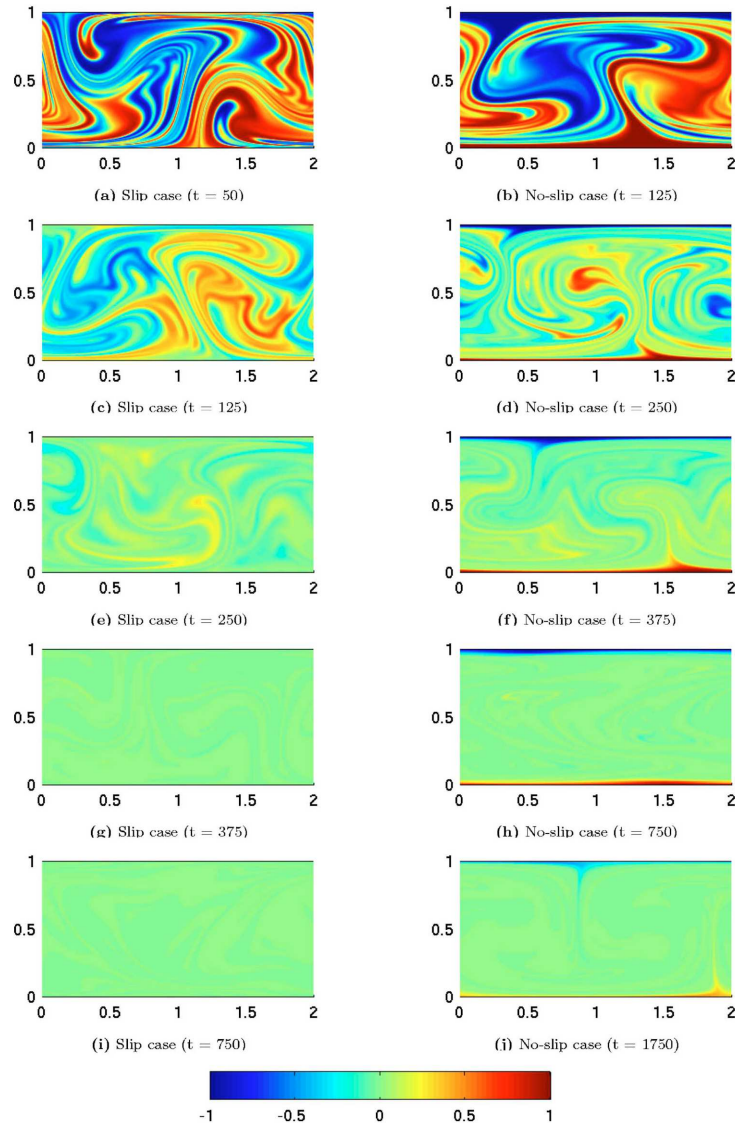


Figure 1.12: Scalar distribution of a random flow in a plane layer with slip boundaries (left column) and no-slip boundaries (right column) with Neumann boundary conditions at $t =$ (a) 50, (b,c) 125, (d,e) 250, (f,g) 375, (h,i) 750 and (j) 1750 (Salman & Haynes, 2007).

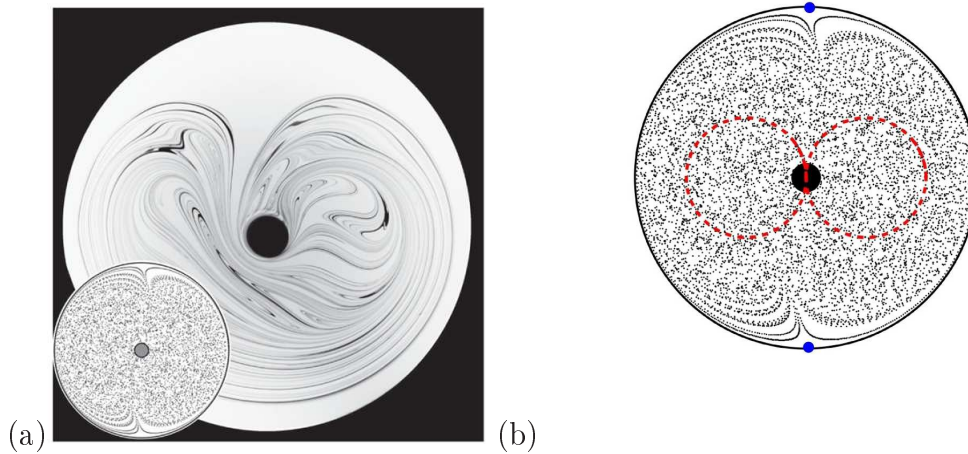


Figure 1.13: (a) Chaotic mixing experiment in a closed vessel. The figure-eight stirring protocol. (b) Poincaré section obtained numerically for the corresponding flow (Gouillart *et al.*, 2007).

Experimentally, most interesting are observations of the mixing dynamics in two dimensions, conducted with numerical simulations in a closed vessel using fully chaotic flows by Gouillart *et al.* (2007, 2008); Gouillart, Thiffeault & Dauchot (2010). Gouillart *et al.* (2007) investigated dye homogenisation conducted in a closed vessel, where a single rod has gently been stirred the fluid with a figure of eight motion (see Fig. 1.13). Such mixers showed an important effect of 'slow' algebraic decay imposed by no-slip walls. The no-slip boundary condition at the walls of the vessel can strongly influence the decay of the scalar. The existence of parabolic points on such boundaries (as a result of the hydrodynamics of the no-slip walls) considerably slows down mixing, turning an exponential decay into a power law (Gouillart *et al.*, 2007, 2008; Gouillart, Thiffeault & Dauchot, 2010). Furthermore, the distinct stages of mixing successfully have been examined in a closed system by Gouillart *et al.* (2008) (see Fig. 1.14). In fact, three stages of

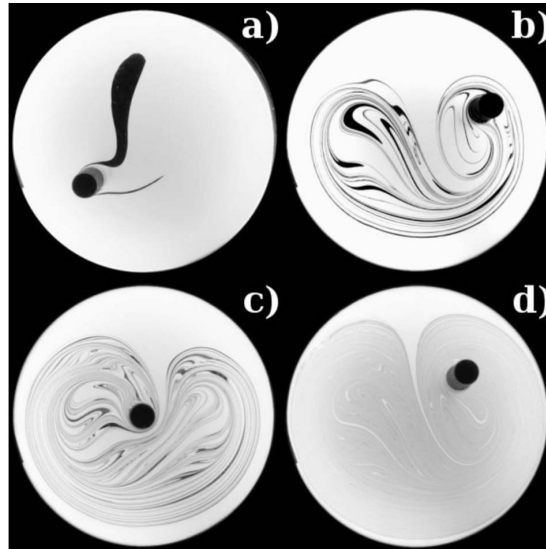


Figure 1.14: Successive stages of homogenisation for a blob of dye stirred by the figure-8 protocol (Gouillart *et al.*, 2008).

mixing have been observed and can be linked to the four stages discussed earlier in this section. These stages show the homogenisation for a blob of dye stirred by the figure-eight protocol. We can see the boundary layer thinning in Fig. 1.14(c,d).

These experimental (Burghelea *et al.*, 2004; Burghelea, Segre & Steinberg, 2004; Simonnet & Groisman, 2005; Jun & Steinberg, 2010) and numerical (Chertkov & Lebedev, 2003a; Lebedev & Turitsyn, 2004; Salman & Haynes, 2007; Chernykh & Lebedev, 2008) studies obtained an exponential decay for the scalar field in a chaotic mixer at large times. It has been observed that this behaviour is attributed to convergence the scalar field to the ‘strange’ eigenmode discussed by Pierrehumbert & Yang (1993); Gouillart *et al.* (2009) and later by El Omari & Le Guer (2010).

In spite of the importance of the Dirichlet case in linking questions of chaotic advection to heat transfer, and possible applications, it has been little studied.

However, the recent numerical work of El Omari & Le Guer (2010) considers decay of temperature within a two-rod mixing device under various protocols for rotating the rods. The full Navier-Stokes equation for the fluid flow is solved. The main result of this work is that the heat transfer is controlled by boundary layers on the no-slip boundaries.

Several other studies have used flows with 2π -periodicity, but with a focus on the presence of islands and other structures in the fluid flow, rather than on boundary conditions for the fluid flow and scalar (Cerbelli, Adrover & Giona, 2003; Turner, Thuburn & Gilbert, 2009).

1.8 Mixing in open flows

Chaotic advection in open hydrodynamical flows is a ubiquitous phenomenon. Undergoing chaotic advection, mixing has been investigated experimentally in open systems. A further element of the study of Lebedev & Turitsyn (2004) concerns the decay of the scalar variance in the open system consisting of a flow down a pipe under the influence of no-slip boundary conditions; this geometry allows experimental verification of theory, and is particularly important in mixing applications for microfluidics (Burghelea *et al.*, 2004; Burghelea, Segre & Steinberg, 2004; Simonnet & Groisman, 2005; Jun & Steinberg, 2010). For example, the experiment of Burghelea was carried out in a microchannel using viscous fluid with polymer. In this experiment, it has been verified that following an initial rapid mixing of the scalar concentration, a decreasing rate was observed close to the boundaries. Moreover, the scaling of mixing length with Péclet number derived by Chertkov & Lebedev (2003a) and Lebedev & Turitsyn (2004) in the intermediate regime were also observed in this work. Numerical simulations of open flow were done also by

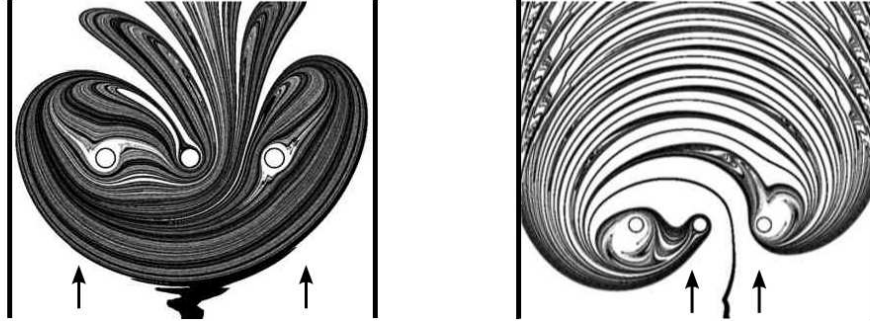


Figure 1.15: Numerical simulations of a flow in an open channel with a figure-eight rod stirring protocol. (Thiffeault *et al.*, 2008).

Thiffeault *et al.* (2008) and Gouillart *et al.* (2009) as a subsequent work to Gouillart *et al.* (2007). As mixing can greatly be enhanced by stirring a fluid, Thiffeault *et al.* (2008) considered a figure-eight rod stirring protocol in an open channel shown in Fig. 1.15. This protocol is capable of producing intense stretching that is important for chaotic mixing. In the second paper (Gouillart *et al.*, 2009), two different stirring protocols are studied; while the mixing region is separated from the walls in the first one, it extends to the walls in the second. This study provided an experimental evidence for convergence of the scalar to the strange eigenmode that is previously discussed by Pierrehumbert & Yang (1993) in a closed system. Besides, this research emphasised on the importance of no-slip boundaries in producing non-self similar mixing dynamics.

Numerically and experimentally, these works obtained an exponential decay rate for the variance of the scalar in chaotic mixers with the focus on the important role played by the no-slip boundaries on the decay of the scalar variance. Although

the experimental results provided the confirmation of some scaling laws derived by Chertkov & Lebedev (2003a); Lebedev & Turitsyn (2004) and Chernykh & Lebedev (2008) they do not fully and exclusively test other elements of theory. Furthermore, the slowly evolving stage of mixing implies that a very long time is required to realise the final stage of mixing. In the experiment of Burghlea *et al.*, (2004) this means that a very long channel is required making it difficult to realise the full behaviour of mixing.

1.9 Thesis outline

In Part I of this thesis we investigate numerically the decay rate of the scalar variance outlined in previous sections for two-dimensional flows focusing on the effect of a variety of boundary conditions on this rate.

Chapter 2 considers the main stream functions used to represent our families of the flows and the scalar fields addressed specifically in this thesis. We draw and develop a general framework for governing equations and scalar fields generated in terms of stream functions. Then we set up our mathematical tools represented by a symmetry group and different transformations that govern the scalar distribution of our flows described later. The methodology used is detailed at the end of this chapter.

In Chapter 3 we simulate scalar advection and diffusion in a square domain \mathcal{D} for random, ‘renewing’ flows with a variety of boundary conditions. We survey the different types of scaling that may occur with consideration of slip and no-slip conditions for the flows and Neumann and Dirichlet boundary conditions for the scalar fields. In the first case of a Neumann boundary condition the focus is on the mixing and homogenisation of temperature within the domain \mathcal{D} and how fast

Chapter 1. INTRODUCTION AND MOTIVATION

fluctuations are destroyed. In the second case of a Dirichlet boundary condition, the aim is to understand how rapidly heat leaves the domain and so how fast the fluid cools; as heat must cross the boundaries, boundary layers are crucial in controlling the flux (Balmforth & Young, 2003).

To make contact with previous work and to assess the role of domain shape, in Chapter 4 we expand upon the investigation of the flows addressed in a geometry of a plane layer, with the development of further directions making use of Bloch wavenumbers within our work. Simulations of time-periodic flows and results in the square domain are provided and discussed at the end of this chapter. We end Chapter 4 with some remarks and analysis of results.

In Part II of this thesis we develop and apply further theory for passive scalar evolution for random flows. We introduce a general framework for identifying and confirming our previous results obtained numerically in Part I.

In Chapter 5 we analyse the key arguments of the passive scalar dynamics leading to prediction of the decay rate of variance of the scalar controlled by the peripheral region in the plane layer. Following these theoretical arguments, in Chapter 6, we present our previous model flows considered for the numerical simulations along with more details for analytical results. We end this chapter by providing some key findings and a short comparison with the numerical simulations combined with some scaling laws obtained theoretically.

In Part III of this work, we extend the work set out in Part I and II to the polar co-ordinate system and explore how the passive scalar evolution can be approximated near to corners. We introduce a general discussion for a flow driven specifically near a corner in Chapter 7 linking it to Moffatt corner eddies in Chapter 8.

Chapter 1. INTRODUCTION AND MOTIVATION

Finally, Chapter 9 offers the general conclusion and suggestions for the extension of this study.

2

MAIN FUNCTIONS AND TRANSFORMATIONS

2.1 Outline

Our aim in this chapter is to outline the set of basic symmetries and transformations that govern the scalar distribution in the flows described in the first part of this work. We start the chapter by highlighting the main stream functions in Section §2.2 used to represent our families of flows and scalar fields. We proceed in this section by defining families of flows with slip and no-slip boundary conditions on the boundary \mathcal{C} of a square domain \mathcal{D} . In order to pave the way for the group of symmetries to be exploited later, general stream functions and governing equations are presented in Section §2.3 and Section §2.4, respectively. These symmetries will be motivated further in Section §2.5 and Section §2.6, but at this point we only focus on the important ones in our work. Investigation of these governing symmetries and scalar evolution will then form the basis of the first part of this thesis.

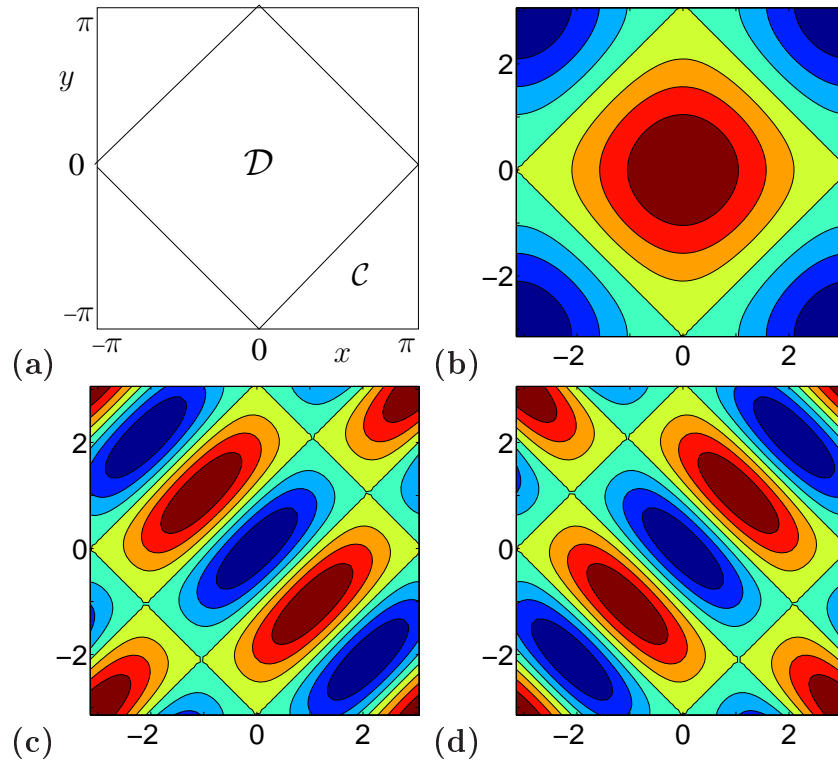


Figure 2.1: Within \mathbb{T}^2 are depicted (a) the square \mathcal{C} and the domain \mathcal{D} , together with the functions (b) $\phi_{1,1}$, (c) $\phi_{1,3}$ and (d) $\phi_{3,1}$.

Numerically, our method used in this work is introduced in Section §2.7. Furthermore, in order to make use of an efficient numerical method we embed our square domain \mathcal{D} in a region which is 2π -periodic in x and y (Fig. 2.1(a)). By suitable combinations of Fourier modes we can easily write down flows that have zero normal flow $\mathbf{n} \cdot \mathbf{u} = 0$ or obey no-slip $\mathbf{u} = 0$ on the boundary \mathcal{C} of \mathcal{D} . We then simulate passive scalars in these flows using a code which is completely spectral, as discussed in Section §2.7.

2.2 Main stream functions

In this section we introduce the main stream functions and the flows that satisfy boundary conditions used in this work. Our aim is to impose no-slip or slip boundary conditions on the velocity field on the boundary \mathcal{C} of the domain \mathcal{D} in the fluid. We do this within the 2π -periodic space \mathbb{T}^2 by building fields that satisfy certain symmetry properties. Consider the square \mathcal{C} with vertices at $(\pi, 0)$, $(0, \pi)$, $(-\pi, 0)$ and $(0, -\pi)$ depicted in Fig. 2.1(a) with interior \mathcal{D} . The stream functions we focus on particularly are defined by

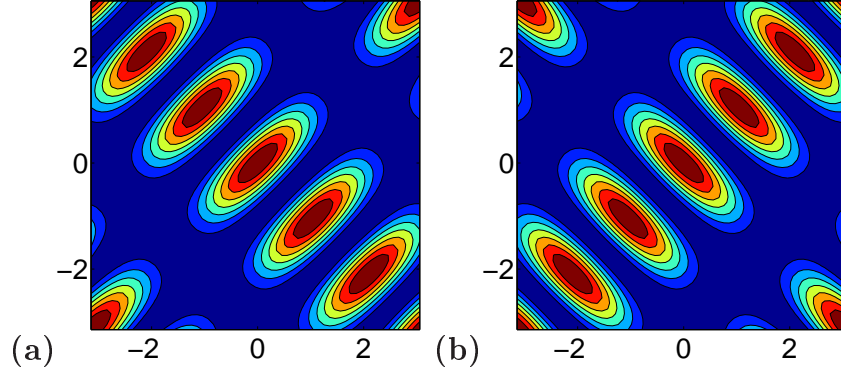
$$\phi_{1,1} = \cos x + \cos y, \quad (2.2.1)$$

$$\phi_{1,3} = -\cos(2x - y) - \cos(2y - x), \quad (2.2.2)$$

$$\phi_{3,1} = -\cos(2x + y) - \cos(x + 2y), \quad (2.2.3)$$

shown in Fig. 2.1(b,c,d), and are used to compose periodic fields and flows satisfying boundary conditions on the boundary \mathcal{C} of \mathcal{D} . More specifically, we use these fields as building blocks for flows with slip and no-slip boundary conditions and also for initial scalar fields. Such fields obey certain symmetries described in Section §2.5 which are preserved during the evolution of scalar variance as time increases. We define flows which have a free-slip and the full no-slip boundary condition given respectively by the stream functions

$$\psi_{\text{slip}} = \phi_{1,3}(x, y) \sin[\omega t + \chi(t)] + \phi_{3,1}(x, y) \cos[\omega t + \chi(t)], \quad (2.2.4)$$


 Figure 2.2: Stream functions (a) $\phi_{1,3}^2$, (b) $\phi_{3,1}^2$.

and

$$\psi_{no-slip} = \phi_{1,3}(x, y)^2 \sin[\omega t + \chi(t)] + \phi_{3,1}(x, y)^2 \cos[\omega t + \chi(t)]. \quad (2.2.5)$$

Here $\chi(t)$ is a phase that can be a constant, say zero, giving a time-periodic flow, or depend randomly on time as we detail later. Stream functions of the fields $\phi_{1,3}(x, y)^2$ and $\phi_{3,1}(x, y)^2$ are shown in Fig. 2.2.

2.3 General stream functions

Based on the structure of the 2π -periodic space \mathbb{T}^2 provided in the previous section we generate our flows and initial scalar fields from a family of functions $\phi_{m,n}$

$$\phi_{m,n} = 2 \sin \left[\frac{m}{2}(x + y + \pi) \right] \sin \left[\frac{n}{2}(y - x + \pi) \right]. \quad (2.3.1)$$

These functions are zero on the straight lines constituting \mathcal{C} , namely

$$x + y = \pm\pi, \quad y - x = \pm\pi, \quad (2.3.2)$$

and provided $m + n$ is even the fields $\phi_{m,n}$ are 2π -periodic. We thus use the family

$$\Phi_{\text{even}} = \{\phi_{m,n} : m + n \text{ is even}\}, \quad (2.3.3)$$

and in particular the members (2.2.1), (2.2.2) and (2.2.3) introduced in Section §2.2. We use the family (2.3.1) to build our flows and initial scalar fields so as to impose slip and no-slip boundary conditions on \mathcal{C} . These functions (2.3.1) can be rewritten as

$$\phi_{m,n} = 2 \cos\left(\frac{m(x+y)}{2} + \frac{(m-1)\pi}{2}\right) \cos\left(\frac{n(y-x)}{2} + \frac{(n-1)\pi}{2}\right). \quad (2.3.4)$$

with equivalent forms of (2.2.1), (2.2.2) and (2.2.3),

$$\phi_{1,1} = 2 \cos\left(\frac{x+y}{2}\right) \cos\left(\frac{y-x}{2}\right), \quad (2.3.5)$$

$$\phi_{1,3} = -2 \cos\left(\frac{x+y}{2}\right) \cos\left(\frac{3(y-x)}{2}\right), \quad (2.3.6)$$

$$\phi_{3,1} = -2 \cos\left(\frac{3(x+y)}{2}\right) \cos\left(\frac{y-x}{2}\right). \quad (2.3.7)$$

To show how these functions can be generated we take the field $\phi_{1,3}$ as an illustrative example. Based on Eq. (2.3.1), the field $\phi_{1,3}$ is given by

$$\phi_{1,3} = 2 \sin\left[\frac{1}{2}(x+y+\pi)\right] \sin\left[\frac{3}{2}(y-x+\pi)\right]. \quad (2.3.8)$$

Putting

$$A = \frac{1}{2}(x+y+\pi), \quad B = \frac{3}{2}(y-x+\pi), \quad (2.3.9)$$

yields that Eq. (2.3.8) takes the form

$$\begin{aligned}\phi_{1,3} &= 2 \sin A \sin B \\ &= \cos(A - B) - \cos(A + B).\end{aligned}\tag{2.3.10}$$

As a reminder to ourselves

$$\cos(A - B) = \cos A \cos B + \sin A \sin B,\tag{2.3.11}$$

$$\cos(A + B) = \cos A \cos B - \sin A \sin B.\tag{2.3.12}$$

In this case, Eq. (2.3.10) collapses to

$$\begin{aligned}\phi_{1,3} &= \cos(2x - y - \pi) - \cos(-x + 2y + 2\pi) \\ &= -\cos(2x - y) - \cos(2y - x).\end{aligned}\tag{2.3.13}$$

Similarly, the stream function $\phi_{1,1}$ is obtained with the form

$$\phi_{1,1} = 2 \sin \left[\frac{1}{2}(x + y + \pi) \right] \sin \left[\frac{1}{2}(y - x + \pi) \right],\tag{2.3.14}$$

and this is equivalent to

$$\phi_{1,1} = \cos x + \cos y.\tag{2.3.15}$$

Snapshots of stream functions for the flows slip (2.2.4) and no-slip (2.2.5) are shown in Figs. 2.3, 2.4, 2.5 and 2.6. A key difference between the two flows is seen closer to the boundaries. While there is a non-zero flow on the boundary \mathcal{C} of the square in the slip case, a weak flow around the boundary \mathcal{C} is seen in the case of no-slip flow. We will discuss this further in Chapter 3.

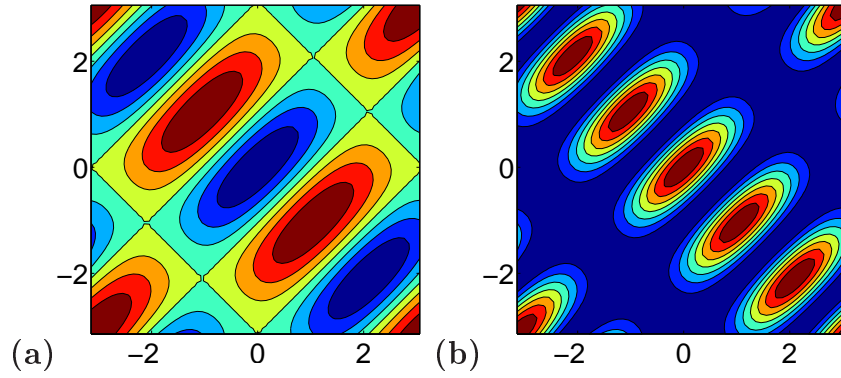


Figure 2.3: Stream functions (a) $\phi_{1,3} \sin t + \phi_{3,1} \cos t$, (b) $\phi_{1,3}^2 \sin t + \phi_{3,1}^2 \cos t$; $t = \pi/2$.

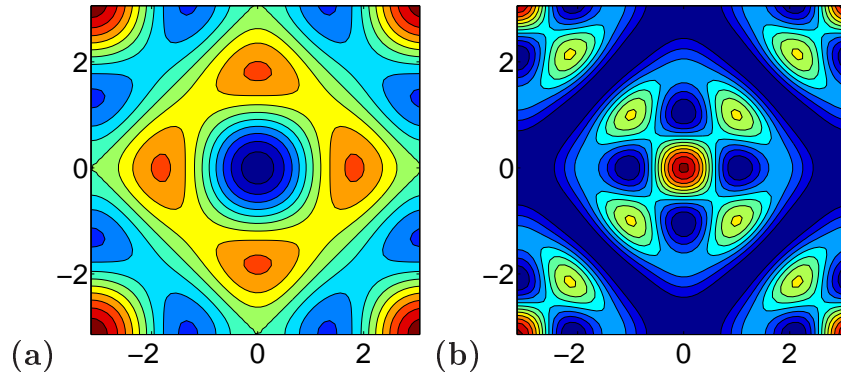


Figure 2.4: Stream functions (a) $\phi_{1,3} \sin t + \phi_{3,1} \cos t$, (b) $\phi_{1,3}^2 \sin t + \phi_{3,1}^2 \cos t$; $t = \pi/4$.

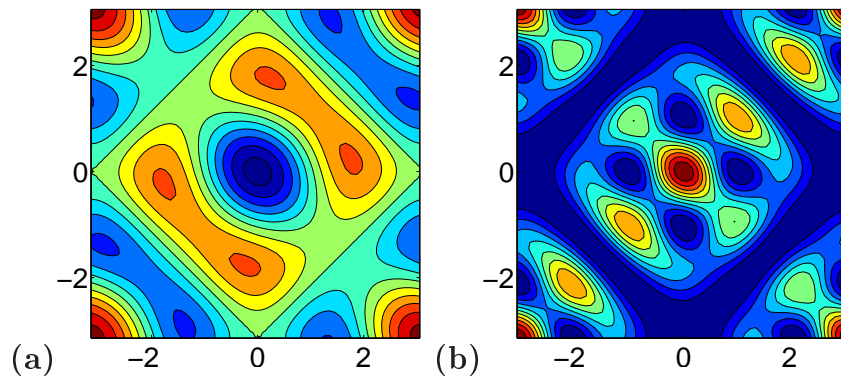


Figure 2.5: Stream functions (a) $\phi_{1,3} \sin t + \phi_{3,1} \cos t$, (b) $\phi_{1,3}^2 \sin t + \phi_{3,1}^2 \cos t$; $t = \pi/6$.

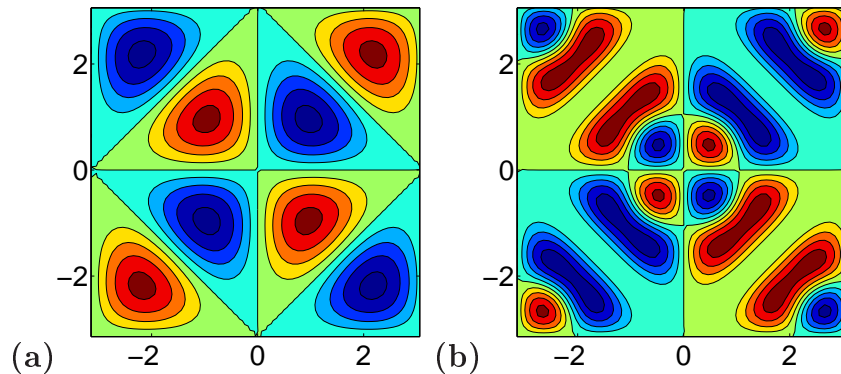


Figure 2.6: Stream functions (a) $\phi_{1,3} \sin t + \phi_{3,1} \cos t$, (b) $\phi_{1,3}^2 \sin t + \phi_{3,1}^2 \cos t$; $t = 3\pi/4$.

2.4 Governing equations

We consider the advection of a passive scalar field $\sigma(\mathbf{r}, t)$ governed by the equation

$$\frac{\partial \sigma}{\partial t} + \mathbf{u} \cdot \nabla \sigma = \kappa \nabla^2 \sigma, \quad (2.4.1)$$

where \mathbf{u} is a specified incompressible flow velocity, so that $\nabla \cdot \mathbf{u} = 0$, and $\kappa > 0$ is the diffusion coefficient. We take a non-dimensional formulation with \mathbf{u} periodic in $(2\pi)^2$ space \mathbb{T}^2 , coordinates $\mathbf{r} = (x, y)$, and $\kappa \equiv \text{Pe}^{-1}$ as the inverse Péclet or Schmidt number. The magnitude of scalar fluctuations in the periodic domain may be measured by the mean-square value,

$$V(t) = (2\pi)^{-2} \int_{-\pi}^{\pi} \int_{-\pi}^{\pi} \sigma^2(\mathbf{r}, t) dx dy. \quad (2.4.2)$$

(In fact this is the variance of the scalar in the full domain \mathbb{T}^2 as the mean is zero for the simulations below). With $\kappa > 0$, for a given flow the scalar has the

long-time exponential decay rate $\gamma(\kappa) > 0$ defined by

$$\gamma = -\frac{1}{2} \lim_{t \rightarrow \infty} t^{-1} \log V(t). \quad (2.4.3)$$

We consider flows \mathbf{u} defined by a stream function ψ

$$\mathbf{u} = (\partial_y \psi, -\partial_x \psi). \quad (2.4.4)$$

with a Fourier decomposition

$$\psi(\mathbf{r}, t) = \sum_{j,k} \hat{\psi}_{j,k}(t) e^{ijx+iky}, \quad \hat{\psi}_{j,k} \equiv \hat{\psi}_{-j,-k}^*. \quad (2.4.5)$$

and likewise for the scalar field,

$$\sigma(\mathbf{r}, t) = \sum_{m,n} \hat{\sigma}_{m,n}(t) e^{imx+iny}, \quad \hat{\sigma}_{m,n} \equiv \hat{\sigma}_{-m,-n}^*. \quad (2.4.6)$$

in periodic space.

2.5 Symmetry group and transformations

In this section we introduce our group of symmetries exploited to construct the flows and the scalar fields that form the basis of this work. These symmetries (together with the 2π -periodicity) guarantee that a flow \mathbf{u} constructed with a stream function ψ that is a linear combination of terms in Φ_{even} will have $\psi = 0$ on the boundary \mathcal{C} of the domain \mathcal{D} depicted in Fig. 2.1(a). Later, we will use these symmetries to apply the boundary conditions on the flows and scalar fields introduced in Section §2.2.

Chapter 2. MAIN FUNCTIONS AND TRANSFORMATIONS

As we mentioned before, our aim is to compose periodic fields and flows satisfying boundary conditions on the boundary \mathcal{C} of the domain \mathcal{D} in the fluid. In order to do this, we need to consider possible symmetries of the flows and scalar fields. The square \mathcal{C} embedded in periodic space \mathbb{T}^2 , as depicted in Fig. 2.1(a), is invariant under a finite group G of transformations shown in table 2.1: we stress that these transformations are taken modulo 2π in x and y directions. The group G may be generated by a rotation R of $\pi/2$ about the origin, a reflection S in the x -axis, and a diagonal translation T ,

$$R(x, y) = (-y, x), \quad S(x, y) = (x, -y), \quad T(x, y) = (x + \pi, y + \pi). \quad (2.5.1)$$

The first two of these generate the dihedral group D_8 , acting on the square \mathcal{C} . As the translation T commutes with R and S (modulo 2π), the full group is $G = D_8 \times \mathbb{Z}_2$.

Under a transformation $g \in G$, a 2π -periodic function $\phi(x, y)$ transforms according to

$$(g\phi)(x, y) = \phi[g^{-1}(x, y)], \quad (2.5.2)$$

giving, explicitly, for $\phi_{m,n} \in \Phi_{\text{even}}$,

$$R\phi_{m,n} = (-1)^{n-1}\phi_{n,m}, \quad S\phi_{m,n} = \phi_{n,m}, \quad T\phi_{m,n} = (-1)^m\phi_{m,n}. \quad (2.5.3)$$

These relationships are proved in Section §2.6. However, symmetries we will find particularly useful are reflections in the lines forming \mathcal{C} . Taking points modulo 2π there are just two of these symmetries, namely reflection S_1 in (either of) the lines

Chapter 2. MAIN FUNCTIONS AND TRANSFORMATIONS

$x + y = \pm\pi$ and reflection S_2 in $y - x = \pm\pi$ given by

$$S_1 = TR^3S, \quad S_1(x, y) = (\pi - y, \pi - x), \quad (2.5.4)$$

$$S_2 = TRS, \quad S_2(x, y) = (y - \pi, x + \pi). \quad (2.5.5)$$

One may check that

$$S_1\phi_{m,n} = S_2\phi_{m,n} = -\phi_{m,n}. \quad (2.5.6)$$

In fact, our group G of transformations (table 2.1) includes a number of important symmetries:

1) Identity I ; $I(x, y) = (x, y)$.

2) Rotation of $\pi/2$ about the origin:

$$R(x, y) = (-y, x). \quad (2.5.7)$$

with $R^4 = I$.

3) Rotation of π about the origin:

$$R^2(x, y) = (-x, -y). \quad (2.5.8)$$

4) Rotation of $3\pi/2$ about the origin:

$$R^3(x, y) = (y, -x). \quad (2.5.9)$$

5) Reflection in the line $y = 0$ (x axis):

$$S(x, y) = (x, -y). \quad (2.5.10)$$

6) Reflection in the line $x = y$:

$$RS(x, y) = (y, x). \quad (2.5.11)$$

7) Reflection in the line $x = 0$ (y axis):

$$R^2S(x, y) = (-x, y). \quad (2.5.12)$$

8) Reflection in the line $x = -y$:

$$R^3S(x, y) = (-y, -x). \quad (2.5.13)$$

9) Translation of π :

$$T(x, y) = (x + \pi, y + \pi). \quad (2.5.14)$$

with $T^2 = I$.

10) Rotation of $\pi/2$ about $(0, \pi)$:

$$TR(x, y) = (\pi - y, \pi + x). \quad (2.5.15)$$

11) Rotation of π about $(\pi/2, \pi/2)$:

$$TR^2(x, y) = (\pi - x, \pi - y). \quad (2.5.16)$$

12) Rotation of $\pi/2$ about $(\pi, 0)$:

$$TR^3(x, y) = (\pi + y, \pi - x). \quad (2.5.17)$$

13) Rotation of $\pi/2$ about the origin followed by a reflection in the line $y - x = \pi$:

$$TS(x, y) = (x - \pi, \pi - y). \quad (2.5.18)$$

14) Reflection in the line $y - x = \pi$:

$$TRS(x, y) = (y - \pi, x + \pi). \quad (2.5.19)$$

with $(TRS)^2 = I$.

15) Rotation of $\pi/2$ about $(0, \pi)$ followed by a reflection in the line $x + y = 2\pi$:

$$TR^2S(x, y) = (\pi - x, \pi + y). \quad (2.5.20)$$

16) Reflection in the line $x + y = \pi$:

$$TR^3S(x, y) = (\pi - y, \pi - x). \quad (2.5.21)$$

with $(TR^3S)^2 = I$.

We have thus specified 16 transformations, members of the group G , under which the basic geometry depicted in Fig. 2.1(a) is invariant. We will use these transformations to specify flows and scalar fields with slip/no-slip or Dirichlet/Neumann conditions on the boundary \mathcal{C} , by requiring that these flows or scalar fields are invariant or change sign under some certain transformations in G . In fact, these flows and fields will not transform simply under all elements of G , but only under a subgroup for each case. Further explanation for this point will be provided in the next two chapters.

To illustrate how the group G of symmetries is obtained we introduce the two following examples:

1) $S_1S_2(x, y) = R^2$:

Acting on a point (x, y) we have

$$\begin{aligned} S_1S_2(x, y) &= S_1(S_2(x, y)) \\ &= S_1(y - \pi, x + \pi) \\ &= (-x, 2\pi - y). \end{aligned} \quad (2.5.22)$$

and because of the 2π -periodicity we get

$$\begin{aligned} S_1 S_2(x, y) &= (-x, -y) \\ &= R^2(x, y). \end{aligned} \tag{2.5.23}$$

2) $S_2 T(x, y) = RS$:

Similarly in this case we find that

$$\begin{aligned} S_2 T(x, y) &= S_2(T(x, y)) \\ &= S_2(x + \pi, y + \pi) \\ &= (y, x + 2\pi) \\ &= (y, x) \\ &= RS(x, y). \end{aligned} \tag{2.5.24}$$

Other elements of the group G (see table 2.1) can be obtained by the same way.

2.6 Some transformations of the stream functions

In this section we introduce some transformations of the stream functions $\phi_{m,n}$ highlighted in Section §2.3 under some of the symmetries we mentioned above.

Acting on the set of 2π -periodic fields Φ_{even} (that is with $m + n$ even) we found that under reflection $S_1 = TR^3S$ in the line $x + y = \pi$, the steam function $\phi_{m,n}$ can be transformed as

$$S_1 \phi_{m,n} = -\phi_{m,n}. \tag{2.6.1}$$

Chapter 2. MAIN FUNCTIONS AND TRANSFORMATIONS

	I	R	R^2	R^3	S	RS	R^2S	R^3S	T	TR	TR^2	TR^3	TS	TRS	TR^2S	TR^3S
I	I	R	R^2	R^3	S	RS	R^2S	R^3S	T	TR	TR^2	TR^3	TS	TRS	TR^2S	TR^3S
R	R	R	R^2	R^3	I	RS	R^2S	R^3S	T	TR	TR^2	TR^3	TS	TRS	TR^2S	TR^3S
R^2	R^2	R^3	I	R	R^2S	R^3S	S	RS	TR^2	TR^3	T	TR	TR^2S	TR^3S	TS	TRS
R^3	R^3	I	R	R^2	R^3S	S	RS	R^2S	TR^3	T	TR	TR^2	TR^3S	TS	TRS	TR^2S
S	S	R^3S	R^2S	RS	I	R^3	R^2	R	TS	TR^3S	TR^2S	TRS	T	TR^3	TR^2	TR
RS	RS	S	R^3S	R^2S	R	I	R^3	R^2	TRS	TS	TR^3S	TR^2S	TR	T	TR^3	TR^2
R^2S	R^2S	RS	S	R^3S	R^2S	R	I	R^3	TR^2S	TRS	TS	TR^3S	TR^2	TR	T	TR^3
R^3S	R^3S	R^2S	RS	S	R^3	R^2	R	I	TR^3S	TR^2S	TRS	TS	TR^3	TR^2	TR	T
T	T	TR	TR^2	TR^3	TS	TRS	TR^2S	TR^3S	I	R	R^2	R^3	S	RS	R^2S	R^3S
TR	TR	TR^2	TR^3	T	TRS	TR^2S	TR^3S	TS	R	R^2	R^3	I	RS	R^2S	R^3S	S
TR^2	TR^2	TR^3	T	TR	TR^2S	TR^3S	TS	TRS	R^2	R^3	I	R	R^2S	R^3S	S	RS
TR^3	TR^3	T	TR	TR^2	TR^3S	TS	TRS	TR^2S	R^3	I	R	R^2	R^3S	S	RS	R^2S
TS	TS	TR^3S	TR^2S	TRS	T	TR^3	TR^2	TR	S	R^3S	R^2S	RS	I	R^3	R^2	R
TRS	TRS	TS	TR^3S	TR^2S	TR	T	TR^3	TR^2	RS	S	R^3S	R^2S	R	I	R^3	R^2
TR^2S	TR^2S	TRS	TS	TR^3S	TR^2	TR	T	TR^3	R^2S	RS	S	R^3S	R^2	R	I	R^3
TR^3S	TR^3S	TR^2S	TRS	TS	TR^3	TR^2	TR	T	R^3S	R^2S	RS	S	R^3	R^2	R	I

Table 2.1: Group G of the symmetries

and for the translation T ,

$$T\phi_{m,n} = (-1)^m \phi_{m,n}. \quad (2.6.2)$$

Passing these fields $\phi_{m,n}$ under the rotation R of $\frac{\pi}{2}$ about the origin we note that

$$R\phi_{m,n} = (-1)^{n-1} \phi_{n,m}, \quad R^2\phi_{m,n} = \phi_{m,n}. \quad (2.6.3)$$

The proof of these transformations is as follows.

1) **The reflection in the line $x + y = \pi$:**

This symmetry is defined by $S_1(x, y) = (\pi - y, \pi - x)$, and so we have

$$\begin{aligned} (S_1\phi_{m,n})(x, y) &= \phi_{m,n}(S_1^{-1}(x, y)) \\ &= \phi_{m,n}(S_1(x, y)) \\ &= \phi_{m,n}(\pi - y, \pi - x). \end{aligned} \quad (2.6.4)$$

From our earlier discussion, we have defined the stream function $\phi_{m,n}$ to be given by either Eq. (2.3.1) or Eq. (2.3.4). Therefore, based on the definition of S_1 , equation (2.6.4) can be written as

$$\begin{aligned} S_1\phi_{m,n}(x, y) &= 2 \cos \left(\frac{m(2\pi - x - y)}{2} + \frac{(m-1)\pi}{2} \right) \cos \left(\frac{n(y-x)}{2} + \frac{(n-1)\pi}{2} \right) \\ &= 2 \cos \left(\frac{3m\pi}{2} - \frac{m(x+y)}{2} - \frac{\pi}{2} \right) \cos \left(\frac{n(y-x)}{2} + \frac{(n-1)\pi}{2} \right), \end{aligned} \quad (2.6.5)$$

This is actually equivalent to

$$\begin{aligned} S_1\phi_{m,n} &= 2 \cos\left(\frac{-m(x+y)}{2} + \frac{(3m-1)\pi}{2}\right) \cos\left(\frac{n(y-x)}{2} + \frac{(n-1)\pi}{2}\right) \\ &= 2 \cos\left(\frac{-m(x+y)}{2} - \frac{(1-3m)\pi}{2}\right) \cos\left(\frac{n(y-x)}{2} + \frac{(n-1)\pi}{2}\right) \end{aligned} \quad (2.6.6)$$

and because of the evenness of \cos (i.e., $\cos(-x) = \cos(x)$) we get

$$S_1\phi_{m,n} = 2 \cos\left(\frac{m(x+y)}{2} + \frac{(1-3m)\pi}{2}\right) \cos\left(\frac{n(y-x)}{2} + \frac{(n-1)\pi}{2}\right). \quad (2.6.7)$$

Since

$$\cos\left(\frac{m(x+y)}{2} + \frac{(1-3m)\pi}{2}\right) = -\cos\left(\frac{m(x+y)}{2} + \frac{(m-1)\pi}{2}\right), \quad (2.6.8)$$

Eq. (2.6.7) takes the form

$$\begin{aligned} S_1\phi_{m,n} &= -2 \cos\left(\frac{m(x+y)}{2} + \frac{(m-1)\pi}{2}\right) \cos\left(\frac{n(y-x)}{2} + \frac{(n-1)\pi}{2}\right) \\ &= -\phi_{m,n}. \end{aligned} \quad (2.6.9)$$

2) The translation of π :

As we have indicated before, this translation is defined by $T(x, y) = (x + \pi, y + \pi)$,

and similarly, we see that

$$\begin{aligned} (T\phi_{m,n})(x, y) &= \phi_{m,n}(T^{-1}(x, y)) \\ &= \phi_{m,n}(T(x, y)) \\ &= \phi_{m,n}(x + \pi, y + \pi). \end{aligned} \quad (2.6.10)$$

In this case

$$T\phi_{m,n}(x, y) = 2 \cos\left(\frac{m(x+y+2\pi)}{2} + \frac{(m-1)\pi}{2}\right) \cos\left(\frac{n(y-x)}{2} + \frac{(n-1)\pi}{2}\right), \quad (2.6.11)$$

which collapses to

$$\begin{aligned} T\phi_{m,n} &= 2(-1)^m \cos\left(\frac{m(x+y)}{2} + \frac{(m-1)\pi}{2}\right) \cos\left(\frac{n(y-x)}{2} + \frac{(n-1)\pi}{2}\right) \\ &= (-1)^m \phi_{m,n}. \end{aligned} \quad (2.6.12)$$

3) The rotation of $\pi/2$ about the origin:

This rotation is given by $R(x, y) = (-y, x)$ and so,

$$\begin{aligned} (R\phi_{m,n})(x, y) &= \phi_{m,n}(R^{-1}(x, y)) \\ &= \phi_{m,n}(R^3(x, y)) \\ &= \phi_{m,n}(y, -x). \end{aligned} \quad (2.6.13)$$

This can be written as

$$R\phi_{m,n}(x, y) = 2 \cos\left(\frac{m(y-x)}{2} + \frac{(m-1)\pi}{2}\right) \cos\left(\frac{n(-x-y)}{2} + \frac{(n-1)\pi}{2}\right). \quad (2.6.14)$$

Because $\cos(-x) = \cos(x)$ we get

$$R\phi_{m,n}(x, y) = 2 \cos\left(\frac{m(y-x)}{2} + \frac{(m-1)\pi}{2}\right) \cos\left(\frac{n(x+y)}{2} + \frac{(1-n)\pi}{2}\right). \quad (2.6.15)$$

We can write (2.6.15) in another equivalent form

$$R\phi_{m,n}(x, y) = 2 \cos\left(\frac{m(y-x)}{2} + \frac{(m-1)\pi}{2}\right) \cos\left(\frac{n(x+y)}{2} + \frac{(n-1)\pi}{2} - (n-1)\pi\right). \quad (2.6.16)$$

which implies

$$\begin{aligned} R\phi_{m,n} &= 2(-1)^{n-1} \cos\left(\frac{n(x+y)}{2} + \frac{(n-1)\pi}{2}\right) \cos\left(\frac{m(y-x)}{2} + \frac{(m-1)\pi}{2}\right) \\ &= (-1)^{n-1} \phi_{n,m}. \end{aligned} \quad (2.6.17)$$

Subsequently, one may check that

$$\begin{aligned} R^2\phi_{m,n} &= (-1)^{2(n-1)}\phi_{m,n} \\ &= \phi_{m,n}. \end{aligned} \quad (2.6.18)$$

4) **The reflection in the x -axis:**

Acting on this symmetry defined by $S(x, y) = (x, -y)$ we find that

$$\begin{aligned} (S\phi_{m,n})(x, y) &= \phi_{m,n}(S^{-1}(x, y)) \\ &= \phi_{m,n}(S(x, y)) \\ &= \phi_{m,n}(x, -y). \end{aligned} \quad (2.6.19)$$

In such a case we have

$$\begin{aligned}
 S\phi_{m,n}(x, y) &= 2 \cos \left(\frac{m(x-y)}{2} + \frac{(m-1)\pi}{2} \right) \cos \left(\frac{n(-x-y)}{2} + \frac{(n-1)\pi}{2} \right) \\
 &= 2 \cos \left(\frac{-m(y-x)}{2} - \frac{(1-m)\pi}{2} \right) \cos \left(\frac{-n(x+y)}{2} - \frac{(1-n)\pi}{2} \right)
 \end{aligned} \tag{2.6.20}$$

Again, the evenness of cos yields

$$\begin{aligned}
 S\phi_{m,n}(x, y) &= 2 \cos \left(\frac{m(y-x)}{2} + \frac{(1-m)\pi}{2} \right) \cos \left(\frac{n(x+y)}{2} + \frac{(1-n)\pi}{2} \right) \\
 &= 2 \cos \left(\frac{m(y-x)}{2} + \frac{(m-1)\pi}{2} - (m-1)\pi \right) \\
 &\quad \times \cos \left(\frac{n(x+y)}{2} + \frac{(n-1)\pi}{2} - (n-1)\pi \right).
 \end{aligned} \tag{2.6.21}$$

and this implies that

$$S\phi_{m,n}(x, y) = 2(-1)^{m+n-2} \cos \left(\frac{m(y-x)}{2} + \frac{(m-1)\pi}{2} \right) \cos \left(\frac{n(x+y)}{2} + \frac{(n-1)\pi}{2} \right). \tag{2.6.22}$$

Under the condition $m+n$ is even we confirm that

$$\begin{aligned}
 S\phi_{m,n} &= 2 \cos \left(\frac{n(x+y)}{2} + \frac{(n-1)\pi}{2} \right) \cos \left(\frac{m(y-x)}{2} + \frac{(m-1)\pi}{2} \right) \\
 &= \phi_{n,m}.
 \end{aligned} \tag{2.6.23}$$

2.7 Numerical scheme

In this section we introduce the numerical method used to solve the scalar decay problem we are interested in.

Chapter 2. MAIN FUNCTIONS AND TRANSFORMATIONS

We consider scalar fields generated by advection and diffusion: specifically we consider a scalar concentration $\sigma(x, y, t)$, whose evolution is governed numerically by the *advection-diffusion* equation

$$\frac{\partial \sigma}{\partial t} + \mathbf{u} \cdot \nabla \sigma = \kappa \nabla^2 \sigma. \quad (2.7.1)$$

The numerical scheme for solving Eq. (2.7.1) transforms the $2N \times 2N = 2\pi \times 2\pi$ domain into Fourier space by writing

$$\sigma(x, y, t) = \sum_{j=-N}^N \sum_{k=-N}^N \hat{\sigma}_{j,k}(t) e^{i(jx+ky)}. \quad (2.7.2)$$

and integrating the $\mathbf{u} \cdot \nabla \sigma$ term in Eq. (2.7.1) using the second order Adams-Bashforth method,

$$X^{j+2} = X^{j+1} + \frac{3}{2} \Delta t f(X^{j+1}) - \frac{1}{2} \Delta t f(X^j). \quad (2.7.3)$$

where Δt is the time-step and $X^j = X(j \Delta t)$. This is for $\frac{dx}{dt} = f(x)$ and we discuss this further below.

This method is non-self started in that it needs another method, for example Euler

$$X^{j+1} = X^j + \Delta t f(X^j). \quad (2.7.4)$$

to start with before the formula (2.7.3) can be used. More specifically, Adams-Bashforth method needs two values; X^{j+1} and X^j to compute the next value X^{j+2} . As the initial value problem ($t = j = 0$) provides only one value X^0 , therefore one possibility to resolve this issue is to use the value X^{j+1} computed by the Euler method as the second value for Adams-Bashforth method. However, the

Adams-Bashforth method is efficient as the determination of X^{j+2} requires only one evaluation of f per step.

For our numerical simulation the flows used are chosen to have relatively few non-zero Fourier modes $\hat{\psi}_{j,k}$. The numerical codes exploit this by keeping the scalar field in Fourier space (except for plotting), retaining up to 256^2 modes for the larger runs, and evaluating the convolution term $\mathbf{u} \cdot \nabla \sigma$ explicitly. Time-stepping is done by the Adams–Bashforth scheme for the $\mathbf{u} \cdot \nabla \sigma$ term with the diffusion term integrated exactly. Mathematically, we explain this point as follows. From Eq. (2.7.1) we have that

$$\frac{d\hat{\sigma}_{m,n}}{dt} + \kappa(m^2 + n^2) \hat{\sigma}_{m,n} = F_{m,n}(\sigma), \quad (2.7.5)$$

where $F(\sigma) = -\mathbf{u} \cdot \nabla \sigma$ and $F_{m,n}$ is the (m, n) Fourier mode of F . Now, Eq. (2.7.5) can be rewritten as

$$\frac{d}{dt} \left(e^{\kappa(m^2+n^2)t} \hat{\sigma}_{m,n} \right) = e^{\kappa(m^2+n^2)t} F_{m,n}(\sigma). \quad (2.7.6)$$

To simplify using Adams-Bashforth method we consider

$$\rho_{m,n} = e^{\kappa(m^2+n^2)t} \hat{\sigma}_{m,n}, \quad G_{m,n} = e^{\kappa(m^2+n^2)t} F_{m,n}(\sigma), \quad (2.7.7)$$

which provides the form

$$\frac{\rho_{m,n}^{j+1} - \rho_{m,n}^j}{\Delta t} = \frac{3}{2} G_{m,n}^j - \frac{1}{2} G_{m,n}^{j-1}. \quad (2.7.8)$$

Chapter 2. MAIN FUNCTIONS AND TRANSFORMATIONS

Substituting with Eq. (2.7.7) for $\rho_{m,n}$ and $G_{m,n}$ into Eq. (2.7.8) we immediately have

$$\frac{e^{\kappa(m^2+n^2)(j+1)\Delta t} \hat{\sigma}_{m,n}^{j+1} - e^{\kappa(m^2+n^2)j\Delta t} \hat{\sigma}_{m,n}^j}{\Delta t} = \frac{3}{2} e^{\kappa(m^2+n^2)j\Delta t} F_{m,n}(\sigma^j) - \frac{1}{2} e^{\kappa(m^2+n^2)(j-1)\Delta t} F_{m,n}(\sigma^{j-1}), \quad (2.7.9)$$

and dividing Eq. (2.7.9) by the term $e^{\kappa(m^2+n^2)(j+1)\Delta t}$ leads us to obtain

$$\frac{\hat{\sigma}_{m,n}^{j+1} - e^{-\kappa(m^2+n^2)\Delta t} \hat{\sigma}_{m,n}^j}{\Delta t} = \frac{3}{2} e^{-\kappa(m^2+n^2)\Delta t} F_{m,n}(\sigma^j) - \frac{1}{2} e^{-2\kappa(m^2+n^2)\Delta t} F_{m,n}(\sigma^{j-1}). \quad (2.7.10)$$

or

$$\hat{\sigma}_{m,n}^{j+1} = e^{-\kappa(m^2+n^2)\Delta t} \hat{\sigma}_{m,n}^j + \frac{3}{2} \Delta t e^{-\kappa(m^2+n^2)\Delta t} F_{m,n}(\sigma^j) - \frac{1}{2} \Delta t e^{-2\kappa(m^2+n^2)\Delta t} F_{m,n}(\sigma^{j-1}). \quad (2.7.11)$$

Consequently, the new value $\hat{\sigma}_{m,n}^{j+1}$ in (2.7.11) can be computed based on the two previous values σ^{j-1} and σ^j .

Numerically, the scalar code we used is based on the dynamo code developed by A. D. Gilbert. However, our simulations are tested by varying a set of *parameters* including: the number of the points ' npt ' used on the mesh-grid we consider, the diffusion coefficient ' κ ' and the time-step ' dt '. Table 2.2 includes some results obtained for the slip flow ψ_{slip} with Dirichlet boundary condition. Note that ' npt ' is N mentioned earlier in (2.7.2). To obtain the values of the decay rate γ of our numerical simulations we do a series of runs as shown in table 2.2 (as an example). We suggest quoting values of γ to say 5 significant figures, but being content when they have converged to about 3 significant digits. So if we see even

Chapter 2. MAIN FUNCTIONS AND TRANSFORMATIONS

ε	npt	dt	T	γ
0.1	32	0.001	100	0.22154
	64	0.001	100	0.22154
0.05	32	0.001	100	0.13034
	64	0.001	100	0.13034
0.02	32	0.001	100	0.065795
	64	0.001	100	0.065792
0.01	32	0.001	100	0.039678
	64	0.001	100	0.039687
0.005	32	0.001	100	0.024077
	64	0.001	100	0.024051
	64	0.0005	100	0.024051
	96	0.0005	100	0.024054
0.002	32	0.001	100	0.012525
	64	0.001	100	blow-up
	64	0.0005	100	0.012352
	96	0.0005	100	0.012361
0.001	32	0.001	100	0.0075652
	64	0.001	100	blow-up
	64	0.0005	100	0.0074083
	96	0.0005	100	0.0074062

Table 2.2: Test for simulation of the slip flow with the Dirichlet initial condition.

more convergence this is better, but 3 figures of convergence is fine - this is the accuracy of a point on a graph.

If the scalar field blows up (say scalar variance greater than 10^{10}) then the run is stopped, and we go on to the next run. In fact, these runs were to decide on the values of npt and dt to use, NOT the value of T . In other words we want to decide what are good values of these two parameters to get a code that is numerically accurate, and to do so we just look at a finite range of time. To find the limiting value of γ means looking at a variety of values of T . Such runs give suggested values for npt and dt to use for typical values of κ . This is for any flow or initial condition. Table 2.3 shows values of npt and dt suggested for different values of

κ	npt	dt	γ
$\kappa \geq 0.01$	32	0.001	usual runs
$0.01 > \kappa \geq 0.001$	32	0.0005	usual runs
	64	0.0005	as a check
$0.001 > \kappa \geq 0.0005$	64	0.0005	usual runs
	96	0.0002	as a check
$0.0005 > \kappa \geq 0.0001$	96	0.0002	usual runs
	128	0.0001	as a check
	128	0.00005	as a check

Table 2.3: Suggested values for \mathbf{npt} and dt for different values of κ related to both random and time-periodic flows.

κ in random and periodic flows. By ‘usual runs’ we mean the runs we usually do with the corresponding parameters and by ‘as a check’ we mean the runs that we do to confirm the usual runs.

2.8 Summary

Symmetries of the flow are both a useful and important analytical tool for understanding simple fluid flows as they are based on only the simplest geometrical characteristics of the flow.

By suitable choice of the flows and initial conditions we construct these symmetries to impose the boundary conditions on the flow and scalar field. The evolution of the scalar under the *advection-diffusion equation* (2.4.1) will preserve the Dirichlet or Neumann boundary conditions exactly for the case of slip flow (2.2.4), or approximately in the case of no-slip flow (2.2.5) as we will see in Chapter 3 and Chapter 4.

An important insight into the decay rate of fluid mixing is provided using these symmetries.

Part I

Numerical simulations

3

NUMERICAL SIMULATIONS

3.1 Outline

Our aim in the current and the next chapter is to look at various cases of flows and to explore the different types of decay rate scaling that may occur. We consider flows in a plane layer domain and also in a square domain possessing corners: here the motion of the flow may be differ from that near a no-slip boundary, and we are interested in the effect this may have. We consider flows with both slip and no-slip boundary conditions, and scalar fields with Neumann ($\mathbf{n} \cdot \nabla \sigma = 0$) and Dirichlet ($\sigma = 0$) conditions on the boundary \mathcal{C} . It will sometimes be useful to think of the passive scalar as temperature for the sake of discussion, although we are not considering convection and our results apply to any passive scalar. In the Neumann case we are interested in understanding mixing and homogenisation of the temperature within the domain \mathcal{D} , while in Dirichlet case the focus is on losing heat across the boundaries. In each case our focus is on the long-time behaviour of the passive scalar, with decay rates scaling as $\gamma(\kappa) \simeq C\kappa^\alpha$ in the limit of small κ

for an exponent α depending on the boundary conditions on fluid flows and passive scalar.

Thus, the interest in this work is where the boundary conditions on the fluid flow may be important for the evolution and decay of passive scalars.

We start this chapter by simulating families of random flows with both slip and no-slip boundary conditions on the boundary \mathcal{C} of a square domain \mathcal{D} introduced in Section §3.2.1 and Section §3.2.2, respectively. Numerical simulations and a specific analysis for such flows are then presented in these sections. Finally, discussion for the key results we obtained with these flows is provided in Section §3.3.

3.2 Simulations of random flows in the square domain

In this study, we use the family Φ_{even} introduced in Section §2.3 to define flows and simulate the evolution of passive scalar fields from an initial condition $\sigma_0(\mathbf{r})$ according to

$$\frac{\partial \sigma}{\partial t} = J(\psi, \sigma) + \kappa \nabla^2 \sigma, \quad (3.2.1)$$

where J is the usual Jacobian defined by

$$J(\sigma, \psi) = \begin{vmatrix} \partial \sigma / \partial x & \partial \sigma / \partial y \\ \partial \psi / \partial x & \partial \psi / \partial y \end{vmatrix} \quad (3.2.2)$$

and $J(\psi, \sigma) = -J(\sigma, \psi)$. Eq. (3.2.2) which implies that

$$J(\sigma, \psi) = (\partial \sigma / \partial x)(\partial \psi / \partial y) - (\partial \sigma / \partial y)(\partial \psi / \partial x). \quad (3.2.3)$$

If under a transformation $g \in G$ we have that

$$J \rightarrow s_J J, \quad \psi \rightarrow s_\psi \psi, \quad \sigma_0 \rightarrow s_\sigma \sigma_0, \quad (3.2.4)$$

where each sign $s = \pm 1$, then the evolution equation (3.2.1) preserves the property $\sigma \rightarrow s_\sigma \sigma$ under g at future times, provided only that

$$s_J s_\psi = 1. \quad (3.2.5)$$

Here $s_J = -1$ if g is a reflection and 1 if g preserves orientation. For example, if

$$g = S_1 \text{ (reflection)} : \quad J \rightarrow -J, \quad (3.2.6)$$

$$g = R^2 \text{ (rotation)} : \quad J \rightarrow J, \quad (3.2.7)$$

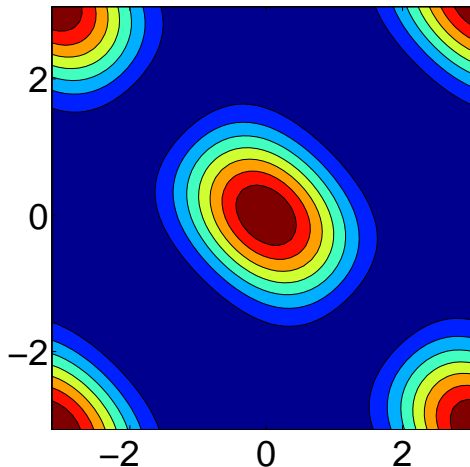
$$g = T \text{ (translation)} : \quad J \rightarrow J. \quad (3.2.8)$$

3.2.1 Numerical simulations for the flow ψ_{slip}

First we define a flow which has a free-slip boundary condition, given by the stream function

$$\psi_{\text{slip}} = \phi_{1,3}(x, y) \sin[\omega t + \chi(t)] + \phi_{3,1}(x, y) \cos[\omega t + \chi(t)]. \quad (3.2.9)$$

Here $\chi(t)$ is a phase that depends randomly on time (where the flow is random) as we mentioned in Section §2.2. Some snapshots of this flow are seen in Figs. (2.3)(a), (2.4)(a), (2.5)(a) and (2.6)(a). This flow has a stream function $\psi_{\text{slip}} = 0$, constant on \mathcal{C} , so there is no normal flow on this boundary, $\mathbf{u} \cdot \mathbf{n} = 0$. There is generally a slip velocity $\mathbf{u} \neq 0$, except at the corners of \mathcal{C} , where necessarily $\mathbf{u} = 0$.

Figure 3.1: Initial scalar field $\sigma_N = \phi_{1,1}^2 - 1$.

We also define initial conditions $\sigma(\mathbf{r}, 0) = \sigma_0(\mathbf{r})$ for simulations of the scalar field, and focus on two,

$$\sigma_D = \phi_{1,1}, \quad \sigma_N = \phi_{1,1}^2 - 1. \quad (3.2.10)$$

Snapshots of the initial scalar fields σ_D and σ_N are shown in Fig. 2.1(b) and Fig. 3.1, respectively. Both of these fields have zero mean in the full $(2\pi)^2$ periodic domain. The former has non-zero average in the square subdomain \mathcal{D} whereas for the latter the average is zero. Under the reflections about the boundaries of \mathcal{C} , we have

$$S_1, S_2 : \quad J \rightarrow -J, \quad \psi \rightarrow -\psi, \quad \sigma \rightarrow \mp \sigma, \quad (3.2.11)$$

where the upper sign is for σ_D and the lower for σ_N . This can be illustrated as follows. Acting on the symmetries S_1 and S_2 we find that

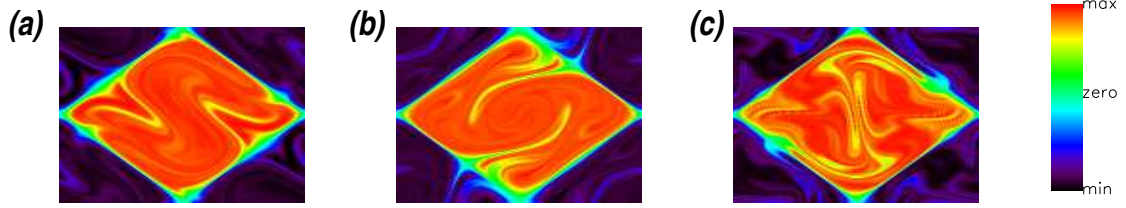


Figure 3.2: Scalar field for $(\psi_{\text{slip}}, \sigma_{\text{D}})$ with $\kappa = 0.001$ with times at (a) $t = 250$, (b) 500 and (c) 750. In the colour scale values go from black (minimum) to red (maximum) with zero green.

1) From the definition (3.2.2):

$$S_1, S_2 : J(\sigma, \psi) \longrightarrow J(\psi, \sigma) = -J(\sigma, \psi). \quad (3.2.12)$$

2) For ψ we have

$$S_1, S_2 : \phi_{1,3} \rightarrow -\phi_{1,3}, \quad (3.2.13)$$

$$\phi_{3,1} \rightarrow -\phi_{3,1}. \quad (3.2.14)$$

since, for example

$$\begin{aligned} S_1 \phi_{1,3} &= TR^3 S \phi_{1,3} \\ &= TR^3 \phi_{3,1} \\ &= TR^2 \phi_{1,3} \\ &= TR \phi_{3,1} \\ &= T \phi_{1,3} \\ &= -\phi_{1,3}. \end{aligned} \quad (3.2.15)$$

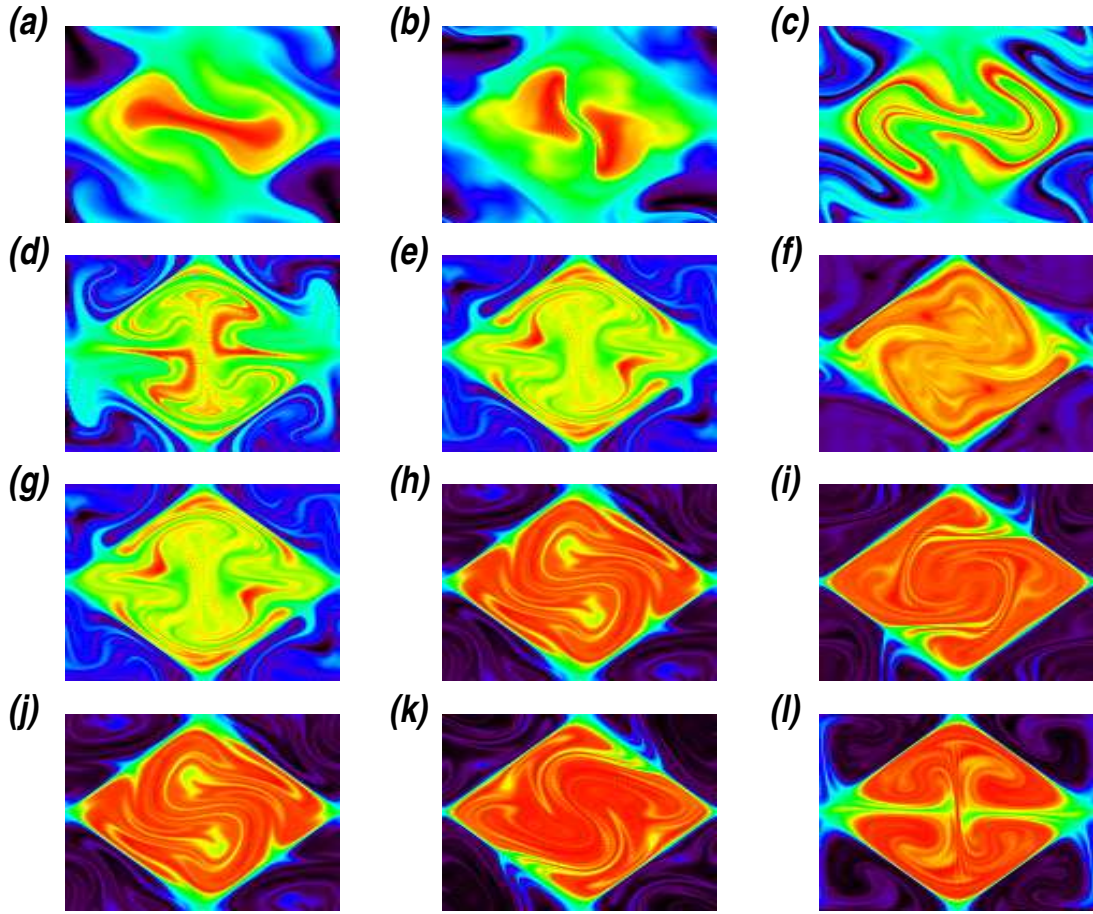


Figure 3.3: Scalar field for $(\psi_{\text{slip}}, \sigma_D)$ with $\kappa = 0.001$ with times at (a-c) $t = 1, 2, 3$, (d-f) $t = 5, 10, 15$, (g-i) $t = 10, 20, 30$ and (j-l) $t = 20, 40$ and 60 .

and one may check this under S_2 , too.

3) also for the initial scalar fields σ_D and σ_N ,

$$S_1, S_2 : \sigma_D = \phi_{1,1} \rightarrow -\phi_{1,1}, \quad (3.2.16)$$

$$\sigma_N = \phi_{1,1}^2 - 1 \rightarrow \phi_{1,1}^2 - 1. \quad (3.2.17)$$

Thus equation (3.2.5) is satisfied and these symmetry properties are preserved under subsequent evolution. As σ_D is odd under the reflections (upper sign), its

values are zero on the boundary \mathcal{C} and so it obeys a Dirichlet boundary condition $\sigma_D = 0$. Considering the passive scalar as temperature, the decay rates we will determine give a measure of how efficient a flow with slip boundary condition is at cooling a fluid through transfer of heat through the boundary. On the other hand σ_N is even under reflections and so must have zero perpendicular gradient $\mathbf{n} \cdot \nabla \sigma_N = 0$ on \mathcal{C} : this is a Neumann boundary condition and (given that σ_N has zero mean in \mathcal{D}) the decay of its mean-square value $V(t)$ gives a measure of how efficient the flow is at destroying temperature fluctuations in the fluid in the presence of insulating boundaries.

We have investigated these mixing processes by means of numerical simulations and we begin by considering the case of ψ_{slip} with Dirichlet boundary condition. We use (3.2.9) to create a random, ‘renewing’ flow by selecting $\chi(t)$ to be a piecewise constant random function with values on time-intervals $j\tau \leq t < (j+1)\tau$ distributed uniformly and independently between 0 and 2π (Salman & Haynes, 2007). We have taken $\tau = 0.64$ and $\omega = 1$ in this case and in all subsequent random flows. Figure 3.3 shows snapshots of the evolution of a scalar field in a simulation of one realisation of this random flow, using σ_D in (3.2.10) as initial condition to impose a Dirichlet boundary condition. The oddness of the scalar field under the reflections S_1, S_2 in (3.2.11) is evident, with invariance under R^2 , the half-turn rotation about the origin. The scalar field clearly tends to become well-mixed (red) within the square \mathcal{D} , and on the boundary \mathcal{C} there is a thin layer where the values rapidly tend to zero (green), together with cooler plumes (yellow) being entrained into the interior of the box. These boundary layers control the cooling of the fluid within, and so the decay rate of the scalar field.

To obtain an accurate measure of the decay rate we use longer runs, rescaling the

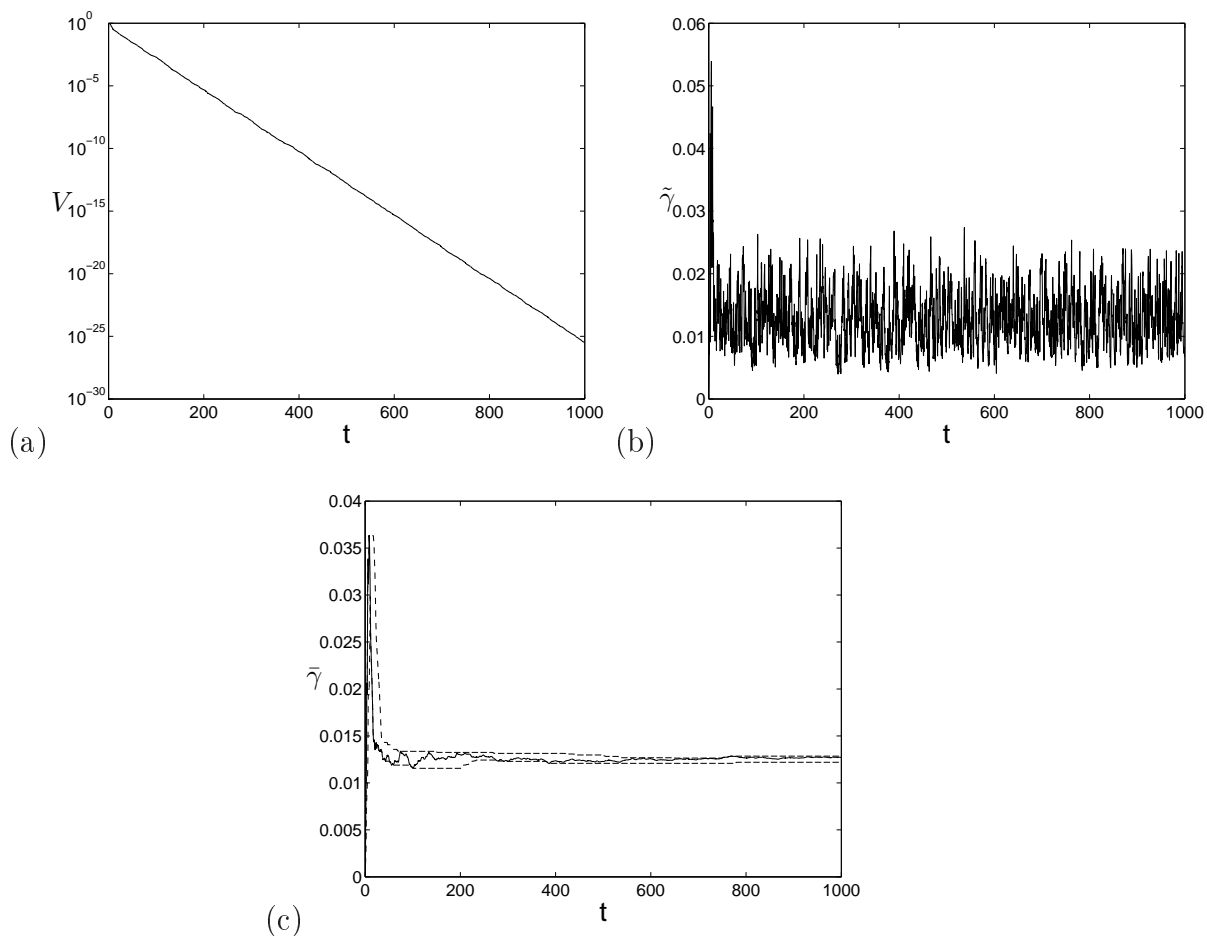


Figure 3.4: Plots for $(\psi_{\text{slip}}, \sigma_{\text{D}})$ against time t of (a) $V(t)$, (b) $\tilde{\gamma}(t)$, and (c) $\bar{\gamma}(t)$ (solid), $\bar{\gamma}_{\text{min}}(t)$ and $\bar{\gamma}_{\text{max}}(t)$ (dashed).

scalar field to avoid underflow when required. Figure 3.4 shows the evolution of (a) $V(t)$ as a function of time, together with (b) the instantaneous decay rate $\tilde{\gamma}(t)$ (measured between successive time-steps). There are strong random fluctuations and to obtain an accurate average decay rate, we take a running average over the window $[t/2, t]$ to define

$$\bar{\gamma}(t) = -t^{-1} \log[V(t)/V(t/2)]. \quad (3.2.18)$$

The choice of expanding time window eliminates transient behaviour and gives better averages as time increases. In a run up to time $t = T$ our best estimate of the scalar decay rate is $\bar{\gamma}(T)$ but to put a plausible error bar on this quantity we track upper and lower values of the average, defined by

$$\bar{\gamma}_{\max}(t) = \max_{t/2 \leq s \leq t} \bar{\gamma}(s), \quad \bar{\gamma}_{\min}(t) = \min_{t/2 \leq s \leq t} \bar{\gamma}(s). \quad (3.2.19)$$

In figure 3.4(c) $\bar{\gamma}(t)$ (solid), together with $\bar{\gamma}_{\min}(t)$ and $\bar{\gamma}_{\max}(t)$ (dashed) are shown. At the end of the run our final estimate of the decay rate and error bar is

$$\gamma(\kappa) \simeq \bar{\gamma} \pm \Delta\gamma, \quad \bar{\gamma} = \bar{\gamma}(T), \quad \Delta\gamma = \bar{\gamma}_{\max}(T) - \bar{\gamma}_{\min}(T). \quad (3.2.20)$$

Most runs of the random flows were taken to $T = 1000$ (tables 3.1, 3.3 and 3.4), to obtain the error bars shown, plotted in all graphs but often too small to be easily visible. However in the cases of slip flows with a Neumann boundary condition in a square or a plane layer (figures 3.5(b), 4.8(b)) the runs were taken to $T = 2000$ to obtain better convergence of decay rates (tables 3.2 and 4.2). With a range of runs for different values of κ we can seek the scaling behaviour of the decay rate as a function of κ in the limit of small diffusivity,

$$\gamma(\kappa) \simeq C\kappa^\alpha \quad (\kappa \rightarrow 0). \quad (3.2.21)$$

Figure 3.5(a) shows $\gamma(\kappa)$ (circles) plotted against κ . Error bars are indicated (plus signs) but these bars are small and hardly visible. There is a clear straight-line scaling and the solid line fit has a slope of $\alpha \simeq 0.546$: this is close to $\alpha = 0.5$ and this slope is also indicated by a dashed line. There is clear evidence of scaling and

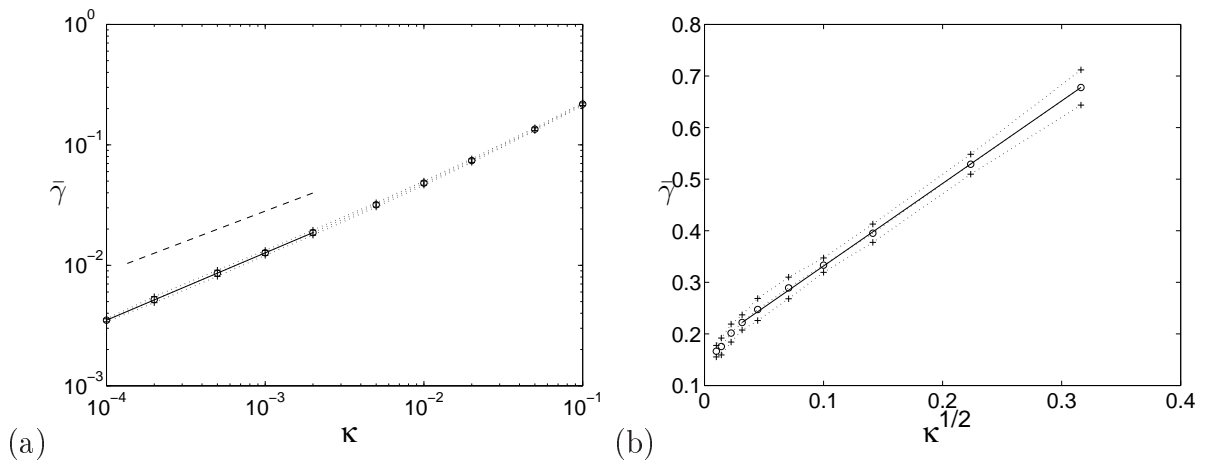


Figure 3.5: Plots (a) for $(\psi_{\text{slip}}, \sigma_D)$ showing $\bar{\gamma}$ (circles) and $\bar{\gamma} \pm \Delta\gamma$ (plus signs) against κ , and (b) for $(\psi_{\text{slip}}, \sigma_N)$ showing $\bar{\gamma}$ (circles), and $\bar{\gamma} \pm \Delta\gamma$ (plus signs) against $\sqrt{\kappa}$. In (a) the solid line is a fit with slope 0.546 while the dashed line has slope 0.5; in (b) the solid line has slope 1.6.

our measurement of the exponent α is consistent with a value of $1/2$ as discussed in Chapter 6. To give a definite range of values of α from the data, we estimate the maximum and minimum slopes of straight lines that pass through the error bars in (3.2.20) for the range of κ used for the fit (namely $10^{-4} \leq \kappa \leq 2 \times 10^{-3}$). More specifically, in this case (flow $\psi_{\text{slip}, \sigma_D}$), for the upper estimate of the slope α we use the data points $\kappa = 2 \times 10^{-3}$ with $\gamma = 0.01853 + 0.0009$, and $\kappa = 10^{-4}$ with $\gamma = 0.00360 - 0.00019$ to yield $\alpha = 0.562$. For a lower estimate, we use $\kappa = 2 \times 10^{-3}$ with $\gamma = 0.01853 - 0.0008$ and $\kappa = 10^{-4}$ with $\gamma = 0.00360 + 0.00019$ to yield $\alpha = 0.528$. This procedure yields $\alpha \in [0.528, 0.562]$, although we note that there is some curvature seen in the data points, consistent with an overestimate of the limiting value as $\kappa \rightarrow 0$.

Having treated this case in some detail we now proceed more quickly. For the Neumann or no-flux condition figures 3.5(b) and 3.8 are analogous to those for the Dirichlet case. However, for the Neumann boundary condition the scalar field

decays much more rapidly and some care has to be taken. Basically, in this case, we start with Neumann boundary condition σ_N and the field evolves, decaying quite rapidly, but then because of numerical error, a small component of Dirichlet field is generated (see Fig. 3.6)(a-c). This dominates after about $t = 200$ as shown in Fig. 3.6(b-c) and Fig. 3.7(a-c). Looking at these plots of the scalar field we can see that the field changes from Neumann symmetry (even about the boundary of the square) to Dirichlet symmetry. In Fig. 3.7(a-c) the rescaling in 3.7(a) is taken into account and in 3.7(b) we show the instantaneous decay rate (i.e., over each time step) and in 3.7(c) the average decay rate. Around $t = 200$ we see a sudden decrease in decay rate from about 0.2 to 0.02. We rescale the scalar field to avoid underflow when required as seen in panel (d) in this figure.

This problem arises because the Neumann field decays much more rapidly than the Dirichlet field, where numerical error leads to pollution by the Dirichlet symmetry class and an incorrect measure of the decay rate.

Recall that the field σ transforms according to (3.2.11) under the reflections S_1, S_2 given in (2.5.4, 2.5.5). From these we also obtain $R^2\sigma = \sigma$. Looking at the Fourier decomposition (2.4.6) we then have,

$$R^2\hat{\sigma}_{m,n} = \hat{\sigma}_{-m,-n}, \quad S_1\hat{\sigma}_{m,n} = (-1)^{m+n}\hat{\sigma}_{-n,-m}, \quad S_2\hat{\sigma}_{m,n} = (-1)^{m+n}\hat{\sigma}_{n,m}. \quad (3.2.22)$$

Mathematically, we proceed to prove the forms (3.2.22) with respect to the Neumann initial condition σ_N , and similarly, it can be proved with respect to the Dirichlet initial condition σ_D .

ϵ	npt	dt	T	γ
0.1	32	0.001	1000	0.218
0.05	32	0.001	1000	0.135
0.02	32	0.001	1000	0.0741
0.01	32	0.001	1000	0.0482
0.005	64	0.0005	1000	0.0318
0.002	64	0.0005	1000	0.0185
0.001	64	0.0005	1000	0.0127
0.0005	128	0.00005	1000	0.00868
0.0002	128	0.00005	1000	0.00528
0.0001	128	0.00005	1000	0.00360

Table 3.1: Computed values for the decay rate of the scalar variance for the slip flow with Dirichlet boundary condition.

As mentioned before, we have defined our scalar field σ via

$$\sigma(\mathbf{r}, t) = \sum_{m,n} \hat{\sigma}_{m,n} e^{imx+iny}, \quad \hat{\sigma}_{m,n} \equiv \hat{\sigma}_{-m,-n}^*. \quad (3.2.23)$$

with σ_N given in (3.2.10). Subsequently,

1) **Under a rotation of π about the origin;** $R^2(x, y) = (-x, -y)$ we can see that

$$\begin{aligned}
R^2\sigma_N &= \sigma_N(R^2(x, y)) \\
&= \sigma_N(-x, -y) \\
&= (\cos(x) + \cos(y))^2 - 1 \\
&= \phi_{1,1}^2 - 1 \\
&= \sigma_N.
\end{aligned} \quad (3.2.24)$$

Therefore, in this case, we get

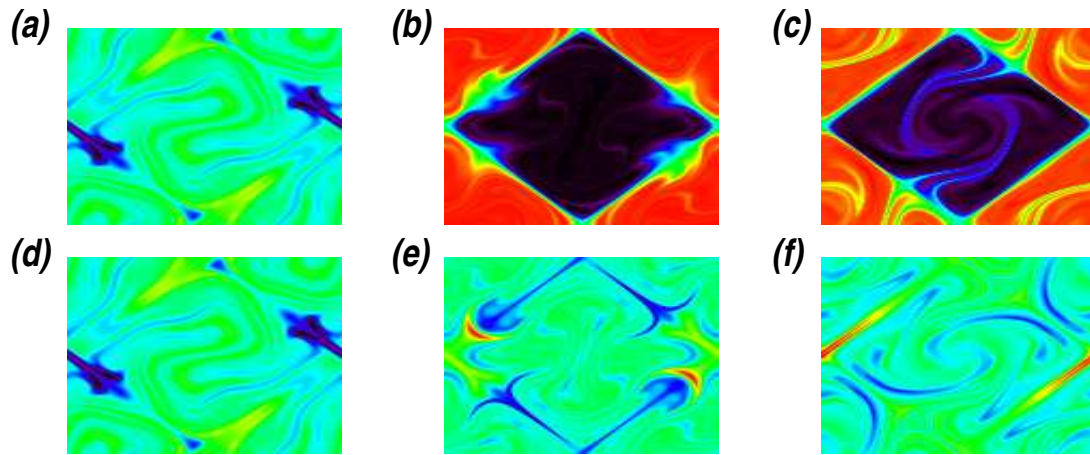


Figure 3.6: Scalar field for $(\psi_{\text{slip}}, \sigma_N)$ with $\kappa = 0.001$ with (a-c) losing symmetry and (d-f) imposing symmetry at (a,d) $t = 100$, (b,e) 200 and (c,f) 300.

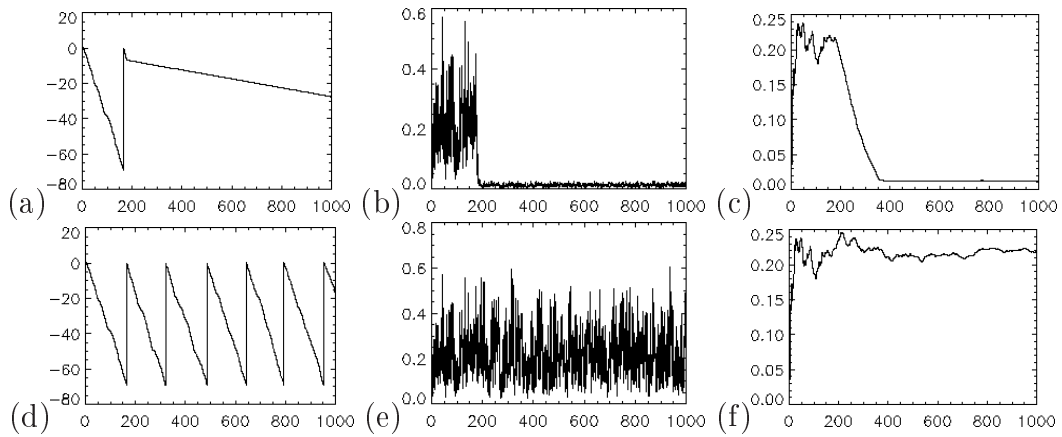


Figure 3.7: Plots for $(\psi_{\text{slip}}, \sigma_N)$ against time t of (a,d) $\log V(t)$, (b,e) $\tilde{\gamma}(t)$, and (c,f) $\bar{\gamma}(t)$. Panels of the flow show (a-c) losing symmetry and (d-f) imposing symmetry.

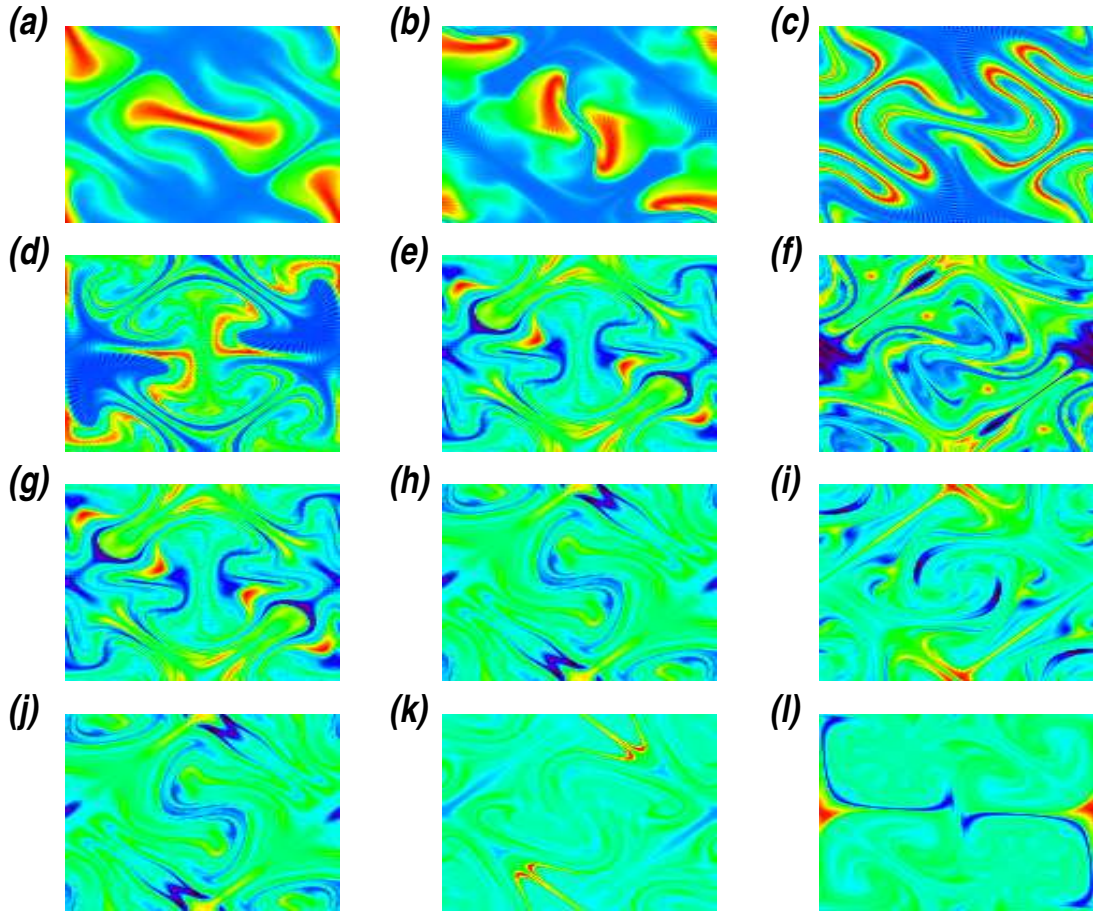


Figure 3.8: Scalar field for $(\psi_{\text{slip}}, \sigma_N)$ with $\kappa = 0.001$ with time at (a-c) $t = 1, 2, 3$, (d-f) $t = 5, 10, 15$, (g-i) $t = 10, 20, 30$ and (j-l) $t = 20, 40$ and 60 .

$$\begin{aligned}
 R^2\sigma(x, y) &= \sigma((R^2)^{-1}(x, y)) \\
 &= \sigma(R^2(x, y)) \\
 &= \sigma(-x, -y),
 \end{aligned} \tag{3.2.25}$$

This can be written as

$$R^2\sigma(x, y) = \sum_{m,n} \hat{\sigma}_{m,n} e^{-imx-iny}, \tag{3.2.26}$$

Putting $m' = -m$ and $n' = -n$, leads us to get

$$R^2\sigma(x, y) = \sum_{m', n'} \hat{\sigma}_{-m', -n'} e^{im'x + in'y}, \quad (3.2.27)$$

Again, if we put $m = m'$ and $n = n'$, Eq. (3.2.27) becomes

$$R^2\sigma(x, y) = \sum_{m, n} \hat{\sigma}_{-m, -n} e^{imx + iny}, \quad (3.2.28)$$

Consequently, if $R^2\sigma = \sigma$ then comparing Eq. (3.2.23) with Eq. (3.2.28) yields

$$\hat{\sigma}_{m, n} = \hat{\sigma}_{-m, -n}. \quad (3.2.29)$$

which is valid for both Neumann and Dirichlet cases.

2) **Similarly, under the transformation** $S_2(x, y) = (y - \pi, x + \pi)$ we have $S_2\sigma_N = +\sigma_N$. Therefore, one gets that

$$\begin{aligned} S_2\sigma(x, y) &= \sigma(S_2^{-1}(x, y)) \\ &= \sigma(S_2(x, y)) \\ &= \sigma(y - \pi, x + \pi), \end{aligned} \quad (3.2.30)$$

Therefore,

$$\begin{aligned} S_2\sigma(x, y, t) &= \sum_{m, n} \hat{\sigma}_{m, n}(t) e^{im(y-\pi) + in(x+\pi)} \\ &= \sum_{m, n} (-1)^{n-m} \hat{\sigma}_{m, n}(t) e^{imy + inx}. \end{aligned} \quad (3.2.31)$$

Putting $m' = n$ and $n' = m$ yields

$$S_2\sigma = \sum_{n',m'} (-1)^{n'-m'} \hat{\sigma}_{n',m'} e^{im'x+in'y}, \quad (3.2.32)$$

Thus Eq. (3.2.32) can be rewritten as

$$S_2\sigma = \sum_{n,m} (-1)^{n+m} \hat{\sigma}_{n,m} e^{imx+iny}, \quad (3.2.33)$$

Now, comparing Eq. (3.2.23) with Eq. (3.2.33) yields

$$\hat{\sigma}_{m,n} = (-1)^{m+n} \hat{\sigma}_{n,m}. \quad (3.2.34)$$

provided that $S_2\sigma = +\sigma$ in the Neumann case and

$$\hat{\sigma}_{m,n} = -(-1)^{m+n} \hat{\sigma}_{n,m}. \quad (3.2.35)$$

in the Dirichlet case.

3) **For** $S_1(x, y) = (\pi - y, \pi - x)$, one can obtain

$$S_1\sigma = \sum_{n,m} (-1)^{m+n} \hat{\sigma}_{-n,-m} e^{imx+iny}, \quad (3.2.36)$$

and if $S_1\sigma = \sigma$ (in the Neumann case) then

$$\hat{\sigma}_{m,n} = (-1)^{m+n} \hat{\sigma}_{-n,-m}. \quad (3.2.37)$$

and

$$\hat{\sigma}_{m,n} = -(-1)^{m+n} \hat{\sigma}_{-n,-m}. \quad (3.2.38)$$

ϵ	npt	dt	T	γ
0.1	32	0.001	2000	0.678
0.05	32	0.001	2000	0.529
0.02	32	0.001	2000	0.395
0.01	32	0.001	2000	0.333
0.005	64	0.0005	2000	0.289
0.002	64	0.0005	2000	0.247
0.001	64	0.0005	2000	0.222
0.0005	96	0.0002	2000	0.202
0.0002	96	0.0002	2000	0.176
0.0001	96	0.0002	2000	0.166

Table 3.2: Computed values for the decay rate of the scalar variance for the slip flow with Neumann boundary condition.

in the Dirichlet case.

Thus all the coefficients are real in view of (3.2.23) and for the two symmetry classes we have

$$\hat{\sigma}_{m,n} = \hat{\sigma}_{-m,-n} = \mp(-1)^{m+n}\hat{\sigma}_{-n,-m} = \mp(-1)^{m+n}\hat{\sigma}_{n,m} \in \mathbb{R}. \quad (3.2.39)$$

(with Neumann lower sign and Dirichlet upper sign). For the Neumann case, the code was modified to impose these symmetries at occasional intervals, and so remove any parasitic Dirichlet solution (see Fig. 3.6 and Fig. 3.7). We explain this point as following: in the case of imposing symmetry the flow ψ_{slip} preserves symmetry under the reflections S_1 , S_2 and the rotation R^2 , so that

$$\sigma = S_1\sigma = S_2\sigma = R^2\sigma, \quad (3.2.40)$$

In terms of Fourier modes, this implies that

$$\hat{\sigma}_{m,n} = (-1)^{m+n} \hat{\sigma}_{n,m} = (-1)^{m+n} \hat{\sigma}_{-n,-m} = \hat{\sigma}_{-m,-n}, \quad (3.2.41)$$

Looking to the case of losing symmetry, we see that these relationships are not preserved as they are polluted by Dirichlet symmetry. Consequently, in order to preserve these symmetries again we have to impose (3.2.41). This can be done numerically: here are some steps that show that

If $(m+n)$ is even then

$$(\text{new}\hat{\sigma})_{m,n} = \frac{1}{4}(\hat{\sigma}_{m,n} + \hat{\sigma}_{n,m} + \hat{\sigma}_{-n,-m} + \hat{\sigma}_{-m,-n}) \quad (3.2.42)$$

and if $(m+n)$ is odd

$$(\text{new}\hat{\sigma})_{m,n} = \frac{1}{4}(\hat{\sigma}_{m,n} - \hat{\sigma}_{n,m} - \hat{\sigma}_{-n,-m} + \hat{\sigma}_{-m,-n}) \quad (3.2.43)$$

Applying this numerically imposes those symmetries again.

Figure 3.8 shows typical results for a simulation. The Neumann boundary condition is evident in the evenness of the field under the reflection symmetries S_1 , S_2 . Except for this, though, there is no obvious role in the boundaries \mathcal{C} in controlling the actual structure of the field, even though $\mathbf{u} \cdot \mathbf{n} = 0$ there (Salman & Haynes, 2007). Even at the corners where $\mathbf{u} = 0$, there is no obvious concentration of scalar field. The decay may therefore be expected to be similar to the decay for a random flow without boundaries (see, e.g., Toussaint *et al.*, 2000; Salman & Haynes, 2007) and indeed in Fig. 3.5(b) we observe a long-time decay rate $\gamma(\kappa)$ (on a linear-square root scale) that appears to tend to a constant as κ tends to

zero, with a correction that appears to be of order $\sqrt{\kappa}$. This data is consistent with an exponent $\alpha = 0$. We note that decay on such a time-scale independent of κ indicates the presence of diffusive structures of scale $\kappa^{1/2}$ in the scalar field, and so corrections to the decay rate with this $\kappa^{1/2}$ scaling are likely.

Now we can analyse our simulations of the slip flow with Dirichlet (Fig. 3.3) and Neumann (Fig. 3.8) boundary conditions obtained at various times. The behaviour of the scalar variance in such cases is described by two stages (regimes) identified from analysis presented in Salman & Haynes (2007). In the first stage, the scalar is characterised by thin structures of scalar within the bulk of the flow which is clearly seen in Fig. 3.3(a-c)(d-e) and Fig. 3.8(a-c)(d-e). These structures correspond to the ‘elongated thin stripes’ indicated by Salman & Haynes (2007) (see 1.12(f,j)). The thickness of such ‘stripes’ decreases gradually, and once it decreases enough the flow enters its second stage in which scalar begins to decay (Fig. 3.3(f,h,i) and Fig. 3.8(f,h,i)). The long-exponential decay is the key character for the scalar in the second (final) stage in these simulations, where the scalar decays more rapidly and becomes fully mixed within the body of the flow even near the boundaries (Fig. 3.3(k,l) and Fig. 3.8(k,l)).

3.2.2 Numerical simulations for the flow $\psi_{\text{no-slip}}$

We now consider scalar decay in flows that satisfy a no-slip condition, $\mathbf{u} = 0$ on \mathcal{C} ; to do so we simply square the components $\phi_{m,n}$ in (2.2.2) and (2.2.3) that are used to build stream functions and initial conditions. The quadratic vanishing of the stream function along the boundary \mathcal{C} ensures that the full no-slip condition

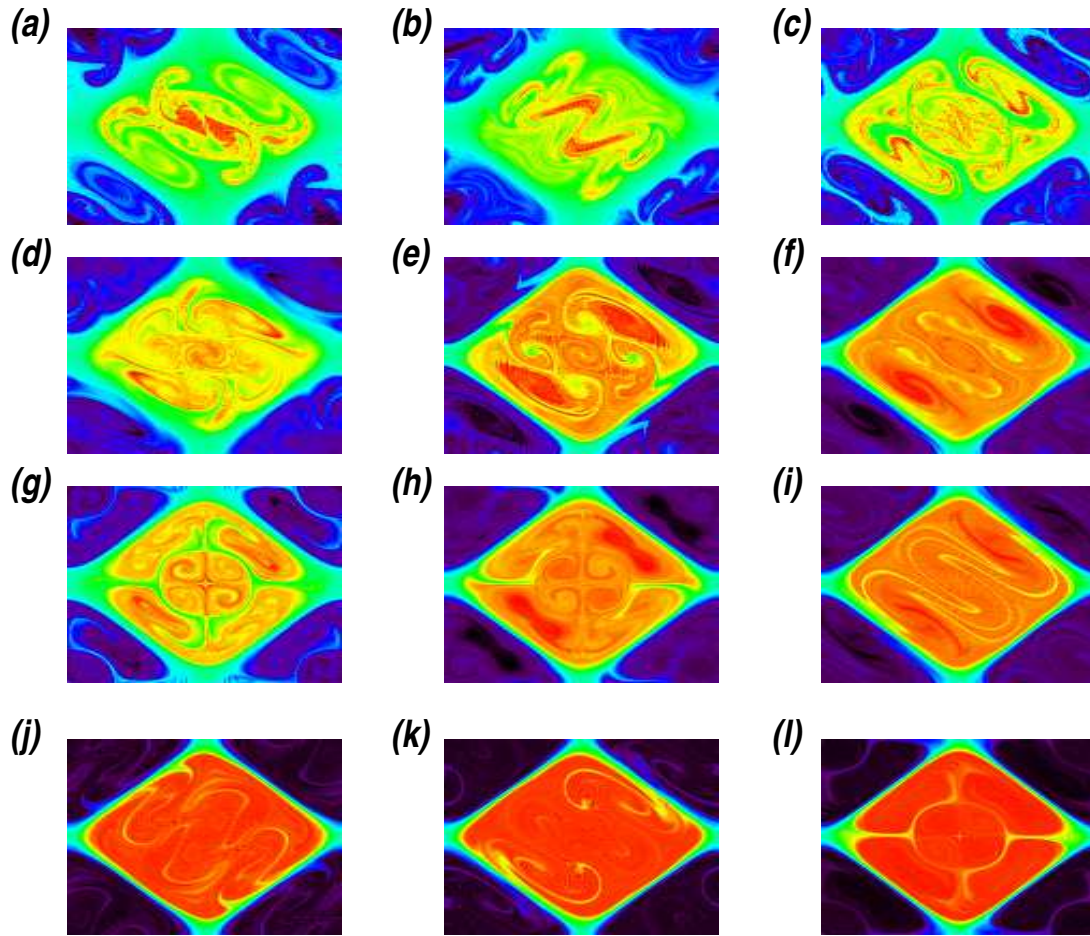


Figure 3.9: Scalar field for (a-c) $(\psi_{\text{no-slip}}, \sigma_D)$ with $\kappa = 0.001$. With time (a-c) $t = 1, 2, 3$, (d-f) $t = 4, 8, 12$, (g-i) $t = 5, 10, 15$ and (j-l) $t = 20, 40$, and 60 .

is satisfied there. Similar to (3.2.9) we will use the random flow

$$\psi_{\text{no-slip}} = \phi_{1,3}(x, y)^2 \sin[\omega t + \chi(t)] + \phi_{3,1}(x, y)^2 \cos[\omega t + \chi(t)]. \quad (3.2.44)$$

Some snapshots for this flow are shown in Figs. 2.3(b), 2.4(b), 2.5(b) and 2.6(b).

The stream function now does not change sign under reflections (2.5.4, 2.5.5) in the boundaries \mathcal{C} and so (3.2.5) can no longer be satisfied. We have to discard these reflection symmetries in the no-slip case. Instead the relevant symmetries to

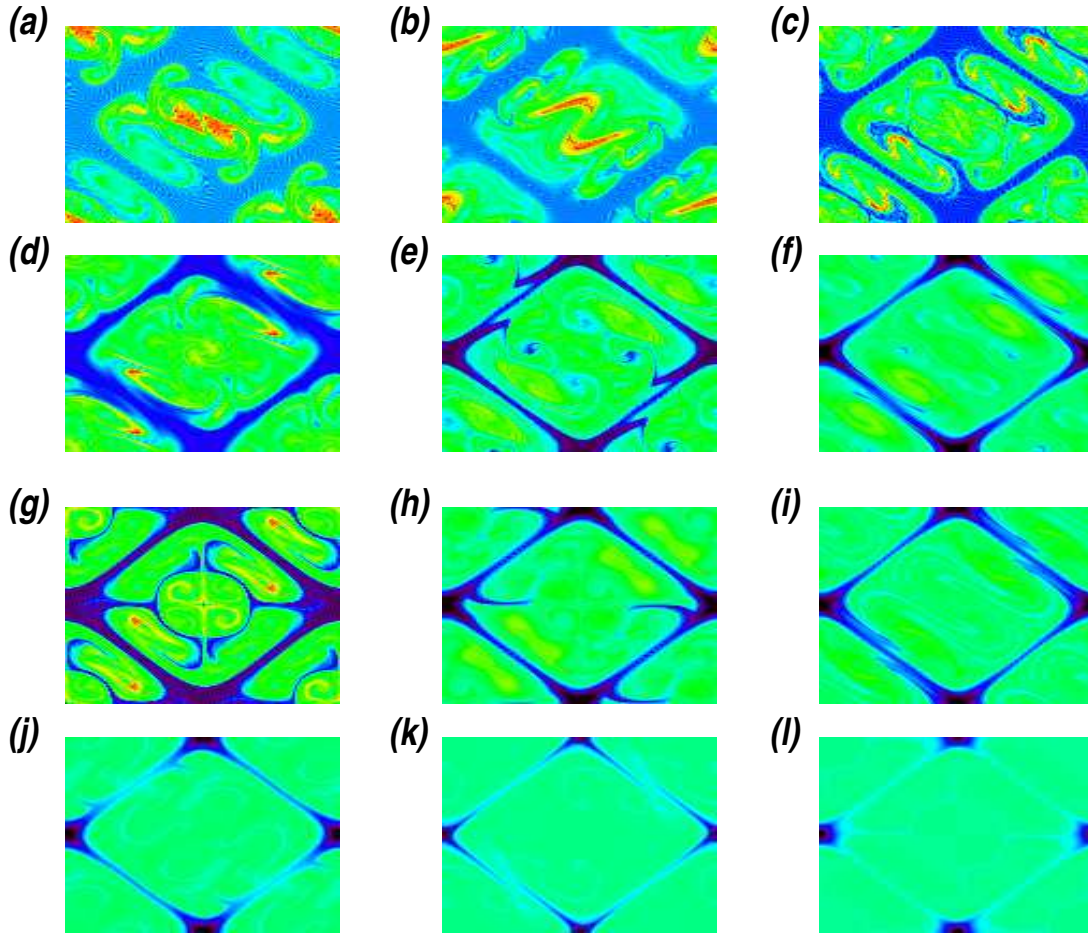


Figure 3.10: Scalar field for $(\psi_{\text{no-slip}}, \sigma_N)$ with $\kappa = 0.001$. With time (a-c) $t = 1, 2, 3$, (d-f) $t = 4, 8, 12$, (g-i) $t = 5, 10, 15$ and (j-l) $t = 20, 40$ and 60 .

consider are those that preserve orientation, in particular the translation T , the rotation R^2 about the origin, and the rotation TR^2 about $(\pi/2, \pi/2)$. We now have

$$T, TR^2 : \psi \rightarrow \psi, \quad \sigma \rightarrow \mp \sigma, \quad J \rightarrow J, \quad (3.2.45)$$

with the upper sign holding for scalar evolution from σ_D and the lower sign from σ_N . This can be proved for σ_D as follows. As $\sigma_D = \phi_{1,1} = \cos x + \cos y$, and acting

on translation $T(x, y) = (x + \pi, y + \pi)$ we have

$$\begin{aligned}
 T\sigma_D &= \sigma_D(T^{-1}(x, y)) \\
 &= \sigma_D(T(x, y)) \\
 &= \sigma_D(x + \pi, y + \pi) \\
 &= \cos(x + \pi) + \cos(y + \pi).
 \end{aligned} \tag{3.2.46}$$

Since $\cos(A + \pi) = -\cos A$ then

$$\begin{aligned}
 T\sigma_D &= -(\cos x + \cos y) \\
 &= -\phi_{1,1},
 \end{aligned} \tag{3.2.47}$$

which implies that

$$T\sigma_D = -\sigma_D. \tag{3.2.48}$$

Similarly, for σ_N , where $T\sigma_N = \sigma_N$ and the same procedure can be followed for the rotation TR^2 . Under T, TR^2 one may check that

$$\begin{aligned}
 T, TR^2 : \phi_{1,3} &\rightarrow -\phi_{1,3}, \\
 \phi_{1,3}^2 &\rightarrow \phi_{1,3}^2, \\
 \phi_{3,1}^2 &\rightarrow \phi_{3,1}^2.
 \end{aligned} \tag{3.2.49}$$

For more illustration we give results of simulations starting with σ_D and σ_N , shown in Fig. 3.9 and 3.10, respectively. This can be compared with Fig. 3.3 and Fig. 3.8.

It is important to note that because we no longer have reflectional symmetries S_1

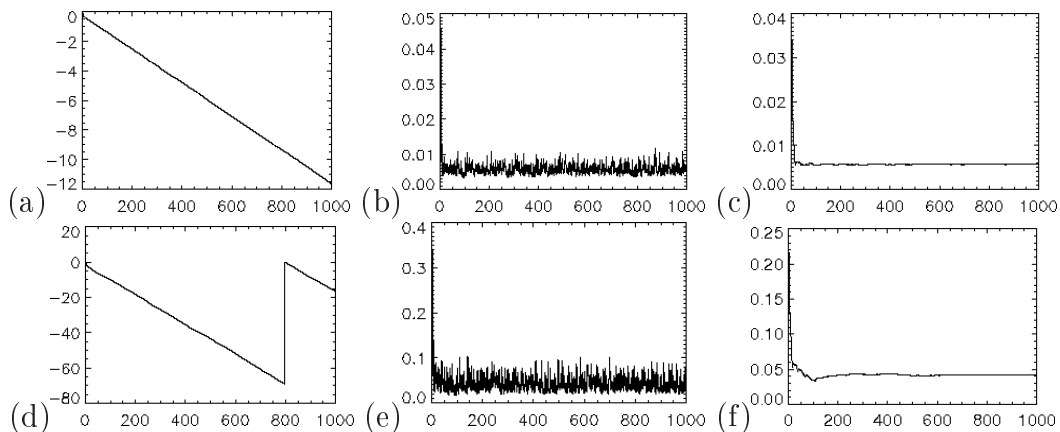


Figure 3.11: Plots for (a-c) $(\psi_{\text{no-slip}}, \sigma_{\text{D}})$ and (d-f) $(\psi_{\text{no-slip}}, \sigma_{\text{N}})$ against time t of (a,d) $\log V(t)$, (b,e) $\tilde{\gamma}(t)$, and (c,f) $\bar{\gamma}(t)$.

and S_2 in the boundaries of the square domain \mathcal{D} , we can not easily impose strict Dirichlet and Neumann boundary conditions on the scalar field. Instead the scalar field is odd or even respectively under the rotation through π about the midpoint of each side, seen clearly in Fig. 3.9 and Fig. 3.10. In fact we observe numerically in this and other figures that the Dirichlet and Neumann boundary conditions hold approximately, and so we will continue to use this terminology.

However, we now proceed to analyse the behaviour that arises in the evolution of the passive scalar flow satisfying no slip boundaries. This behaviour as is indicated in Salman & Haynes (2007) is described by four stages; in the first stage, the flow starts mixing; thin fluctuations characterise the interior of the flow where diffusion is not important (Fig. 3.9(a-c) and Fig. 3.10(a-c)). After a rapid mixing in the bulk of the fluid, an intermediate regime of mixing begins to start, where diffusion becomes important in the interior of the flow and removes fluctuations therein (Fig. 3.9(d)(g), and Fig. 3.10(d)(g)). This intermediate stage is characterised by ‘tongues’ of the scalar indicated also by ‘localised ejections’ in Salman &

ϵ	npt	dt	T	γ
0.1	32	0.001	1000	0.201
0.05	32	0.001	1000	0.116
0.02	32	0.001	1000	0.0563
0.01	32	0.001	1000	0.0329
0.005	64	0.0005	1000	0.0194
0.002	64	0.0005	1000	0.00966
0.001	64	0.0005	1000	0.00570
0.0005	128	0.00005	1000	0.00335
0.0002	128	0.00005	1000	0.00166
0.0001	128	0.00005	1000	0.000976

Table 3.3: Computed values for the decay rate of the scalar variance for the no-slip flow with Dirichlet boundary condition.

Haynes (2007) seen in Fig. 1.12(f)(j). The slow release of tongues leads to a slow algebraic decay of the concentration variance viewed experimentally by Gouillart *et al.* (2007, 2008); Gouillart, Thiffeault & Dauchot (2010) and indicated numerically by Lebedev & Turitsyn (2004); Salman & Haynes (2007) and Chernykh & Lebedev (2008). In the third stage, the interior of the flow becomes well-mixed and the scalar is a constant there, but there is a shrinking region near the boundaries, where the scalar has not mixed yet, and the flow is slow (Fig. 3.9(f)(i), Fig. 3.10(f)(i)). From theoretical discussion presented by Salman & Haynes (2007), the width of this shrinking region decreases with time, and once it reaches the diffusive boundary layer width, the decreasing stops, and the scalar begins to enter its final regime. There, in the wall region near the boundary the scalar has not mixed yet and the boundary region shrinks to a scale controlled by diffusion. In this final stage, the scalar decays exponentially with time (Fig. 3.9(j-l) and Fig. 3.10(j-l)).

On the other hand, in comparing with the slip case (Fig. 3.3 and Fig. 3.8), the behaviour of the passive scalar evolution in the no-slip flow (Fig. 3.9 and Fig. 3.10)

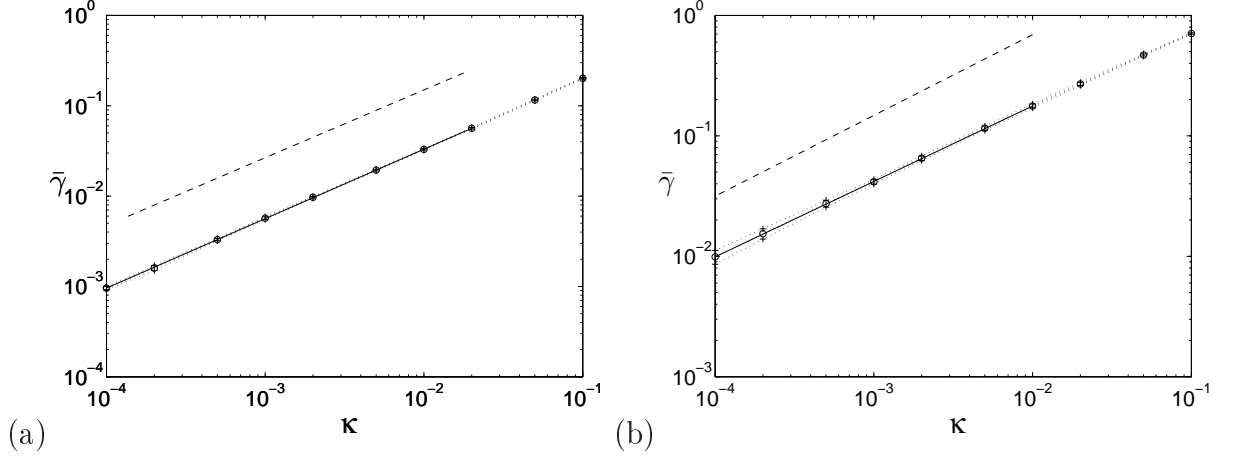


Figure 3.12: Plot for (a) $(\psi_{\text{no-slip}}, \sigma_{\text{D}})$ and (b) $(\psi_{\text{no-slip}}, \sigma_{\text{N}})$ of $\bar{\gamma}$ (circles) and $\bar{\gamma} \pm \Delta\gamma$ (plus signs) against κ . The solid lines are fits with slope (a) 0.765 and (b) 0.625. The dashed lines have slope 0.75 in (a) and 0.67 in (b).

appears to be similar, except near the boundaries. The region near the walls is thicker in the no-slip flow than in the slip one. This difference of the thickness near the boundaries leads to the slow transfer of heat through the no-slip boundaries and hence to slow mixing near such boundaries.

In place of (3.2.22) we now have

$$R^2 \hat{\sigma}_{m,n} = \hat{\sigma}_{-m,-n}, \quad T \hat{\sigma}_{m,n} = (-1)^{m+n} \hat{\sigma}_{m,n}, \quad TR^2 \hat{\sigma}_{m,n} = (-1)^{m+n} \hat{\sigma}_{-m,-n}, \quad (3.2.50)$$

and so fields satisfy

$$\hat{\sigma}_{m,n} = \hat{\sigma}_{-m,-n} = \mp (-1)^{m+n} \hat{\sigma}_{m,n} = \mp (-1)^{m+n} \hat{\sigma}_{-m,-n} \in \mathbb{R}, \quad (3.2.51)$$

starting with σ_{D} (upper sign) or σ_{N} (lower sign). Half the coefficients are identically zero in each case. (Note, we have not put this in our code). Here, we provide mathematical confirmation for (3.2.50). (Note that, for R^2 , this has been proved

ϵ	npt	dt	T	γ
0.1	32	0.001	1000	0.707
0.05	32	0.001	1000	0.469
0.02	32	0.001	1000	0.270
0.01	32	0.001	1000	0.177
0.005	64	0.0005	1000	0.116
0.002	64	0.0005	1000	0.0652
0.001	64	0.0005	1000	0.0416
0.0005	96	0.0002	1000	0.0274
0.0002	96	0.0002	1000	0.0154
0.0001	96	0.0002	1000	0.00994

Table 3.4: Computed values for the decay rate of the scalar variance for the no-slip flow with Neumann boundary condition.

in Section §3.2.1). However,

1) **Under translation** $T(x, y) = (x + \pi, y + \pi)$ we have

$$\begin{aligned}
 T\sigma(x, y) &= \sigma(T^{-1}(x, y)) \\
 &= \sigma(T(x, y)) \\
 &= \sigma(x + \pi, y + \pi),
 \end{aligned} \tag{3.2.52}$$

This can be written as

$$\begin{aligned}
 T\sigma(x, y) &= \sum_{m,n} \hat{\sigma}_{m,n} e^{im(x+\pi)+in(y+\pi)} \\
 &= (-1)^{m+n} \sum_{m,n} \hat{\sigma}_{m,n} e^{imx+iny},
 \end{aligned} \tag{3.2.53}$$

So, if $T\sigma = \sigma$ (in the Neumann case) then comparing Eq. (3.2.23) with Eq. (3.2.53) yields

$$\hat{\sigma}_{m,n} = (-1)^{m+n} \hat{\sigma}_{m,n}. \tag{3.2.54}$$

or $T\sigma = -\sigma$ in the Dirichlet case leading to

$$\hat{\sigma}_{m,n} = -(-1)^{m+n}\hat{\sigma}_{m,n}. \quad (3.2.55)$$

2) **Similarly for** $TR^2(x, y) = (\pi - x, \pi - y)$:

$$\begin{aligned} TR^2\sigma(x, y) &= \sigma(TR^2(x, y)), \\ &= \sigma(\pi - x, \pi - y). \end{aligned} \quad (3.2.56)$$

We write this as

$$\begin{aligned} TR^2\sigma(x, y) &= \sum_{m,n} \hat{\sigma}_{m,n} e^{im(\pi-x)+in(\pi-y)}, \\ &= \sum_{m,n} (-1)^{m+n} \hat{\sigma}_{m,n} e^{-imx-iny}, \end{aligned} \quad (3.2.57)$$

Putting $m' = -m$ and $n' = -n$, leads us to get

$$TR^2\sigma = \sum_{m',n'} (-1)^{m'+n'} \hat{\sigma}_{-m',-n'} e^{im'x+in'y}, \quad (3.2.58)$$

Again, if we put $m = m'$ and $n = n'$, Eq. (3.2.58) collapses to

$$TR^2\sigma = \sum_{m,n} (-1)^{m+n} \hat{\sigma}_{-m,-n} e^{imx+iny}, \quad (3.2.59)$$

Consequently, if $TR^2\sigma = +\sigma$ (in the Neumann case), then we get

$$\hat{\sigma}_{m,n} = (-1)^{m+n} \hat{\sigma}_{-m,-n}. \quad (3.2.60)$$

or $TR^2\sigma = -\sigma$ in the Dirichlet case and leads to

$$\hat{\sigma}_{m,n} = -(-1)^{m+n}\hat{\sigma}_{-m,-n}. \quad (3.2.61)$$

3.3 Summary and discussion

Turning now to the results of the simulations, for the Dirichlet case we see overall similar behaviour in the no-slip case (Fig. 3.9) compared with the slip case (Fig. 3.3), except that no-slip boundary conditions appear to give thicker boundary layers, likely to slow down the loss of heat from the system in the Dirichlet case, or to give a reservoir of heat in the Neumann case. This slowing is evident in the scaling law for the decay rate $\gamma(\kappa)$ in Fig. 3.12(a) which shows a fall-off with exponent α measured as approximately 0.765, close to a suggested theoretical value of $3/4$, as we shall discuss later. For the Neumann case, whereas for the slip boundary condition the boundaries play no apparent role in the destruction of temperature fluctuations (Fig. 3.8) the long-time scalar distribution for the no-slip flow in Fig. 3.10 consists of a region of cool fluid (blue) in the relatively stagnant region near the boundary and a luke-warm interior (green). As argued by Lebedev & Turitsyn (2004) these ‘peripheral regions’ control the mixing. However we find a larger exponent than the value $\alpha = 1/2$ in their paper. Later in Chapter 6 we will argue that it is $2/3$ in this case, with the corners now playing a controlling role. The results of this chapter are summarised in lines (*i-iv*) of table 6.1.

Note that, in all the figures presented the colour scale (given in Fig. 3.2) is chosen with zero centred on green and the extremities of the scale (red or black) chosen to correspond to $\pm \max |\sigma|$. Thinking of the passive scalar fields as temperature, in

Chapter 3. NUMERICAL SIMULATIONS

the plots in Fig. 3.9, by symmetry there is fluid at both extremes of temperature whereas in Fig. 3.10 the scalar field is asymmetrical, there being very cold fluid near the boundary and no corresponding very hot fluid in the system.

4

LARGE SCALES AND BLOCH WAVENUMBERS

4.1 Outline

In this chapter we aim to look at the passive scalar decay in scalar fields embedded in a plane layer. For this goal, in Section §4.2 we consider random flows in a plane layer geometry, using Bloch wavenumbers within our numerical code. The scaling exponents α that we obtain show values close to simple fractions and later in Chapter 6 we will link these exponents to the theory of Lebedev & Turitsyn (2004) and extensions. Section §4.3 includes a brief summary of simulations in a plane layer. Mixed Dirichlet/Neumann boundary conditions for random flows considered in the square domain are presented in Section §4.4. In Section §4.5 we also present sample runs of periodic flows to investigate the validity of scaling behaviour $\gamma \simeq C\kappa^\alpha$ and compare exponents between random and deterministic, periodic flows. Finally, in Section §4.6 we summarise our findings of this chapter

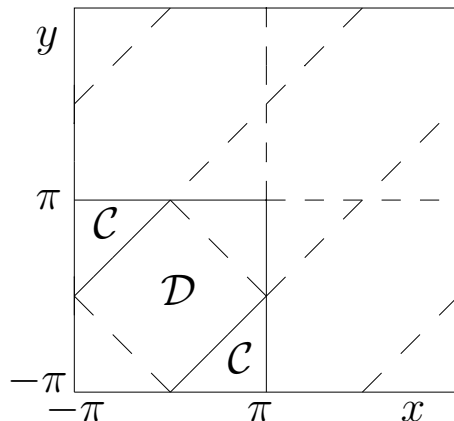


Figure 4.1: Geometry of a plane layer embedded in 2π -periodic space.

with some concluding remarks.

4.2 Simulations in a plane layer and Bloch wavenumbers

Previous work by Salman & Haynes (2007) focuses on the evolution of passive scalars in an infinite plane layer. In this section we give some comparison with their work, and develop some further directions using Bloch wavenumbers. In our doubly periodic domain we take the plane layer to be the region, again called \mathcal{D} , with the lines $y - x = \pm\pi$ forming its boundary \mathcal{C} depicted solid in Fig. 4.1: note how the plane layer continues periodically. To obtain a suitable flow all we need to do is to ensure that the flow breaks the previous symmetries that preserved the lines $x + y = \pm\pi$, while retaining the plane layer boundaries $y - x = \pm\pi$ as invariant. The symmetry group of the new, plane layer domain is reduced to 8 elements, generated by $\{R^2, T, RS\}$ and includes the reflections S_1 and S_2 defined in (2.5.4, 2.5.5).

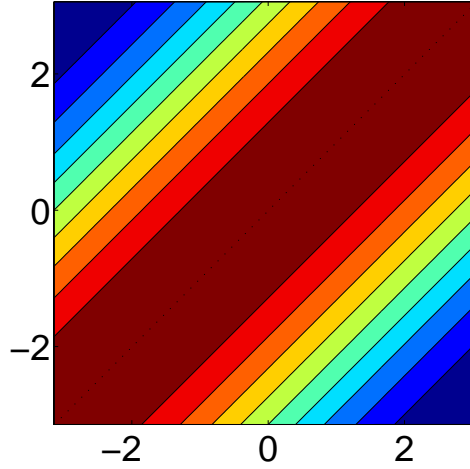


Figure 4.2: Initial scalar field $\sigma_{\frac{1}{2}\text{D}} = \cos \frac{1}{2}(y - x)$.

For Neumann boundary conditions we may again take the σ_{N} given in (3.2.10) as initial condition. But for Dirichlet boundary conditions, in which the layers of fluid are alternately hot and cold, it is evident from Fig. 4.1 that we need to take an initial condition of greater periodicity than 2π , for example

$$\sigma_{\frac{1}{2}\text{D}} = \cos \frac{1}{2}(y - x). \quad (4.2.1)$$

This greater periodicity may easily be accommodated by redefining σ in (4.2.2) to allow periodicity 4π via the Bloch form

$$\sigma(\mathbf{r}, t) = e^{ix/2+iy/2} \sum_{m,n} \hat{\sigma}_{m,n}(t) e^{imx+iny}, \quad \hat{\sigma}_{m,n} = \hat{\sigma}_{-m-1,-n-1}^*. \quad (4.2.2)$$

In this case the initial condition (4.2.1) corresponds to setting $\hat{\sigma}_{-1,0} = \hat{\sigma}_{0,-1} = 1/2$. (Note also that $V(t)$ in Eq. (2.4.2) is now taken as the mean-square scalar over the 4π -periodic domain).

Figure 4.2 shows the temperature field for the initial condition $\sigma_{\frac{1}{2}\text{D}}$ given by (4.2.1).

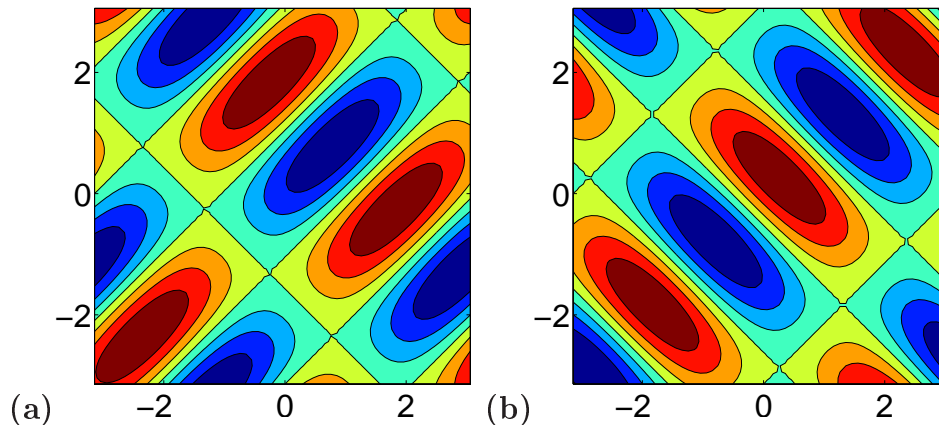


Figure 4.3: Plots of the stream functions (a) $\phi_{1,3}(x - ct, y - ct)$ and (b) $\phi_{3,1}(x + ct, y + ct)$ at $t = \pi/4$ with $c = 1$.

See how the layers of fluid are alternately hot (red) and blue (cold).

4.2.1 Numerical simulations for random flow $\psi_{slip,pl}$

We set up the following flow which obeys a slip condition on the plane layer (subscript ‘pl’) boundaries,

$$\psi_{slip,pl} = \phi_{1,3}(x - ct, y - ct) \sin[\omega t + \chi(t)] + \phi_{3,1}(x + ct, y + ct) \cos[\omega t + \chi(t)]. \quad (4.2.3)$$

The flow can now be thought of as travelling waves depicted in Fig. 4.3, travelling in the $\pm(1, 1)$ directions and having their phase $\chi(t)$ reset randomly at each renewing time $t = j\tau$. Particles may now cross the lines $x + y = \pm\pi$ and this breaks the symmetry S_1 used earlier. We take $c = \omega = 1$ in what follows and as usual $\tau = 0.64$. Statistically, the flow is translationally invariant parallel to the line $y = x$.

Again, in the case of Neumann boundary conditions (Fig. 4.4 and Fig. 4.5), some care has to be taken. Numerical rounding error leads to losing symmetry of the

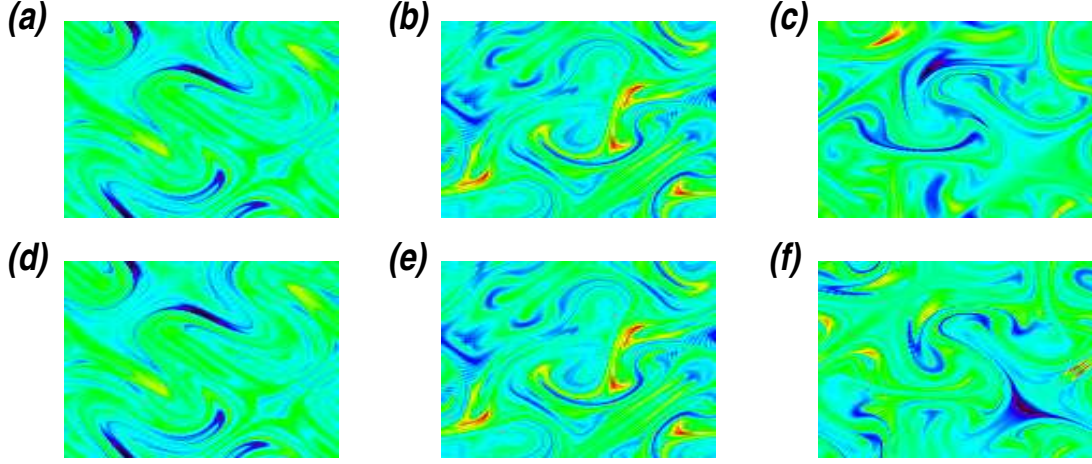


Figure 4.4: Scalar field for $(\psi_{slip,pl}, \sigma_N)$ with (a-c) losing symmetry and (d-f) imposing symmetry at $t =$ (a,d) 75, (b,e) 150, and (c,f) 225.

scalar field and an incorrect measure of the decay rate. This can be demonstrated approximately after $t = 200$ as shown in Fig. 4.4(a-c) and Fig. 4.5(a-c). Some gradients of the scalar have been smeared out at around $T = 200$ (Fig. 4.4(c)) and the fast decay of fluctuations seen earlier tends to be reduced as time increases (Fig. 4.5(a-c)). The code was modified to impose these symmetries and remove any parasitic solution (Fig. 4.4(d-f) and Fig. 4.5(d-f)). Typical simulations of the slip flow $\psi_{slip,pl}$ with Neumann boundary condition are shown in Fig. 4.6. (We will discuss this later).

Figure 4.7 shows runs for $\psi_{slip,pl}$ with $\sigma_{\frac{1}{2}D}$ and σ_N : the only symmetry left in these fields is that of being odd or even under the reflection S_2 in (2.5.5). For the Dirichlet case we now have for the coefficients

$$\hat{\sigma}_{m,n} = -(-1)^{m+n} \hat{\sigma}_{n,m} = \hat{\sigma}_{-m-1,-n-1} = -(-1)^{m+n} \hat{\sigma}_{-n-1,-m-1}. \quad (4.2.4)$$

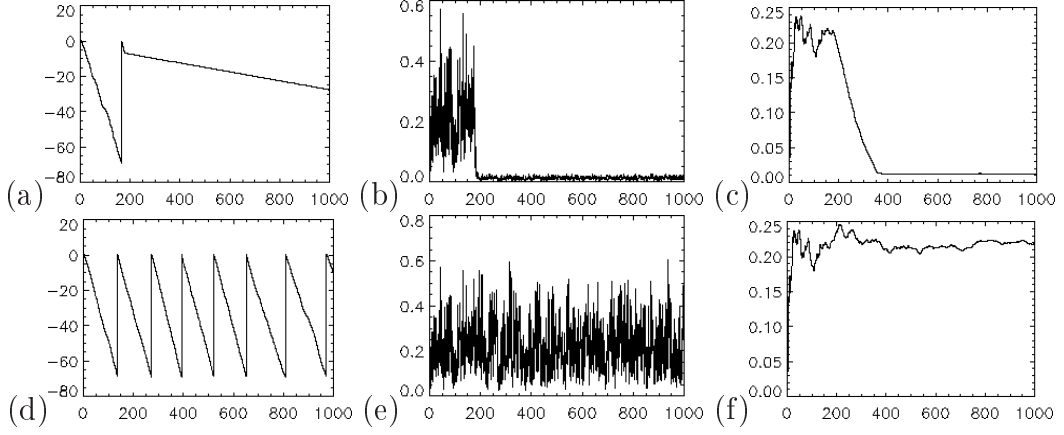


Figure 4.5: Plots for $(\psi_{slip,pl}, \sigma_N)$ against time t of (a,d) $\log V(t)$, (b,e) $\tilde{\gamma}(t)$, and (c,f) $\bar{\gamma}(t)$. Panels (a-c) losing symmetry and (d-f) imposing symmetry.

(incorporating (4.2.2)) while in the Neumann case they are governed by

$$\hat{\sigma}_{m,n} = (-1)^{m+n} \hat{\sigma}_{n,m} = \hat{\sigma}_{-m,-n} = (-1)^{m+n} \hat{\sigma}_{-n,-m}. \quad (4.2.5)$$

(incorporating (2.4.6)).

Turning to our results of simulations for the slip flow in the plane layer (Fig. 4.6 and Fig. 4.7), we see that for the Dirichlet case (Fig. 4.7(a-c)), the red well-mixed region is seen in the body of the fluid together with a thin layer (green) along the boundaries where the scalar tends to vanish. Yellow cooler plumes are also driven into the interior. Compared with the slip flow simulated in the square domain (Fig. 3.3), oddness of the scalar is clearly evident under the reflection S_2 along the boundaries. The scalar is invariant under the half-rotation R^2 and also under the reflection RS parallel to the line $x = y$. For the slip flow with Neumann boundary condition (Fig. 4.6 and Fig. 4.7(d-f)), the two stages of mixing are completely evident. Occurrence of the ‘elongated stripes’ within the interior of the flow characterises the first stage of mixing. This is clearly seen in Fig. 4.6(a-c)(d-

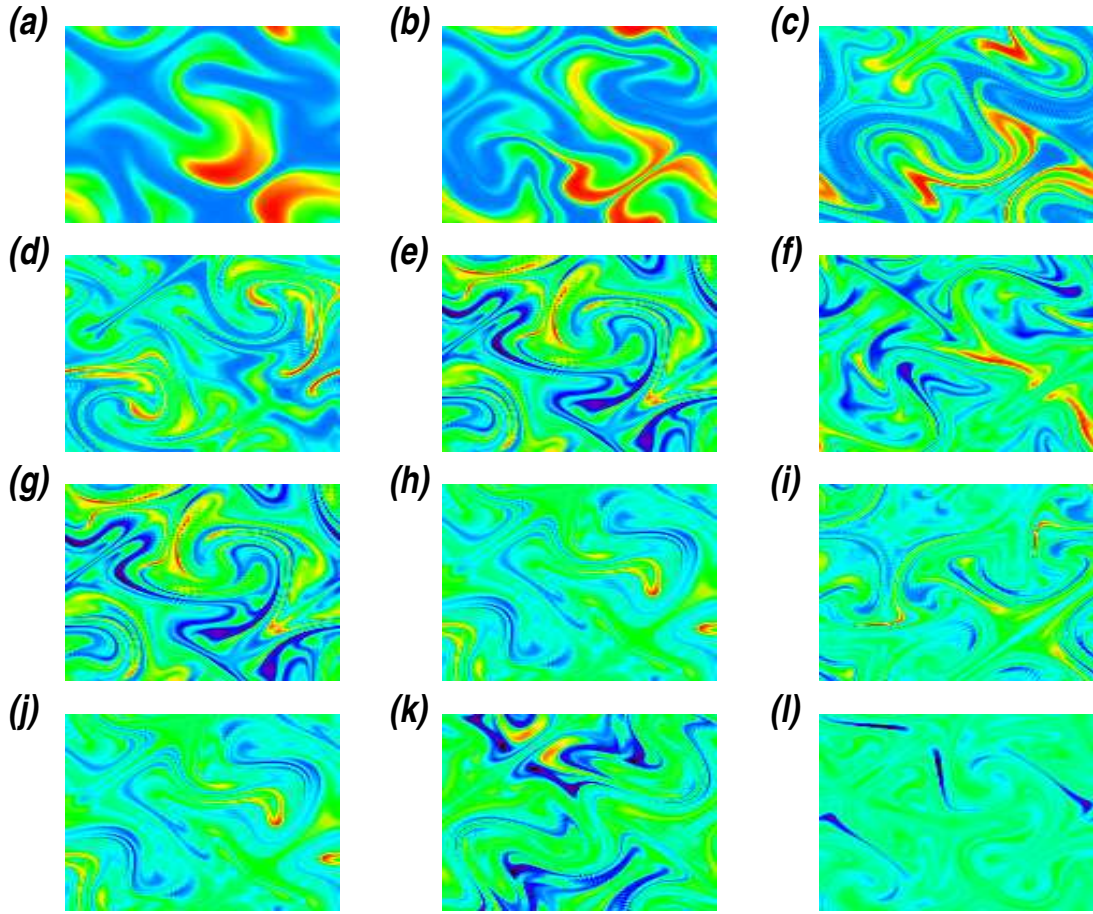


Figure 4.6: Scalar field for (a–c) $(\psi_{slip,pl}, \sigma_N)$ with $\kappa = 0.001$ at (a–c) $t = 1, 2, 3$, (d–f) 5, 10, 15, (g–i) 10, 20, 30 and (j–l) 20, 40 and 60.

f). With continued decreasing of these stripes, as time increases, scalar begins to decay in its second (final) stage (Fig. 4.6(h–i)(k–l)). Therein, the scalar is decaying more rapidly along the layer, and again no influence of the layer boundaries where the scalar is well-mixed everywhere as seen in Fig 4.7(d–f).

Note that, the relationships in (4.2.5) have been proved earlier in Chapter 3 and here we just provide the mathematical proof for all relationships in (4.2.4). With Dirichlet boundary condition $(\sigma_{\frac{1}{2}D})$ and acting on:

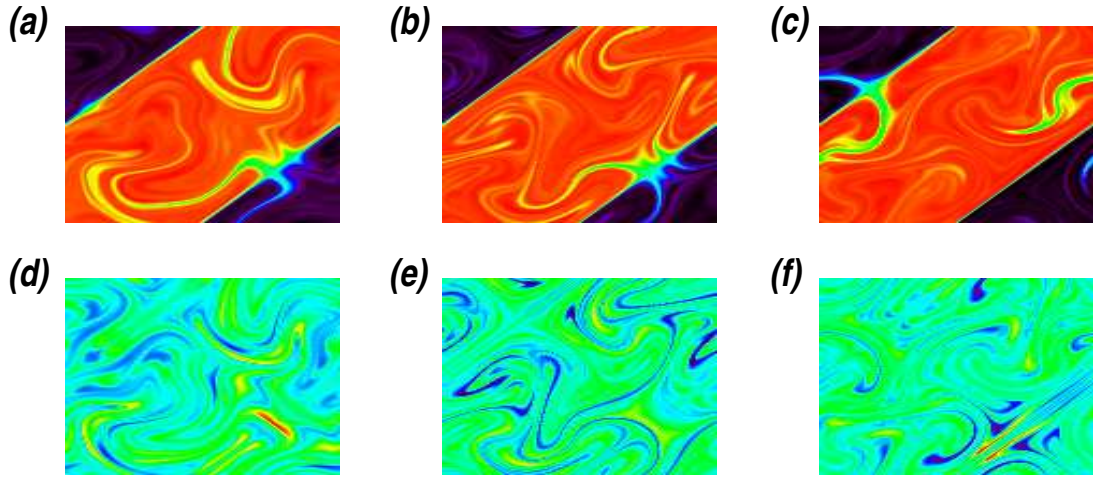


Figure 4.7: Scalar field for (a–c) $(\psi_{slip,pl}, \sigma_{\frac{1}{2}D})$ and (d–f) $(\psi_{slip,pl}, \sigma_N)$ with $\kappa = 0.001$ at (a,d) $t = 100$, (b,e) 200 and (c,f) 300.

1) The **reflection** $S_2(x, y) = (y - \pi, x + \pi)$ we have

$$\begin{aligned}
 S_2 \sigma_{\frac{1}{2}D} &= \sigma_{\frac{1}{2}D}(S_2^{-1}(x, y)) \\
 &= \sigma_{\frac{1}{2}D}(S_2(x, y)) \\
 &= \sigma_{\frac{1}{2}D}(y - \pi, x + \pi).
 \end{aligned} \tag{4.2.6}$$

This can be written as

$$\begin{aligned}
 S_2 \sigma_{\frac{1}{2}D} &= \cos \frac{1}{2}(x - y + 2\pi) \\
 &= \cos\left(\frac{1}{2}(y - x) - \pi\right),
 \end{aligned} \tag{4.2.7}$$

Since $\cos(A - \pi) = -\cos A$ then

$$\begin{aligned} S_2\sigma_{\frac{1}{2}\mathbb{D}} &= -\cos\frac{1}{2}(y-x) \\ &= -\sigma_{\frac{1}{2}\mathbb{D}}. \end{aligned} \tag{4.2.8}$$

Now, based on (4.2.2),

$$\begin{aligned} S_2\sigma &= \sigma(S_2^{-1}(x, y)) \\ &= \sigma(S_2(x, y)) \\ &= \sigma(y - \pi, x + \pi). \end{aligned} \tag{4.2.9}$$

which is written as

$$\begin{aligned} S_2\sigma &= e^{i(y-\pi)/2+i(x+\pi)/2} \sum_{m,n} \hat{\sigma}_{m,n} e^{im(y-\pi)+in(x+\pi)} \\ &= e^{ix/2+iy/2} \sum_{m,n} (-1)^{m+n} \hat{\sigma}_{m,n} e^{imy+inx}, \end{aligned} \tag{4.2.10}$$

If we put $m' = n$ and $n' = m$, then we get

$$S_2\sigma = e^{ix/2+iy/2} \sum_{n',m'} (-1)^{m'+n'} \hat{\sigma}_{n',m'} e^{im'x+in'y}, \tag{4.2.11}$$

Similarly, putting $m = m'$ and $n = n'$ gives

$$S_2\sigma = e^{ix/2+iy/2} \sum_{n,m} (-1)^{m+n} \hat{\sigma}_{n,m} e^{imx+iny}, \tag{4.2.12}$$

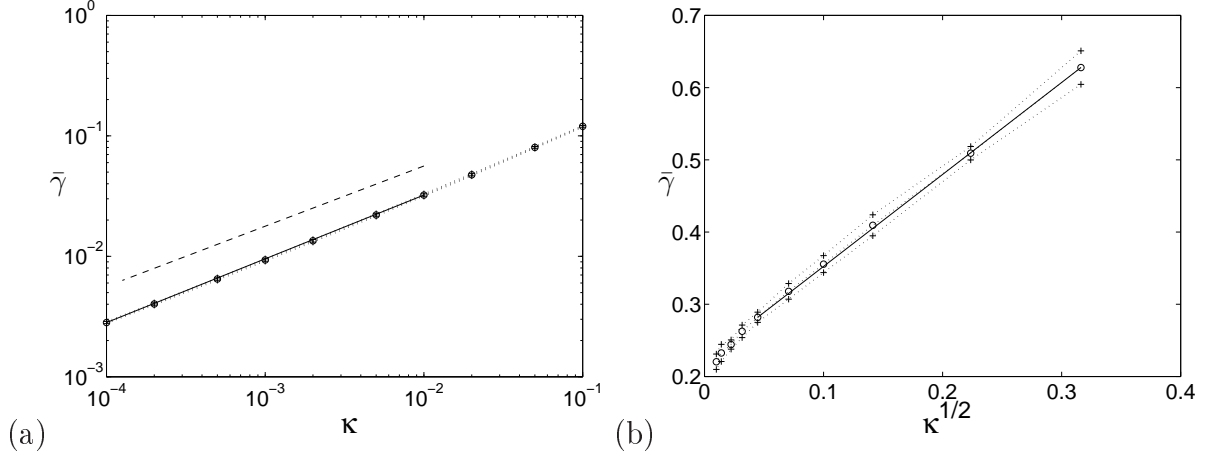


Figure 4.8: Plots (a) for $(\psi_{slip,pl}, \sigma_{\frac{1}{2}D})$ showing $\bar{\gamma}$ (circles) and $\bar{\gamma} \pm \Delta\gamma$ (plus signs) against κ , and (b) for $(\psi_{slip,pl}, \sigma_N)$ showing $\bar{\gamma}$ (circles), and $\bar{\gamma} \pm \Delta\gamma$ (plus signs) against $\sqrt{\kappa}$. The solid lines are fits with slopes (a) 0.53 and (b) 1.27, while in (a) the dashed line has slope 0.5.

So, motivated by Dirichlet condition, if $S_2\sigma = -\sigma$ then one can obtain

$$\hat{\sigma}_{m,n} = -(-1)^{m+n}\hat{\sigma}_{n,m}. \quad (4.2.13)$$

2) With the **rotation** $R^2(x, y) = (-x, -y)$, one finds that $R^2\sigma_{\frac{1}{2}D} = \sigma_{\frac{1}{2}D}$. In this case and acting on R^2 , Eq. (4.2.2) can be written as

$$\begin{aligned} R^2\sigma &= \sigma((R^2)^{-1}(x, y)) \\ &= \sigma(R^2(x, y)) \\ &= \sigma(-x, -y), \end{aligned} \quad (4.2.14)$$

to yield

$$R^2\sigma = e^{-ix/2-iy/2} \sum_{m,n} \hat{\sigma}_{m,n} e^{-imx-iny}, \quad (4.2.15)$$

Chapter 4. LARGE SCALES AND BLOCH WAVENUMBERS

ϵ	npt	dt	T	γ
0.1	32	0.001	1000	0.120
0.05	32	0.001	1000	0.0802
0.02	32	0.001	1000	0.0476
0.01	32	0.001	1000	0.0323
0.005	64	0.0005	1000	0.0221
0.002	64	0.0005	1000	0.0135
0.001	64	0.0005	1000	0.00932
0.0005	96	0.0002	1000	0.00648
0.0002	96	0.0002	1000	0.00402
0.0001	96	0.0002	1000	0.00282

Table 4.1: Computed values for the decay rate of the scalar variance for the slip flow $\psi_{slip,pl}$ with Bloch wavenumbers: $M = N = 0.5$.

In another equivalent form,

$$R^2\sigma = e^{ix/2+iy/2} \sum_{m,n} \hat{\sigma}_{m,n} e^{-i(m+1)x-i(n+1)y}, \quad (4.2.16)$$

Putting $m' = -(m + 1)$ and $n' = -(n + 1)$ gives

$$R^2\sigma = e^{ix/2+iy/2} \sum_{m',n'} \hat{\sigma}_{-m'-1,-n'-1} e^{im'x+in'y}. \quad (4.2.17)$$

again, if we put $m = m'$ and $n = n'$, we get

$$R^2\sigma = e^{ix/2+iy/2} \sum_{m,n} \hat{\sigma}_{-m-1,-n-1} e^{imx+iny}. \quad (4.2.18)$$

and simply, if $R^2\sigma = \sigma$, then

$$\hat{\sigma}_{m,n} = \hat{\sigma}_{-m-1,-n-1} \quad (4.2.19)$$

Chapter 4. LARGE SCALES AND BLOCH WAVENUMBERS

ϵ	npt	dt	T	γ
0.1	32	0.001	2000	0.628
0.05	32	0.001	2000	0.509
0.02	32	0.001	2000	0.409
0.01	32	0.001	2000	0.356
0.005	64	0.0005	2000	0.318
0.002	64	0.0005	2000	0.282
0.001	64	0.0005	2000	0.263
0.0005	96	0.0002	2000	0.244
0.0002	96	0.0002	2000	0.233
0.0001	96	0.0002	2000	0.220

Table 4.2: Computed values for the decay rate of the scalar variance for the slip flow $\psi_{slip,pl}$ with Neumann boundary condition.

3) **Under reflection** $S_1(x, y) = (\pi - y, \pi - x)$:

Similarly, one may check that $S_1\sigma_{\frac{1}{2}D} = \sigma_{\frac{1}{2}D}$ and therefore, based on (4.2.2),

$$\begin{aligned}
 S_1\sigma &= \sigma(S_1^{-1}(x, y)) \\
 &= \sigma(S_1(x, y)) \\
 &= \sigma(\pi - y, \pi - x).
 \end{aligned} \tag{4.2.20}$$

which gives

$$\begin{aligned}
 S_1\sigma &= e^{i(\pi-y)/2+i(\pi-x)/2} \sum_{m,n} \hat{\sigma}_{m,n} e^{im(\pi-y)+in(\pi-x)} \\
 &= -e^{ix/2+iy/2} \sum_{m,n} (-1)^{m+n} \hat{\sigma}_{m,n} e^{-i(m+1)y-i(n+1)x}.
 \end{aligned} \tag{4.2.21}$$

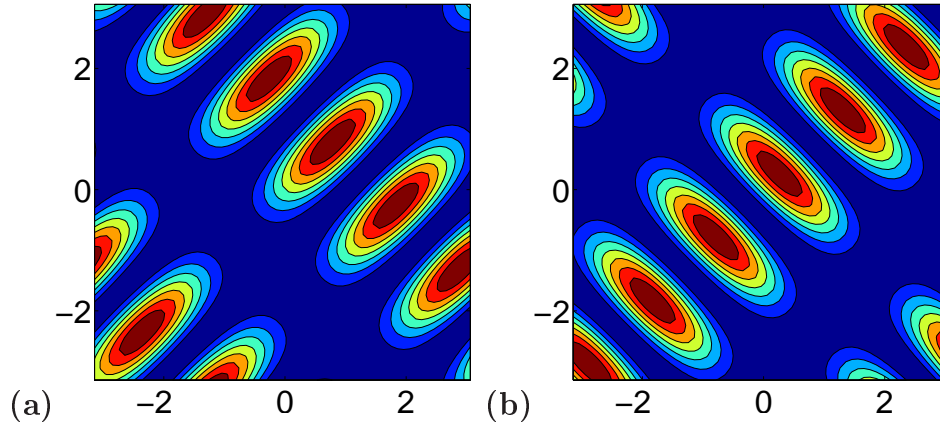


Figure 4.9: Stream functions: (a) $\phi_{1,3}(x - ct, y - ct)^2$ and (b) $\phi_{3,1}(x + ct, y + ct)^2$ at $t = \pi/4$ with $c = 1$.

Putting $m' = -(n + 1)$ and $n' = -(m + 1)$ yields

$$S_1\sigma = -e^{ix/2+iy/2} \sum_{n',m'} (-1)^{-m'-n'-2} \hat{\sigma}_{-n'-1,-m'-1} e^{im'x+in'y}, \quad (4.2.22)$$

or

$$S_1\sigma = -e^{ix/2+iy/2} \sum_{m,n} (-1)^{m+n} \hat{\sigma}_{-n-1,-m-1} e^{imx+iny}. \quad (4.2.23)$$

Consequently, if $S_1\sigma = \sigma$, then

$$\hat{\sigma}_{m,n} = -(-1)^{m+n} \hat{\sigma}_{-n-1,-m-1} \quad (4.2.24)$$

Figure 4.8 shows decay rates with exponent $\alpha \simeq 1/2$ in the Dirichlet case and zero in the Neumann case: in the latter case again the boundaries appear to play no particular role in the mixing and destruction of fluctuations.

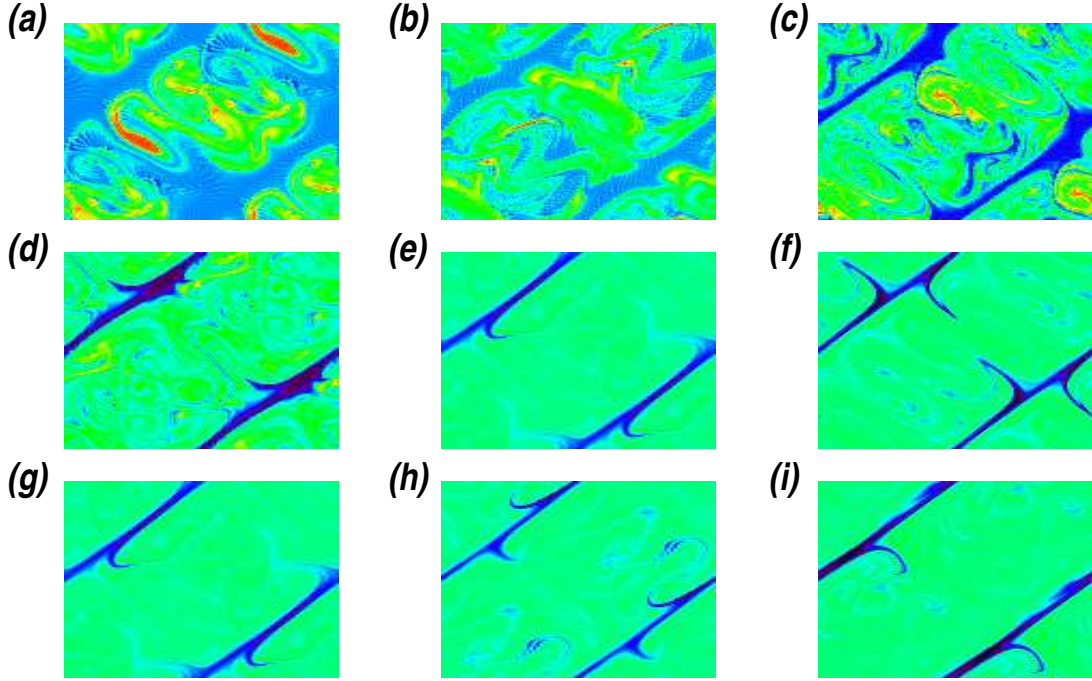


Figure 4.10: Scalar field for $(\psi_{no-slip,pl}, \sigma_N)$ with $\kappa = 0.001$ at (a-c) $t = 1, 2, 3$, (d-f) $t = 5, 10, 15$ and (g-i) $t = 10, 20$ and 30 .

4.2.2 Numerical simulations for random flow $\psi_{no-slip,pl}$

We now reach the problem studied in Salman & Haynes (2007), of flow in a plane layer with a no-slip condition and a Neumann scalar boundary condition. We consider the following random flow which obeys a no-slip condition and is statistically translationally invariant,

$$\psi_{no-slip,pl} = \phi_{1,3}(x - ct, y - ct)^2 \sin[\omega t + \chi(t)] + \phi_{3,1}(x + ct, y + ct)^2 \cos[\omega t + \chi(t)]. \quad (4.2.25)$$

Figure 4.9 shows stream functions for $\phi_{1,3}(x - ct, y - ct)^2$ and $\phi_{3,1}(x + ct, y + ct)^2$ with $c = 1$ at $t = \pi/4$.

Investigation of the simulations of the no-slip flow (Fig. 4.10 and Fig. 4.12) reveals

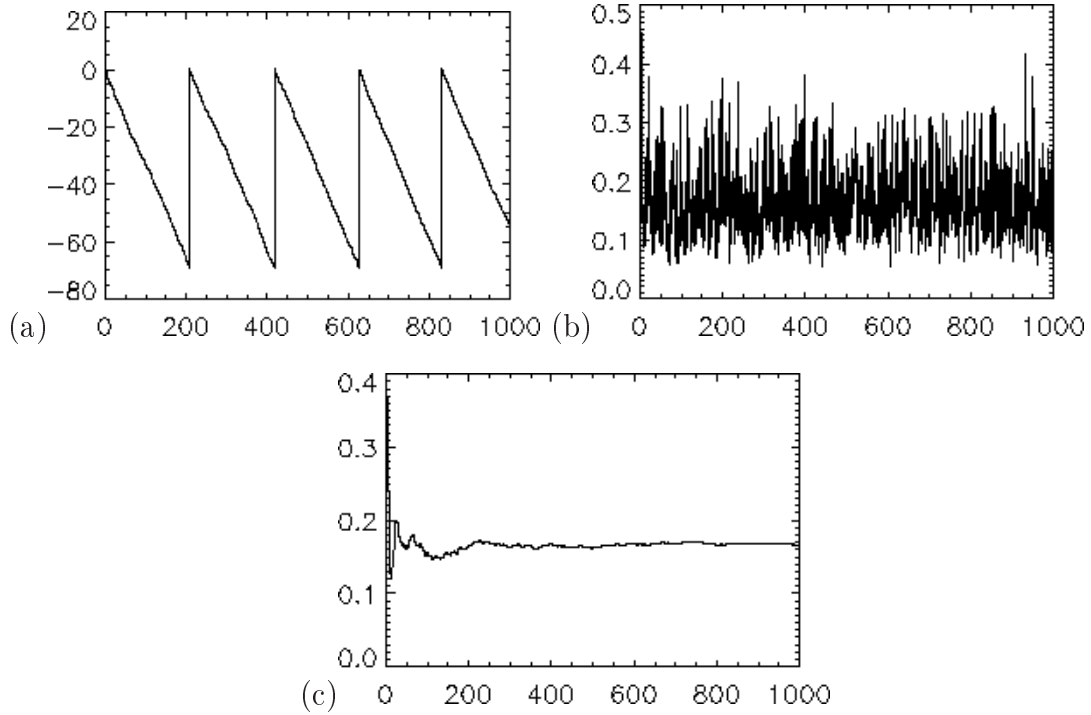


Figure 4.11: Plots for $(\psi_{no-slip,pl}, \sigma_N)$ against time t of (a) $\log V(t)$, (b) $\tilde{\gamma}(t)$, and (c) $\bar{\gamma}(t)$.

similar behaviour of the scalar comparing with the same flow in the square domain (Fig. 3.8). The four stages of mixing are the actual description for the scalar in such a case as seen in Fig. 4.10. While the scalar mixes rapidly in the first stage (Fig. 4.10)(a-c), an intermediate regime is seen in Fig. 4.10(d-e), where diffusion smears out fluctuations. In the third stage, a well-mixed region is observed on the core part of the flow with decreasing region along the layer seen in Fig. 4.10(f-i). Finally, while poor mixing holds near the boundaries, the flow completely continues mixing well in the interior where scalar decays exponentially (Fig. 4.12(d-f)). In contrast with the no-slip case in the square domain shown in Fig. 3.10, the scalar is decaying more rapidly than in the square domain where the scalar concentrates in the corners, and is slowly supplied into the body of the fluid (Fig. 3.10(j-l)).

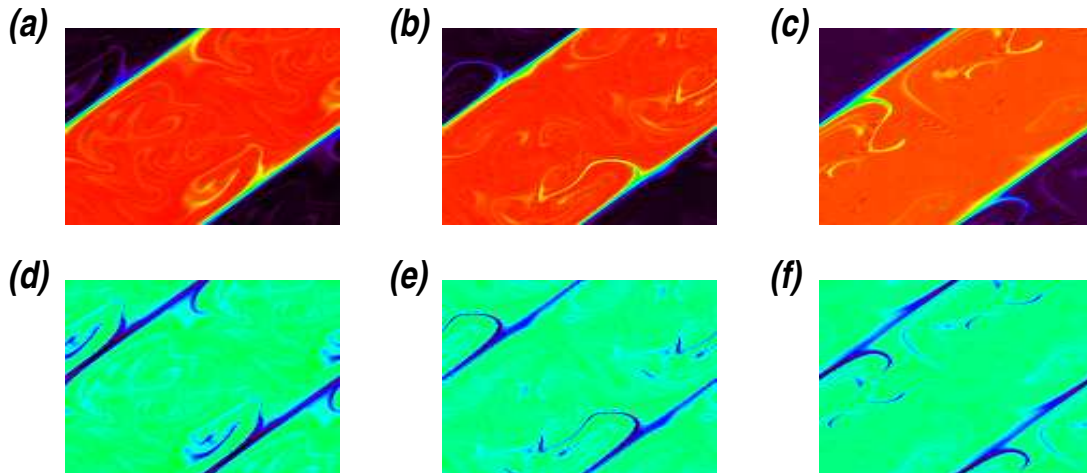


Figure 4.12: Scalar field for (a–c) $(\psi_{no-slip,pl}, \sigma_{\frac{1}{2}D})$ and (d–f) $(\psi_{no-slip,pl}, \sigma_N)$ with $\kappa = 0.001$ at (a,d) $t = 100$, (b,e) 200 and (c,f) 300.

Plots for the decay rate γ against time t for the no-slip flow $\psi_{no-slip}$ in layer with Neumann boundary condition are shown in Fig. 4.11.

Figure 4.12 shows the corresponding scalar fields with Dirichlet and Neumann conditions and Fig. 4.13 measurements of the scaling exponents. For both Dirichlet and Neumann conditions the scalar field maps to itself only under the translation T . For the Dirichlet conditions we again obtain an exponent $\alpha \simeq 3/4$, as for the case of no-slip flow in a square domain. For Neumann boundary conditions the exponent is $\alpha \simeq 1/2$ in keeping with Lebedev & Turitsyn (2004), although convergence is rather slow and the slope poorly determined; we offer further comparison with theory in Chapter 6.

4.3 Summary of results in the plane layer

Our results for the flows simulated in a plane layer reveal that similar behaviour of the scalar field is obtained when comparing with the square domain. In the slip

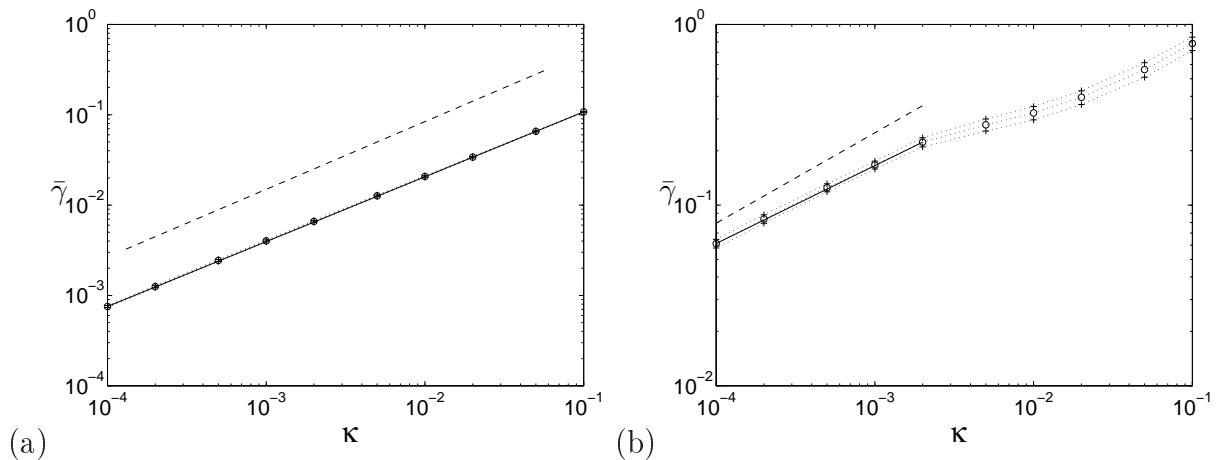


Figure 4.13: Plot for (a) $(\psi_{no-slip, pl}, \sigma_{\frac{1}{2}D})$ and (b) $(\psi_{no-slip, pl}, \sigma_N)$ of $\bar{\gamma}$ (circles) and $\bar{\gamma} \pm \Delta\gamma$ (plus signs) against κ for the case. The solid line is a fit with slope (a) 0.718, (b) 0.43 while the dashed line has slope 0.75 in (a) and 0.5 in (b).

case with Neumann boundary conditions, no controlling role can be observed by the boundaries. While the scalar decays slowly with the exponent $\alpha = 1/2$ in the Dirichlet problem, a faster decay is achieved with Neumann boundary condition in each case (square or layer). Here, the decay rate is obtained with $\alpha = 0$. In the no-slip case, for flows with Neumann boundary conditions the motion of the flow leads to a decay near corners ($\alpha = 2/3$) that is slower than near the layer boundaries ($\alpha = 1/2$). The remaining exponent is $\alpha = 3/4$ characterising the no-slip case with Dirichlet boundary condition. These results are summarised in lines (*v-viii*) of table 6.1.

4.4 Mixed Dirichlet/Neumann boundary conditions for flow in a square domain

Finally, for our simulations of random flows, we note that with the Bloch wavenumber form (4.2.2) of the scalar field we may also consider flows ψ_{slip} and $\psi_{no-slip}$ in

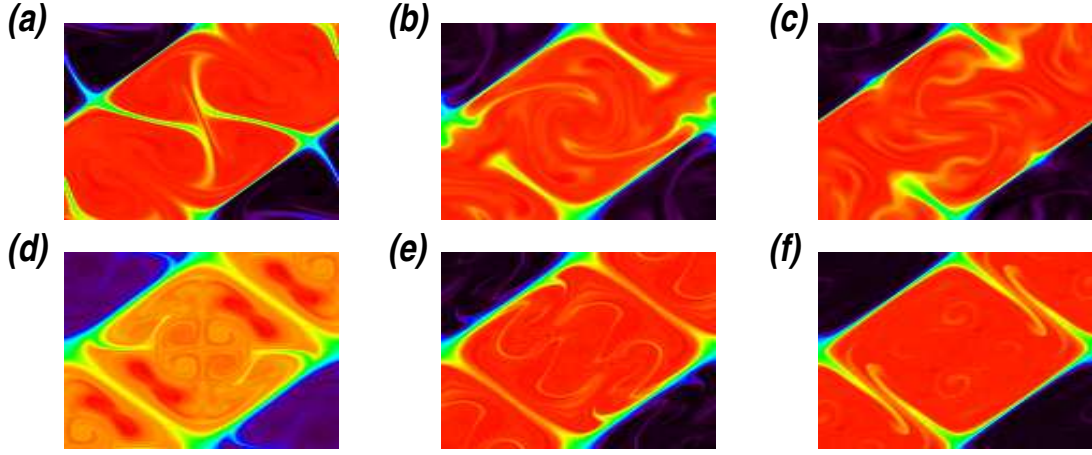


Figure 4.14: Scalar field for (a–c) $(\psi_{\text{slip}}, \sigma_{\frac{1}{2}\text{D}})$, (d–f) $(\psi_{\text{no-slip}}, \sigma_{\frac{1}{2}\text{D}})$ with $\kappa = 0.001$ at (a) $t = 25$, (b) 50, (c) 75, (d) $t = 10$, (e) 20 and (f) 30.

the square domain of Section §3.2. In this case, the Dirichlet boundary conditions are considered on the lines $y - x = \pm\pi$ and Neumann boundary conditions on the lines $x + y = \pm\pi$, simply by taking the initial condition $\sigma_{\frac{1}{2}\text{D}}$ in (4.2.1). Results for the flows ψ_{slip} and $\psi_{\text{no-slip}}$ are shown in figures 4.14 and 4.15. For ψ_{slip} the scalar field satisfies

$$\sigma = S_1\sigma = -S_2\sigma = R^2\sigma \quad (4.4.1)$$

and Fourier coefficients obey

$$\hat{\sigma}_{m,n} = -(-1)^{m+n}\hat{\sigma}_{-n-1,-m-1} = -(-1)^{m+n}\hat{\sigma}_{n,m} = \hat{\sigma}_{-m-1,-n-1}. \quad (4.4.2)$$

Similarly for $\psi_{\text{no-slip}}$ we have

$$\sigma = R^2\sigma = T\sigma = TR^2\sigma, \quad (4.4.3)$$

Chapter 4. LARGE SCALES AND BLOCH WAVENUMBERS

ϵ	npt	dt	T	γ
0.1	32	0.001	1000	0.119
0.05	32	0.001	1000	0.0773
0.02	32	0.001	1000	0.0440
0.01	32	0.001	1000	0.0291
0.005	64	0.0005	1000	0.0195
0.002	64	0.0005	1000	0.0116
0.001	64	0.0005	1000	0.00788
0.0005	96	0.0002	1000	0.00540
0.0002	96	0.0002	1000	0.00327
0.0001	96	0.0002	1000	0.00224

Table 4.3: Computed values for the decay rate of the scalar variance for the slip flow with Bloch wavenumbers: $M = N = 0.5$.

and

$$\hat{\sigma}_{m,n} = \hat{\sigma}_{-m-1,-n-1} = -(-1)^{m+n} \hat{\sigma}_{m,n} = -(-1)^{m+n} \hat{\sigma}_{-m-1,-n-1}. \quad (4.4.4)$$

Note that, the relationships in (4.4.2) were proved earlier in Section §4.2.1. While the first relationship (with R^2) in (4.4.4) is proved in Section §4.2.1 we now offer the proof of last two in (4.4.4). Based on the Bloch wavenumber form (4.2.2) and acting on:

1) **Translation of $T(x, y) = (x + \pi, y + \pi)$** we have that

$$\begin{aligned} T\sigma_{\frac{1}{2}\text{D}} &= \sigma_{\frac{1}{2}\text{D}}(T^{-1}(x, y)) \\ &= \sigma_{\frac{1}{2}\text{D}}(T(x, y)) \\ &= \sigma_{\frac{1}{2}\text{D}}(x + \pi, y + \pi) \\ &= \cos \frac{1}{2}(y - x) \\ &= \sigma_{\frac{1}{2}\text{D}}. \end{aligned} \quad (4.4.5)$$

Chapter 4. LARGE SCALES AND BLOCH WAVENUMBERS

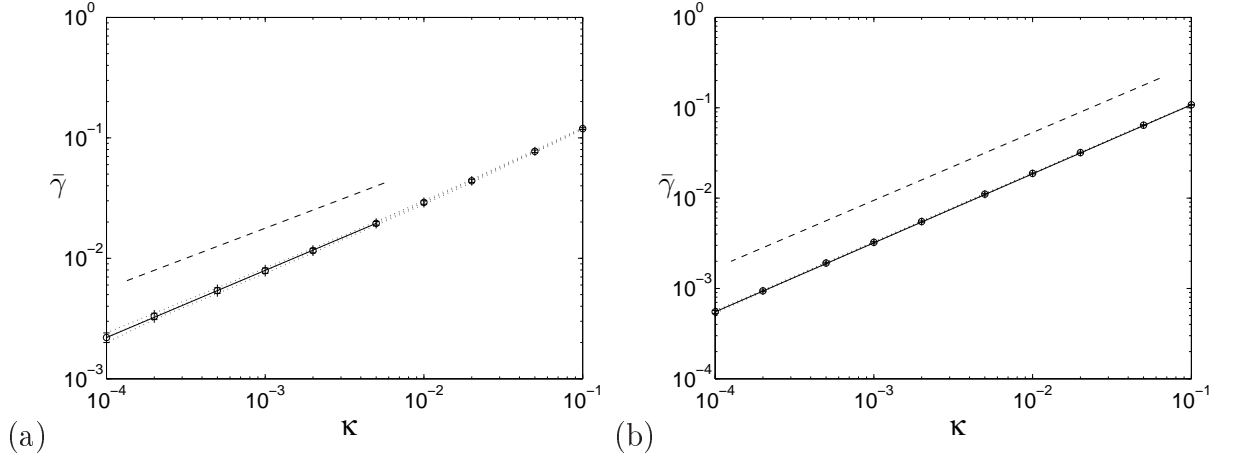


Figure 4.15: Plot for (a) $(\psi_{\text{slip}}, \sigma_{\frac{1}{2}\text{D}})$ and (b) $(\psi_{\text{no-slip}}, \sigma_{\frac{1}{2}\text{D}})$ of $\bar{\gamma}$ (circles) and $\bar{\gamma} \pm \Delta\gamma$ (plus signs) against κ . The solid line is a fit with slope (a) 0.553, (b) 0.762 and the dashed line has slope (a) 0.5, (b) 0.75.

In this case, the scalar field σ can be transformed via

$$\begin{aligned}
 T\sigma &= \sigma(T^{-1}(x, y)) \\
 &= \sigma(T(x, y)) \\
 &= \sigma(x + \pi, y + \pi).
 \end{aligned} \tag{4.4.6}$$

which is written as

$$\begin{aligned}
 T\sigma &= e^{i(x+\pi)/2+i(y+\pi)/2} \sum_{m,n} \hat{\sigma}_{m,n} e^{im(x+\pi)+in(y+\pi)} \\
 &= -e^{ix/2+iy/2} \sum_{m,n} (-1)^{m+n} \hat{\sigma}_{m,n} e^{imx+iny}.
 \end{aligned} \tag{4.4.7}$$

So, if $T\sigma = \sigma$, then,

$$\hat{\sigma}_{m,n} = -(-1)^{m+n} \hat{\sigma}_{m,n} \tag{4.4.8}$$

2) **Under rotation** $TR^2(x, y) = (\pi - x, \pi - y)$:

One may check that $TR^2\sigma_{\frac{1}{2}D} = \sigma_{\frac{1}{2}D}$ and consequently,

$$\begin{aligned} TR^2\sigma &= \sigma(TR^2(x, y)) \\ &= \sigma(\pi - x, \pi - y), \end{aligned} \quad (4.4.9)$$

This implies that

$$\begin{aligned} TR^2\sigma &= e^{i(\pi-x)/2+i(\pi-y)/2} \sum_{m,n} \hat{\sigma}_{m,n} e^{im(\pi-x)+in(\pi-y)} \\ &= -e^{ix/2+iy/2} \sum_{m,n} (-1)^{m+n} \hat{\sigma}_{m,n} e^{-i(m+1)x-i(n+1)y}. \end{aligned} \quad (4.4.10)$$

Similarly to previous cases, putting $m' = -(m + 1)$ and $n' = -(n + 1)$ yields

$$TR^2\sigma = -e^{ix/2+iy/2} \sum_{m',n'} (-1)^{-m'-n'-2} \hat{\sigma}_{-m'-1,-n'-1} e^{im'x+in'y}, \quad (4.4.11)$$

or

$$TR^2\sigma = -e^{ix/2+iy/2} \sum_{m,n} (-1)^{m+n} \hat{\sigma}_{-m-1,-n-1} e^{imx+iny}. \quad (4.4.12)$$

and so if $TR^2\sigma = \sigma$, then

$$\hat{\sigma}_{m,n} = -(-1)^{m+n} \hat{\sigma}_{-m-1,-n-1} \quad (4.4.13)$$

In addition (4.2.2) holds in both cases. We again obtain exponents of $\alpha \simeq 1/2$ and $\alpha \simeq 3/4$ for the decay of scalar in the square domain: the Neumann boundary

condition and the corners appear to play no particular role. There are clearly stagnant regions of fluid near the corners, but it is the large gradients along the boundaries where the Dirichlet boundary condition is applied that control the decay of the passive scalar in the square domain. The results of this section are summarised in lines (*ix-x*) of table 6.1.

We will summarise all of our results for the random flows in Chapter 6 where we have given suggested ‘analytical’ values of exponent α in the last column of table 6.1, and then present justification for these values.

4.5 Numerical simulations for time-periodic flows in a square domain

We now consider the question of how well the scaling results for random flows give guidance to the behaviour of passive scalars in deterministic flows with realistic boundary conditions. Clearly we can only touch on this broad problem, and we focus on the time-periodic versions of the random flows we considered in last chapter by taking the phase $\chi(t) = 0$, namely,

$$\psi_{\text{slip}} = \phi_{1,3}(x, y) \sin \omega t + \phi_{3,1}(x, y) \cos \omega t, \quad \psi_{\text{no-slip}} = \phi_{1,3}(x, y)^2 \sin \omega t + \phi_{3,1}(x, y)^2 \cos \omega t, \quad (4.5.1)$$

with $\omega = 1$. Poincaré sections for these flows are shown in Fig. 4.16 and it may be seen that the phase space (within the invariant boundary \mathcal{C}) appears completely chaotic in (a) for ψ_{slip} . In (b) there is a thin region around the boundary \mathcal{C} where the chaotic trajectories in the bulk of the domain appear not to have penetrated. In fact this region close to the boundaries is quite complicated and panel (c) shows

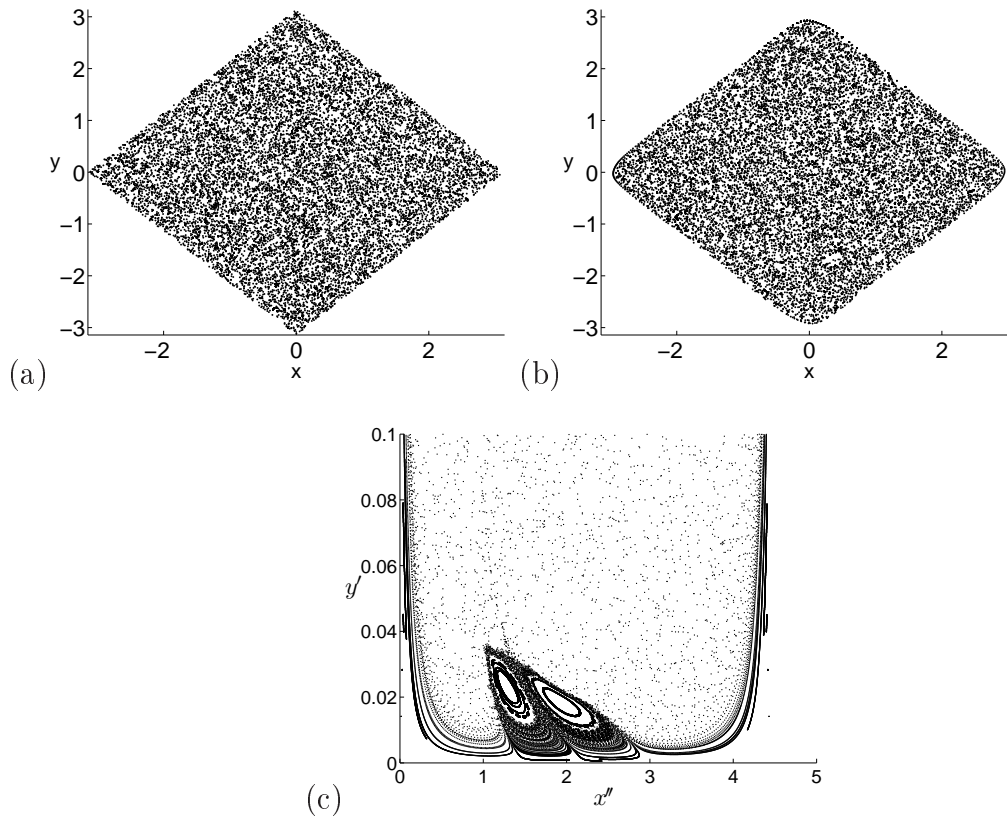


Figure 4.16: Poincaré sections for the time-periodic flows (a) ψ_{slip} and (b) $\psi_{\text{no-slip}}$ with $\omega = 1$. Panel (c) shows a part of a section zoomed in on the boundary, using coordinates $2^{-1/2}(x + y + \pi)$ (horizontal) and $2^{-1/2}(-x + y + \pi)$ (vertical); note the small range of the vertical scale, from 0 to 0.1, compared with the horizontal scale, from 0 to $\pi\sqrt{2}$.

a Poincaré section, rotated by $\pi/4$, along the boundary joining $(-\pi, 0)$ and $(\pi, 0)$. The vertical scale is much exaggerated to show structures that in fact are squashed very close to the boundary. Here, it may be seen that there appear to be trajectories, with very slow motion, arbitrary close to the boundary that then leave to enter the main chaotic region. There are also some integrable island structures. Note that our simulations below are not at a diffusivity small enough for the scalar field to ‘resolve’ these island structures, but the slow motion near the no-slip boundary again will be important in slowing the decay of scalars.

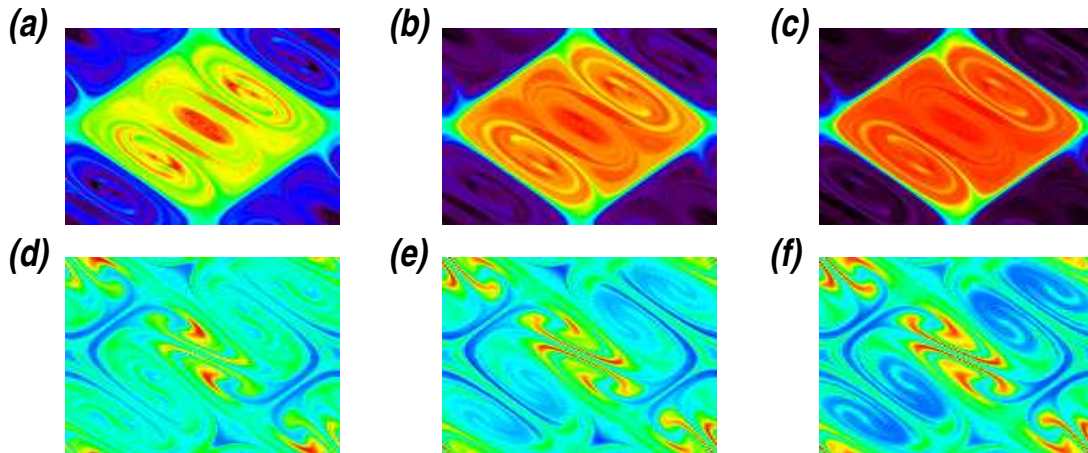


Figure 4.17: Scalar field for (a–c) $(\psi_{\text{no-slip}}, \sigma_{\text{D}})$ and (d–f) $(\psi_{\text{slip}}, \sigma_{\text{N}})$ with $\kappa = 0.001$ at (a,d) $t = 2\pi$, (b,e) 4π and (c,f) 6π .

For these deterministic periodic flows the symmetry properties discussed in the random case continue to hold for the initial conditions σ_{D} and σ_{N} and we need not consider this further.

Figure 4.17 shows sample runs of scalar field with (a–c) no-slip and Dirichlet boundary conditions, and (d–f) slip and Neumann conditions. The scalar field looks similar to that in the corresponding cases of random flow, in figures 3.9 and 3.8. We are showing stroboscopic pictures, at the first few multiples of the period 2π of the flow and one can see the build-up of structure on small scales throughout the domain in (d–f) or the destruction of scalar fluctuations leaving only boundary layers in (a–c).

Decay rates plotted against time t for the flow $(\psi_{\text{slip}}, \sigma_{\text{N}})$ and $(\psi_{\text{slip}}, \sigma_{\text{D}})$ are shown in Fig. 4.18 and snapshots for the flow (a–c) $\psi_{\text{slip}, \sigma_{\text{D}}}$ and (d–f) $\psi_{\text{no-slip}, \sigma_{\text{N}}}$ are seen in Fig. 4.19. Some results for periodic flows are seen in table 4.5 and table 4.6. As we can see in these tables, the runs of deterministic flows were taken to $T = 100$. Results for periodic flows are summarised in table 4.4. Scaling laws for the four key

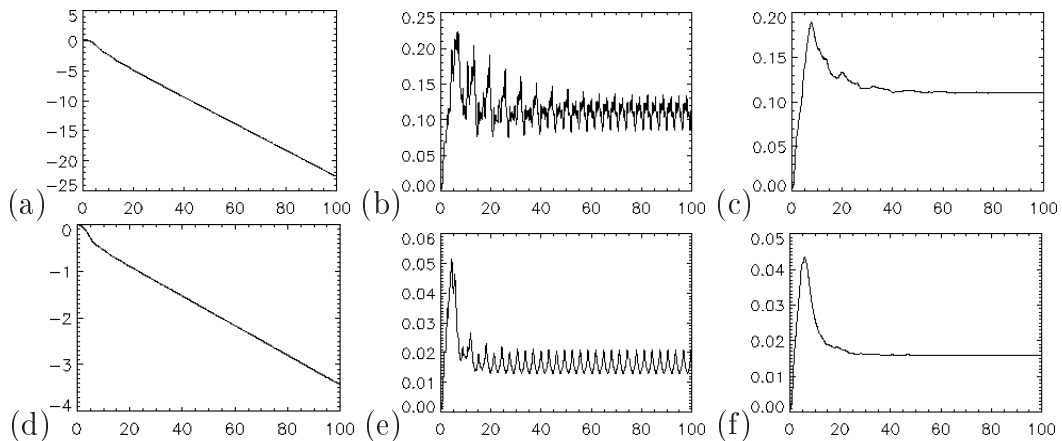


Figure 4.18: Plots for (ψ_{slip}, σ_N) and (ψ_{slip}, σ_D) against time t of (a,d) $\log V(t)$, (b,e) $\tilde{\gamma}(t)$, and (c,f) $\bar{\gamma}(t)$.

cases for the periodic flow are shown in Fig. 4.20 for ψ_{slip} or $\psi_{no-slip}$ and Dirichlet or Neumann conditions and we may compare these with the corresponding random flows. The closest points of comparing scaling laws of periodic flows with those of random case are for the panels 4.20(a,c) which show exponents $\alpha \simeq 0.5$ and $\alpha \simeq 0.75$ for Dirichlet boundary condition with slip and no-slip flows respectively. These are in good agreement with the values in table 6.1 for random flows. However, we should note that in the case of the no-slip flow while the observed scaling is very clear, it is possible that it will change as $\kappa \rightarrow 0$ in view of the Poincaré section 4.16(b). As κ is reduced the $\kappa^{1/4}$ scale of the scalar field boundary layer will become comparable with the non-chaotic (island) region near the boundary apparent in 4.16(c), transfer of scalar to and from the boundary may well become poorer and the value of α is likely to increase. For the slip case with Neumann boundary conditions the log-log plot in Fig. 4.20(b) shows a curve flattening to a very shallow power law with exponent $\alpha \simeq 0.126$. The result for the corresponding random flow is $\alpha = 0$ and at present we cannot conclude whether there really is a weak power law scaling or not present in 4.20(b), in particular given the small

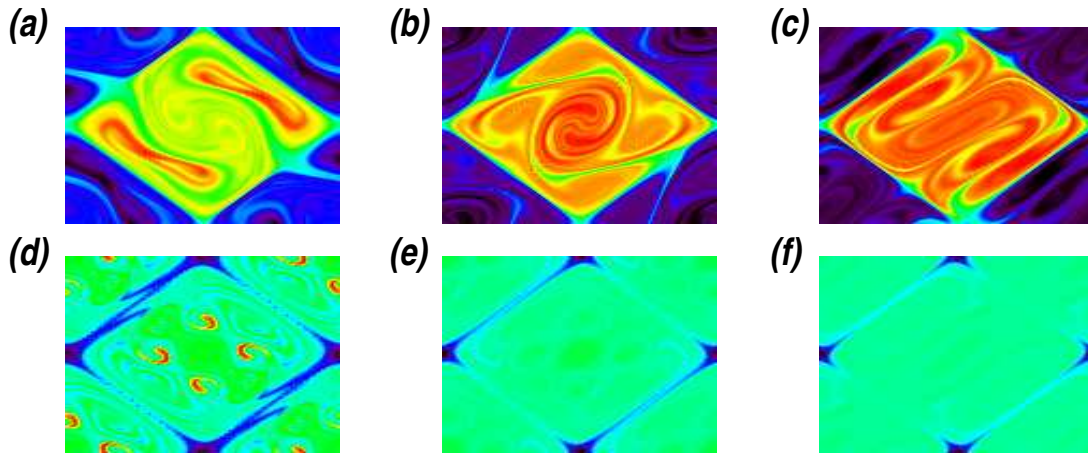


Figure 4.19: Scalar field for (a–c) $(\psi_{\text{slip}}, \sigma_{\text{D}})$ and (d–f) $(\psi_{\text{no-slip}}, \sigma_{\text{N}})$ with $\kappa = 0.001$ at (a,d) $t = 10$, (b,e) 20 and (c,f) 30.

range of scale on the vertical axis. Figure 4.20(d) for the no-slip flow and Neumann boundary condition shows another bent curve with slope increasing from around 0.5 to $\alpha \simeq 0.75$ for small κ . This is a rather steeper power law than the value $\alpha \simeq 2/3$ for the random case. The decay of scalar fluctuations is controlled by a reservoir of scalar in the very sluggish flow near the corners (seen clearly in the random case in Fig. 3.10(j–l)). Plots of the scalar distribution for the deterministic case (Fig. 4.19(d–f)) show a very similar picture but with a greater contrast between regions of cold scalar in the corners and the well-mixed warm fluid in the bulk of the container.

In Chapter 6, we will analyse and summarise these scaling laws obtained for periodic flows together with comparing random ones.

4.6 Summary

Based on our investigations for the simulations presented in this chapter our results reveal that the scaling laws obtained for time-periodic flows appear to be

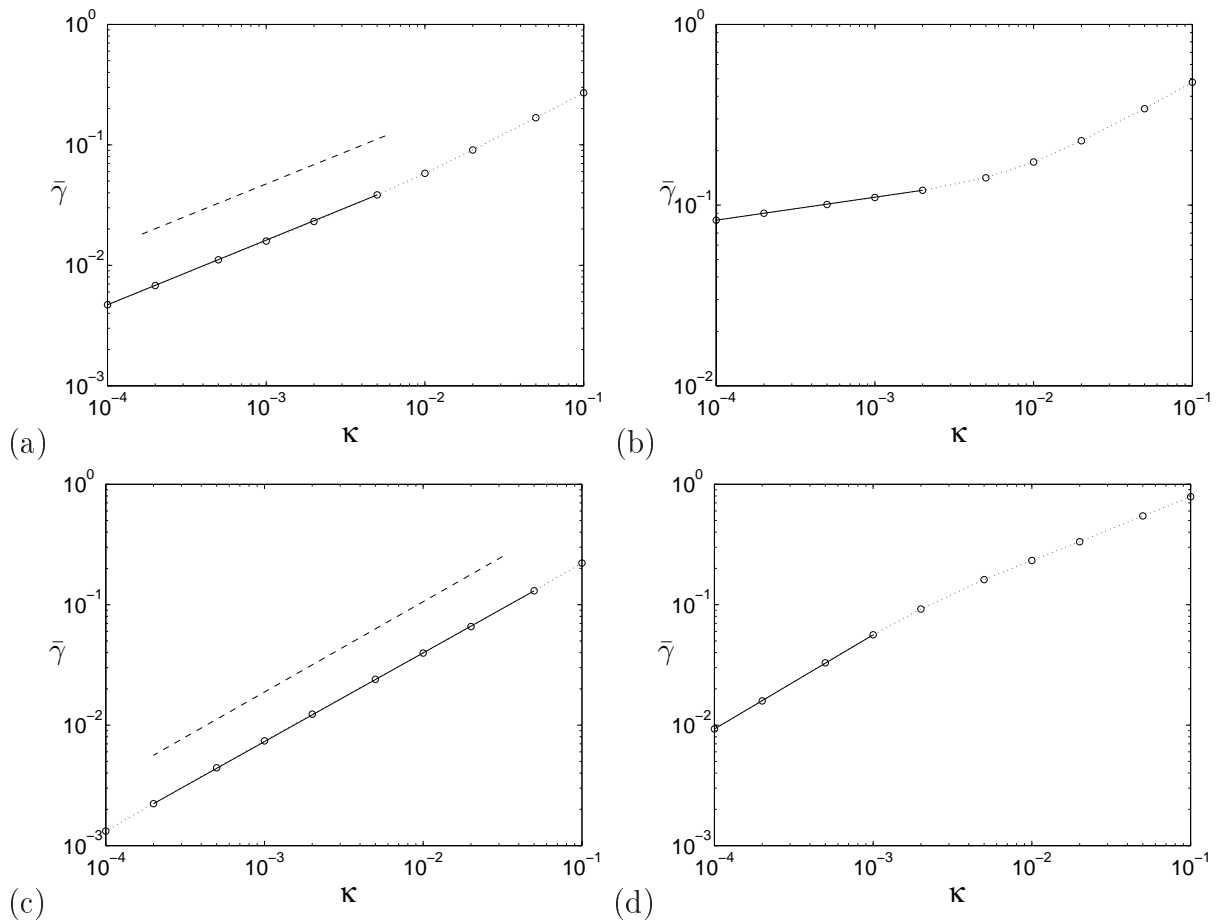


Figure 4.20: Plots of $\bar{\gamma}$ against κ for the time-periodic flows. We have the cases (a) $(\psi_{\text{slip}}, \sigma_D)$, with solid and dashed lines of slopes 0.53 and 0.5, (b) $(\psi_{\text{slip}}, \sigma_N)$, slope 0.126 (c) $(\psi_{\text{no-slip}}, \sigma_D)$, slopes 0.765 and 0.75, and (d) $(\psi_{\text{no-slip}}, \sigma_N)$, slope 0.784.

similar to those of random flows in most cases. Such scaling exponents are in good agreement with the results of Lebedev & Turitsyn (2004) and Salman & Haynes (2007). We will give further confirmation of our results by comparing these with theory in Chapter 6.

The advantage of considering periodic flow is that measuring the decay rate is relatively easy as there is no need to take a long time average (see Fig. 4.18) over the different possibilities in the random distribution of renewing flows. However, the disadvantage is that we tend to lose the clear scaling behaviour of $\gamma(\kappa)$ with

	domain	flow	initial scalar	ω	measured α	analytical α
(i)	square	ψ_{slip}	σ_{D}	1	0.53	1/2
	square	ψ_{slip}	σ_{D}	2	0.546	—
(ii)	square	ψ_{slip}	σ_{N}	1	0.127	—
(iii)	square	$\psi_{\text{no-slip}}$	σ_{D}	0.25	0.686	3/4
	square	$\psi_{\text{no-slip}}$	σ_{D}	0.5	0.709	—
	square	$\psi_{\text{no-slip}}$	σ_{D}	1	0.737	—
	square	$\psi_{\text{no-slip}}$	σ_{D}	2	0.766	—
(iv)	square	$\psi_{\text{no-slip}}$	σ_{N}	1	0.78	2/3
(v)	layer	$\psi_{\text{slip,pl}}$	$\sigma_{\frac{1}{2}\text{D}}$	1	0.524	1/2
	layer	$\psi_{\text{slip,pl}}$	$\sigma_{\frac{1}{2}\text{D}}$	2	0.485	—
(vii)	layer	$\psi_{\text{no-slip,pl}}$	$\sigma_{\frac{1}{2}\text{D}}$	1	0.701	3/4
	layer	$\psi_{\text{no-slip,pl}}$	$\sigma_{\frac{1}{2}\text{D}}$	2	0.661	—
(ix)	square	ψ_{slip}	$\sigma_{\frac{1}{2}\text{D}}$	1	0.547	1/2
(x)	square	$\psi_{\text{no-slip}}$	$\sigma_{\frac{1}{2}\text{D}}$	1	0.74	3/4

Table 4.4: Summary of results: periodic flows.

κ , and we do not have theory to fall back on.

For the flows embedded in a square domain \mathcal{D} , we crucially have shown that the corner plays no obvious role on the decay rate of the scalar, except in the case of no-slip flow with Neumann scalar boundary condition. The corner in this case can be treated as a resource that is slowly supplying the scalar into the body of the flow. From asymptotic point of view, here, the motion of the flow is slower than near the no-slip boundaries with decaying rate characterised with the exponent $\alpha = 2/3$ rather than $\alpha = 1/2$.

Our results appear to indicate that the random flow is more effective at transporting scalar in and out of corners, whereas the periodic flow is, presumably because of averaging, much poorer at persistent transport.

An important observation made from our numerical simulations is that for the time-periodic flows applied in the square domain (table 4.4), the exponent α in-

Chapter 4. LARGE SCALES AND BLOCH WAVENUMBERS

ϵ	npt	dt	T	γ
0.1	32	0.001	100	0.270
0.05	32	0.001	100	0.168
0.02	32	0.001	100	0.0906
0.01	32	0.001	100	0.0581
0.005	64	0.0005	100	0.0384
0.002	64	0.0005	100	0.0231
0.001	64	0.0005	100	0.0159
0.0005	96	0.0002	100	0.0111
0.0002	96	0.0002	100	0.00678
0.0001	96	0.0002	100	0.00444
0.0001	128	0.00005	100	0.00476

Table 4.5: Computed values for the decay rate of the scalar variance for the slip flow with Dirichlet boundary condition: periodic flow with $\omega = 1$.

creases a little as ω is increased, in contrast to the results in the plane layer, where a decreasing in the values of the exponent α has been observed as ω is increased (for some cases we investigated). Furthermore, as we have noted, these differences of the exponents α depend on the type of the flow as they depend on the values of ω as well as on the boundary conditions.

Chapter 4. LARGE SCALES AND BLOCH WAVENUMBERS

ϵ	npt	dt	T	γ
0.1	32	0.001	100	0.479
0.05	32	0.001	100	0.342
0.02	32	0.001	100	0.227
0.01	32	0.001	100	0.173
0.005	64	0.0005	100	0.142
0.002	64	0.0005	100	0.121
0.001	64	0.0005	100	0.110
0.0005	96	0.0002	100	0.101
0.0002	96	0.0002	100	0.0901
0.0001	96	0.0002	100	0.0852
0.0001	128	0.00005	100	0.0825

Table 4.6: Computed values for the decay rate of the scalar variance for the slip flow with Neumann boundary condition: periodic flow with $\omega = 1$.

Part II

Theory and developments

5

THEORETICAL FOUNDATIONS

5.1 Outline

Theory of passive scalar evolution for random flows has recently been developed by Lebedev & Turitsyn (2004) and Salman & Haynes (2007). These researchers obtained analytical results concerning the passive scalar moments and their correlation functions in the peripheral region (This refers to the region next to the boundaries where the slip and no-slip conditions are imposed) for arbitrary velocity correlation times. Thus, this theory provides important analytical results and insight into the effect of random fluctuations on the rate of decay of the concentration field of a passive scalar.

In this part of the thesis we are interested in applying further the theory of passive scalar evolution in the peripheral regions for the two-dimensional random flows studied numerically in Part I. More specifically, our aim is to establish the connection between the above theory and our results obtained numerically for simulations

in square and plane layer domains with slip and no-slip boundaries. In particular, in this situation, we check how well is the agreement between theory and simulations, and obtain scaling laws similar to those found by Lebedev & Turitsyn (2004) and Salman & Haynes (2007).

In order to achieve this goal, we extend our models of flows studied in Part I of this work. We begin this theoretical framework by analysing some of the key arguments of the passive scalar dynamics introduced in Section §5.2, followed by a discussion of the structure of the effective diffusivity tensor given in Section §5.3. Calculations for the boundary layer are provided in §5.4. Such calculations help in prediction of the decay rate of the scalar variance controlled by the peripheral region in the plane layer discussed in Section §5.5.

5.2 General foundations

In this section we reformulate and classify a variety of relations which our analysis of the decaying problem described previously depends upon. In doing so, we introduce V to denote the total integral of σ^2 over a fixed domain \mathcal{D} ,

$$V = \int_{\mathcal{D}} \sigma^2 dS, \quad (5.2.1)$$

where dS is the element of area. Note that the definition (5.2.1) is different from the previous definition (2.4.2) provided earlier in Chapter 2, where it is easiest here if V in (5.2.1) is the total scalar σ^2 in the domain \mathcal{D} .

From Eq. (5.2.1), we find directly that

$$\begin{aligned}\frac{dV}{dt} &= \int_{\mathcal{D}} 2\sigma \frac{\partial\sigma}{\partial t} dx dy \\ &= \int_{\mathcal{D}} 2\sigma (-\mathbf{u} \cdot \nabla\sigma + \kappa \cdot \nabla^2\sigma) dx dy,\end{aligned}\quad (5.2.2)$$

Because the velocity field \mathbf{u} is incompressible, we have

$$\mathbf{u} \cdot \nabla\sigma = \nabla \cdot (\sigma \mathbf{u}), \quad (5.2.3)$$

and also,

$$\nabla^2\sigma = \nabla \cdot (\nabla\sigma). \quad (5.2.4)$$

Thus, we then get

$$\begin{aligned}\frac{dV}{dt} &= \int_{\mathcal{D}} (-\mathbf{u} \cdot \nabla\sigma^2 + 2\sigma\kappa \nabla \cdot \nabla\sigma) dx dy \\ &= \int_{\mathcal{D}} (-\nabla \cdot (\mathbf{u}\sigma^2) + 2\kappa\sigma \nabla \cdot \nabla\sigma) dx dy.\end{aligned}\quad (5.2.5)$$

Based on

$$\nabla \cdot (a \nabla b) = a \nabla \cdot \nabla b + (\nabla a) \cdot (\nabla b), \quad (5.2.6)$$

the expression given by Eq. (5.2.5) is expanded as

$$\frac{dV}{dt} = \int_{\mathcal{D}} [-\nabla \cdot (\mathbf{u}\sigma^2) + 2\kappa(\nabla \cdot (\sigma \nabla\sigma) - (\nabla\sigma) \cdot (\nabla\sigma))] dx dy, \quad (5.2.7)$$

Now using the divergence theorem, Eq. (5.2.7) can be rewritten as

$$\frac{dV}{dt} = \int_{\mathcal{C}} (-\mathbf{n} \cdot \mathbf{u}\sigma^2 + 2\kappa \mathbf{n} \cdot \sigma \nabla\sigma) ds - 2\kappa \int_{\mathcal{D}} |\nabla\sigma|^2 dS, \quad (5.2.8)$$

where ds is the arc length over the boundary \mathcal{C} of \mathcal{D} and \mathbf{n} is the normal vector to \mathcal{C} . It is important to note that, in Eq. (5.2.8), the first two terms on the right hand side vanish with boundary conditions; slip ($\mathbf{n} \cdot \mathbf{u} = 0$), Dirichlet ($\sigma = 0$) and Neumann ($\mathbf{n} \cdot \nabla \sigma = 0$) on the boundary \mathcal{C} . Consequently, one can get

$$\frac{dV}{dt} = -2\kappa \int_{\mathcal{D}} (|\nabla \sigma|^2) dS. \quad (5.2.9)$$

Though, the effect of diffusion remains in this case. It is clear that, the right-hand side of Eq. (5.2.9) is negative or zero:

- $\frac{dV}{dt} = 0$ for $\kappa = 0$.
- $\frac{dV}{dt} < 0$ for $\kappa > 0$ unless $\sigma = \text{constant}$.

which means that V always decreases or is a constant. If $\nabla \sigma$ vanishes everywhere, that is σ is a constant in space, then V stops decreasing.

5.3 Structure of the effective diffusivity tensor

Following the work of several other investigators (Chertkov & Lebedev, 2003a; Lebedev & Turitsyn, 2004; Salman & Haynes, 2007; Chernykh & Lebedev, 2008), we begin this section by considering the advection-diffusion equation for the concentration field $\sigma(\mathbf{r}, t)$ advected passively by an incompressible velocity field \mathbf{u} (i.e., $\nabla \cdot \mathbf{u} = 0$) and diffused with diffusivity κ ,

$$\frac{\partial \sigma}{\partial t} + \mathbf{u} \cdot \nabla \sigma = \kappa \nabla^2 \sigma. \quad (5.3.1)$$

For this situation, we divide time into intervals $(j\tau, (j+1)\tau)$, each of which is of length a correlation time τ . This had been done by Salman & Haynes (2007) and is

very convenient numerically. The random flows used are chosen to be independent and identically distributed on each time interval $(j\tau, (j+1)\tau)$.

To simplify the theoretical analysis of passive scalar field under these considerations, we consider the flow \mathbf{u} to be steady in each time interval (but this condition may easily be relaxed). If we consider evolution of the scalar field over one interval, say $(0, \tau)$ with $\sigma = \sigma_0(x, y)$ at $\tau = 0$ and use a Taylor series expansion for the scalar field we obtain

$$\sigma = \sigma_0(x, y) + t \sigma_1(x, y) + \frac{t^2}{2} \sigma_2(x, y) + \dots \quad (5.3.2)$$

for small t . Differentiating Eq. (5.3.2) with respect to time t and substituting into Eq. (5.3.1) leads us to obtain

$$\sigma_1 + t \sigma_2 + \dots = -\mathbf{u} \cdot \nabla (\sigma_0 + t \sigma_1(x, y) + \frac{t^2}{2} \sigma_2(x, y) + \dots) + \kappa \nabla^2 (\sigma_0 + t \sigma_1 + \dots), \quad (5.3.3)$$

If we equate powers of t related to Eq. (5.3.3)

$$t^0 : \quad \sigma_1 = -\mathbf{u} \cdot \nabla \sigma_0 + \kappa \nabla^2 \sigma_0, \quad (5.3.4)$$

$$t^1 : \quad \sigma_2 = -\mathbf{u} \cdot \nabla \sigma_1 + \kappa \nabla^2 \sigma_1 \quad (5.3.5)$$

then we get

$$\begin{aligned} \sigma(x, y, \tau) &= \sigma_0 + \tau (-\mathbf{u} \cdot \nabla \sigma_0 + \kappa \nabla^2 \sigma_0) \\ &+ \frac{\tau^2}{2} [(-\mathbf{u} \cdot \nabla (-\mathbf{u} \cdot \nabla \sigma_0 + \kappa \nabla^2 \sigma_0)) \\ &+ \kappa \nabla^2 (-\mathbf{u} \cdot \nabla \sigma_0 + \kappa \nabla^2 \sigma_0) + \dots \end{aligned} \quad (5.3.6)$$

Averaging over the family of flows and taking them to have the property that $\langle \mathbf{u} \rangle = 0$ leads us to obtain, with $t = \tau$,

$$\langle \sigma(x, y, \tau) \rangle = \langle \sigma_0 \rangle + \kappa \tau \nabla^2 \langle \sigma_0 \rangle + \frac{\tau^2}{2} \langle \mathbf{u} \cdot \nabla (\mathbf{u} \cdot \nabla \sigma_0) \rangle + \dots \quad (5.3.7)$$

Here we have kept just the leading order effect of the flow and the leading order effect of diffusion. Since

$$\mathbf{u} \cdot \nabla \sigma = \nabla \cdot (\mathbf{u} \sigma) - \sigma \nabla \cdot \mathbf{u} \quad (5.3.8)$$

Because of the incompressibility condition $\nabla \cdot \mathbf{u} = 0$, we have

$$\mathbf{u} \cdot \nabla \sigma = \nabla \cdot (\mathbf{u} \sigma), \quad (5.3.9)$$

According to this one can find that for σ_0 ,

$$\begin{aligned} \mathbf{u} \cdot \nabla (\mathbf{u} \cdot \nabla \sigma_0) &= \nabla \cdot (\mathbf{u} (\mathbf{u} \cdot \nabla \sigma_0)) \\ &= \frac{\partial}{\partial x_i} \left(u_i u_j \frac{\partial \sigma_0}{\partial x_j} \right). \end{aligned} \quad (5.3.10)$$

Crucially, we have to use the independence of the flow \mathbf{u} for the time interval $jt \leq t \leq (j+1)\tau$ and the scalar field $\bar{\sigma}(j\tau)$ at the beginning of this interval. This allows us to write, for example, $\langle \mathbf{u}(t) \mathbf{u}(t) \sigma(j\tau) \rangle = \langle \mathbf{u}(t) \mathbf{u}(t) \rangle \bar{\sigma}(j\tau)$ and make analytical progress,

$$\langle \mathbf{u} \cdot \nabla (\mathbf{u} \cdot \nabla \sigma_0) \rangle = \frac{\partial}{\partial x_i} \left(\langle u_i u_j \rangle \frac{\partial \langle \sigma_0 \rangle}{\partial x_j} \right). \quad (5.3.11)$$

where $\bar{\sigma}$ denotes the ensemble-averaged scalar field. In this case, Eq. (5.3.7) can be written as

$$\frac{\langle \sigma(x, y, \tau) \rangle - \langle \sigma_0 \rangle}{\tau} = \frac{\partial}{\partial x_i} \left(D_{ij} \frac{\partial}{\partial x_j} \langle \sigma_0 \rangle \right) + \kappa \nabla^2 \langle \sigma_0 \rangle, \quad (5.3.12)$$

where D_{ij} is the diffusivity tensor that can be defined as

$$D_{ij} = \frac{1}{2} \tau \langle u_i u_j \rangle. \quad (5.3.13)$$

If we now consider the evolution of the scalar field over time scales much longer than τ , then (5.3.12) is a finite difference approximation to a diffusion equation,

$$\frac{\partial \bar{\sigma}}{\partial t} = \frac{\partial}{\partial x_i} \left(D_{ij} \frac{\partial \bar{\sigma}}{\partial x_j} \right) + \kappa \nabla^2 \bar{\sigma}, \quad (5.3.14)$$

The diffusivity tensor D_{ij} is generally a function of both spatial coordinates. Note there is an extra factor of $\frac{1}{2}$ in (5.3.13) compared with the calculation in equation (36) of Salman & Haynes (2007). No such a factor is present in the equivalent, integral formula for a *stationary* random flow given in equation (1.5) and (5.3.17) below of Lebedev & Turitsyn (2004), and appears because our flows are not stationary. It can be thought of as arising in our case since starting from a randomly chosen starting time t , the steady flow at that time *continues* to act for a time $\tau/2$ on average. Applying the formula for *stationary* random flows is likely to have caused the disagreement that appears between theory and numerical simulation performed by Salman & Haynes (2007).

Now although we have obtained (5.3.13) as an expansion in powers of a correlation time τ , it is in fact an expansion in powers of $\tau \mathbf{u}$ and the key observation

of Lebedev & Turitsyn (2004) is that near a no-slip boundary $\mathbf{u} \rightarrow 0$ and so the approximation becomes good near to that boundary regardless of whether the correlation time τ for the bulk of the flow is small or not.

Thus the results obtained for no-slip boundary layers forced by random flows have a universal nature. For this point, Lebedev & Turitsyn (2004) and Salman & Haynes (2007) argued that the mixing time scale associated with the fluctuating velocity field will be much longer near the boundary than within the bulk. Using these arguments, for a stationary random flow, Lebedev & Turitsyn (2004) introduced D_{ij} via the integral

$$D_{ij} = \int_0^\infty \langle u_i(x, y, 0) u_j(x, y, \tau) \rangle d\tau. \quad (5.3.15)$$

However, for small τ we have obtained the equation (5.3.14) with an effective diffusivity D_{ij} in (5.3.13) that can be calculated for given families of flows \mathbf{u} . This equation can be expanded as

$$\begin{aligned} \frac{\partial \bar{\sigma}}{\partial t} &= \frac{\partial}{\partial x} \left(D_{xx} \frac{\partial \bar{\sigma}}{\partial x} \right) + \frac{\partial}{\partial x} \left(D_{xy} \frac{\partial \bar{\sigma}}{\partial y} \right) \\ &+ \frac{\partial}{\partial y} \left(D_{yx} \frac{\partial \bar{\sigma}}{\partial x} \right) + \frac{\partial}{\partial y} \left(D_{yy} \frac{\partial \bar{\sigma}}{\partial y} \right) \\ &+ \kappa \nabla^2 \bar{\sigma}. \end{aligned} \quad (5.3.16)$$

Under consideration of the presence of no-slip walls in a plane layer where the flow is statistically invariant only in x , the first three terms on the right-hand side of Eq. (5.3.16) vanish as $\bar{\sigma} = \bar{\sigma}(y, t)$, $\bar{\sigma}_x(y, t) = 0$ and the quantities D_{xx} , D_{xy} , D_{yx} and D_{yy} are functions of y only. In this case we shall see that Eq. (5.3.16) collapses

to

$$\frac{\partial \bar{\sigma}}{\partial t} = \mu \frac{\partial}{\partial y} \left(y^4 \frac{\partial \bar{\sigma}}{\partial y} \right) + \kappa \frac{\partial^2 \bar{\sigma}}{\partial y^2}, \quad (5.3.17)$$

This equation represents the y -evolution of the scalar profile. Here, the coefficient μ can be considered as a measure of the flow intensity near the boundary and later we shall show how this coefficient is determined. However, the first term (with μ) on the right-hand side of (5.3.17) describes the role of chaotic advection in terms of an eddy diffusivity,

$$D_{yy} = \frac{\tau}{2} \langle v(y, 0) v(y, 0) \rangle, \quad (5.3.18)$$

whose leading behaviour close to the wall gives $D_{yy} \simeq \mu y^4$ for small y . It had been observed (Chertkov & Lebedev, 2003a) that the advection term (with μ) in Eq. (5.3.17) dominates in $y \gg r_{bl}$ while the diffusion term (with κ) dominates at $y \ll r_{bl}$. Here r_{bl} is the thickness of the boundary diffusion layer given by $(\frac{\kappa}{\mu})^{\frac{1}{4}}$ as argued by Lebedev & Turitsyn (2004) and Salman & Haynes (2007).

For a smooth two-dimensional flow field, Lebedev & Turitsyn (2004) and Salman & Haynes (2007) showed that there is a region close to the wall boundaries, characterised by the scales $u \propto y$ and $v \propto y^2$ that generate components of the effective diffusivity D_{ij} . To illustrate how these scales are obtained we consider a coordinate system (x, y) with velocity u along the horizontal boundary and velocity v perpendicular to it and y is the vertical distance from the wall (with the obvious notation $(x_1, x_2) = (x, y)$). For this discussion the axes are rotated and translated with respect to the ones we have been using up to now, in our simulations; the meaning should be clear from the context. If we expand the velocity components

at the boundary using Taylor expansion then

$$u(x, y) = u_0(x) + u_1(x)y + u_2(x)\frac{y^2}{2} + \dots \quad (5.3.19)$$

$$v(x, y) = v_0(x) + v_1(x)y + v_2(x)\frac{y^2}{2} + \dots \quad (5.3.20)$$

Now applying the incompressibility condition ($\nabla \cdot \mathbf{u} = 0$) yields

$$u'_0(x) + u'_1(x)y + \dots + v_1(x) + v_2(x)y + \dots = 0, \quad (5.3.21)$$

which at the boundary $y = 0$ gives that

$$u'_0(x) + v_1(x) = 0. \quad (5.3.22)$$

If we apply the no-slip boundary condition ($\mathbf{u} = 0$) one can get $u_0(x) = v_0(x) = 0$.

This implies that $v_1(x) = 0$. Therefore, we see that the x -velocity u will scale as y while the y -velocity v will scale as y^2 ,

$$u(x, y) = u_1(x)y + u_2(x)\frac{y^2}{2} + \dots \quad (5.3.23)$$

$$v(x, y) = v_2(x)\frac{y^2}{2} + \dots \quad (5.3.24)$$

which imply that

$$u \propto y, \quad v \propto y^2. \quad (5.3.25)$$

These scales show a very specific dependence of D_{ij} with distance from the wall.

For the no-slip boundary conditions, such a dependence forms the proportionality laws,

$$D_{xx} \propto y^2, \quad D_{xy} \propto y^3, \quad D_{yy} \propto y^4, \quad (y \rightarrow 0). \quad (5.3.26)$$

Now using the slip condition ($\mathbf{n} \cdot \mathbf{u} = 0$) at the boundary we get $v = 0$ and consequently the velocity component perpendicular to the wall will scale as y ,

$$v(x, y) = v_1(x)y + v_2(x)\frac{y^2}{2} + \dots \quad (5.3.27)$$

and the proportionality laws in this case will be given from (5.3.19) and (5.3.27) as

$$D_{xx} \propto y^0, \quad D_{xy} \propto y, \quad D_{yy} \propto y^2, \quad (y \rightarrow 0) \quad (5.3.28)$$

as we use this later for the width of the boundary layer $\kappa^{1/2}$ for the slip with Dirichlet conditions. Near wall boundaries $D_{yy} \ll D_{xx}$, where the scalar will mix more effectively along the boundary than normal to the boundary. Further details are provided in the next section.

The theoretical analysis detailed above will simplify the connection between this structure of D_{ij} and the results of our numerical simulations to be compared later.

5.4 Calculations of boundary layers

In this section we provide certain arguments that help us to predict a specific form of the evolution of the scalar variance. The idea concerns dependence of the scales of the effective diffusivity components (5.3.26) on the distance from the walls and so we will provide detailed discussion on this point.

For more understanding, let us start with the case when the passive scalar represents the concentration of pollutants, which recently, has been studied in more detail by Salman & Haynes (2007). (By ‘pollutants’ we mean Neumann boundary condition; $\mathbf{n} \cdot \nabla \sigma = 0$ on the boundaries). In analysing of such a problem un-

der a no-slip condition, Lebedev & Turitsyn (2004) and Salman & Haynes (2007) described the y -evolution of the passive scalar profile by Eq. (5.3.17). This evolution is dominated by advection as long as the thickness of peripheral region $\delta \geq r_{bl} = (\frac{\kappa}{\mu})^{\frac{1}{4}}$, the thickness of the diffusive boundary layer (Lebedev & Turitsyn, 2004; Salman & Haynes, 2007). In this case, the diffusive contribution subject to the previous condition can be neglected,

$$\frac{\partial \bar{\sigma}}{\partial t} = \mu \frac{\partial}{\partial y} \left(y^4 \frac{\partial \bar{\sigma}}{\partial y} \right), \quad (5.4.1)$$

In contrast, in the final stage of the scalar mixing, in which the diffusion can not be neglected, the full form of Eq. (5.3.17) is required. This equation is supplemented by Neumann condition; $\frac{\partial \bar{\sigma}}{\partial y} = 0$. The time derivative can not be omitted in this case because of the Neumann boundary condition. This scenario leads to an eigenvalue problem,

$$-\gamma \bar{\sigma} = \mu \frac{\partial}{\partial y} \left(y^4 \frac{\partial \bar{\sigma}}{\partial y} \right) + \kappa \frac{\partial^2 \bar{\sigma}}{\partial y^2}. \quad (5.4.2)$$

that yields an exponential decay $\bar{\sigma} \simeq \exp(-\gamma t)$. The value of γ is estimated from the structure of (5.4.2) as a power law;

$$\gamma = 1.81 \sqrt{\kappa \mu}, \quad (5.4.3)$$

where the factor 1.81 has been found numerically.

Theoretically, Salman & Haynes (2007) obtained good agreement with their numerical simulations. Furthermore, in spite of some discrepancies that arose between their predictions and theory which we indicated in Section §5.3, their approach provided an important insight into the role of the no-slip boundaries on the decay of passive scalar.

Let us now turn to the Dirichlet case when the passive scalar σ represents temperature, assuming that it is fixed at the boundary; $\sigma(y = 0) = 0$. For this case, Lebedev & Turitsyn (2004) argued that the peripheral region near the wall boundaries acts as a quasi-stationary source for the scalar that slowly supplies the scalar into the bulk of the flow.

As we have highlighted in Section §5.3 the diffusivity tensor obtained is a function of both spatial coordinates and an expansion in powers of $\tau\mathbf{u}$. Lebedev & Turitsyn (2004) argued that if a no-slip boundary is given by $y = 0$, say, then the components of the diffusivity tensor will scale with the form

$$D_{xx} \simeq y^2 f_{xx}(x), \quad D_{xy} \simeq y^3 f_{xy}(x), \quad D_{yy} \simeq y^4 f_{yy}(x) \quad (y \rightarrow 0). \quad (5.4.4)$$

See Eq. (5.3.26). So, if the flow is statistically translationally invariant in x then f_{xx} , f_{xy} and f_{yy} are constants.

In a situation in which the layer has a thickness controlled by diffusion, as is the case in the final exponential decay regime we are studying, the two terms in (5.3.14) balance and this leads to the scalar field variation being concentrated in a boundary layer with scales

$$x = O(1), \quad y = O(\kappa^{1/4}) \quad (\kappa \rightarrow 0). \quad (5.4.5)$$

With these scales, none of the diffusive terms on the right-hand side of (5.3.14) may be neglected. In the case of Neumann boundary conditions, it is now the slow decay of the scalar field in the boundary layer that is the source of fluctuations in the interior (where they mix rapidly on the advective time scale), and this decay is measured in the final regime.

To analyse the boundary layer structure for the Dirichlet case, we assume that the decay rate γ is of the order $O(\kappa^{\frac{3}{4}})$ as we found numerically (see Fig. 4.13(a)). Turning again to Eq. (5.3.17), one can see that the left-hand side

$$\frac{\partial \bar{\sigma}}{\partial t} = O(\kappa^{\frac{3}{4}}) \bar{\sigma}, \quad (5.4.6)$$

while the second term on the right-hand side,

$$\begin{aligned} \kappa \frac{\partial^2 \bar{\sigma}}{\partial y^2} &= O\left(\frac{\kappa}{(\kappa^{\frac{1}{4}})^2}\right) \bar{\sigma} \\ &= O\left(\kappa^{\frac{1}{2}}\right) \bar{\sigma}. \end{aligned} \quad (5.4.7)$$

Note that as $y \propto \kappa^{\frac{1}{4}}$, then $\frac{\partial}{\partial y} \propto \kappa^{-\frac{1}{4}}$.

As reminder for ourselves, the thickness of the boundary layer is $O(\kappa^{\frac{1}{4}})$ (Lebedev & Turitsyn, 2004; Salman & Haynes, 2007). Similarly, for the first term on the right-hand side of (5.3.17),

$$\begin{aligned} \frac{\partial}{\partial y} \left(\mu y^4 \frac{\partial \bar{\sigma}}{\partial y} \right) &= O\left(\frac{(\kappa^{\frac{1}{4}})^4}{(\kappa^{\frac{1}{4}})^2}\right) \bar{\sigma} \\ &= O\left(\kappa^{\frac{1}{2}}\right) \bar{\sigma}. \end{aligned} \quad (5.4.8)$$

Now comparing the left-hand side of Eq. (5.3.17) with the terms on the right-hand side of the same equation easily leads us to see that $(\kappa^{\frac{3}{4}}) \ll (\kappa^{\frac{1}{2}})$. Consequently, for $\kappa \rightarrow 0$, the term with the time derivative in (5.3.17) can be omitted,

$$\frac{\partial}{\partial y} \left(\mu y^4 \frac{\partial \bar{\sigma}}{\partial y} \right) + \kappa \frac{\partial^2 \bar{\sigma}}{\partial y^2} = 0. \quad (5.4.9)$$

This implies that

$$(\mu y^4 + \kappa) \frac{\partial \bar{\sigma}}{\partial y} = C, \quad (5.4.10)$$

where C is a constant and one can get

$$\bar{\sigma} = \int_0^y \frac{C}{\mu y^4 + \kappa} dy, \quad (5.4.11)$$

To satisfy $\bar{\sigma} = 0$ on the boundary $y = 0$ we have

$$\bar{\sigma} = \int_0^y \frac{C}{\mu r^4 + \kappa} dr, \quad (5.4.12)$$

and one can rewrite this as

$$\bar{\sigma} = C \int_0^y \frac{\frac{1}{\kappa}}{\left(\frac{\mu^{\frac{1}{4}} r}{\kappa^{\frac{1}{4}}}\right)^4 + 1} dr, \quad (5.4.13)$$

The expression (5.4.13) can be simplified by putting $s = \left[\left(\frac{\mu}{\kappa}\right)^{\frac{1}{4}} r\right]$ to obtain

$$\bar{\sigma} = \frac{C}{\kappa^{\frac{3}{4}} \mu^{\frac{1}{4}}} \int_0^{y\left(\frac{\mu}{\kappa}\right)^{\frac{1}{4}}} \frac{1}{s^4 + 1} ds, \quad (5.4.14)$$

where

$$\lim_{\kappa \rightarrow 0} y \left(\frac{\mu}{\kappa}\right)^{\frac{1}{4}} \rightarrow \infty$$

for any fixed $y > 0$ as $\kappa \rightarrow 0$.

Suppose now the average of the concentration field fixed away from the boundary is $\bar{\sigma}_0$, say at the middle of the region at $y = 1/2$, then

$$\bar{\sigma} \simeq \frac{C}{\kappa^{\frac{3}{4}} \mu^{\frac{1}{4}}} \int_0^\infty \frac{1}{s^4 + 1} ds = \bar{\sigma}_0 \quad (5.4.15)$$

Therefore, the factor C in (5.4.15) can be calculated as

$$C = \frac{\bar{\sigma}_0 \kappa^{\frac{3}{4}} \mu^{\frac{1}{4}}}{\int_0^\infty \frac{ds}{s^4+1}}. \quad (5.4.16)$$

with value of integral computed by **Maple**,

$$\int_0^\infty \frac{ds}{s^4+1} = \frac{\pi}{2\sqrt{2}}, \quad (5.4.17)$$

Consequently, if we substitute Eq. (5.4.17) into Eq. (5.4.16), we get

$$C = \frac{2\sqrt{2}}{\pi} \bar{\sigma}_0 \kappa^{\frac{3}{4}} \mu^{\frac{1}{4}}, \quad (5.4.18)$$

Now, substituting with (5.4.18) into (5.4.11) gives

$$\bar{\sigma} = \frac{2\sqrt{2}}{\pi} \bar{\sigma}_0 \kappa^{\frac{3}{4}} \mu^{\frac{1}{4}} \int_0^y \frac{dy}{\mu y^4 + \kappa}. \quad (5.4.19)$$

This equation forms the quasi-stationary distribution of $\bar{\sigma}$ mentioned by Lebedev & Turitsyn (2004), relevant to Dirichlet conditions with no-slip boundaries.

5.5 Decay of the scalar in a plane layer

Our aim in this section is to obtain a theoretical form of the decay rate γ of the passive scalar variance in the presence of no-slip walls controlled by the peripheral regions in a plane layer. Before doing so, it is important to mention that the general average $\bar{\sigma}$ away from the boundaries is approximately a constant in space; say $\bar{\sigma}_0$ (because of fast mixing outside the boundary layer). Let us now consider a square cell \mathcal{D} of side L in an infinite plane layer. Let S be the total scalar in the

cell \mathcal{D} ,

$$S = \int_0^L \int_0^L \sigma dS. \quad (5.5.1)$$

Note that for us $L = \pi\sqrt{2}$, but we keep it to be L for the general discussion. However, in this case, the flux F can be defined as

$$F = \frac{dS}{dt} \quad (5.5.2)$$

Based on (5.3.1) we see that

$$F = \frac{d}{dt} \int_{\mathcal{D}} \sigma dS = \int_{\mathcal{D}} -\mathbf{u} \cdot \nabla \sigma dS + \kappa \int_{\mathcal{D}} \nabla^2 \sigma dS. \quad (5.5.3)$$

Owing to the incompressibility of the flow \mathbf{u} and the divergence theorem we can rewrite (5.5.3) as follows

$$\begin{aligned} F &= \frac{d}{dt} \int_{\mathcal{D}} \sigma dS = \int_{\mathcal{D}} \nabla \cdot (-\mathbf{u} \sigma + \kappa \nabla \sigma) dS \\ &= \int_{\mathcal{C}} \mathbf{n} \cdot (-\mathbf{u} \sigma + \kappa \nabla \sigma) ds \\ &= \kappa \int_{\mathcal{C}} \mathbf{n} \cdot \nabla \sigma ds. \end{aligned} \quad (5.5.4)$$

where \mathcal{C} is the boundary of \mathcal{D} . Based on (5.5.4) and due to presence of the no-slip ($\mathbf{u} = 0$) or slip ($\mathbf{n} \cdot \mathbf{u} = 0$) boundaries, the average flux through the top ($y = L$) and bottom ($y = 0$) boundaries can be calculated by

$$F = \kappa \int_0^L -\frac{\partial \bar{\sigma}}{\partial y}(x, 0) dx + \kappa \int_0^L \frac{\partial \bar{\sigma}}{\partial y}(x, L) dx, \quad (5.5.5)$$

As our square cell \mathcal{D} is in an infinite plane layer then by symmetry the top and the bottom walls will be similar. We are actually assuming the same value of

μ - turbulence intensity - for top and bottom walls, which holds for our flows by symmetry. This leads us to rewrite the total flux on the top and bottom boundaries as follows

$$F = -2 \kappa \int_{\mathcal{C}} \mathbf{n} \cdot \nabla \bar{\sigma} ds, \quad (5.5.6)$$

where \mathcal{C} in (5.5.6) refers to the bottom boundary only. Applying the symmetry and using the property of translational invariance of the flow, Eq. (5.5.6) is easily simplified to

$$F = -2 \kappa L \frac{\partial \bar{\sigma}}{\partial y}(x, 0). \quad (5.5.7)$$

From our discussion in the previous section, we demonstrate that the scalar distribution of the quasi-stationary case is given by Eq. (5.4.19), and so one finds that

$$\frac{\partial \bar{\sigma}}{\partial y} = \frac{2\sqrt{2}}{\pi} \bar{\sigma}_0 \kappa^{\frac{3}{4}} \mu^{\frac{1}{4}} \frac{1}{\mu y^4 + \kappa}, \quad (5.5.8)$$

Subsequently, at the boundary ($y = 0$) we see that

$$\frac{\partial \bar{\sigma}}{\partial y}(x, 0) = \frac{2\sqrt{2}}{\pi} \bar{\sigma}_0 \kappa^{-\frac{1}{4}} \mu^{\frac{1}{4}}, \quad (5.5.9)$$

In this case, we can rewrite the flux F with substituting with Eq. (5.5.9) into Eq. (5.5.7) to obtain

$$F = -\frac{4\sqrt{2}}{\pi} L \bar{\sigma}_0 \kappa^{\frac{3}{4}} \mu^{\frac{1}{4}}, \quad (5.5.10)$$

Returning to Eq. (5.5.1) we find that $S \simeq L^2 \bar{\sigma}_0$ and consequently

$$F = \frac{dS}{dt} = \frac{d\bar{\sigma}_0}{dt} L^2 = -\gamma \bar{\sigma}_0 L^2, \quad (5.5.11)$$

where $\bar{\sigma}_0 \propto e^{-\gamma t}$.

Now, from equations (5.5.10) and (5.5.11) we get

$$\gamma \bar{\sigma}_0 L^2 = \frac{4\sqrt{2}}{\pi} L \bar{\sigma}_0 \kappa^{\frac{3}{4}} \mu^{\frac{1}{4}}, \quad (5.5.12)$$

Over such a situation the long-time decay rate of the scalar variance simply can be identified by

$$\gamma = \frac{4\sqrt{2}}{L\pi} \kappa^{\frac{3}{4}} \mu^{\frac{1}{4}}, \quad L = \pi \sqrt{2}. \quad (5.5.13)$$

Thus, the decay rate we obtained confirms our assumption in the previous section that is $\gamma = O(\kappa^{\frac{3}{4}})$. This is an important consistency check on our calculations; see (5.4.6). The analytical value (5.5.13) obtained for the decay rate will be used in the next chapter to confirm our numerical result for the no-slip flow considered in the peripheral regions with Dirichlet boundary condition.

6

THEORETICAL DEVELOPMENTS

6.1 Outline

Following the theoretical arguments provided in Chapter 5, and in order to link our numerical results to the theory of Lebedev & Turitsyn (2004) we present in this chapter our model flows simulated numerically in Chapter 3 and Chapter 4, along with a detailed analysis for the scaling laws introduced in Section §6.2.

6.2 Scaling laws

In this section we analyse our results obtained for the random and time-periodic flows and summarised in table 6.1 and 4.4, respectively. Here we have given suggested ‘analytical’ values of exponent α in the last column, and we now present justification for these results.

	domain	flow	initial scalar	ω	measured α	analytical α
(i)	square	ψ_{slip}	σ_{D}	1	0.546	1/2
(ii)	square	ψ_{slip}	σ_{N}	1	0	0
(iii)	square	$\psi_{\text{no-slip}}$	σ_{D}	1	0.765	3/4
(iv)	square	$\psi_{\text{no-slip}}$	σ_{N}	1	0.625	2/3
(v)	layer	$\psi_{\text{slip,pl}}$	$\sigma_{\frac{1}{2}\text{D}}$	1	0.53	1/2
(vi)	layer	$\psi_{\text{slip,pl}}$	σ_{N}	1	0	0
(vii)	layer	$\psi_{\text{no-slip,pl}}$	$\sigma_{\frac{1}{2}\text{D}}$	1	0.718	3/4
(viii)	layer	$\psi_{\text{no-slip,pl}}$	σ_{N}	1	0.43	1/2
(ix)	square	ψ_{slip}	$\sigma_{\frac{1}{2}\text{D}}$	1	0.553	1/2
(x)	square	$\psi_{\text{no-slip}}$	$\sigma_{\frac{1}{2}\text{D}}$	1	0.762	3/4

Table 6.1: Summary of results: random flows.

6.2.1 Theory for decay of no-slip flow with Neumann boundary conditions in a plane layer

Our starting point is the theoretical result derived by Lebedev & Turitsyn (2004) and Salman & Haynes (2007) who give the value $\alpha = 1/2$ for no-slip flow in a plane layer with Neumann boundary conditions, corresponding to line (viii) of the table 6.1 as this provides the key to understanding all of our results where the decay rate is indicated by

$$\gamma = C(\mu\kappa)^{1/2}, \quad C \simeq 1.81. \quad (6.2.1)$$

in this case (see Section §5.4).

This has been tested on the no-slip flow $\psi_{\text{no-slip,pl}}$ in the plane layer given by (4.2.25) and detailed in the next subsection for which $\mu = 45\tau/2 \simeq 14.4$. Figure 6.1(a) shows a comparison between the numerical and theoretical decay rates for the no-slip flow with Neumann boundary condition. In this figure, the theoretical decay rate is scaled by $\kappa^{-1/2}\gamma(\kappa)$ that results from (6.2.1). We can see good

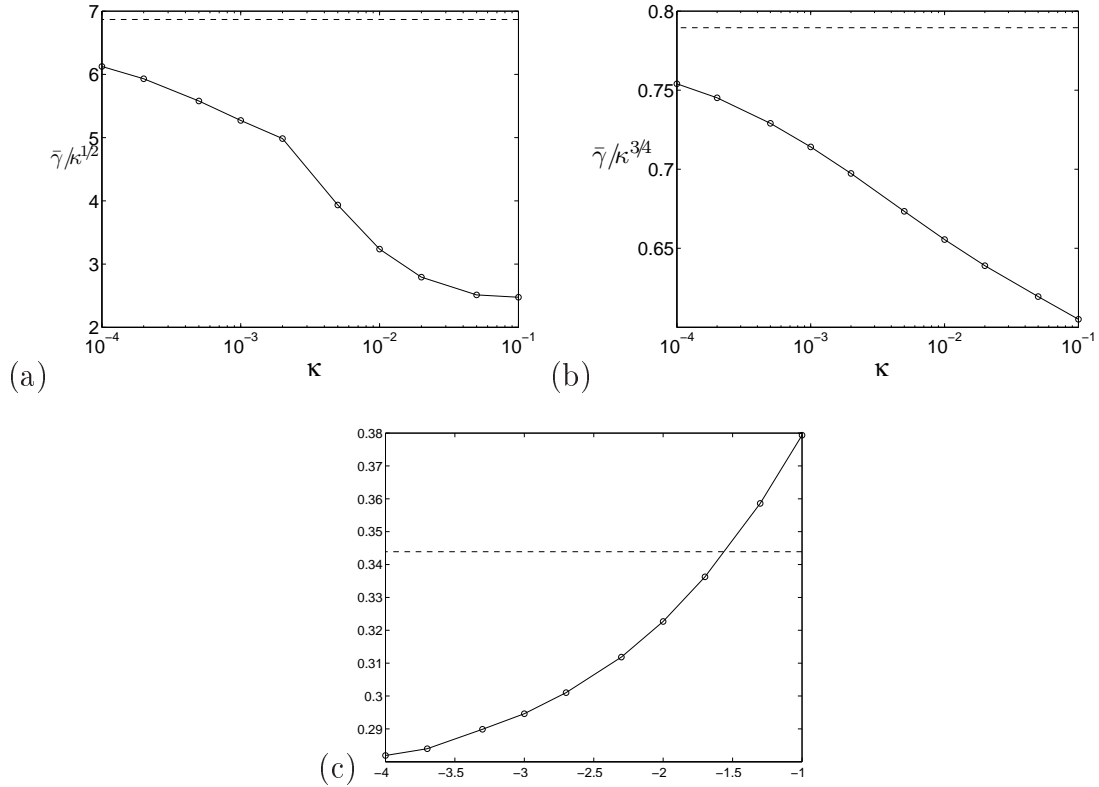


Figure 6.1: Log-linear plot for scalar decay rate (a) $\kappa^{-1/2}\gamma(\kappa)$ against κ for no-slip flow $\psi_{no-slip,pl}$ with Neumann boundary conditions. Panel (b) shows $\kappa^{-3/4}\gamma(\kappa)$ against κ for no-slip flow $\psi_{no-slip,pl}$ and (c) $\kappa^{-1/2}\gamma(\kappa)$ against κ for slip flow $\psi_{slip,pl}$, both with Dirichlet boundary conditions. In each case numerical results are given by markers (solid lines) and theoretical results from (6.2.1), (6.2.17) and (6.2.48) are dashed.

convergence consistent with the theoretical result, in view of the $\kappa^{1/4}$ corrections that would be present in the theory and the values of κ down to only 10^{-4} in these simulations. Note the factor $\frac{1}{2}$ in our μ mentioned above that does not appear in the corresponding equation (36) in Salman & Haynes (2007) which would give a convergence to a value that is twice of our μ (i.e., about 14).

6.2.2 Theory for decay in other configurations

In this section we are seeking an appropriate scaling for the decay rates in other types of flows. To do so, we introduce a number of configurations of the flows in the following sections.

1) No-slip flow $\psi_{no-slip}$ with Dirichlet boundaries

As is discussed in the previous chapter, Lebedev & Turitsyn (2004) indicated that for a no-slip flow containing a scalar satisfying Dirichlet boundary conditions, equation (5.3.14) remains valid. However, now the time derivative term on the left-hand side drops out as the decay rate $\gamma = O(\kappa^{3/4})$ as was indicated in Chapter 5 and so this term is asymptotically smaller than the terms on the right-hand side. As we have mentioned in the previous chapter, the scalar distribution in the boundary layer is quasi-static. The slow decay of the scalar in a square or plane layer domain is controlled by the loss of scalar through the boundary layer, which may be calculated using

$$\frac{\partial}{\partial t} \int_{\mathcal{D}} \bar{\sigma} dS = \kappa \int_{\mathcal{C}} \mathbf{n} \cdot \nabla \bar{\sigma} ds. \quad (6.2.2)$$

Since $\mathbf{n} \cdot \nabla \bar{\sigma} = O(\kappa^{-1/4})\bar{\sigma}$ the decay rate is calculated to scale as $\gamma = O(\kappa^{3/4})$, confirming the scaling results given in lines (iii,vii,x) in the table 6.1. Note that the boundary layers thicken near the corners (as we shall discuss below) but they make a negligible contribution to the integral. In the case where the domain is a plane layer, so that translational invariance along the boundary holds, then equation (5.3.14) remains valid, except that the time-derivative is now asymptotically negligible as $\kappa \rightarrow 0$.

Motivated by the work of Salman & Haynes (2007), in this case, we wish to calculate the quantity μ that can help us to test the decay rate ($\gamma \simeq 1.81\sqrt{\mu\kappa}$) indicated by Salman & Haynes (2007) for the no-slip flow $\psi_{no-slip}$ in the plane layer. The flow we consider for this purpose satisfies no-slip boundary conditions in a plane layer,

$$\psi_{no-slip,pl} = \phi_{1,3}(x - ct, y - ct)^2 \sin(\omega t + \chi(t)) + \phi_{3,1}(x + ct, y + ct)^2 \cos(\omega t + \chi(t)). \quad (6.2.3)$$

Simulations for this flow are shown in Fig. 4.10. The axes x and y are rotated by $\pi/4$ and translated to $(\frac{\pi}{2}, -\frac{\pi}{2})$ where the corner in this case becomes $(x, y) = (\frac{\pi}{2}, -\frac{\pi}{2})$ or $(x', y') = (0, 0)$ (see Fig. 6.2). We will use the theory in Section §5.3 where we took x along the layer (corresponding to x') and y perpendicular (corresponding here to y'). Here, it is convenient to distinguish clearly the coordinates (x, y) and (x', y') . Such a flow now becomes statistically invariant in x , but not in y due to the presence of no-slip boundaries. With respect to (x', y') axes the original spatial co-ordinates (x, y) can be found as

$$x = \frac{\pi}{2} + \frac{x' - y'}{\sqrt{2}}, \quad y = -\frac{\pi}{2} + \frac{x' + y'}{\sqrt{2}}. \quad (6.2.4)$$

We take $c = \omega = 1$ in this case and define the components $\phi_{1,3}(x - ct, y - ct)$ and $\phi_{3,1}(x + ct, y + ct)$ as follows

$$\phi_{1,3}(x - ct, y - ct) = -2 \cos\left(\frac{1}{2}(x + y - 2t)\right) \cos\left(\frac{3}{2}(y - x)\right), \quad (6.2.5)$$

$$\phi_{3,1}(x + ct, y + ct) = -2 \cos\left(\frac{3}{2}(x + y + 2t)\right) \cos\left(\frac{1}{2}(y - x)\right), \quad (6.2.6)$$

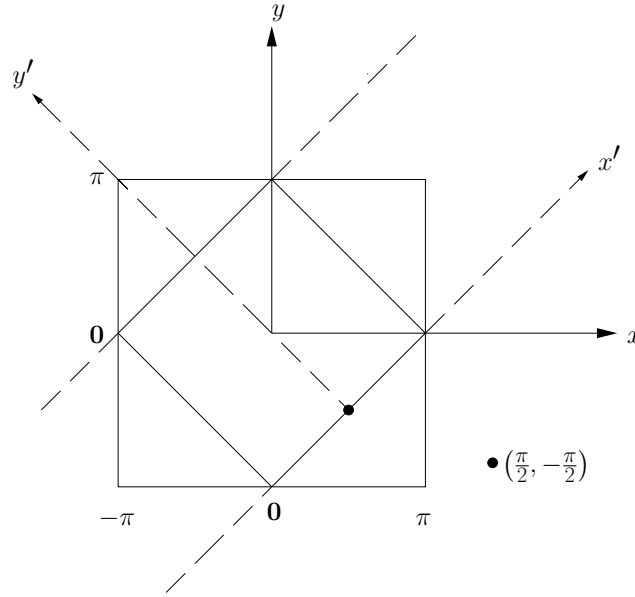


Figure 6.2: Diagram showing the x' and y' axes for a no-slip flow in a plane layer domain.

Based on (6.2.4) in terms of x' and y' , the above equations are rewritten as

$$\phi_{1,3}(x - ct, y - ct)^2 = 4 \cos^2 \left(\frac{x'}{\sqrt{2}} - t \right) \sin^2 \left(\frac{3y'}{\sqrt{2}} \right), \quad (6.2.7)$$

$$\phi_{3,1}(x + ct, y + ct)^2 = 4 \cos^2 \left(\frac{3x'}{\sqrt{2}} + 3t \right) \sin^2 \left(\frac{y'}{\sqrt{2}} \right). \quad (6.2.8)$$

Thus, the flow (6.2.3) takes the form

$$\begin{aligned} \psi &= 4 \cos^2 \left(\frac{x'}{\sqrt{2}} - t \right) \sin^2 \left(\frac{3y'}{\sqrt{2}} \right) \sin(\omega t + \chi(t)) \\ &+ 4 \cos^2 \left(\frac{3x'}{\sqrt{2}} + 3t \right) \sin^2 \left(\frac{y'}{\sqrt{2}} \right) \cos(\omega t + \chi(t)). \end{aligned} \quad (6.2.9)$$

Through the picture drawn above the challenge that appears in such a case is how to calculate the value of the quantity μ . To simplify the situation, we write down

the components of the velocity field for the flow (6.2.9)

$$\begin{aligned}
 u' &= \frac{24}{\sqrt{2}} \cos^2 \left(\frac{x'}{\sqrt{2}} - t \right) \sin \left(\frac{3y'}{\sqrt{2}} \right) \cos \left(\frac{3y'}{\sqrt{2}} \right) \sin(\omega t + \chi(t)) \\
 &+ \frac{8}{\sqrt{2}} \cos^2 \left(\frac{3x'}{\sqrt{2}} + 3t \right) \sin \left(\frac{y'}{\sqrt{2}} \right) \cos \left(\frac{y'}{\sqrt{2}} \right) \cos(\omega t + \chi(t)), \quad (6.2.10)
 \end{aligned}$$

and

$$\begin{aligned}
 v' &= \frac{8}{\sqrt{2}} \cos \left(\frac{x'}{\sqrt{2}} - t \right) \sin \left(\frac{x'}{\sqrt{2}} - t \right) \sin^2 \left(\frac{3y'}{\sqrt{2}} \right) \sin(\omega t + \chi(t)) \\
 &+ \frac{24}{\sqrt{2}} \cos \left(\frac{3x'}{\sqrt{2}} + 3t \right) \sin \left(\frac{3x'}{\sqrt{2}} + 3t \right) \sin^2 \left(\frac{y'}{\sqrt{2}} \right) \cos(\omega t + \chi(t)). \quad (6.2.11)
 \end{aligned}$$

For small y' , we immediately see that these components can be expressed as

$$u' = 36 y' \cos^2 \left(\frac{x'}{\sqrt{2}} - t \right) \sin(\omega t + \chi(t)) + 4 y' \cos^2 \left(\frac{3x'}{\sqrt{2}} + 3t \right) \cos(\omega t + \chi(t)), \quad (6.2.12)$$

$$v' = \frac{18}{\sqrt{2}} y'^2 \sin 2 \left(\frac{x'}{\sqrt{2}} - t \right) \sin(\omega t + \chi(t)) + \frac{6}{\sqrt{2}} y'^2 \sin 2 \left(\frac{3x'}{\sqrt{2}} + 3t \right) \cos(\omega t + \chi(t)). \quad (6.2.13)$$

These forms confirm the scaling we had earlier in Eq. (5.3.25), where $u \propto y$ and $v \propto y^2$. Based on the effective diffusion tensor given by (5.3.13) our approximation produces

$$\begin{aligned}
 D_{yy}(x', y') &= \frac{\tau}{2} \left\langle \left[\frac{18}{\sqrt{2}} y'^2 \sin 2 \left(\frac{x'}{\sqrt{2}} - t \right) \sin(\omega t + \chi(t)) \right. \right. \\
 &\quad \left. \left. + \frac{6}{\sqrt{2}} y'^2 \sin 2 \left(\frac{3x'}{\sqrt{2}} + 3t \right) \cos(\omega t + \chi(t)) \right]^2 \right\rangle. \quad (6.2.14)
 \end{aligned}$$

Now averaging over the random phase $\chi(t)$ followed with averaging over time t inside the interval $[0, 2\pi]$,

$$D_{yy} = \frac{\tau}{2} \left(\frac{18^2}{4} y'^4 \left(\frac{1}{2\pi} \right) \int_0^{2\pi} \left[2 \sin \left(\frac{x'}{\sqrt{2}} - t \right) \cos \left(\frac{x'}{\sqrt{2}} - t \right) \right]^2 dt + \frac{36}{4} y'^4 \left(\frac{3}{2\pi} \right) \int_0^{\frac{2\pi}{3}} \left[2 \sin \left(\frac{3x'}{\sqrt{2}} + 3t \right) \cos \left(\frac{3x'}{\sqrt{2}} + 3t \right) \right]^2 dt \right) \quad (6.2.15)$$

yields

$$D_{yy} = 45\tau/2 y'^4, \quad (6.2.16)$$

This implies that $\mu = 45\tau/2 \simeq 14.4$; $\tau = 0.64$.

Under this scenario, the long-time exponential decay rate predicted in Section §5.5 for the no-slip flow with Dirichlet boundary condition is given by

$$\gamma(\kappa) = \frac{4\sqrt{2}}{\pi L} \kappa^{\frac{3}{4}} \mu^{\frac{1}{4}}, \quad (6.2.17)$$

This decay now can be evaluated by substituting with $L = \pi\sqrt{2}$,

$$\gamma = c_E \kappa^{\frac{3}{4}} \mu^{\frac{1}{4}}, \quad c_E = \frac{4}{\pi^2}. \quad (6.2.18)$$

Figure 6.1(b) shows very good agreement between this theoretical prediction and corresponding simulation. We clearly see the rapid convergence of the numerical result given by markers to the theoretical one from (6.2.18) (dashed line) as κ tends to zero, particularly noting the scale on the vertical axis.

2) No-slip flow $\psi_{no-slip}$ with Neumann boundaries in a square domain

The second model flow is the no-slip flow with Neumann boundary conditions in a square domain. As we have shown in Chapter 3, this flow has a specific decay rate characterised by $\alpha \simeq 0.625$ which is fundamentally slower than is the case for a plane layer. Interestingly, if we go back to the scalar field distribution of this flow (Fig. 3.10), careful examination will reveal why. The corners of the square act as reservoirs, that slowly release the scalar into the body of the fluid and this controls the time-scale of homogenisation in the domain. Such a clear observation strongly encourages us to justify theoretically our computed scaling law obtained for this flow. Turning again to our flow considered in this case, with respect to x' and y' axes we have

$$\psi(x', y', t) = \phi_{1,3}^2(x', y') \sin(\omega t + \chi(t)) + \phi_{3,1}^2(x', y') \cos(\omega t + \chi(t)), \quad (6.2.19)$$

with main functions $\phi_{1,3}$ and $\phi_{3,1}$,

$$\phi_{1,3}(x', y') = -\cos\left(\frac{3\pi}{2} + \frac{x'}{\sqrt{2}} - \frac{3y'}{\sqrt{2}}\right) - \cos\left(-\frac{3\pi}{2} + \frac{x'}{\sqrt{2}} + \frac{3y'}{\sqrt{2}}\right), \quad (6.2.20)$$

$$\phi_{3,1}(x', y') = -\cos\left(\frac{\pi}{2} + \frac{3x'}{\sqrt{2}} - \frac{y'}{\sqrt{2}}\right) - \cos\left(-\frac{\pi}{2} + \frac{3x'}{\sqrt{2}} + \frac{y'}{\sqrt{2}}\right). \quad (6.2.21)$$

Note that this flow is not invariant in x' nor y' due to the presence of the boundaries of the square domain along the x' and y' axes. Furthermore, the corner shown in Fig. 6.3 is $(x, y) = (0, -\pi)$ which becomes $(x', y') = (-\pi/\sqrt{2}, 0)$ or $(x'', y') = (0, 0)$ where $x'' = x' + \pi/\sqrt{2}$. This procedure enables us to obtain a simple approximation for such a flow. Therefore, in terms of x'' and y' , Eqs. (6.2.20) and (6.2.21) can be

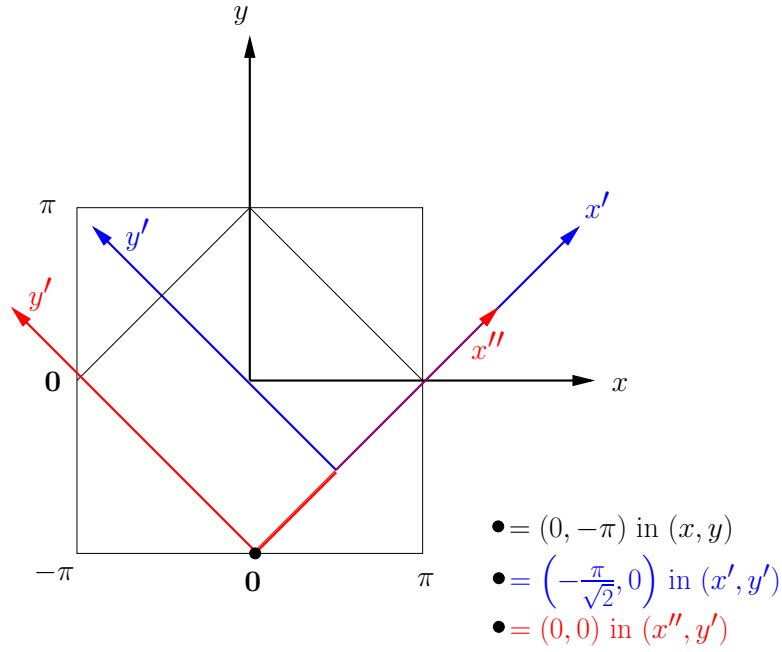


Figure 6.3: Diagram showing the x'' and y' axes for the no-slip flow in a square domain.

written as

$$\phi_{1,3}(x'', y') = \cos\left(\frac{x''}{\sqrt{2}} - \frac{3y'}{\sqrt{2}}\right) - \cos\left(\frac{x''}{\sqrt{2}} + \frac{3y'}{\sqrt{2}}\right), \quad (6.2.22)$$

$$\phi_{3,1}(x'', y') = \cos\left(\frac{3x''}{\sqrt{2}} - \frac{y'}{\sqrt{2}}\right) - \cos\left(\frac{3x''}{\sqrt{2}} + \frac{y'}{\sqrt{2}}\right). \quad (6.2.23)$$

On simplification, for small x'' and y' these two equations take the form

$$\phi_{1,3}(x'', y') = \phi_{3,1}(x'', y') \simeq 3x''y'. \quad (6.2.24)$$

So for $x'' \ll 1$ and $y' \ll 1$, the flow (6.2.19) will be expanded as

$$\psi(x'', y', t) = 9x''^2y'^2 \sin(\omega t + \chi(t)) + 9x''^2y'^2 \cos(\omega t + \chi(t)). \quad (6.2.25)$$

with components of velocity field

$$u = 18 x''^2 y' \sin(\omega t + \chi(t)) + 18 x''^2 y' \cos(\omega t + \chi(t)), \quad (6.2.26)$$

$$v = -18 x'' y'^2 \sin(\omega t + \chi(t)) - 18 x'' y'^2 \cos(\omega t + \chi(t)). \quad (6.2.27)$$

Overall, averaging over phase $t \in [0, 2\pi]$ yields the following scaling for the diffusivity tensor as the corners are approached

$$D_{x''x''}(x'', y') = \mu x''^4 y'^2; \quad \mu = (18)^2 \left(\frac{\tau}{2}\right), \quad (6.2.28)$$

$$D_{x''y'}(x'', y') = \lambda x''^3 y'^3; \quad \lambda = -(18)^2 \left(\frac{\tau}{2}\right), \quad (6.2.29)$$

$$D_{y'y'}(x'', y') = \nu x''^2 y'^4; \quad \nu = (18)^2 \left(\frac{\tau}{2}\right). \quad (6.2.30)$$

To estimate how the thickness of the layer of scalar trapped in the corners varies, we introduce a length scale l for the scalar defined as the thickness of the square boundary layer in which $x, y \sim l$. Using this parameter on terms appearing in Eq. (5.3.14),

$$\gamma \bar{\sigma} \sim \frac{1}{l} (\mu l^4 l^2 \frac{\bar{\sigma}}{l}) + \frac{1}{l} (\lambda l^3 l^3 \frac{\bar{\sigma}}{l}) \sim \kappa \left(\frac{1}{l^2}\right) \bar{\sigma}, \quad (6.2.31)$$

one finds that

$$\gamma \bar{\sigma} \sim l^4 (\mu + \lambda) \bar{\sigma} \sim \frac{\kappa}{l^2} \bar{\sigma}, \quad (6.2.32)$$

This implies a decay rate

$$\gamma \sim \frac{\kappa}{l^2}, \quad (6.2.33)$$

with

$$l^6 \sim \frac{\kappa}{(\mu + \lambda)}, \quad (6.2.34)$$

This satisfies that

$$l = \left(\frac{\kappa}{\mu + \lambda} \right)^{\frac{1}{6}}. \quad (6.2.35)$$

Therefore, seeking the appropriate scaling reveals that the scalar in the corners has spatial scales $l = O(\kappa^{\frac{1}{6}})$ and, from consideration of the time-derivative, the decay rate is found of order $\gamma = O(\kappa^{\frac{2}{3}})$ (by substituting (6.2.35) into (6.2.33)) as seen in line (iv) of the table 6.1.

3) Slip flow with Neumann boundaries

We now turn to the slip flows. In the case of Neumann boundary conditions, it is clear that the boundaries do not play a controlling role in the decay of the scalar field (Salman & Haynes, 2007): there is no evidence of boundary layers in Fig. 3.8. However, the slip flow considered in the square domain has the form

$$\psi_{slip}(x'', y', t) = \phi_{1,3}(x'', y') \sin(\omega t + \chi(t)) + \phi_{3,1}(x'', y') \cos(\omega t + \chi(t)). \quad (6.2.36)$$

where the main functions $\phi_{1,3}(x'', y')$ and $\phi_{3,1}(x'', y')$ are given by (6.2.22) and (6.2.23), respectively. For small x'' and y' , and from Eq. (6.2.24) we get that

$$\psi_{slip}(x'', y', t) = 3x''y' \sin(\omega t + \chi(t)) + 3x''y' \cos(\omega t + \chi(t)). \quad (6.2.37)$$

and hence

$$u = 3x'' \sin(\omega t + \chi(t)) + 3x'' \cos(\omega t + \chi(t)), \quad (6.2.38)$$

$$v = -3y' \sin(\omega t + \chi(t)) - 3y' \cos(\omega t + \chi(t)). \quad (6.2.39)$$

In a short correlation time limit, the diffusivity tensor near the boundary will have components,

$$D_{x''x''}(x'', y') = \mu x''^2; \quad \mu = 9 \left(\frac{\tau}{2} \right), \quad (6.2.40)$$

$$D_{x''y'}(x'', y') = \lambda x'' y'; \quad \lambda = -9 \left(\frac{\tau}{2} \right), \quad (6.2.41)$$

$$D_{y'y'}(x'', y') = \nu y'^2; \quad \nu = 9 \left(\frac{\tau}{2} \right). \quad (6.2.42)$$

These dependences lead us to write Eq. (5.3.14) in terms of a length scale l ,

$$\gamma \bar{\sigma} \sim \frac{1}{l} (\mu l^2 \frac{\bar{\sigma}}{l}) + \frac{1}{l} (\lambda l^2 \frac{\bar{\sigma}}{l}) \sim \frac{\kappa}{l^2} \bar{\sigma}, \quad (6.2.43)$$

which is simplified to

$$\gamma \bar{\sigma} \sim (\mu + \lambda) \bar{\sigma} \sim \frac{\kappa}{l^2} \bar{\sigma}, \quad (6.2.44)$$

This yields that

$$\gamma \sim \frac{\kappa}{l^2}, \quad (6.2.45)$$

and

$$l^2 \sim \frac{\kappa}{\mu + \lambda}. \quad (6.2.46)$$

Substituting with (6.2.46) into (6.2.45) gives a decay rate $\gamma = O(1)$ and a corresponding boundary layer scaling of $l = O(\kappa^{1/2})$. These spatial and temporal scales are the same as for the destruction of scalar fluctuations in the body of the fluid. So for Neumann boundary conditions, there is no boundary layer present, that is no separation of space or time scales. The decay rate has $\alpha = 0$ and we expect $\gamma = \gamma_0 + O(\sqrt{\kappa})$ as found numerically, confirming lines (ii, vi) of the table 6.1.

4) Slip flow with Dirichlet boundaries

The situation is different for the Dirichlet boundary condition, because with scales $y = O(\kappa^{1/2})$ in the boundary layer, relationship (6.2.2) now implies that the total scalar in the domain will decay at a rate $\gamma = O(\kappa^{1/2})$ as $\kappa \rightarrow 0$, confirming lines (i, v, ix) of the table 6.1. The scalar again mixes on an advective time scale in the cell, and its flux out is controlled by the boundary layers. In the case of a layer that is statistically translationally invariant in x we will obtain that $D_{yy} \simeq \mu y^2$. Integrating the boundary layer equation will give

$$\bar{\sigma} = \bar{\sigma}_0(t) \frac{2}{\pi} \tan^{-1} \left(y \sqrt{\frac{\mu}{\kappa}} \right) \quad (6.2.47)$$

and a decay rate

$$\gamma(\kappa) = \frac{4}{\pi L} \mu^{1/2} \kappa^{1/2}, L = \pi \sqrt{2}. \quad (6.2.48)$$

For the flow $\psi_{slip,pl}$ in (4.2.3) this is checked in Fig. 6.1(c), the value of μ being $\mu = 9\tau/4 \simeq 1.44$. There is rapid convergence of $\kappa^{-1/2}\gamma(\kappa)$ to the numerical one in this figure.

6.3 Transfer of heat between cells of the flow

We now consider heat transfer over many fields in periodic flows. As we know, based on our numerical results of simulations obtained in Chapter 3 and Chapter 4, the boundary layer has an important role in controlling the lose of heat from the system. This is evident in all the cases we studied except in the slip case with Neumann boundary conditions, where there is no obvious role of the boundaries on the transport of the scalar. Therefore, our interest in this section is in under-

standing how much heat can be transferred between the cells of the flow in the presence of no-slip boundaries. Specifically, we aim to establish links between the decay rate with Dirichlet boundary conditions and transport of the scalar field over large scales.

6.3.1 Approximating scalar decay in large-scale fields

Our starting point will be large-scale fields using a formalism of Bloch wavenumbers for the flows considered in a square cell. We know in advance (from our previous discussion in Section §5.4) how the average of the scalar $\bar{\sigma}$ in the boundary layer is determined. This encourages us to start from here and to do so, we consider scalar fields of the general form

$$\sigma(\mathbf{r}, t) = e^{iMx+iNy} \sum_{m,n} \hat{\sigma}_{m,n}(t) e^{imx+iny} + c.c., \quad (6.3.1)$$

with $0 < M, N \leq 1/2$. This equation (6.3.1) gives the full scalar field which has a period of $2\pi/M$ in x direction and $2\pi/N$ in y direction.

Suppose now the scalar field σ is given by

$$\sigma \simeq e^{iMx'} e^{-\gamma t}. \quad (6.3.2)$$

where we are taking $N = 0$ and using (6.3.2) to give the well-mixed value in the interior of each square, at $x = Ln$. We now consider the cells of the flow to be the squares as shown in Fig. 6.4 and denote the value of the well-mixed scalar in the square **A** by σ_n . This will be the same amount for the top and bottom squares, **D** and **B**, while it is σ_{n+1} and σ_{n-1} for the right and left ones; **C** and **E**, respectively.

In this case we have

$$\sigma_n \simeq e^{iMLn} e^{-\gamma t}, \quad (6.3.3)$$

where L is the side of the square.

Based on our discussion presented in Section §5.5, the amount of the scalar S in a square cell is calculated by (5.5.1). Therefore, in a square, say \mathbf{A} that is seen in Fig. 6.4 one finds that the total scalar is given from (6.3.2) by

$$\begin{aligned} S_A &= \int_A \sigma \, dx' \, dy' \\ &= L^2 \sigma_A \\ &= L^2 \sigma_n \\ &= L^2 e^{iMLn} e^{-\gamma t}. \end{aligned} \quad (6.3.4)$$

Subsequently,

$$\frac{dS_n}{dt} = -\gamma L^2 e^{iMLn} e^{-\gamma t}. \quad (6.3.5)$$

As we discussed in last chapter, the average of the scalar field in the boundary layer is given by

$$\bar{\sigma} = \frac{2\sqrt{2}}{\pi} \bar{\sigma}_0 \kappa^{\frac{3}{4}} \mu^{\frac{1}{4}} \int_0^{y'} \frac{dy'}{\mu y'^4 + \kappa}. \quad (6.3.6)$$

where $\bar{\sigma}_0$ is the limiting value as $(y'/\kappa^{1/4}) \rightarrow \infty$ and $\bar{\sigma} = 0$ on the boundary $y' = 0$. Note that we will use (6.4.16) (valid for a plane layer) here and generalise it in Section §6.3.2 for analysing transfer of heat in a square cell. However, Eq. (6.4.16) can be rewritten as

$$\bar{\sigma} = \left(\frac{\sigma_n + \sigma_{n+1}}{2} \right) + \frac{2\sqrt{2}}{\pi} \left(\frac{\sigma_{n+1} - \sigma_n}{2} \right) \kappa^{\frac{3}{4}} \mu^{\frac{1}{4}} \int_0^{y'} \frac{dy'}{\mu y'^4 + \kappa}. \quad (6.3.7)$$

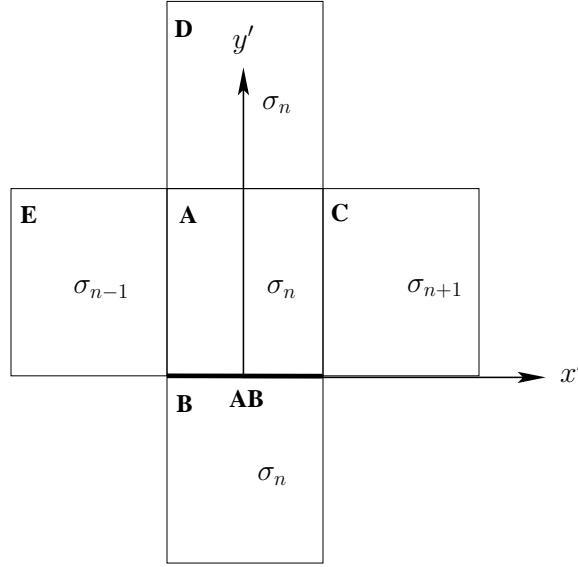


Figure 6.4: Diagram for the transfers of the scalar field between cells.

where adding the term $(\frac{\sigma_n + \sigma_{n+1}}{2})$ does not affect the behaviour of the scalar. It is important to note that in Eq. (6.3.7) $\bar{\sigma} \rightarrow \sigma_{n+1}$ for large y' ($y' > 0$), $\bar{\sigma} \rightarrow \sigma_n$ for large $-y'$ and $\bar{\sigma} = (\sigma_n + \sigma_{n+1})/2$ when $y' = 0$.

We have found that in a square, for example **A** that is seen in Fig. 6.4 the amount of the scalar is expressed as

$$S_A = L^2 \sigma_A, \quad (6.3.8)$$

This yields that the total flux across the boundaries of one cell (i.e., the square **A**) is obtained by

$$\frac{dS_A}{dt} = -\kappa \int_{\partial A} \mathbf{n} \cdot \nabla \sigma ds, \quad (6.3.9)$$

which gives

$$\frac{dS_A}{dt} = -\kappa \int_{AC} \frac{\partial \sigma}{\partial y'} \Big|_{y'=0} dx' + \kappa \int_{AE} \frac{\partial \sigma}{\partial y'} \Big|_{y'=\pi\sqrt{2}} dx', \quad (6.3.10)$$

Here in each case x' is along the layer and y' is perpendicular. Returning to Eq. (6.3.7), we find that

$$\begin{aligned} \frac{\partial \bar{\sigma}}{\partial y'} \Big|_{y'=0} &= \frac{2\sqrt{2}}{\pi} \kappa^{\frac{3}{4}} \mu^{\frac{1}{4}} \left(\frac{\sigma_{n+1} - \sigma_n}{2} \right) \frac{1}{\mu y'^4 + \kappa} \Big|_{y'=0} \\ &= \frac{2\sqrt{2}}{\pi} \left(\frac{\mu}{\kappa} \right)^{\frac{1}{4}} \left(\frac{\sigma_{n+1} - \sigma_n}{2} \right). \end{aligned} \quad (6.3.11)$$

Particularly, on each boundary of the square **A**, **AC** or **AE** (say the boundary **AC**) one gets

$$-\kappa \int_{AC} \frac{\partial \sigma}{\partial y'} dx' = -\kappa L \left(\frac{2\sqrt{2}}{\pi} \right) \left(\frac{\mu}{\kappa} \right)^{\frac{1}{4}} \left(\frac{\sigma_{n+1} - \sigma_n}{2} \right). \quad (6.3.12)$$

Returning to Eq. (6.3.9), we find that the total flux across the boundaries of this square can be calculated by

$$\begin{aligned} \frac{dS_n}{dt} &= -\kappa_{eff} [(\sigma_n - \sigma_{n-1}) + (\sigma_n - \sigma_{n+1})] \\ &= -\kappa_{eff} [2\sigma_n - \sigma_{n-1} - \sigma_{n+1}] \\ &= -\kappa_{eff} [2e^{iMnL} - e^{iM(n-1)L} - e^{iM(n+1)L}] e^{-\gamma t} \\ &= -\kappa_{eff} [2 - e^{-iML} - e^{iML}] e^{iMLn} e^{-\gamma t}. \end{aligned} \quad (6.3.13)$$

Here κ_{eff} is an effective diffusivity being defined as the flux of heat across the boundaries divided by the temperature difference and is given by

$$\kappa_{eff}(\kappa) = L \kappa^{\frac{3}{4}} \mu^{\frac{1}{4}} \left(\frac{2\sqrt{2}}{\pi} \right) \left(\frac{1}{2} \right). \quad (6.3.14)$$

Therefore, Eq. (6.3.13) can be written for small M as

$$\begin{aligned}\frac{dS_n}{dt} &= -\kappa_{eff}\left[2 - \left(1 - iML - \frac{M^2L^2}{2!} + \dots\right) - \left(1 + iML - \frac{M^2L^2}{2!} + \dots\right)\right]e^{iMLn}e^{-\gamma t} \\ &= -M^2L^2e^{iMLn}e^{-\gamma t}\kappa_{eff}.\end{aligned}\quad (6.3.15)$$

Now, comparing Eq. (6.3.5) with Eq. (6.3.15) leads us to demonstrate that the decay rate γ in this case can be found as

$$\gamma(\kappa) \simeq M^2\kappa_{eff}(\kappa), \quad (M \rightarrow 0). \quad (6.3.16)$$

With mixing on the advective time scale within individual cells, the transport of the scalar field on large scales is completely controlled by the flux of heat across boundary layers along the cell edges, as is evident from the picture of the scalar that we present in Fig. 6.4. Furthermore, solving the equation

$$\frac{\partial\sigma}{\partial t} = \kappa_{eff}\frac{\partial^2\sigma}{\partial x^2} \quad (6.3.17)$$

gives a scalar field $\sigma = e^{iMx}e^{-\kappa_{eff}M^2t}$ that justifies the name “effective diffusivity κ_{eff} ” appearing in Eq. (6.3.16), where $\gamma \simeq M^2\kappa_{eff}(\kappa)$.

6.3.2 Approximating scalar decay in a square cell

Similarly, based on our discussion presented above, we expand in this section the approximation of transferring heat across the boundary in a square domain, but with absence of the translational invariance property. For this purpose we consider the two cells of the flow to be the squares **A** and **B** as depicted in Fig. 6.5. We denote the value of the scalar in both squares **A** and **B** by σ_A and σ_B , respectively

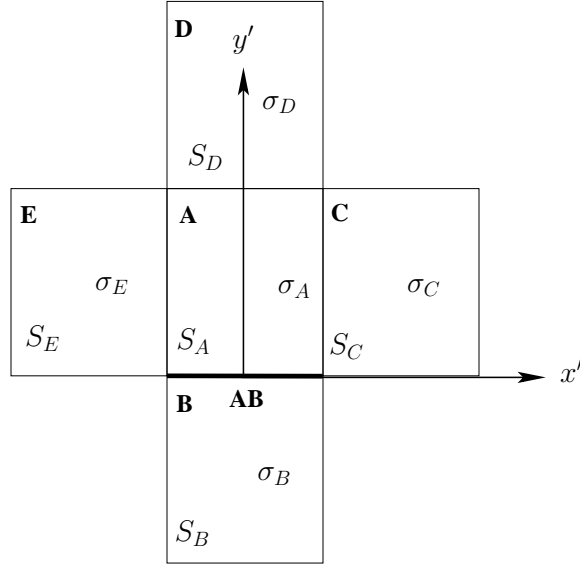


Figure 6.5: Diagram showing a heat transfers between cells.

and similarly for the squares **C**, **D** and **E** shown in Fig. 6.5. In this case, Eq. (6.4.16) (under consideration of the cells **A** and **B**) can be rewritten as

$$\bar{\sigma} = \left(\frac{\sigma_A + \sigma_B}{2} \right) + \left(\frac{\sigma_A - \sigma_B}{2} \right) F \left(x', \frac{y'}{\kappa^{1/4}} \right) \quad (6.3.18)$$

with considerations based on our previous discussion,

$$F(x', s) \longrightarrow 1, \quad s \rightarrow \infty, \quad (6.3.19)$$

$$F(x', s) \longrightarrow -1, \quad s \rightarrow -\infty, \quad (6.3.20)$$

$$F(x', 0) \longrightarrow 0, \quad s \rightarrow 0, \quad (6.3.21)$$

where $s = \frac{y'}{\kappa^{1/4}}$.

Based on (6.3.9) and similarly to the previous calculations, the flux across one

boundary of the square **A** (say **AB**) will be given by

$$\begin{aligned}
 \frac{dS_A}{dt} &= -\kappa \int_{AB} \frac{\partial \sigma}{\partial y} dx' \\
 &= -\kappa \int_0^L \frac{\sigma_A - \sigma_B}{2} \kappa^{-1/4} \frac{\partial F}{\partial s} dx' \\
 &= -\kappa^{3/4} \left(\frac{\sigma_A - \sigma_B}{2} \right) \int_0^L \frac{\partial F}{\partial s} dx' \\
 &= -C(\sigma_A - \sigma_B).
 \end{aligned} \tag{6.3.22}$$

where

$$C = \frac{1}{2} \kappa^{3/4} \int_0^L \frac{\partial F}{\partial s} dx'. \tag{6.3.23}$$

Therefore, the total flux across the boundaries of the square **A** can be determined as

$$\frac{dS_A}{dt} = -\kappa \int_{AB} \frac{\partial \sigma}{\partial y'} dx' - \kappa \int_{AD} -\frac{\partial \sigma}{\partial y'} dx' - \kappa \int_{AE} \frac{\partial \sigma}{\partial x'} dy' - \kappa \int_{AC} -\frac{\partial \sigma}{\partial x'} dy', \tag{6.3.24}$$

where in each case x' is along the layer and y' is perpendicular. Now (6.3.24) determines the amount of the flux across the boundaries of the square **A**, which can be calculated by

$$\frac{dS_A}{dt} = -C [(\sigma_A - \sigma_B) + (\sigma_A - \sigma_C) + (\sigma_A - \sigma_D) + (\sigma_A - \sigma_E)]. \tag{6.3.25}$$

In the case of Dirichlet boundary conditions one can find

$$\sigma_B = \sigma_C = \sigma_D = \sigma_E = -\sigma_A. \tag{6.3.26}$$

which ensures $\sigma = 0$ on the boundaries, as in our simulations. Substitution with (6.3.26) into (6.3.25) yields

$$\frac{dS_A}{dt} = -8C\sigma_A \quad (6.3.27)$$

Similarly, substitution with (6.3.8) into (6.3.27) gives

$$\frac{d}{dt}(L^2\sigma_A) = -8C\sigma_A, \quad (6.3.28)$$

and hence

$$\frac{d}{dt}(\sigma_A) = -\frac{8C\sigma_A}{L^2} = -\gamma\sigma_A, \quad (6.3.29)$$

as $\bar{\sigma} \simeq e^{-\gamma t}$.

This forms the long-time decay rate $\gamma_D(\kappa)$ for Dirichlet boundary conditions,

$$\gamma_D(\kappa) = \frac{8C}{L^2}, \quad (\kappa \rightarrow 0). \quad (6.3.30)$$

where C is given by (6.3.23) and the same of κ_{eff} appearing in the equations from (6.3.13) to (6.3.16). Equation (6.3.16) can be linked to the transport of the scalar (6.3.30) in the square using a Bloch wavenumber M as follows,

$$\gamma(\kappa) \simeq \frac{M^2 L^2 \gamma_D}{8}, \quad (M \rightarrow 0). \quad (6.3.31)$$

It is important to note that this equation does not depend on the boundary layer structure as we did not use the details of the boundary layer nor no-slip condition.

6.3.3 Extending Bloch wavenumbers

Analogously, in this section we continue our work set up in Section §6.3.1 with Bloch wavenumbers. We consider two Bloch wavenumbers M and N and suppose the average scalar in each square $x' = mL$ and $y' = nL$ (as seen in Fig. 6.5) is given by

$$\sigma \simeq e^{iMx' + iNy'} e^{-\gamma t}. \quad (6.3.32)$$

Based on our earlier discussion we get

$$\frac{d}{dt}(L^2 \sigma_A) = -\kappa_{eff}[4\sigma_A - \sigma_B - \sigma_C - \sigma_D - \sigma_E]. \quad (6.3.33)$$

Substituting with Eq. (6.3.32) into Eq. (6.3.33) one can see that

$$\begin{aligned} -\gamma L^2 e^{iMmL + iNnL} e^{-\gamma t} = & -\kappa_{eff} e^{-\gamma t} [4e^{iMmL + iNnL} - e^{iMmL + iN(n-1)L} \\ & - e^{iM(m+1)L + iNnL} - e^{iMmL + iN(n+1)L} - e^{iM(m-1)L + iNnL}] \end{aligned} \quad (6.3.34)$$

which is expanded as

$$\begin{aligned} -\gamma L^2 = & -\kappa_{eff}[4 - e^{-iNL} - e^{iNL} - e^{-iML} - e^{iML}] \\ = & -\kappa_{eff}[4 - (1 - iNL - \frac{N^2 L^2}{2!} + \dots) - (1 + iNL - \frac{N^2 L^2}{2!} + \dots) - \dots]. \end{aligned} \quad (6.3.35)$$

This leads us to obtain a simple link between the decay rate $\gamma(\kappa)$ and $\kappa_{eff}(\kappa)$ using the Bloch wavenumbers M, N

$$\gamma L^2 = \kappa_{eff}(M^2 + N^2)L^2, \quad (6.3.36)$$

which implies that

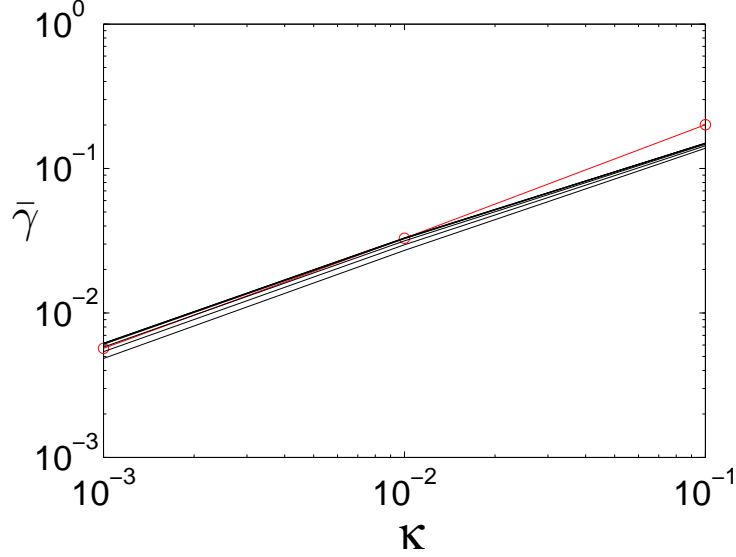


Figure 6.6: Log-log plot for the numerical and theoretical decay rate $\gamma(\kappa)$ against κ for the no-slip flow $\psi_{\text{no-slip}}$ with Dirichlet boundary conditions, corresponding to the Bloch wavenumbers $M = 0$ and $N = 1/2, 3/8, 2/8, 1/8, 1/16,$ and $1/32$ for $\kappa = 0.1, 0.01$ and 0.001 . Numerical result for the flow (circles) is compared with theoretical results (solid) from (6.3.30). The factor C in (6.3.30) is determined from (6.3.16); $C = \kappa_{eff} = \gamma(\kappa)/N^2$ for each value of N .

$$\gamma(\kappa) = \kappa_{eff}(\kappa)(M^2 + N^2), \quad (M, N \rightarrow 0). \quad (6.3.37)$$

Thus, for small M, N with a flow in the square domain, an isotropic transport of scalar fields on large scales can be observed with a decay rate formed by Eq. (6.3.37).

Figures 6.6 and 6.7 show convergence of the theoretical decay rate (6.3.30) to the numerical one corresponding respectively to both flows $\psi_{\text{no-slip}}$ (3.2.44) and ψ_{slip} (3.2.9) with Dirichlet boundary conditions simulated in the square.

For simplicity, in this comparison we chose the Bloch wavenumbers $M = 0$ and the

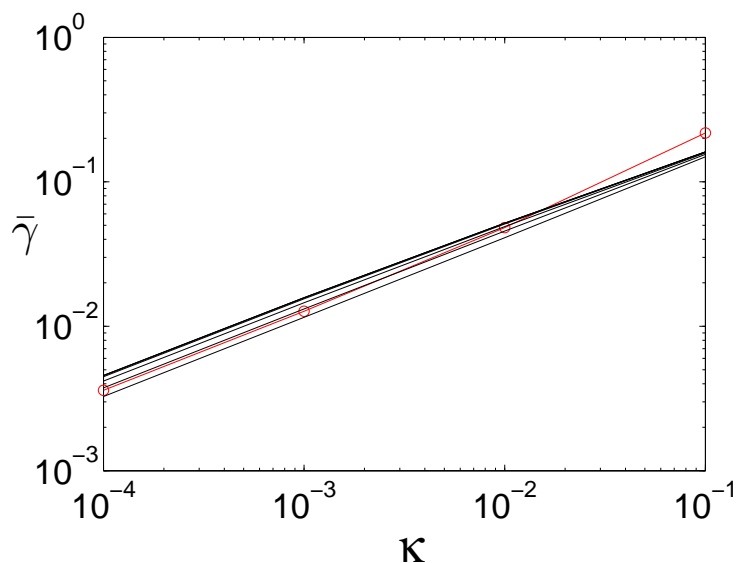


Figure 6.7: Log-log plot for the numerical and theoretical decay rate $\gamma(\kappa)$ against κ for the slip flow ψ_{slip} with Dirichlet boundary conditions, corresponding to the Bloch wavenumbers $M = 0$ and $N = 1/2, 3/8, 2/8, 1/8, 1/16, 1/32$ and $1/64$ for $\kappa = 0.1, 0.01, 0.001$ and 0.0001 . Numerical result for the flow (circles) is compared with theoretical results (solid) from (6.3.30). The factor C in (6.3.30) is determined from (6.3.16); $C = \kappa_{\text{eff}} = \gamma(\kappa)/N^2$ for each value of N .

fractions $N = 1/2, 3/8, 2/8, 1/8, 1/16, 1/32$ and $1/64$. These values correspond to the theoretical decay rate (6.3.30) (with C in (6.3.30) determined from (6.3.16) and given by $C = \gamma(\kappa)/N^2$) against the values of $\kappa = 0.1, 0.01, 0.001$ and 0.0001 . Particularly, satisfactory agreement between the two is clearly seen in Fig. 6.6, for the flow $\psi_{\text{no-slip}}$. In such a case, rapid convergence for the theoretical decay rates (solid) to the numerical one (circles) is observed in this figure as $N \rightarrow 0$.

6.4 A cross section of the boundary layer

In light of our discussion provided earlier in this part of the thesis, we have demonstrated that the behaviour of the passive scalar evolution is described by

$$\frac{\partial \bar{\sigma}}{\partial t} = \frac{\partial}{\partial x_i} \left(D_{ij} \frac{\partial \bar{\sigma}}{\partial x_j} \right) + \kappa \nabla^2 \bar{\sigma}. \quad (6.4.1)$$

This is expanded to

$$\begin{aligned} \frac{\partial \bar{\sigma}}{\partial t} &= \frac{\partial}{\partial x} \left(D_{xx} \frac{\partial \bar{\sigma}}{\partial x} \right) + \frac{\partial}{\partial x} \left(D_{xy} \frac{\partial \bar{\sigma}}{\partial y} \right) \\ &+ \frac{\partial}{\partial y} \left(D_{yx} \frac{\partial \bar{\sigma}}{\partial x} \right) + \frac{\partial}{\partial y} \left(D_{yy} \frac{\partial \bar{\sigma}}{\partial y} \right) \\ &+ \kappa \nabla^2 \bar{\sigma}. \end{aligned} \quad (6.4.2)$$

Actually, we have defined the scalar field $\bar{\sigma}$ by

$$\bar{\sigma}(x, y, t) = \sum_{m,n} \hat{\sigma}_{m,n}(t) e^{imx+iny}. \quad (6.4.3)$$

If we write the factors D_{xx} , D_{xy} and D_{yy} (where $D_{xy} = D_{yx}$ by symmetry) appearing in Eq. (6.4.2) as units of sum of modes $e^{ikx+ily}$ (i.e., pick out a single Fourier mode for simplicity), then

$$D_{xx} = \hat{D}_{xx} e^{ikx+ily}, \quad (6.4.4)$$

$$D_{xy} = \hat{D}_{xy} e^{ikx+ily}, \quad (6.4.5)$$

$$D_{yy} = \hat{D}_{yy} e^{ikx+ily}. \quad (6.4.6)$$

Working out on these terms in (6.4.2) we get

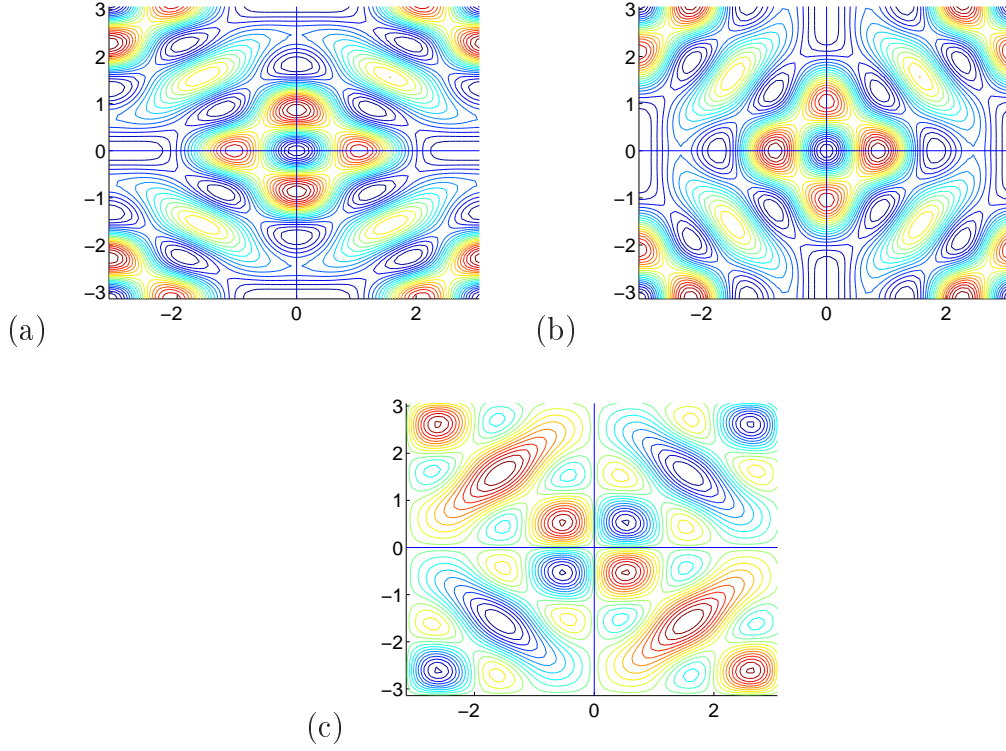


Figure 6.8: Plots of (a) D_{xx} , (b) D_{yy} and (c) D_{xy} for the slip flow in a square domain.

$$\begin{aligned}
 D_{xx} \frac{\partial \bar{\sigma}}{\partial x} &= \hat{D}_{xx} e^{ikx+ily} \sum_{m,n} (im) \hat{\sigma}_{m,n} e^{imx+iny} \\
 &= \hat{D}_{xx} \sum_{m,n} (im) \hat{\sigma}_{m,n} e^{i(m+k)x+i(n+l)y}.
 \end{aligned} \tag{6.4.7}$$

Now, substituting $m' = m + k$ and $n' = n + l$ into Eq. (6.4.7) yields

$$D_{xx} \frac{\partial \bar{\sigma}}{\partial x} = \hat{D}_{xx} \sum_{m'-k, n'-l} i(m' - k) \hat{\sigma}_{m'-k, n'-l} e^{im'x+in'y}, \tag{6.4.8}$$

and consequently,

$$\frac{\partial}{\partial x} \left(D_{xx} \frac{\partial \bar{\sigma}}{\partial x} \right) = \hat{D}_{xx} \sum_{m,n} -m(m - k) \hat{\sigma}_{m-k, n-l} e^{imx+iny}, \tag{6.4.9}$$

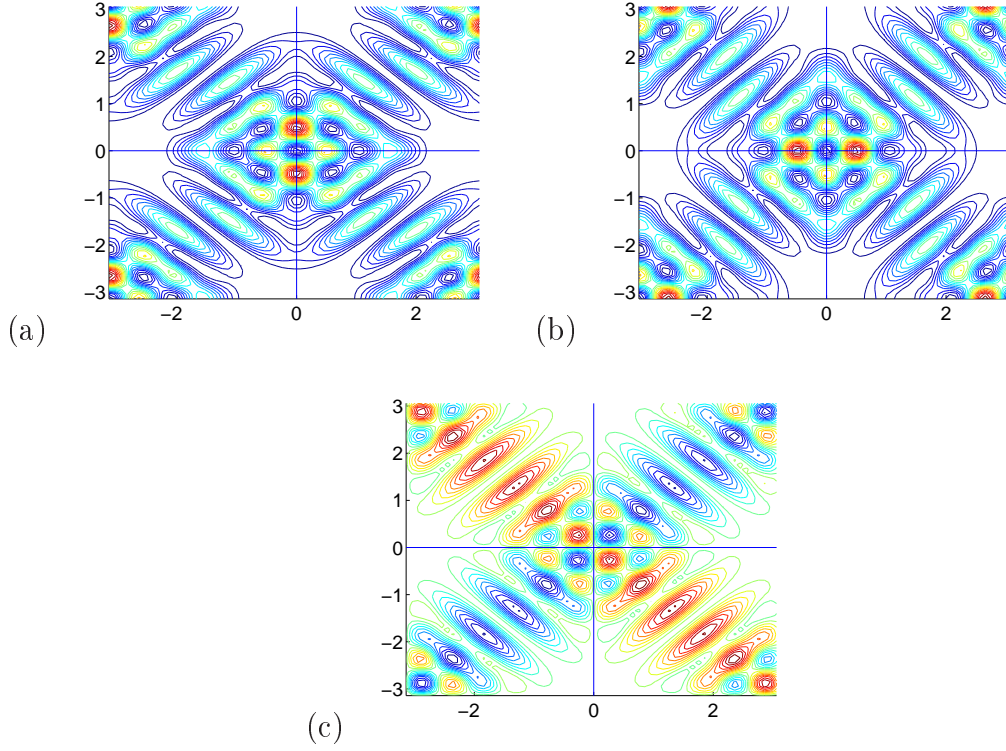


Figure 6.9: D_{xx} , (b) D_{yy} and (c) D_{xy} for the no-slip flow in a square domain.

Similarly, the other three terms on the right-hand side of Eq. (6.4.2) can be obtained,

$$\frac{\partial}{\partial x} \left(D_{xy} \frac{\partial \bar{\sigma}}{\partial y} \right) = \hat{D}_{xy} \sum_{m,n} -m(n-l) \hat{\sigma}_{m-k,n-l} e^{imx+iny}, \quad (6.4.10)$$

$$\frac{\partial}{\partial y} \left(D_{yx} \frac{\partial \bar{\sigma}}{\partial x} \right) = \hat{D}_{yx} \sum_{m,n} -n(m-k) \hat{\sigma}_{m-k,n-l} e^{imx+iny}, \quad (6.4.11)$$

and

$$\frac{\partial}{\partial y} \left(D_{yy} \frac{\partial \bar{\sigma}}{\partial y} \right) = \hat{D}_{yy} \sum_{m,n} -n(n-l) \hat{\sigma}_{m-k,n-l} e^{imx+iny}. \quad (6.4.12)$$

We will use these calculated D_{ij} to follow the scalar numerically in the whole square and compare pictures with the averaged σ from the full simulation.

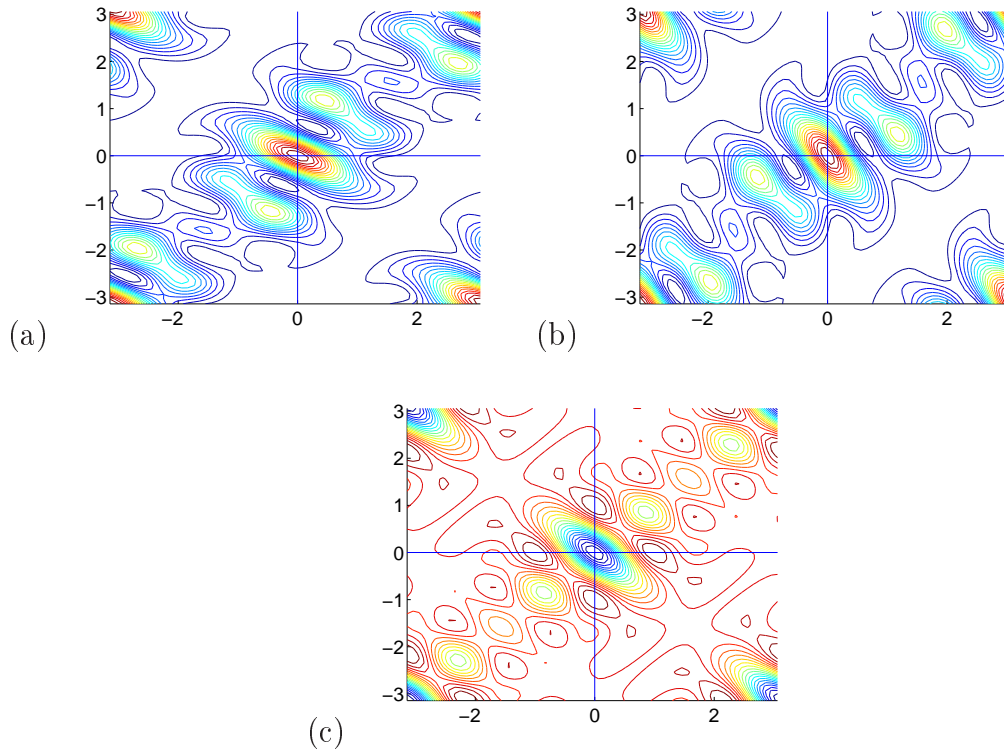


Figure 6.10: Plots of (a) D_{xx} , (b) D_{yy} and (c) D_{xy} for the no-slip flow in a plane layer domain.

Figure 6.8 shows plots of the D_{ij} components for the slip flow in the square domain given by (2.2.4), while for the no-slip flow (2.2.5) they are shown in Fig. 6.9. In the plane layer domain, these components are plotted for the no-slip flow (4.2.25) as seen in Fig. 6.10.

The question now is how do we average the field in the full numerical program which follows $\sigma(x, y, t)$ in a given random flow \mathbf{u} . The starting point to answer this question is to define the scalar field as

$$\sigma(x, y, t) = e^{iMx+iNy} \sum_{m,n} \hat{\sigma}_{m,n}(t) e^{imx+iny}. \quad (6.4.13)$$

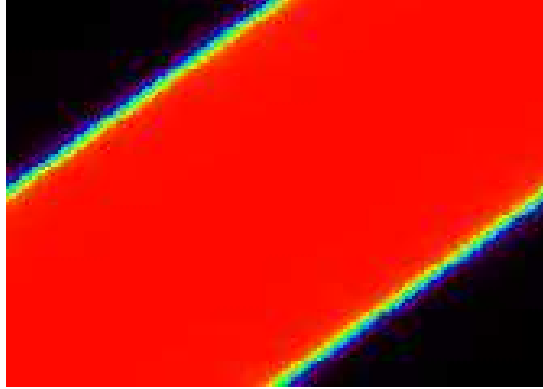


Figure 6.11: Averaging scalar field obtained numerically for the no-slip flow $\psi_{no-slip}$ with Dirichlet boundary condition in a plane layer with $M = N = 0.5$ and $\kappa = 0.001$ at $t = 250$.

with Bloch wavenumbers M, N . We take

$$\sigma_{max}(t) = \max_{x,y} |\sigma(x, y, t)|$$

and define the normalised scalar by dividing the scalar field $\sigma(x, y, t)$ by σ_{max} ,

$$\sigma_{norm}(x, y, t) = \sigma(x, y, t) / \sigma_{max}(t), \quad (6.4.14)$$

which takes values between -1 and 1. Now we average $\sigma_{norm}(x, y, t)$ as

$$\sigma_{ave}(x, y) = \frac{1}{Q} \sum_{m=1}^Q \sigma_{norm}(x, y, mT). \quad (6.4.15)$$

where the right-hand side of (6.4.15) is accumulated in the program. In Eq. (6.4.15), Q refers to the number of the flows and T to the time between each period. A typical value of Q is 10000 and of T is 0.1 in this simulation. The averaged scalar field for the flow no-slip with Dirichlet boundaries is seen in Fig.

6.11. As seen in this figure, the scalar values change rapidly in thin boundary layers that are translationally invariant confirming the theory.

We have compared the averaged scalar field $\bar{\sigma}$ from numerical simulations in a plane layer with theoretical one obtained in Chapter 5 by

$$\bar{\sigma} = \frac{2\sqrt{2}}{\pi} \bar{\sigma}_0 \kappa^{\frac{3}{4}} \mu^{\frac{1}{4}} \int_0^y \frac{dy}{\mu y^4 + \kappa}. \quad (6.4.16)$$

as shown in Fig. 6.12 using the rescaled co-ordinate $Y = y'(\mu/\kappa)^{1/4}$ or in Figs. 6.13 and 6.14 in terms of the y' co-ordinate. This comparison shows satisfactory agreement between the two as $\kappa \rightarrow 0$. In these figures, we can see that $\bar{\sigma} \rightarrow 1$ as Y increases and $\bar{\sigma} \rightarrow 0$ as $Y \rightarrow 0$. Figure 6.12 shows that $\bar{\sigma}_{num} \rightarrow \bar{\sigma}_{theo}$ as $\kappa \rightarrow 0$. Note the cross section in both figures 6.13 and 6.14 that is taken along the axis y' between the co-ordinates $y' = -\pi\sqrt{2}/2$ and $y' = 3\pi\sqrt{2}/2$.

6.5 Summary and discussion

In this part of the thesis we developed the theory of passive scalar decay by averaging over an ensemble of realisations of a random flow. This theory provides elegant insight into the scaling of the decay rates which confirm previous results, particularly of Lebedev & Turitsyn (2004) and Salman & Haynes (2007). We extend this theory to predict scaling laws for a variety of boundary conditions in the square and plane layer domains.

For a minor point, the new prediction of the effective diffusive tensor explains the discrepancies arising between theory and numerical simulations discussed by Salman & Haynes (2007). Applying stationary flows starting from a randomly chosen time t can cause such a disagreement between theory and computed results.

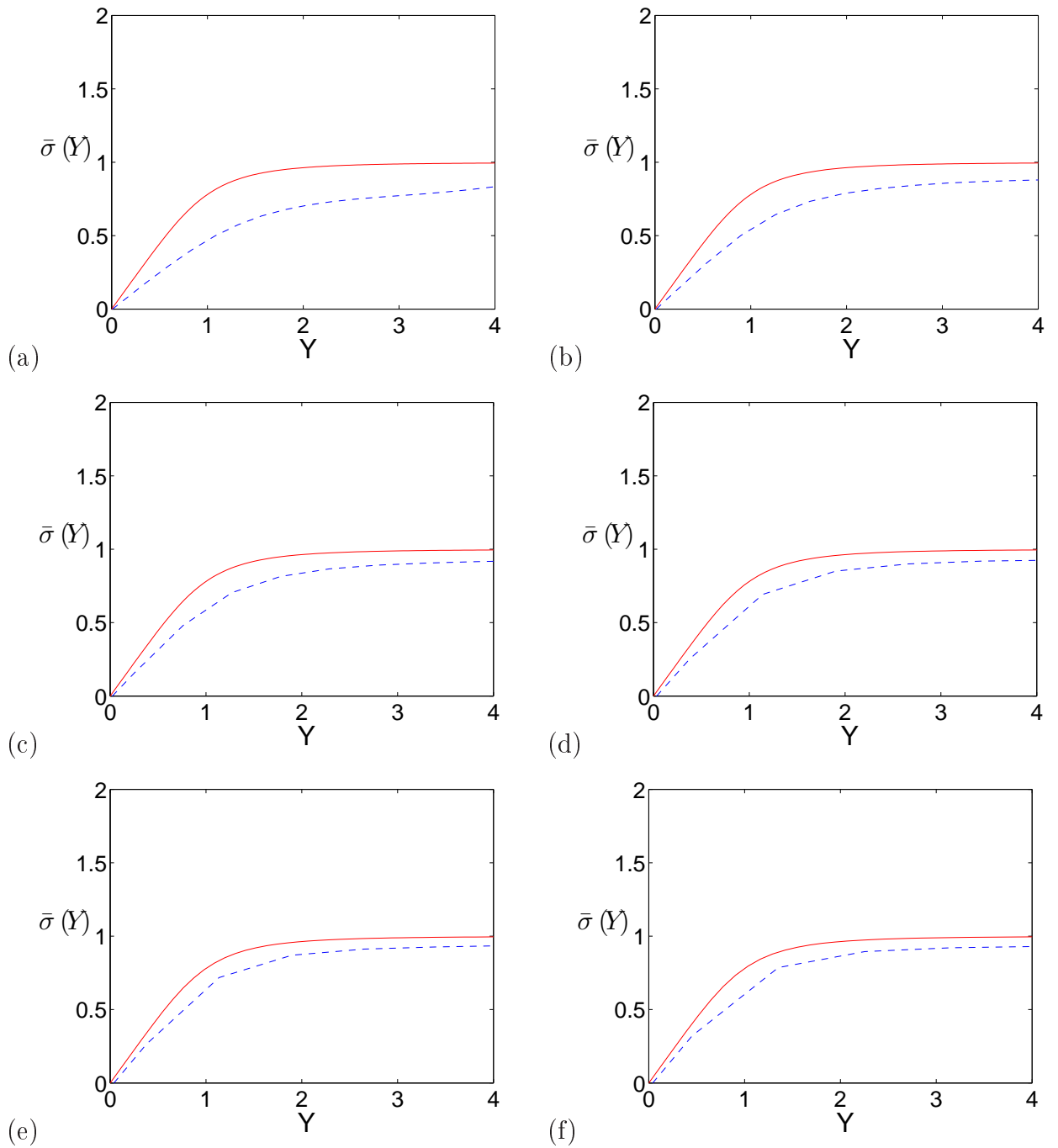


Figure 6.12: Plots of averaged $\bar{\sigma}_{theo}(Y)$ (solid) and $\bar{\sigma}_{num}(Y)$ (dashed), against Y ; $Y = y'(\mu/\kappa)^{1/4}$ corresponding to (a) $\kappa = 0.1$, (b) $\kappa = 0.02$, (c) $\kappa = 0.005$, (d) $\kappa = 0.001$, (e) $\kappa = 0.0002$ and (f) $\kappa = 0.0001$ for the no-slip flow with Dirichlet boundary condition. $\bar{\sigma}_{theo}$ and $\bar{\sigma}_{num}$ refers to the averaged scalar field obtained theoretically and numerically, respectively.

Further confirmation of this point introduced in Section §5.3 bears this out.

However, our key finding obtained for the flows considered in the corner regions in a square domain remains a valuable conclusion of this work. The slow release of the scalar from the corners to the body of the flow controls the decay of fluctuations for small diffusivity κ . Mixing being slower near the corners than on curved boundaries is an important result for applications.

With mixing within individual cells, the flux of heat across the boundary layers of the cells completely controls the transport of the scalar between the cells. We have observed the controlling role of such fluxes for scalar decay with Dirichlet boundary condition, which indicates decay rate γ_D for this boundary condition linked to $\kappa_{eff}(\kappa)$ for large-scale fields given by (6.3.30).

Part III

Approximating passive scalar evolution in polar co-ordinate system

7

PASSIVE SCALAR EVOLUTION IN POLAR CO-ORDINATE SYSTEM

7.1 Outline

As an extension to the work set out in the previous chapters of this thesis, we here explore the evolution of the passive scalar field addressed specifically in Chapter 3 and Chapter 4 by generating governing equations in a plane polar co-ordinate system (r, θ) . In fact, the corner in our square domain \mathcal{D} (Fig. 7.1) becomes a two dimensional wedge $0 \leq \theta \leq \pi/2$, $r > 0$, in the polar co-ordinate system. Our aim in this Chapter is to give a theoretical basis in the polar co-ordinate system to the $\kappa^{\frac{2}{3}}$ decay rate scaling ($\alpha = 2/3$) obtained in Chapter 3 and confirmed theoretically in Chapter 6. This scaling is obtained for the no-slip flow with Neumann boundary condition by analysing the decaying scalar concentration near corners, extending the results of Lebedev & Turitsyn (2004) and Salman & Haynes (2007). This is a local approximation to the concentration of scalar found with the Neumann

boundary condition for the no-slip problem (Fig. 3.10). In this case, comparison between the behaviour of the passive scalar and its decay rate in both systems, Cartesian and polar, allows us to extend to other corner flows.

The structure of this chapter is as follows. In Section 7.2 a general framework is introduced by reformulating essential equations describing the fluid flow of our models near a corner. Such equations form the basis of our work in this chapter. In Section 7.3 and Section 7.4 we analyse and formulate the evolution of the scalar field in terms of polar co-ordinates (r, θ) by decomposing the scalar field using a Fourier series in θ . In Section §7.5 we outline the numerical strategy used to solve our mathematical system and show numerical results for the solutions obtained in Section 7.4. A comparison of the principal decay rate in the case of the corner with the corresponding ones for the two-dimensional wedge is made in Section 7.6, with numerical results transferred into the Cartesian system presented in Section 7.7.

Thus, our plan is to use the corresponding relations between the Cartesian and polar co-ordinates. Highlighting the specific structure of flows near corners is the goal in order to pave the way for the well known Moffatt corner eddies described in the next chapter.

7.2 Governing equations for no-slip flow near a corner

In this section we provide the basis for generating our flow considered in Chapter 3 near to the corners in the polar co-ordinate system and restate the structure of

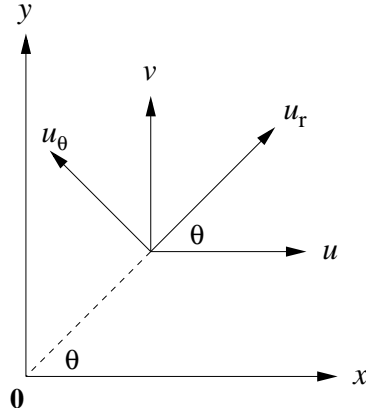


Figure 7.1: Velocity components with respect to (x, y) and (r, θ) axes.

the effective diffusivity tensor (5.3.13) addressed in Chapter 5 in such a system. In order to do so, we start by reformulating the basic equation for the no-slip flow $\psi_{no-slip}$ given by (3.2.44). It is known that, in the polar system the Cartesian co-ordinates x and y are formed as functions of the co-ordinates r and θ ,

$$x = r \cos \theta, \quad y = r \sin \theta. \quad (7.2.1)$$

The velocity components u and v as seen in Fig. 7.1 can be written with respect to their corresponding components in the polar co-ordinates u_r and u_θ as follows

$$u = u_r \cos \theta - u_\theta \sin \theta, \quad (7.2.2)$$

$$v = u_r \sin \theta + u_\theta \cos \theta, \quad (7.2.3)$$

or

$$u_r = u \cos \theta + v \sin \theta, \quad (7.2.4)$$

$$u_\theta = -u \sin \theta + v \cos \theta. \quad (7.2.5)$$

Chapter 7. PASSIVE SCALAR EVOLUTION IN POLAR CO-ORDINATE SYSTEM

In terms of a stream function ψ both components u_r and u_θ are formed by

$$u_r = \frac{1}{r} \frac{\partial \psi}{\partial \theta}, \quad u_\theta = -\frac{\partial \psi}{\partial r}. \quad (7.2.6)$$

Returning to the Cartesian co-ordinate system, our model of no-slip flow $\psi_{no-slip}$ considered in the square was given by

$$\psi(x, y, t) = \phi_{1,3}^2 \sin(\omega t + \chi(t)) + \phi_{3,1}^2 \cos(\omega t + \chi(t)). \quad (7.2.7)$$

As we have indicated in Chapter 6, the axes x and y are rotated and translated and the corner shown in Fig. 6.3 is $(x, y) = (0, -\pi)$ which becomes $(x', y') = (-\pi/\sqrt{2}, 0)$ or $(x'', y'') = (0, 0)$.

This procedure enabled us to obtain a simple approximation for such a flow,

$$\psi(x'', y'', t) = 9 x''^2 y''^2 \sin(\omega(t) + \chi(t)) + 9 x''^2 y''^2 \cos(\omega t + \chi(t)). \quad (7.2.8)$$

which is valid for $x'', y'' \ll 1$. In polar co-ordinates (r, θ) this stream function takes the form

$$\begin{aligned} \psi &= 9 (f(t) + g(t)) r^4 \cos^2 \theta \sin^2 \theta \\ &= \frac{9}{8} (f(t) + g(t)) r^4 (1 - \cos 4\theta). \end{aligned} \quad (7.2.9)$$

For convenience we set $f(t) = \sin(\omega(t) + \chi(t))$ and $g(t) = \cos(\omega t + \chi(t))$.

Consequently, in this case the components u_r and u_θ given in (7.2.6) will be found

as

$$u_r = \left(\frac{9}{2}\right) (f + g) r^3 \sin 4\theta, \quad (7.2.10)$$

$$u_\theta = -\left(\frac{9}{2}\right) (f + g) r^3 (1 - \cos 4\theta). \quad (7.2.11)$$

and the ensemble averages of products f and g are:

$$\langle f^2 \rangle = \frac{1}{2}, \quad \langle g^2 \rangle = \frac{1}{2}, \quad \langle fg \rangle = 0, \quad (7.2.12)$$

and so

$$\langle (f + g)^2 \rangle = 1. \quad (7.2.13)$$

If we now determine the components of the diffusivity tensor with respect to r and θ we see that

$$D_{rr} = \frac{\tau}{2} \langle u_r u_r \rangle = \mu r^6 \sin^2 4\theta, \quad (7.2.14)$$

$$D_{r\theta} = \frac{\tau}{2} \langle u_r u_\theta \rangle = -\mu r^6 \sin 4\theta (1 - \cos 4\theta), \quad (7.2.15)$$

$$D_{\theta\theta} = \frac{\tau}{2} \langle u_\theta u_\theta \rangle = \mu r^6 (1 - \cos 4\theta)^2. \quad (7.2.16)$$

Here we set $\mu = \left(\frac{9}{2}\right)^2 \left(\frac{\tau}{2}\right) = 6.48$ for convenience, where $\tau = 0.64$.

These terms are essential in writing the Cartesian components of D_{ij} as terms in

(r, θ) :

$$\begin{aligned}
 D_{xx} &= \langle uu \rangle \\
 &= \langle (u_r \cos \theta - u_\theta \sin \theta)^2 \rangle \\
 &= \langle u_r^2 \cos^2 \theta - 2u_r u_\theta \cos \theta \sin \theta + u_\theta^2 \sin^2 \theta \rangle \\
 &= \langle u_r^2 \rangle \cos^2 \theta - 2\langle u_r u_\theta \rangle \cos \theta \sin \theta + \langle u_\theta^2 \rangle \sin^2 \theta \\
 &= D_{rr} \cos^2 \theta - 2D_{r\theta} \sin \theta \cos \theta + D_{\theta\theta} \sin^2 \theta, \tag{7.2.17}
 \end{aligned}$$

with components in the polar co-ordinate system given by Eqs. (7.2.14), (7.2.15) and (7.2.16). Similarly,

$$D_{yy} = \langle vv \rangle = D_{rr} \sin^2 \theta + 2D_{r\theta} \sin \theta \cos \theta + D_{\theta\theta} \cos^2 \theta, \tag{7.2.18}$$

$$D_{xy} = \langle uv \rangle = D_{rr} \cos \theta \sin \theta - D_{r\theta}(\sin^2 \theta - \cos^2 \theta) - D_{\theta\theta} \sin \theta \cos \theta. \tag{7.2.19}$$

where the velocity components u and v are given by (7.2.2) and (7.2.3), respectively. These components (7.2.17), (7.2.18) and (7.2.19) of the effective diffusivity tensor will be used in the next section to obtain the equation of the scalar field evolution averaged in the polar co-ordinate system.

7.3 Approximating passive scalar evolution near to the corners

In this section, we consider the evolution of the scalar field $\bar{\sigma}$ and show how this evolution is transformed in the region near to a corner in terms of the polar co-ordinates. As we have shown in Chapter 5, the evolution of the passive scalar field

$\bar{\sigma}$ can be described by the equation

$$\frac{\partial \bar{\sigma}}{\partial t} = \frac{\partial}{\partial x_i} \left(D_{ij} \frac{\partial \bar{\sigma}}{\partial x_j} \right) + \kappa \nabla^2 \bar{\sigma}. \quad (7.3.1)$$

in the Cartesian co-ordinates $(x, y) = (x_1, x_2)$.

Crucially, in such a situation the question that can be introduced is what does this equation look like in the polar co-ordinate system?. To answer this question (i.e., transfer this equation into polar co-ordinates) we have in mind two ways of proceeding:

- (1) Re-deriving Eq. (7.3.1) starting in (r, θ) co-ordinates.
- (2) Transforming Eq. (7.3.1) from the Cartesian co-ordinates (x, y) to the polar co-ordinates (r, θ) .

To obtain a confirmation of our results, we will work with both procedures. Here we start with the first one.

Re-deriving the evolution equation of the passive scalar leads us to deal with the two terms on the right-hand side of Eq. (7.3.1). Starting with the first one, from our general discussion detailed in the first section of Chapter 5 we found that

$$\begin{aligned} \mathbf{u} \cdot \nabla (\mathbf{u} \cdot \nabla \sigma_0) &= \nabla \cdot (\mathbf{u} (\mathbf{u} \cdot \nabla \sigma_0)) \\ &= \frac{\partial}{\partial x_i} \left(u_i u_j \frac{\partial}{\partial x_j} \sigma_0 \right). \end{aligned} \quad (7.3.2)$$

It is known that in the polar co-ordinate system the gradient ∇ is defined by

$$\nabla = \hat{\mathbf{r}} \frac{\partial}{\partial r} + \frac{1}{r} \hat{\boldsymbol{\theta}} \frac{\partial}{\partial \theta}, \quad (7.3.3)$$

where the unit vectors $\hat{\mathbf{r}}$ and $\hat{\boldsymbol{\theta}}$ are defined with respect to the Cartesian axes as

$$\hat{\mathbf{r}} = (\cos \theta, \sin \theta), \quad \hat{\boldsymbol{\theta}} = (-\sin \theta, \cos \theta). \quad (7.3.4)$$

In this case the flow \mathbf{u} has the form

$$\mathbf{u} = u_r \hat{\mathbf{r}} + u_\theta \hat{\boldsymbol{\theta}}, \quad (7.3.5)$$

with the quantity $\mathbf{u} \cdot \nabla \bar{\sigma}$ determined as follows

$$\mathbf{u} \cdot \nabla \bar{\sigma} = u_r \frac{\partial \bar{\sigma}}{\partial r} + \frac{u_\theta}{r} \frac{\partial \bar{\sigma}}{\partial \theta}. \quad (7.3.6)$$

Similarly, the determination of $\mathbf{u}(\mathbf{u} \cdot \nabla \bar{\sigma})$ produces

$$\mathbf{u}(\mathbf{u} \cdot \nabla \bar{\sigma}) = u_r \hat{\mathbf{r}} \left(u_r \frac{\partial \bar{\sigma}}{\partial r} + \frac{u_\theta}{r} \frac{\partial \bar{\sigma}}{\partial \theta} \right) + u_\theta \hat{\boldsymbol{\theta}} \left(u_r \frac{\partial \bar{\sigma}}{\partial r} + \frac{u_\theta}{r} \frac{\partial \bar{\sigma}}{\partial \theta} \right). \quad (7.3.7)$$

Since

$$\nabla \cdot \mathbf{F} = \frac{1}{r} \frac{\partial}{\partial r} (r F_r) + \frac{1}{r} \frac{\partial}{\partial \theta} F_\theta. \quad (7.3.8)$$

If we put $\mathbf{F} = \mathbf{u}(\mathbf{u} \cdot \nabla \bar{\sigma})$, then from Eq. (7.3.7) it results that

$$F_r = \left(u_r^2 \frac{\partial \bar{\sigma}}{\partial r} + u_r \frac{u_\theta}{r} \frac{\partial \bar{\sigma}}{\partial \theta} \right), \quad (7.3.9)$$

and

$$F_\theta = \left(u_\theta u_r \frac{\partial \bar{\sigma}}{\partial r} + \frac{u_\theta^2}{r} \frac{\partial \bar{\sigma}}{\partial \theta} \right). \quad (7.3.10)$$

Therefore, substitution of (7.3.9) and (7.3.10) into (7.3.8) yields

$$\nabla \cdot (\mathbf{u} (\mathbf{u} \cdot \nabla \bar{\sigma})) = \frac{1}{r} \frac{\partial}{\partial r} \left(r u_r^2 \frac{\partial \bar{\sigma}}{\partial r} + u_r u_\theta \frac{\partial \bar{\sigma}}{\partial \theta} \right) + \frac{1}{r} \frac{\partial}{\partial \theta} \left(u_\theta u_r \frac{\partial \bar{\sigma}}{\partial r} + \frac{u_\theta^2}{r} \frac{\partial \bar{\sigma}}{\partial \theta} \right), \quad (7.3.11)$$

Consequently, averaging Eq. (7.3.11) over an ensemble of flows one can obtain

$$\langle \nabla \cdot (\mathbf{u} (\mathbf{u} \cdot \nabla \bar{\sigma})) \rangle = \frac{1}{r} \frac{\partial}{\partial r} \left(r D_{rr} \frac{\partial \bar{\sigma}}{\partial r} + D_{r\theta} \frac{\partial \bar{\sigma}}{\partial \theta} \right) + \frac{1}{r} \frac{\partial}{\partial \theta} \left(D_{r\theta} \frac{\partial \bar{\sigma}}{\partial r} + \frac{D_{\theta\theta}}{r} \frac{\partial \bar{\sigma}}{\partial \theta} \right). \quad (7.3.12)$$

For the second term on the right-hand side of Eq. (7.3.1) we have based on (7.3.3) and (7.3.8)

$$\begin{aligned} \nabla^2 \bar{\sigma} &= \nabla \cdot \nabla \bar{\sigma} \\ &= \nabla \cdot \left(\hat{\mathbf{r}} \frac{\partial \bar{\sigma}}{\partial r} + \hat{\boldsymbol{\theta}} \frac{1}{r} \frac{\partial \bar{\sigma}}{\partial \theta} \right) \\ &= \frac{1}{r} \frac{\partial}{\partial r} \left(r \frac{\partial \bar{\sigma}}{\partial r} \right) + \frac{1}{r^2} \frac{\partial^2 \bar{\sigma}}{\partial \theta^2}, \end{aligned} \quad (7.3.13)$$

and so

$$\kappa \nabla^2 \bar{\sigma} = \kappa \left(\frac{1}{r} \frac{\partial}{\partial r} \left(r \frac{\partial \bar{\sigma}}{\partial r} \right) + \frac{1}{r^2} \frac{\partial^2 \bar{\sigma}}{\partial \theta^2} \right). \quad (7.3.14)$$

In this case, the evolution of the scalar field can be described in the polar system by

$$\begin{aligned} \frac{\partial \bar{\sigma}}{\partial t} &= \frac{1}{r} \frac{\partial}{\partial r} \left(r D_{rr} \frac{\partial \bar{\sigma}}{\partial r} + D_{r\theta} \frac{\partial \bar{\sigma}}{\partial \theta} \right) \\ &+ \frac{1}{r} \frac{\partial}{\partial \theta} \left(D_{r\theta} \frac{\partial \bar{\sigma}}{\partial r} + \frac{1}{r} D_{\theta\theta} \frac{\partial \bar{\sigma}}{\partial \theta} \right) \\ &+ \kappa \left(\frac{1}{r} \frac{\partial}{\partial r} \left(r \frac{\partial \bar{\sigma}}{\partial r} \right) + \frac{1}{r^2} \frac{\partial^2 \bar{\sigma}}{\partial \theta^2} \right). \end{aligned} \quad (7.3.15)$$

Chapter 7. PASSIVE SCALAR EVOLUTION IN POLAR CO-ORDINATE SYSTEM

In order to confirm this result we have to work with the second method in which case the original equation (7.3.1) is transformed from the Cartesian co-ordinates (x, y) to the polar co-ordinates (r, θ) . According to Eq. (7.3.1), averaging the scalar field σ requires transforming both terms on the right-hand side of (7.3.1) into the polar co-ordinate system. We here start with the first term $\frac{\partial}{\partial x_i} \left(D_{ij} \frac{\partial \bar{\sigma}}{\partial x_j} \right)$. As we have shown in Chapter 5, this term is expanded as

$$\frac{\partial}{\partial x_i} \left(D_{ij} \frac{\partial \bar{\sigma}}{\partial x_j} \right) = \frac{\partial}{\partial x} \left(D_{xx} \frac{\partial \bar{\sigma}}{\partial x} \right) + \frac{\partial}{\partial x} \left(D_{xy} \frac{\partial \bar{\sigma}}{\partial y} \right) + \frac{\partial}{\partial y} \left(D_{yx} \frac{\partial \bar{\sigma}}{\partial x} \right) + \frac{\partial}{\partial y} \left(D_{yy} \frac{\partial \bar{\sigma}}{\partial y} \right).$$

To explore this equation we have from Eq. (7.2.1) that

$$\frac{\partial(x, y)}{\partial(r, \theta)} = \begin{pmatrix} \partial x / \partial r & \partial x / \partial \theta \\ \partial y / \partial r & \partial y / \partial \theta \end{pmatrix} = \begin{pmatrix} \cos \theta & -r \sin \theta \\ \sin \theta & r \cos \theta \end{pmatrix} \quad (7.3.16)$$

Therefore, by inverting we get

$$\frac{\partial(r, \theta)}{\partial(x, y)} = \begin{pmatrix} \partial r / \partial x & \partial r / \partial y \\ \partial \theta / \partial x & \partial \theta / \partial y \end{pmatrix}$$

or

$$\frac{\partial(r, \theta)}{\partial(x, y)} = r^{-1} \begin{pmatrix} r \cos \theta & r \sin \theta \\ -\sin \theta & \cos \theta \end{pmatrix}$$

Thus

$$\frac{\partial}{\partial x} = \frac{\partial r}{\partial x} \frac{\partial}{\partial r} + \frac{\partial \theta}{\partial x} \frac{\partial}{\partial \theta} = \cos \theta \frac{\partial}{\partial r} - \frac{\sin \theta}{r} \frac{\partial}{\partial \theta}, \quad (7.3.19)$$

Chapter 7. PASSIVE SCALAR EVOLUTION IN POLAR CO-ORDINATE SYSTEM

$$\frac{\partial}{\partial y} = \frac{\partial r}{\partial y} \frac{\partial}{\partial r} + \frac{\partial \theta}{\partial y} \frac{\partial}{\partial \theta} = \sin \theta \frac{\partial}{\partial r} + \frac{\cos \theta}{r} \frac{\partial}{\partial \theta}. \quad (7.3.20)$$

Now starting with the first term,

$$\begin{aligned} \frac{\partial}{\partial x} \left(D_{xx} \frac{\partial \bar{\sigma}}{\partial x} \right) &= \frac{\partial}{\partial x} \left[D_{xx} \left(\cos \theta \frac{\partial \bar{\sigma}}{\partial r} - \frac{\sin \theta}{r} \frac{\partial \bar{\sigma}}{\partial \theta} \right) \right] \\ &= \frac{\partial}{\partial x} \left[(D_{rr} \cos^2 \theta - 2D_{r\theta} \sin \theta \cos \theta + D_{\theta\theta} \sin^2 \theta) \right. \\ &\quad \left. \times \left(\cos \theta \frac{\partial \bar{\sigma}}{\partial r} - \frac{\sin \theta}{r} \frac{\partial \bar{\sigma}}{\partial \theta} \right) \right]. \end{aligned} \quad (7.3.21)$$

Let us define

$$F_1 = (D_{rr} \cos^2 \theta - 2D_{r\theta} \sin \theta \cos \theta + D_{\theta\theta} \sin^2 \theta) \times \left(\cos \theta \frac{\partial \bar{\sigma}}{\partial r} - \frac{\sin \theta}{r} \frac{\partial \bar{\sigma}}{\partial \theta} \right),$$

Then

$$\begin{aligned} \frac{\partial}{\partial x} \left(D_{xx} \frac{\partial \bar{\sigma}}{\partial x} \right) &= \frac{\partial F_1}{\partial x} \\ &= \cos \theta \frac{\partial F_1}{\partial r} - \frac{\sin \theta}{r} \frac{\partial F_1}{\partial \theta}. \end{aligned} \quad (7.3.22)$$

We retype this equation by assembling the coefficients of $\frac{\partial \bar{\sigma}}{\partial \theta}$ and $\frac{\partial \bar{\sigma}}{\partial r}$ from F_1 ,

$$\begin{aligned} \frac{\partial}{\partial x} \left(D_{xx} \frac{\partial \bar{\sigma}}{\partial x} \right) &= \cos \theta \frac{\partial}{\partial r} \left[(D_{rr} \cos^3 \theta - 2D_{r\theta} \sin \theta \cos^2 \theta + D_{\theta\theta} \sin^2 \theta \cos \theta) \frac{\partial \bar{\sigma}}{\partial r} \right. \\ &\quad \left. + \left(-D_{rr} \frac{\cos^2 \theta \sin \theta}{r} + 2D_{r\theta} \frac{\sin^2 \theta \cos \theta}{r} - D_{\theta\theta} \frac{\sin^3 \theta}{r} \right) \frac{\partial \bar{\sigma}}{\partial \theta} \right] \\ &\quad - \left(\frac{\sin \theta}{r} \right) \frac{\partial}{\partial \theta} \left[(D_{rr} \cos^3 \theta - 2D_{r\theta} \sin \theta \cos^2 \theta + D_{\theta\theta} \sin^2 \theta \cos \theta) \frac{\partial \bar{\sigma}}{\partial r} \right. \\ &\quad \left. + \left(-D_{rr} \frac{\cos^2 \theta \sin \theta}{r} + 2D_{r\theta} \frac{\sin^2 \theta \cos \theta}{r} - D_{\theta\theta} \frac{\sin^3 \theta}{r} \right) \frac{\partial \bar{\sigma}}{\partial \theta} \right]. \end{aligned} \quad (7.3.23)$$

Similar steps are done for the other three terms with

$$\begin{aligned}
 \frac{\partial}{\partial x} \left(D_{xy} \frac{\partial \bar{\sigma}}{\partial y} \right) &= \frac{\partial}{\partial x} \left[D_{xy} \left(\sin \theta \frac{\partial \bar{\sigma}}{\partial r} + \frac{\cos \theta}{r} \frac{\partial \bar{\sigma}}{\partial \theta} \right) \right] \\
 &= \frac{\partial}{\partial x} \left[(D_{rr} \cos \theta \sin \theta - D_{r\theta}(\sin^2 \theta - \cos^2 \theta) + D_{\theta\theta} \sin \theta \cos \theta) \right. \\
 &\quad \left. \times \left(\sin \theta \frac{\partial \bar{\sigma}}{\partial r} + \frac{\cos \theta}{r} \frac{\partial \bar{\sigma}}{\partial \theta} \right) \right], \tag{7.3.24}
 \end{aligned}$$

$$\begin{aligned}
 \frac{\partial}{\partial y} \left(D_{xy} \frac{\partial \bar{\sigma}}{\partial x} \right) &= \frac{\partial}{\partial y} \left[D_{xy} \left(\cos \theta \frac{\partial \bar{\sigma}}{\partial r} - \frac{\sin \theta}{r} \frac{\partial \bar{\sigma}}{\partial \theta} \right) \right] \\
 &= \frac{\partial}{\partial y} \left[(D_{rr} \cos \theta \sin \theta - D_{r\theta}(\sin^2 \theta - \cos^2 \theta) - D_{\theta\theta} \sin \theta \cos \theta) \right. \\
 &\quad \left. \times \left(\cos \theta \frac{\partial \bar{\sigma}}{\partial r} - \frac{\sin \theta}{r} \frac{\partial \bar{\sigma}}{\partial \theta} \right) \right], \tag{7.3.25}
 \end{aligned}$$

and

$$\begin{aligned}
 \frac{\partial}{\partial y} \left(D_{yy} \frac{\partial \bar{\sigma}}{\partial y} \right) &= \frac{\partial}{\partial y} \left[D_{yy} \left(\sin \theta \frac{\partial \bar{\sigma}}{\partial r} + \frac{\cos \theta}{r} \frac{\partial \bar{\sigma}}{\partial \theta} \right) \right] \\
 &= \frac{\partial}{\partial y} \left[(D_{rr} \sin^2 \theta + 2D_{r\theta} \sin \theta \cos \theta + D_{\theta\theta} \cos^2 \theta) \right. \\
 &\quad \left. \times \left(\sin \theta \frac{\partial \bar{\sigma}}{\partial r} + \frac{\cos \theta}{r} \frac{\partial \bar{\sigma}}{\partial \theta} \right) \right]. \tag{7.3.26}
 \end{aligned}$$

Summing the four quantities mentioned above and collecting the similar terms leads us to obtain

$$\begin{aligned}
 \frac{\partial}{\partial x_i} \left(D_{ij} \frac{\partial \bar{\sigma}}{\partial x_j} \right) &= \frac{1}{r} \frac{\partial}{\partial r} \left(r D_{rr} \frac{\partial \bar{\sigma}}{\partial r} + D_{r\theta} \frac{\partial \bar{\sigma}}{\partial \theta} \right) \\
 &\quad + \frac{1}{r} \frac{\partial}{\partial \theta} \left(D_{r\theta} \frac{\partial \bar{\sigma}}{\partial r} + \frac{1}{r} D_{\theta\theta} \frac{\partial \bar{\sigma}}{\partial \theta} \right). \tag{7.3.27}
 \end{aligned}$$

Similarly, transforming the second term on the right-hand side of (7.3.1) into (r, θ) co-ordinates yields

$$\kappa \nabla^2 \bar{\sigma} = \kappa \left(\frac{1}{r} \frac{\partial}{\partial r} \left(r \frac{\partial \bar{\sigma}}{\partial r} \right) + \frac{1}{r^2} \frac{\partial^2 \bar{\sigma}}{\partial \theta^2} \right). \quad (7.3.28)$$

Now by assembling Eqs. (7.3.27) and (7.3.28) and substituting into Eq. (7.3.1) we declare that the equation for the evolution of the average scalar field over time t can be given by

$$\begin{aligned} \frac{\partial \bar{\sigma}}{\partial t} &= \frac{1}{r} \frac{\partial}{\partial r} \left(r D_{rr} \frac{\partial \bar{\sigma}}{\partial r} + D_{r\theta} \frac{\partial \bar{\sigma}}{\partial \theta} \right) \\ &+ \frac{1}{r} \frac{\partial}{\partial \theta} \left(D_{r\theta} \frac{\partial \bar{\sigma}}{\partial r} + \frac{1}{r} D_{\theta\theta} \frac{\partial \bar{\sigma}}{\partial \theta} \right) \\ &+ \kappa \left(\frac{1}{r} \frac{\partial}{\partial r} \left(r \frac{\partial \bar{\sigma}}{\partial r} \right) + \frac{1}{r^2} \frac{\partial^2 \bar{\sigma}}{\partial \theta^2} \right). \end{aligned} \quad (7.3.29)$$

In the next section we will detail how the evolution of the scalar according to this equation can be simulated.

7.4 Simplifying the equation of averaged scalar field evolution

It is part of our aim in this work to solve the equation of the averaged scalar field given by (7.3.29), numerically. One of the possible ways to achieve this goal is using the Fourier series in θ of the quantity $\bar{\sigma}(r, \theta, t)$.

Chapter 7. PASSIVE SCALAR EVOLUTION IN POLAR CO-ORDINATE
SYSTEM

We consider the scalar field $\bar{\sigma}$ as being identified in terms of r and θ via

$$\bar{\sigma}(r, \theta, t) = \sum_{j=-\infty}^{\infty} \bar{\sigma}_j(r, t) e^{ij\theta}. \quad (7.4.1)$$

For simplicity, we drop the dependence on t in what follows. However, we consider the scalar field $\bar{\sigma}$ to be composed of modes with j a multiple of 4,

$$\bar{\sigma}(r, \theta) = \bar{\sigma}_0(r) + \bar{\sigma}_4(r) e^{4i\theta} + \bar{\sigma}_{-4}(r) e^{-4i\theta} + \bar{\sigma}_8(r) e^{8i\theta} + \bar{\sigma}_{-8}(r) e^{-8i\theta} + \dots \quad (7.4.2)$$

This special form ensures satisfying Neumann boundary condition for our flow near the corner. In fact, we use the following truncated version

$$\bar{\sigma}(r, \theta) = \bar{\sigma}_0(r) + \bar{\sigma}_4(r) e^{4i\theta} + \bar{\sigma}_{-4}(r) e^{-4i\theta} + \bar{\sigma}_8(r) e^{8i\theta} + \bar{\sigma}_{-8}(r) e^{-8i\theta}, \quad (7.4.3)$$

which can be expanded to the Fourier series including also $\bar{\sigma}_{12}$, $\bar{\sigma}_{16}$ and $\bar{\sigma}_{20}$,

$$\begin{aligned} \bar{\sigma}(r, \theta) = & \bar{\sigma}_0(r) + \bar{\sigma}_4(r) e^{4i\theta} + \bar{\sigma}_{-4}(r) e^{-4i\theta} + \bar{\sigma}_8(r) e^{8i\theta} + \bar{\sigma}_{-8}(r) e^{-8i\theta} + \bar{\sigma}_{12} e^{12i\theta} \\ & + \bar{\sigma}_{-12} e^{-12i\theta} + \bar{\sigma}_{16} e^{16i\theta} + \bar{\sigma}_{-16} e^{-16i\theta} + \bar{\sigma}_{20} e^{20i\theta} + \bar{\sigma}_{-20} e^{-20i\theta}. \end{aligned} \quad (7.4.4)$$

Later we will show how these quantities $\bar{\sigma}_0, \bar{\sigma}_4, \bar{\sigma}_{-4}, \bar{\sigma}_8, \dots, \bar{\sigma}_{-20}$ can be calculated. Under these considerations, the challenge now becomes how to reformulate the three terms on the right-hand side of Eq. (7.3.29) into terms of these components. However, in the next calculations, we will set μ to be 1 and later it will be scaled

out. We have shown that from Eq. (7.2.14), the term D_{rr} is written as

$$\begin{aligned} D_{rr} &= r^6 \sin^2 4\theta \\ &= r^6 \left(-\frac{1}{4}e^{8i\theta} + \frac{1}{2} - \frac{1}{4}e^{-8i\theta} \right). \end{aligned} \quad (7.4.5)$$

Consequently, the term $D_{rr} \frac{\partial \bar{\sigma}}{\partial r}$ can be expressed as

$$\begin{aligned} D_{rr} \frac{\partial \bar{\sigma}}{\partial r} &= r^6 \left(-\frac{1}{4}e^{8i\theta} + \frac{1}{2} - \frac{1}{4}e^{-8i\theta} \right) \\ &\quad \frac{\partial}{\partial r} \left(\bar{\sigma}_0(r) + \bar{\sigma}_4(r) e^{4i\theta} + \bar{\sigma}_{-4}(r) e^{-4i\theta} + \bar{\sigma}_8(r) e^{8i\theta} + \dots + \bar{\sigma}_{-20}(r) e^{-20i\theta} \right), \end{aligned} \quad (7.4.6)$$

which leads us to obtain

$$\begin{aligned}
 rD_{rr} \frac{\partial \bar{\sigma}}{\partial r} &= r^7 \left(-\frac{1}{4} \frac{\partial \bar{\sigma}_8}{\partial r} + \frac{1}{2} \frac{\partial \bar{\sigma}_0}{\partial r} - \frac{1}{4} \frac{\partial \bar{\sigma}_{-8}}{\partial r} \right) e^{0(i\theta)} \\
 &+ r^7 \left(\frac{1}{2} \frac{\partial \bar{\sigma}_4}{\partial r} - \frac{1}{4} \frac{\partial \bar{\sigma}_{-4}}{\partial r} - \frac{1}{4} \frac{\bar{\sigma}_{12}}{\partial r} \right) e^{4(i\theta)} \\
 &+ r^7 \left(\frac{1}{2} \frac{\partial \bar{\sigma}_{-4}}{\partial r} - \frac{1}{4} \frac{\partial \bar{\sigma}_4}{\partial r} - \frac{1}{4} \frac{\bar{\sigma}_{-12}}{\partial r} \right) e^{-4(i\theta)} \\
 &+ r^7 \left(\frac{1}{2} \frac{\partial \bar{\sigma}_8}{\partial r} - \frac{1}{4} \frac{\partial \bar{\sigma}_0}{\partial r} - \frac{1}{4} \frac{\bar{\sigma}_{16}}{\partial r} \right) e^{8(i\theta)} \\
 &+ r^7 \left(\frac{1}{2} \frac{\partial \bar{\sigma}_{-8}}{\partial r} - \frac{1}{4} \frac{\partial \bar{\sigma}_0}{\partial r} - \frac{1}{4} \frac{\bar{\sigma}_{-16}}{\partial r} \right) e^{-8(i\theta)} \\
 &+ r^7 \left(\frac{1}{2} \frac{\partial \bar{\sigma}_{12}}{\partial r} - \frac{1}{4} \frac{\partial \bar{\sigma}_4}{\partial r} - \frac{1}{4} \frac{\bar{\sigma}_{20}}{\partial r} \right) e^{12(i\theta)} \\
 &+ r^7 \left(\frac{1}{2} \frac{\partial \bar{\sigma}_{-12}}{\partial r} - \frac{1}{4} \frac{\partial \bar{\sigma}_{-4}}{\partial r} - \frac{1}{4} \frac{\bar{\sigma}_{-20}}{\partial r} \right) e^{-12(i\theta)} \\
 &+ r^7 \left(\frac{1}{2} \frac{\partial \bar{\sigma}_{16}}{\partial r} - \frac{1}{4} \frac{\partial \bar{\sigma}_8}{\partial r} \right) e^{16(i\theta)} \\
 &+ r^7 \left(\frac{1}{2} \frac{\partial \bar{\sigma}_{-16}}{\partial r} - \frac{1}{4} \frac{\partial \bar{\sigma}_{-8}}{\partial r} \right) e^{-16(i\theta)} \\
 &+ r^7 \left(\frac{1}{2} \frac{\partial \bar{\sigma}_{20}}{\partial r} - \frac{1}{4} \frac{\partial \bar{\sigma}_{12}}{\partial r} \right) e^{20(i\theta)} \\
 &+ r^7 \left(\frac{1}{2} \frac{\partial \bar{\sigma}_{-20}}{\partial r} - \frac{1}{4} \frac{\partial \bar{\sigma}_{-12}}{\partial r} \right) e^{-20(i\theta)}.
 \end{aligned} \tag{7.4.7}$$

Similarly for the term $D_{r\theta}$ we have

$$\begin{aligned}
 D_{r\theta} &= -r^6 \sin 4\theta (1 - \cos 4\theta) \\
 &= -\frac{r^6}{2i} \left(e^{4i\theta} - e^{-4i\theta} - \frac{1}{2} e^{8i\theta} + \frac{1}{2} e^{-8i\theta} \right).
 \end{aligned} \tag{7.4.8}$$

Chapter 7. PASSIVE SCALAR EVOLUTION IN POLAR CO-ORDINATE
SYSTEM

Therefore, one finds that

$$D_{r\theta} \frac{\partial \bar{\sigma}}{\partial \theta} = -\frac{r^6}{2i} \left(e^{4i\theta} - e^{-4i\theta} - \frac{1}{2}e^{8i\theta} + \frac{1}{2}e^{-8i\theta} \right). \\ (4i \bar{\sigma}_4 e^{i4\theta} - 4i \bar{\sigma}_{-4} e^{-4i\theta} + 8i \bar{\sigma}_8 e^{8i\theta} - 8i \bar{\sigma}_{-8} e^{-8i\theta} + \dots - 20i \bar{\sigma}_{-20} e^{-20i\theta}). \quad (7.4.9)$$

In fact, this can be written as

$$D_{r\theta} \frac{\partial \bar{\sigma}}{\partial \theta} = \begin{aligned} & -2r^6(-\bar{\sigma}_{-4} - \bar{\sigma}_4 + \bar{\sigma}_8 + \bar{\sigma}_{-8}) e^{0(i\theta)} \\ & - r^6(-4\bar{\sigma}_8 + \bar{\sigma}_{-4} + 3\bar{\sigma}_{12}) e^{4i\theta} \\ & - r^6(-4\bar{\sigma}_{-8} + \bar{\sigma}_4 + 3\bar{\sigma}_{-12}) e^{-4i\theta} \\ & - 2r^6(\bar{\sigma}_4 - 3\bar{\sigma}_{12} + 2\bar{\sigma}_{16}) e^{8i\theta} \\ & - 2r^6(\bar{\sigma}_{-4} - 3\bar{\sigma}_{-12} + 2\bar{\sigma}_{-16}) e^{-8i\theta} \\ & - r^6(4\bar{\sigma}_8 - 8\bar{\sigma}_{16} - \bar{\sigma}_4 + 5\bar{\sigma}_{20}) e^{12i\theta} \\ & - r^6(4\bar{\sigma}_{-8} - 8\bar{\sigma}_{-16} - \bar{\sigma}_{-4} + 5\bar{\sigma}_{-20}) e^{-12i\theta} \\ & - 2r^6(3\bar{\sigma}_{12} - 5\bar{\sigma}_{20} - \bar{\sigma}_8) e^{16i\theta} \\ & - 2r^6(3\bar{\sigma}_{-12} - 5\bar{\sigma}_{-20} - \bar{\sigma}_{-8}) e^{-16i\theta} \\ & - r^6(8\bar{\sigma}_{16} - 3\bar{\sigma}_{12}) e^{20i\theta} \\ & - r^6(8\bar{\sigma}_{-16} - 3\bar{\sigma}_{-12}) e^{-20i\theta}. \end{aligned} \quad (7.4.10)$$

Chapter 7. PASSIVE SCALAR EVOLUTION IN POLAR CO-ORDINATE
SYSTEM

For the term $\frac{\partial}{\partial \theta} \left(D_{r\theta} \frac{\partial \bar{\sigma}}{\partial r} \right)$ we have

$$D_{r\theta} \frac{\partial \bar{\sigma}}{\partial r} = -\frac{r^6}{2i} \left(e^{4i\theta} - e^{-4i\theta} - \frac{1}{2}e^{8i\theta} + \frac{1}{2}e^{-8i\theta} \right).$$

$$\frac{\partial}{\partial r} (\bar{\sigma}_0 + \bar{\sigma}_4 e^{i4\theta} + \bar{\sigma}_{-4} e^{-4i\theta} + \bar{\sigma}_8 e^{8i\theta} + \bar{\sigma}_{-8} e^{-8i\theta} + \dots + \bar{\sigma}_{-20} e^{-20i\theta}).$$

(7.4.11)

Consequently, in this case

$$\begin{aligned} \frac{1}{r} \frac{\partial}{\partial \theta} \left(D_{r\theta} \frac{\partial \bar{\sigma}}{\partial r} \right) &= -r^5 \left(2 \frac{\partial \bar{\sigma}_0}{\partial r} - 2 \frac{\partial \bar{\sigma}_8}{\partial r} - \frac{\partial \bar{\sigma}_{-4}}{\partial r} + \frac{\partial \bar{\sigma}_{12}}{\partial r} \right) e^{4i\theta} \\ &- r^5 \left(2 \frac{\partial \bar{\sigma}_0}{\partial r} - 2 \frac{\partial \bar{\sigma}_{-8}}{\partial r} - \frac{\partial \bar{\sigma}_4}{\partial r} + \frac{\partial \bar{\sigma}_{-12}}{\partial r} \right) e^{-4i\theta} \\ &- 2r^5 \left(2 \frac{\partial \bar{\sigma}_4}{\partial r} - \frac{\partial \bar{\sigma}_0}{\partial r} - 2 \frac{\partial \bar{\sigma}_{12}}{\partial r} + \frac{\partial \bar{\sigma}_{16}}{\partial r} \right) e^{8i\theta} \\ &- 2r^5 \left(2 \frac{\partial \bar{\sigma}_{-4}}{\partial r} - \frac{\partial \bar{\sigma}_0}{\partial r} - 2 \frac{\partial \bar{\sigma}_{-12}}{\partial r} + \frac{\partial \bar{\sigma}_{-16}}{\partial r} \right) e^{-8i\theta} \\ &- 3r^5 \left(2 \frac{\partial \bar{\sigma}_8}{\partial r} - 2 \frac{\partial \bar{\sigma}_{16}}{\partial r} - \frac{\partial \bar{\sigma}_4}{\partial r} + \frac{\partial \bar{\sigma}_{20}}{\partial r} \right) e^{12i\theta} \\ &- 3r^5 \left(2 \frac{\partial \bar{\sigma}_{-8}}{\partial r} - 2 \frac{\partial \bar{\sigma}_{-16}}{\partial r} - \frac{\partial \bar{\sigma}_{-4}}{\partial r} + \frac{\partial \bar{\sigma}_{-20}}{\partial r} \right) e^{-12i\theta} \\ &- 4r^5 \left(\frac{\partial \bar{\sigma}_8}{\partial r} - 2 \frac{\partial \bar{\sigma}_{20}}{\partial r} + 2 \frac{\partial \bar{\sigma}_{12}}{\partial r} \right) e^{16i\theta} \\ &- 4r^5 \left(\frac{\partial \bar{\sigma}_{-8}}{\partial r} - 2 \frac{\partial \bar{\sigma}_{-20}}{\partial r} + 2 \frac{\partial \bar{\sigma}_{-12}}{\partial r} \right) e^{-16i\theta} \\ &- 5r^5 \left(2 \frac{\partial \bar{\sigma}_{16}}{\partial r} - \frac{\partial \bar{\sigma}_{12}}{\partial r} \right) e^{20i\theta} \\ &- 5r^5 \left(2 \frac{\partial \bar{\sigma}_{-16}}{\partial r} - \frac{\partial \bar{\sigma}_{-12}}{\partial r} \right) e^{-20i\theta}. \end{aligned}$$

(7.4.12)

Finally, for the term $\frac{\partial}{\partial \theta} (D_{\theta\theta} \frac{\partial \bar{\sigma}}{\partial \theta})$ we get

$$\begin{aligned} D_{\theta\theta} &= r^6 (1 - \cos 4\theta)^2 \\ &= r^6 \left(\frac{1}{4} e^{8i\theta} - e^{4i\theta} + \frac{3}{2} - e^{-4i\theta} + \frac{1}{4} e^{-8i\theta} \right). \end{aligned} \quad (7.4.13)$$

and then

$$\begin{aligned} D_{\theta\theta} \frac{\partial \bar{\sigma}}{\partial \theta} &= r^6 \left(\frac{1}{4} e^{8i\theta} - e^{4i\theta} + \frac{3}{2} - e^{-4i\theta} + \frac{1}{4} e^{-8i\theta} \right) \\ &\quad (4i\bar{\sigma}_4 e^{4i\theta} - 4i\bar{\sigma}_{-4} e^{-4i\theta} + 8i\bar{\sigma}_8 e^{8i\theta} - 8i\bar{\sigma}_{-8} e^{-8i\theta} + \dots - 20i\bar{\sigma}_{-20} e^{-20i\theta}). \end{aligned} \quad (7.4.14)$$

This can be written as

$$\begin{aligned} \frac{1}{r} \frac{\partial}{\partial \theta} \left(\frac{1}{r} D_{\theta\theta} \frac{\partial \bar{\sigma}}{\partial \theta} \right) &= 4r^4 (\bar{\sigma}_{-4} - 6\bar{\sigma}_4 + 8\bar{\sigma}_8 - 3\bar{\sigma}_{12}) e^{4i\theta} \\ &+ 4r^4 (\bar{\sigma}_4 - 6\bar{\sigma}_{-4} + 8\bar{\sigma}_{-8} - 3\bar{\sigma}_{-12}) e^{-4i\theta} \\ &+ 32r^4 (\bar{\sigma}_4 - 3\bar{\sigma}_8 + 3\bar{\sigma}_{12} - \bar{\sigma}_{16}) e^{8i\theta} \\ &+ 32r^4 (\bar{\sigma}_{-4} - 3\bar{\sigma}_{-8} + 3\bar{\sigma}_{-12} - \bar{\sigma}_{-16}) e^{-8i\theta} \\ &+ 12r^4 (8\bar{\sigma}_8 - 12\bar{\sigma}_4 - 18\bar{\sigma}_{12} + 16\bar{\sigma}_{16} - 5\bar{\sigma}_{20}) e^{12i\theta} \\ &+ 12r^4 (8\bar{\sigma}_{-8} - 12\bar{\sigma}_{-4} - 18\bar{\sigma}_{-12} + 16\bar{\sigma}_{-16} - 5\bar{\sigma}_{-20}) e^{-12i\theta} \\ &+ 32r^4 (-\bar{\sigma}_8 + 6\bar{\sigma}_{12} - 12\bar{\sigma}_{16} + 10\bar{\sigma}_{20}) e^{16i\theta} \\ &+ 32r^4 (-\bar{\sigma}_{-8} + 6\bar{\sigma}_{-12} - 12\bar{\sigma}_{-16} + 10\bar{\sigma}_{-20}) e^{-16i\theta} \\ &+ 20r^4 (16\bar{\sigma}_{16} - 3\bar{\sigma}_{12} - 30\bar{\sigma}_{20}) e^{20i\theta} \\ &+ 20r^4 (16\bar{\sigma}_{-16} - 3\bar{\sigma}_{-12} - 30\bar{\sigma}_{-20}) e^{-20i\theta}. \end{aligned} \quad (7.4.15)$$

Similar steps can be done in transferring the two terms on the right-hand side of Eq. (7.3.28) into terms of $\bar{\sigma}_0, \bar{\sigma}_4, \bar{\sigma}_{-4}, \bar{\sigma}_8, \bar{\sigma}_{-8}, \dots, \bar{\sigma}_{20}$:

$$\begin{aligned}
 \kappa \left(\frac{1}{r} \frac{\partial}{\partial r} \left(r \frac{\partial \bar{\sigma}}{\partial r} \right) \right) &= \frac{\kappa}{r} \frac{\partial}{\partial r} \left(r \frac{\partial \bar{\sigma}_0}{\partial r} \right) e^{0(i\theta)} \\
 &+ \frac{\kappa}{r} \frac{\partial}{\partial r} \left(r \frac{\partial \bar{\sigma}_4}{\partial r} \right) e^{4i\theta} + \frac{\kappa}{r} \frac{\partial}{\partial r} \left(r \frac{\partial \bar{\sigma}_{-4}}{\partial r} \right) e^{-4i\theta} \\
 &+ \frac{\kappa}{r} \frac{\partial}{\partial r} \left(r \frac{\partial \bar{\sigma}_8}{\partial r} \right) e^{8i\theta} + \frac{\kappa}{r} \frac{\partial}{\partial r} \left(r \frac{\partial \bar{\sigma}_{-8}}{\partial r} \right) e^{-8i\theta} \\
 &+ \frac{\kappa}{r} \frac{\partial}{\partial r} \left(r \frac{\partial \bar{\sigma}_{12}}{\partial r} \right) e^{12i\theta} + \frac{\kappa}{r} \frac{\partial}{\partial r} \left(r \frac{\partial \bar{\sigma}_{-12}}{\partial r} \right) e^{-12i\theta} \\
 &+ \frac{\kappa}{r} \frac{\partial}{\partial r} \left(r \frac{\partial \bar{\sigma}_{16}}{\partial r} \right) e^{16i\theta} + \frac{\kappa}{r} \frac{\partial}{\partial r} \left(r \frac{\partial \bar{\sigma}_{-16}}{\partial r} \right) e^{-16i\theta} \\
 &+ \frac{\kappa}{r} \frac{\partial}{\partial r} \left(r \frac{\partial \bar{\sigma}_{20}}{\partial r} \right) e^{20i\theta} + \frac{\kappa}{r} \frac{\partial}{\partial r} \left(r \frac{\partial \bar{\sigma}_{-20}}{\partial r} \right) e^{-20i\theta}.
 \end{aligned} \tag{7.4.16}$$

also

$$\begin{aligned}
 \kappa \left(\frac{1}{r^2} \frac{\partial^2 \bar{\sigma}}{\partial \theta^2} \right) &= -\frac{16\kappa}{r^2} (\bar{\sigma}_4 e^{4i\theta} + \bar{\sigma}_{-4} e^{-4i\theta} + 4\bar{\sigma}_8 e^{8i\theta} + 4\bar{\sigma}_{-8} e^{-8i\theta} \\
 &+ 9\bar{\sigma}_{12} e^{12i\theta} + 9\bar{\sigma}_{-12} e^{-12i\theta} + 16\bar{\sigma}_{16} e^{16i\theta} + 16\bar{\sigma}_{-16} e^{-16i\theta} \\
 &+ 25\bar{\sigma}_{20} e^{20i\theta} + 25\bar{\sigma}_{-20} e^{-20i\theta}).
 \end{aligned} \tag{7.4.17}$$

According to Eq. (7.4.4), determination of the averaging scalar field $\bar{\sigma}$ requires determination of the quantities; $\bar{\sigma}_0, \bar{\sigma}_4, \bar{\sigma}_{-4}, \bar{\sigma}_8, \dots, \bar{\sigma}_{-20}$. In such a case, for example, the average $\bar{\sigma}_0$ can be obtained by assembling the coefficients of $e^{0(i\theta)}$ that arise in the equations (7.4.7), (7.4.10), (7.4.12), (7.4.15), (7.4.16) and (7.4.17). Similar procedures are done for the other terms $\bar{\sigma}_4, \bar{\sigma}_{-4}, \bar{\sigma}_8, \dots$ and $\bar{\sigma}_{20}$.

Before doing so, it is important to note that due to the evenness of the scalar field $\bar{\sigma}$ under changing from (θ) to $(-\theta)$, $\bar{\sigma}_4$ will equal $\bar{\sigma}_{-4}$ and so $\bar{\sigma}_8$ will equal $\bar{\sigma}_{-8}, \dots$

Chapter 7. PASSIVE SCALAR EVOLUTION IN POLAR CO-ORDINATE SYSTEM

Using this, one can simplify the averages mentioned above as follows:

$$\frac{\partial \bar{\sigma}_0}{\partial t} = \frac{1}{r} \frac{\partial}{\partial r} \left[\frac{1}{2} r^7 \left(\frac{\partial \bar{\sigma}_0}{\partial r} - \frac{\partial \bar{\sigma}_8}{\partial r} \right) - 4r^6(\bar{\sigma}_8 - \bar{\sigma}_4) + \kappa \left(r \frac{\partial \bar{\sigma}_0}{\partial r} \right) \right]. \quad (7.4.18)$$

also for $\bar{\sigma}_4$

$$\begin{aligned} \frac{\partial \bar{\sigma}_4}{\partial t} &= \frac{1}{r} \frac{\partial}{\partial r} \left[\frac{1}{4} r^7 \left(\frac{\partial \bar{\sigma}_4}{\partial r} - \frac{\partial \bar{\sigma}_{12}}{\partial r} \right) - r^6(\bar{\sigma}_4 - 4\bar{\sigma}_8 + 3\bar{\sigma}_{12}) + \kappa \left(r \frac{\partial \bar{\sigma}_4}{\partial r} \right) \right] \\ &- r^5 \left(2 \frac{\partial \bar{\sigma}_0}{\partial r} - 2 \frac{\partial \bar{\sigma}_8}{\partial r} - \frac{\partial \bar{\sigma}_4}{\partial r} + \frac{\partial \bar{\sigma}_{12}}{\partial r} \right) \\ &+ 4r^4(8\bar{\sigma}_8 - 5\bar{\sigma}_4 - 3\bar{\sigma}_{12}) \\ &- \frac{16}{r^2} \kappa \bar{\sigma}_4. \end{aligned} \quad (7.4.19)$$

Similarly, for $\bar{\sigma}_8$

$$\begin{aligned} \frac{\partial \bar{\sigma}_8}{\partial t} &= \frac{1}{r} \frac{\partial}{\partial r} \left[\frac{1}{4} r^7 \left(2 \frac{\partial \bar{\sigma}_8}{\partial r} - \frac{\partial \bar{\sigma}_0}{\partial r} - \frac{\partial \bar{\sigma}_{16}}{\partial r} \right) - 2r^6(\bar{\sigma}_4 - 3\bar{\sigma}_{12} + 2\bar{\sigma}_{16}) + \kappa \left(r \frac{\partial \bar{\sigma}_8}{\partial r} \right) \right] \\ &- 2r^5 \left(2 \frac{\partial \bar{\sigma}_4}{\partial r} - 2 \frac{\partial \bar{\sigma}_{12}}{\partial r} - \frac{\partial \bar{\sigma}_0}{\partial r} + \frac{\partial \bar{\sigma}_{16}}{\partial r} \right) \\ &+ 32r^4(\bar{\sigma}_4 - 3\bar{\sigma}_8 + 3\bar{\sigma}_{12} - \bar{\sigma}_{16}) \\ &- \frac{64}{r^2} \kappa \bar{\sigma}_8 \end{aligned} \quad (7.4.20)$$

and

$$\begin{aligned}
\frac{\partial \bar{\sigma}_{12}}{\partial t} &= \frac{1}{r} \frac{\partial}{\partial r} \left[\frac{1}{4} r^7 \left(-\frac{\partial \bar{\sigma}_4}{\partial r} + 2 \frac{\partial \bar{\sigma}_{12}}{\partial r} - \frac{\partial \bar{\sigma}_{20}}{\partial r} \right) - r^6 (4\bar{\sigma}_8 - 8\bar{\sigma}_{16} - \bar{\sigma}_4 + 5\bar{\sigma}_{20}) \right. \\
&\quad \left. + \kappa \left(r \frac{\partial \bar{\sigma}_{12}}{\partial r} \right) \right] \\
&\quad - 3r^5 \left(2 \frac{\partial \bar{\sigma}_8}{\partial r} - 2 \frac{\partial \bar{\sigma}_{16}}{\partial r} - \frac{\partial \bar{\sigma}_4}{\partial r} + \frac{\partial \bar{\sigma}_{20}}{\partial r} \right) \\
&\quad + 12r^4 (8\bar{\sigma}_8 - 12\bar{\sigma}_4 - 18\bar{\sigma}_{12} + 16\bar{\sigma}_{16} - 5\bar{\sigma}_{20}) \\
&\quad - \frac{144}{r^2} \kappa \bar{\sigma}_{12}, \tag{7.4.21}
\end{aligned}$$

$$\begin{aligned}
\frac{\partial \bar{\sigma}_{16}}{\partial t} &= \frac{1}{r} \frac{\partial}{\partial r} \left[\frac{1}{4} r^7 \left(2 \frac{\partial \bar{\sigma}_{16}}{\partial r} - \frac{\partial \bar{\sigma}_8}{\partial r} \right) - 2r^6 (3\bar{\sigma}_{12} - 5\bar{\sigma}_{20} - \bar{\sigma}_8) + \kappa \left(r \frac{\partial \bar{\sigma}_{16}}{\partial r} \right) \right] \\
&\quad - 4r^5 \left(\frac{\partial \bar{\sigma}_8}{\partial r} - 2 \frac{\partial \bar{\sigma}_{20}}{\partial r} + 2 \frac{\partial \bar{\sigma}_{12}}{\partial r} \right) \\
&\quad + 32r^4 (-\bar{\sigma}_8 + 6\bar{\sigma}_{12} - 12\bar{\sigma}_{16} + 10\bar{\sigma}_{20}) \\
&\quad - \frac{256}{r^2} \kappa \bar{\sigma}_{16}. \tag{7.4.22}
\end{aligned}$$

Finally,

$$\begin{aligned}
\frac{\partial \bar{\sigma}_{20}}{\partial t} &= \frac{1}{r} \frac{\partial}{\partial r} \left[\frac{1}{4} r^7 \left(2 \frac{\partial \bar{\sigma}_{20}}{\partial r} - \frac{\partial \bar{\sigma}_{12}}{\partial r} \right) - r^6 (8\bar{\sigma}_{16} - 3\bar{\sigma}_{12}) + \kappa \left(r \frac{\partial \bar{\sigma}_{20}}{\partial r} \right) \right] \\
&\quad - 5r^5 \left(2 \frac{\partial \bar{\sigma}_{16}}{\partial r} - \frac{\partial \bar{\sigma}_{12}}{\partial r} \right) \\
&\quad + 20r^4 (16\bar{\sigma}_{16} - 3\bar{\sigma}_{12} - 30\bar{\sigma}_{20}) \\
&\quad - \frac{400}{r^2} \kappa \bar{\sigma}_{20}. \tag{7.4.23}
\end{aligned}$$

7.5 Numerical framework

In Section §7.4 we have identified that one possible way to show the evolution of the averaged scalar fields and obtain the corresponding solution profiles based on (7.3.29) for the Eqs. (7.4.18), (7.4.19), (7.4.20), (7.4.21), (7.4.22) and (7.4.23) is using the Fourier series for the quantities $\bar{\sigma}_0, \bar{\sigma}_4, \bar{\sigma}_{-4}, \bar{\sigma}_8, \bar{\sigma}_{-8}, \dots$ and $\bar{\sigma}_{20}$. Our attention in this section then concerns with outlining the methodology and numerical strategy used to obtain these solutions and the subsequent analysis and classification of the model output. In Section §7.5.1 we explain the numerical code that solves the mathematical problem (7.3.29). We describe how to track these solutions in time and how we visualise the results by restoring the structure presented by (7.3.1). As an illustrative example we introduce in Section §7.5.2 an analysis of the solution profile of the scalar field $\bar{\sigma}_0$ given by Eq. (7.4.18).

7.5.1 Methodology

One suitable way to solve the mathematical problem (7.3.29) is using a PDE solver called **pdepe** in Matlab that solves diffusion-type PDEs in one space variable and time, i.e., $u(x, t)$. The routine **pdepe** assumes a general form of the parabolic equation

$$c \left(x, t, u, \frac{\partial u}{\partial x} \right) \frac{\partial u}{\partial t} = x^{-m} \frac{\partial}{\partial x} \left(x^m f \left(x, t, u, \frac{\partial u}{\partial x} \right) \right) + s \left(x, t, u, \frac{\partial u}{\partial x} \right) \quad (7.5.1)$$

Here m is a parameter that can be 0, 1 or 2. In our application, we have r replacing x and then a parameter $m = 1$. The function c is normally just $c = 1$, but the program is designed to cope with more general cases. The s term is designed

to cope with problems where there is a source term. Additionally, the boundary conditions must be in the standard form

$$p(x, t, u) + q(x, t) f \left(x, t, u, \frac{\partial u}{\partial x} \right) = 0 \quad (7.5.2)$$

where f is the same f as occurs in the differential equation, and the initial condition at time $t = t_0$ is of the form

$$u(x, t_0) = u_0(x) \quad (7.5.3)$$

We have written this for a scalar $u(x, t)$, but **pdepe** can handle a vector \mathbf{u} and so a vector of PDEs to solve, as we have.

7.5.2 Identifying the mathematical problem

In light of the above remarks, in this section, we reformulate the mathematical problem (7.3.29) into one over the interval $0 \leq r \leq R$. We first have chosen a set of initial conditions at $t = 0$:

$$\bar{\sigma}_0 = \exp(-r^2), \quad \bar{\sigma}_4 = r \exp(-r^2), \quad (7.5.4)$$

$$\bar{\sigma}_8 = r \exp(-r^2), \quad \bar{\sigma}_{12} = r \exp(-r^2), \quad (7.5.5)$$

$$\bar{\sigma}_{16} = r \exp(-r^2), \quad \bar{\sigma}_{20} = r \exp(-r^2). \quad (7.5.6)$$

These initial conditions are chosen to be very simple. The reason for this is clearly seen in Fig. 7.4 as the transient decay obtained at earlier times corresponding to these conditions is eliminated, while scalar continues decaying exponentially at

large times. Next we set up the boundary conditions to be

$$\frac{\partial \bar{\sigma}_0}{\partial r}(0) = 0, \quad \bar{\sigma}_4(0) = \bar{\sigma}_8(0) = \bar{\sigma}_{12}(0) = \bar{\sigma}_{16}(0) = \bar{\sigma}_{20}(0) = 0 \quad (7.5.7)$$

and

$$\bar{\sigma}_0(R) = \bar{\sigma}_4(R) = \bar{\sigma}_8(R) = \bar{\sigma}_{12}(R) = \bar{\sigma}_{16}(R) = \bar{\sigma}_{20}(R) = 0 \quad (7.5.8)$$

Looking at equations (7.5.7) and (7.5.8) and building on Eq. (7.5.2), we can specify both p and q at both boundaries to be as follows.

At the left boundary:

$$p = (0, \quad \bar{\sigma}_4, \quad \bar{\sigma}_8, \quad \bar{\sigma}_{12}, \quad \bar{\sigma}_{16}, \quad \bar{\sigma}_{20}), \quad (7.5.9)$$

$$q = (1, \quad 0, \quad 0, \quad 0, \quad 0, \quad 0). \quad (7.5.10)$$

and at the right boundary:

$$p = (\bar{\sigma}_0, \quad \bar{\sigma}_4, \quad \bar{\sigma}_8, \quad \bar{\sigma}_{12}, \quad \bar{\sigma}_{16}, \quad \bar{\sigma}_{20}), \quad (7.5.11)$$

$$q = (0, \quad 0, \quad 0, \quad 0, \quad 0, \quad 0). \quad (7.5.12)$$

In the next section we will apply this strategy and show numerical results for the averaged scalar fields mentioned before.

7.5.3 Numerical solutions and results

Note that our numerical solutions are obtained with $\kappa = \mu = 1$ (see the next section). Now, based on the strategy discussed above, we first present some snapshots for the evolution of the averaged scalar fields based on (7.3.29) and resulting from

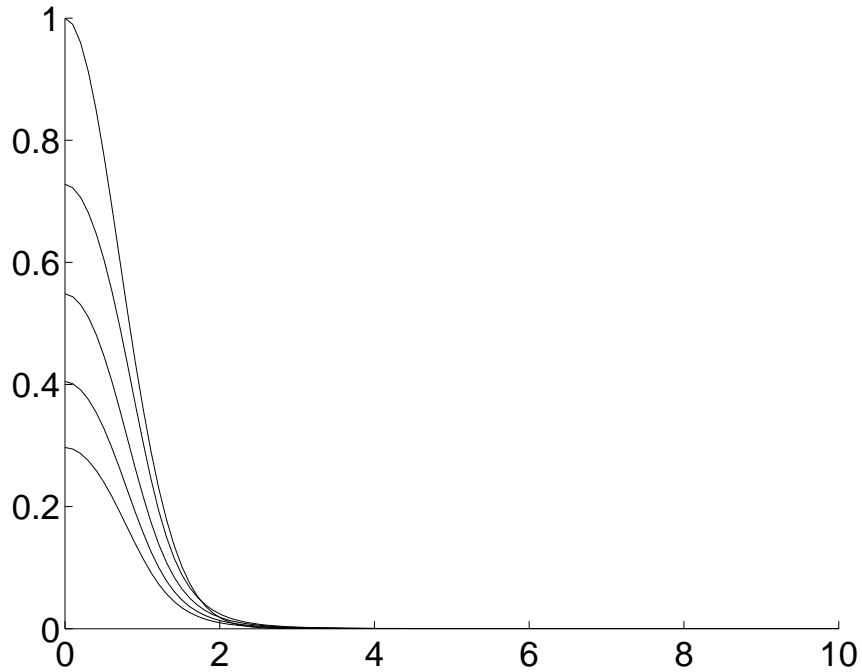


Figure 7.2: Solution profiles computed for averaged scalar field $\bar{\sigma}_0(r, t)$ against r based on (7.3.29) and resulting from (7.7.1) at different times; $0 \leq t \leq 4$ with 201 r -meshpoints between 0 and 10.

(7.4.3) or rather (7.7.1). Figure 7.2 shows solution profiles of the averaged scalar field $\bar{\sigma}_0(r, t)$ with a three-mode truncation resulting from (7.7.1) and computed at different times for $t \in [0, 4]$. Solution profile of $\bar{\sigma}_0(r, t)$ at $t = 0.3$ can be seen in Fig. 7.3. Furthermore, the evolution of averaged scalar field $\bar{\sigma}_0$ has a transient decay at earlier times, turning to an exponential one as time increases as seen in Fig. 7.4. The fit slope in this case is 3.1 as measured by **Matlab**. Other solution profiles of averaged scalar fields $\bar{\sigma}_4$ and $\bar{\sigma}_8$ are shown in Fig. 7.5 and Fig. 7.6, respectively.

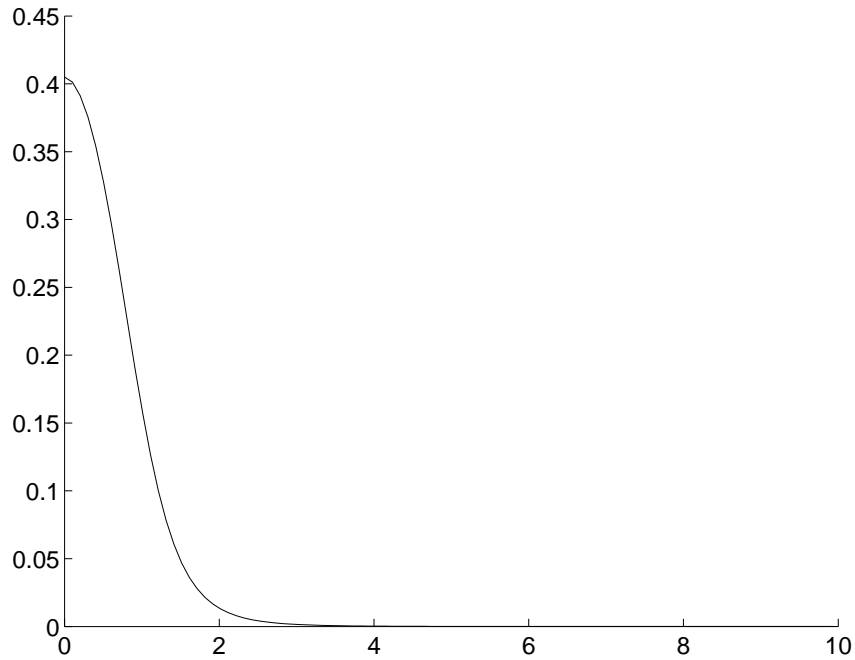


Figure 7.3: Solution profile computed for the averaged scalar field $\bar{\sigma}_0(r, t)$ against r based on (7.3.29) with the three-mode truncation resulting from (7.7.1) at $t=0.3$ with 201 r -meshpoints between 0 and 10.

7.6 Decay rate near a sharp corner with $\alpha = \pi/4$

Motivated by our key observation obtained in Chapter 3 for the no-slip flow $\psi_{no-slip}$ considered in the square domain with Neumann scalar boundary condition we proceed with further investigation of the scaling behaviour of the decay in such a flow in the polar co-ordinate system. The challenge in this section is to establish the theoretical form of the decay rate of this flow in terms of diffusivity κ and μ . As we have shown in Chapter 5, the structure of the evolution of the scalar field is governed by Eq. (7.3.1), where D_{ij} denotes the effective diffusivity tensor. We can now restate this formula to be in a simple form. However, the D_{ij} components shown in Section §7.2 are given by equations (7.2.14), (7.2.15) and (7.2.16). These

Chapter 7. PASSIVE SCALAR EVOLUTION IN POLAR CO-ORDINATE SYSTEM

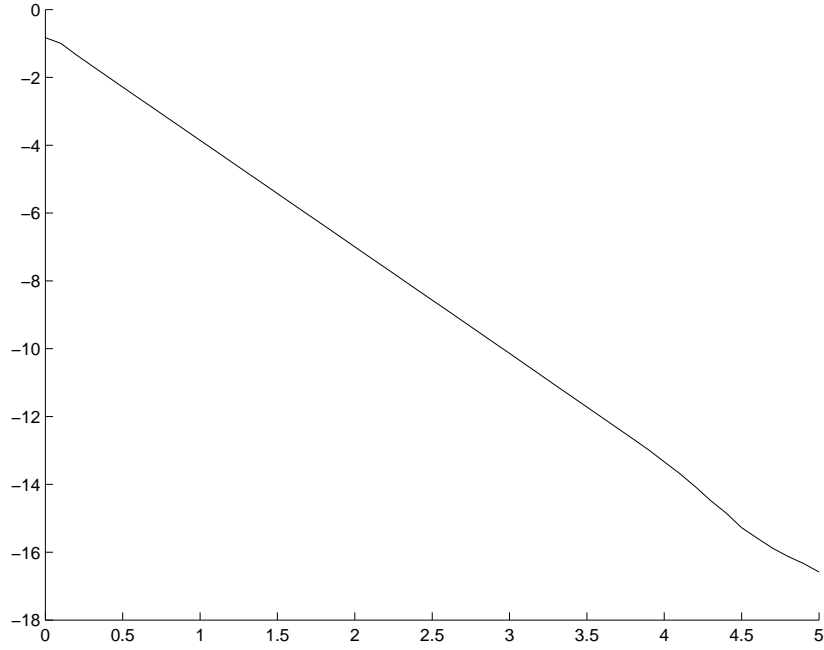


Figure 7.4: Plot of $\log \bar{\sigma}(r, t)$ at $r = 0.45$ against time t ; $0 \leq t \leq 5$ with 201 r -meshpoints between 0 and 10 for the no-slip flow $\psi_{no-slip}$ with Neumann boundary condition. The fit slope C_D is 3.1.

equations subsequently can be in general rewritten as

$$D_{ij} = \mu r^6 F_{ij}(\theta) \tag{7.6.1}$$

Now, equation (7.3.1) takes the form

$$\frac{\partial \bar{\sigma}}{\partial t} = \frac{\partial}{\partial x_i} \left(\mu r^6 F_{ij}(\theta) \frac{\partial \bar{\sigma}}{\partial x_j} \right) + \kappa \nabla^2 \bar{\sigma}. \tag{7.6.2}$$

Moreover, if we restate the scales to be

$$r = a r', \quad x_i = a x'_i, \quad t = b t'. \tag{7.6.3}$$

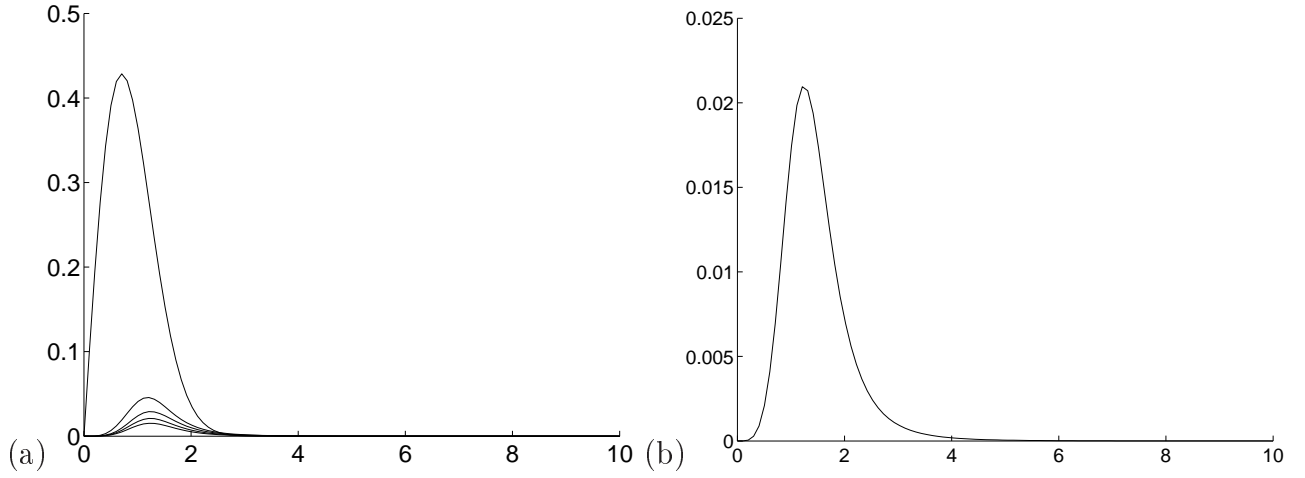


Figure 7.5: Solution profile based on (7.3.29) with the three-mode truncation resulting from (7.7.1) and computed for the averaged scalar field $\bar{\sigma}_4(r, t)$ against r ; panel (a) at different times $0 \leq t \leq t_{max}$; $t_{max}=4$ and (b) at $t=0.3$ with 201 r -meshpoints between 0 and 10.

then, Eq. (7.6.2) turns to

$$\left(\frac{1}{b}\right) \frac{\partial \bar{\sigma}}{\partial t'} = \left(\frac{1}{a}\right) \frac{\partial}{\partial x'_i} \left(\mu a^6 r'^6 F_{ij}(\theta) \frac{1}{a} \frac{\partial \bar{\sigma}}{\partial x'_j} \right) + \left(\frac{\kappa}{a^2}\right) \nabla'^2 \bar{\sigma}. \quad (7.6.4)$$

To simplify this situation we multiply both sides of Eq. (7.6.4) by $\left(\frac{a^2}{\kappa}\right)$ to get

$$\frac{a^2}{\kappa} \left(\frac{1}{b}\right) \frac{\partial \bar{\sigma}}{\partial t'} = \frac{\partial}{\partial x'_i} \left(\frac{\mu}{\kappa} a^6 r'^6 F_{ij}(\theta) \frac{\partial \bar{\sigma}}{\partial x'_j} \right) + \nabla'^2 \bar{\sigma}. \quad (7.6.5)$$

More simplification is obtained by the suitable choice

$$a^6 = \frac{\kappa}{\mu}, \quad \frac{a^2}{\kappa} \left(\frac{1}{b}\right) = 1. \quad (7.6.6)$$

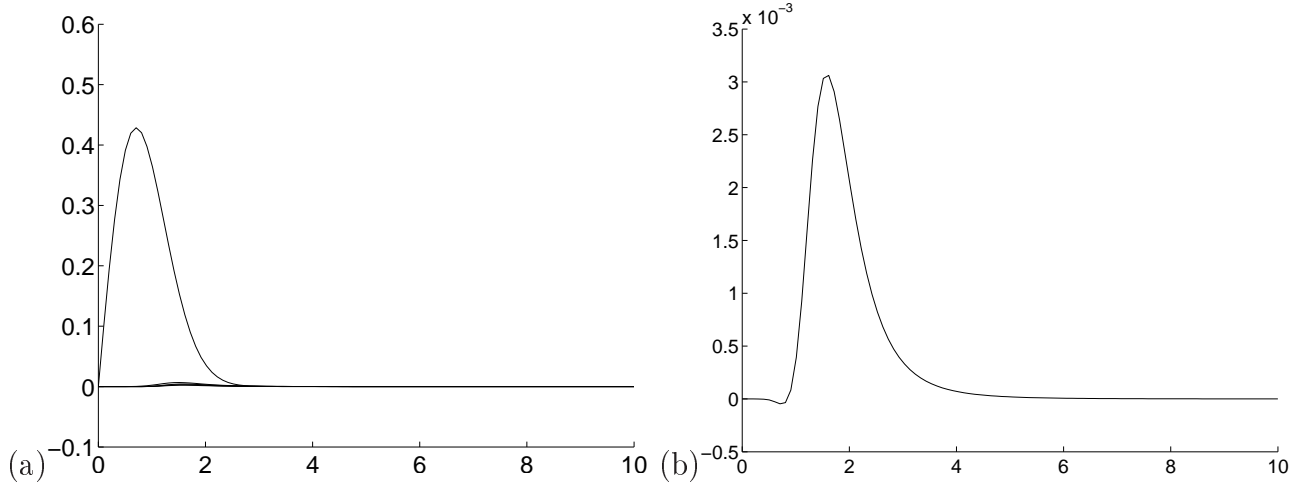


Figure 7.6: Solution profile based on (7.3.29) with the three-mode truncation resulting from (7.7.1) and computed for the averaged scalar field $\bar{\sigma}_8(r, t)$ against r ; panel (a) at different times $0 \leq t \leq t_{max}$; $t_{max}=4$ and (b) at $t=0.3$ with 201 r -meshpoints between 0 and 10. The vertical axis is scaled by 10^{-3} in (b).

where $b = \kappa^{-\frac{2}{3}} \mu^{-\frac{1}{3}}$ is yielded.

The choice (7.6.6) reflects Eq. (7.6.5) into a simpler one in terms of (r', θ) ,

$$\frac{\partial \bar{\sigma}}{\partial t'} = \frac{\partial}{\partial x'_i} \left(r'^6 F_{ij}(\theta) \frac{\partial \bar{\sigma}}{\partial x'_j} \right) + \nabla'^2 \bar{\sigma}. \quad (7.6.7)$$

This equation can be solved numerically for exponential decay γ' as an eigenvalue problem with a no-flux boundary condition to give the solution in the form

$$\bar{\sigma} \propto e^{-\gamma' t'}, \quad (7.6.8)$$

From our above discussion we have specified that

$$\gamma' = C_D, \quad t' = \frac{t}{b}. \quad (7.6.9)$$

Chapter 7. PASSIVE SCALAR EVOLUTION IN POLAR CO-ORDINATE SYSTEM

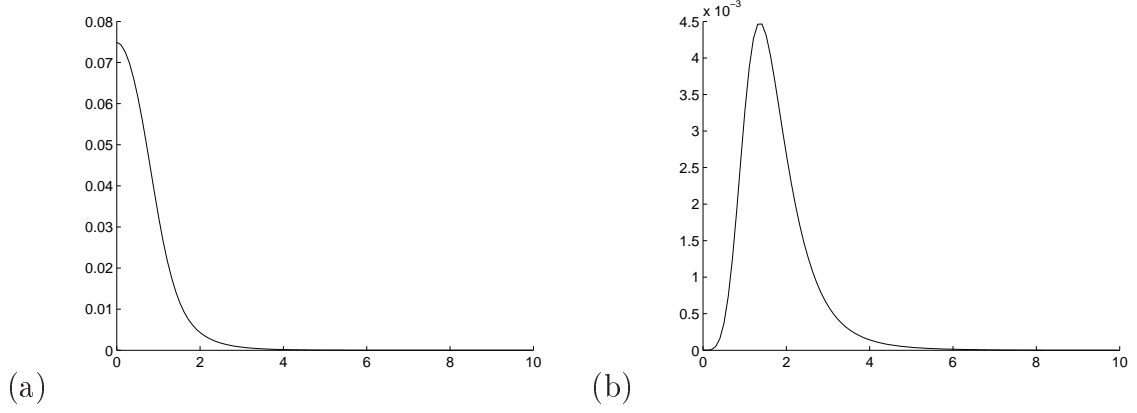


Figure 7.7: Solution profile based on (7.3.29) with the six-mode truncation resulting from (7.7.2) and computed for the averaged scalar field (a) $\bar{\sigma}_0(r, t)$ and (b) $\bar{\sigma}_4(r, t)$ against r at $t=0.9$ with 201 r -meshpoints between 0 and 10. The vertical axis is scaled by 10^{-3} in (b).

Therefore, with these scales, Eq. (7.6.8) is re-expressed by

$$\bar{\sigma} \propto e^{-C_D t/b}, \quad (7.6.10)$$

where $b = \kappa^{-\frac{2}{3}} \mu^{-\frac{1}{3}}$. In this case, we can write the solution (7.6.10) in terms of κ and μ ,

$$\begin{aligned} \bar{\sigma} &= e^{-C_D t (\kappa^{\frac{2}{3}} \mu^{\frac{1}{3}})} \\ &= e^{-\gamma t}. \end{aligned} \quad (7.6.11)$$

where the long-time exponential decay rate is identified with

$$\gamma(\kappa) = C_D \kappa^{\frac{2}{3}} \mu^{\frac{1}{3}}. \quad (7.6.12)$$

In fact, the picture drawn above suggests now the question of how good is the agreement between theory and the full numerical simulation. Here, we emphasise

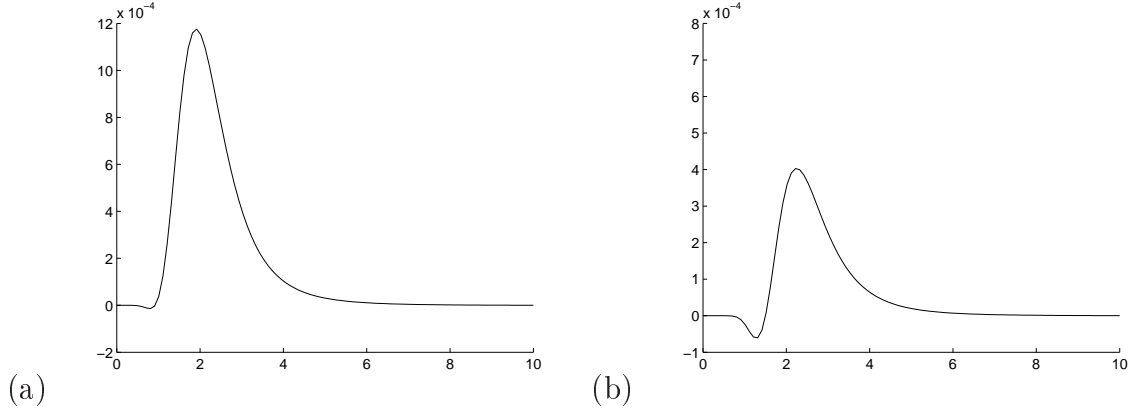


Figure 7.8: Solution profile based on (7.3.29) with the six-mode truncation resulting from (7.7.2) and computed for the averaged scalar field (a) $\bar{\sigma}_8(r,t)$ and (b) $\bar{\sigma}_{12}(r,t)$ against r at $t=0.9$ with 201 r -meshpoints between 0 and 10. The vertical axis in both panels is scaled by 10^{-4} .

that the central point which we need to keep sight of, is that the result (7.6.12) of exponential scale of $\alpha = 2/3$ is an excellent confirmation for our result obtained numerically and theoretically in Chapter 3 and Chapter 6, respectively for the no-slip flow $\psi_{no-slip}$ with Neumann boundary condition. Moreover, such agreement is good for the same flow by comparing this theoretical prediction of $\mu = \left(\frac{81}{4}\right) \left(\frac{\tau}{2}\right) = 6.48$ with the numerical result obtained in Chapter 3.

Figure 7.10 shows good agreement between theory and related simulation of the no-slip flow with Neumann boundary condition in the square domain. In this figure, both approximations (7.7.1) and (7.7.2) are observed very close to each other. This observation supports our approach of truncating a Fourier series expansion. However, better agreement is shown in Fig. 7.11 where the two approximations clearly can be visualised. In this figure, the numerical result appears to be closer to the approximation given by Eq. (7.7.2) (where $C_D \simeq 2.885$) than to that based on (7.7.1); $C_D \simeq 3.1$. Plots for solution profiles based on (7.3.29) with a six-mode truncation resulting from (7.7.2) are shown in Figs. 7.7, 7.8 and 7.9 for averaged

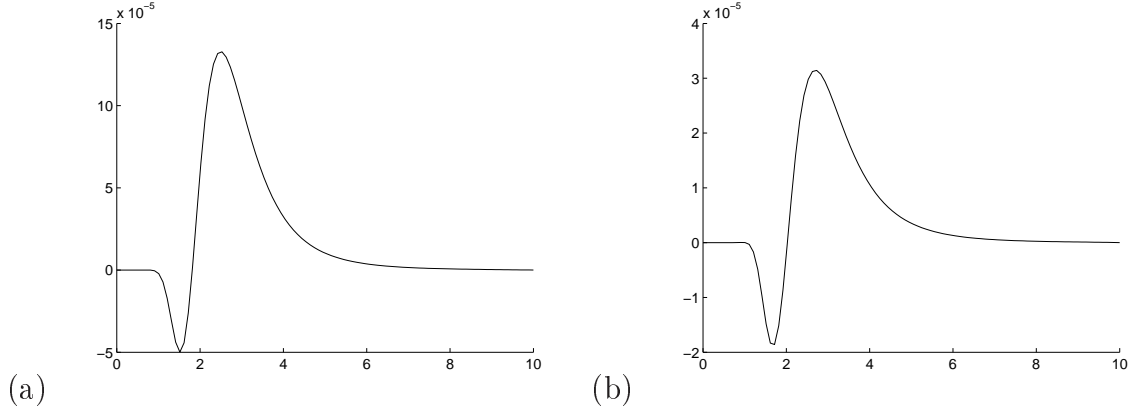


Figure 7.9: Solution profile based on (7.3.29) with the six-mode truncation resulting from (7.7.2) and computed for the averaged scalar field (a) $\bar{\sigma}_{16}(r, t)$ and (b) $\bar{\sigma}_{20}(r, t)$ against r at $t=0.9$ with 201 r -meshpoints between 0 and 10. The vertical axis in both panels is scaled by 10^{-5} .

scalar fields $(\bar{\sigma}_0, \bar{\sigma}_4)$, $(\bar{\sigma}_8, \bar{\sigma}_{12})$ and $(\bar{\sigma}_{16}, \bar{\sigma}_{20})$, respectively.

7.7 Transforming the polar co-ordinate results into the Cartesian co-ordinates

It is aim of this section to obtain further confirmation for our results derived in the last section in terms of polar co-ordinates. In order to do so, we have to transform these results into the Cartesian co-ordinates from polar ones.

As we have discussed in Section §7.4, in the region near to the corners, the evolution of the scalar field of the no-slip flow $\psi_{no-slip}$ with Neumann boundary condition is approximated via a three-mode truncation,

$$\begin{aligned} \bar{\sigma}(r, \theta) = & \bar{\sigma}_0(r, \theta) + \bar{\sigma}_4(r, \theta)(2 \cos 4\theta) \\ & + \bar{\sigma}_8(r, \theta)(2 \cos 8\theta). \end{aligned} \quad (7.7.1)$$

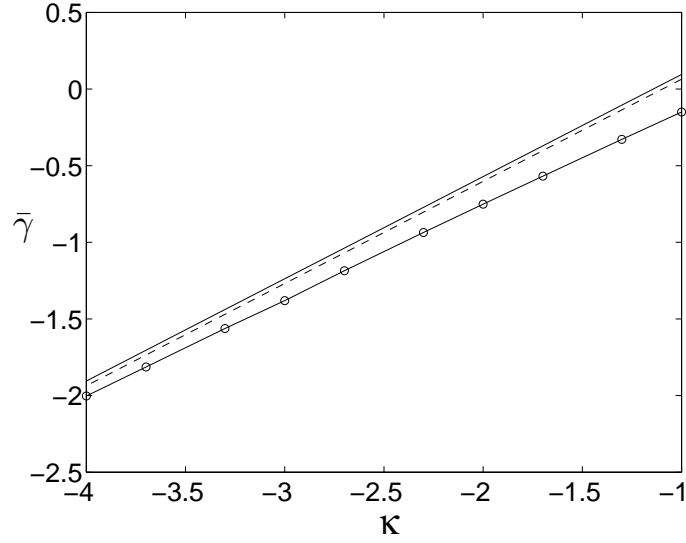


Figure 7.10: Plot of $\log \gamma(\kappa)$ against κ for the no-slip flow $\psi_{no-slip}$ with Neumann boundary condition. Numerical result is given by markers (solid line with circles) and theoretical results from (7.6.12) approximated via three-mode truncation are solid and six-mode truncation (dashed).

This approximation is expanded to a six-mode truncation involving the averages $\bar{\sigma}_{12}$, $\bar{\sigma}_{16}$ and $\bar{\sigma}_{20}$

$$\begin{aligned} \bar{\sigma}(r, \theta) = & \bar{\sigma}_0(r, \theta) + \bar{\sigma}_4(r, \theta)(2 \cos 4\theta) \\ & + \bar{\sigma}_8(r, \theta)(2 \cos 8\theta) + \dots + \bar{\sigma}_{20}(r, \theta)(2 \cos 20\theta). \end{aligned} \quad (7.7.2)$$

Figure 7.12 shows how this scalar field distribution is represented in the Cartesian co-ordinate system. As we see in this figure, both approximations (7.7.1) and (7.7.2) have a good representation, particularly, in panel (b) where the approximation is based on all the quantities $\bar{\sigma}_0, \bar{\sigma}_4, \dots, \bar{\sigma}_{20}$. In this panel, the distribution has a pointed shape which extends along x and y axes, while in panel (a) the approximation is based only on the quantities $\bar{\sigma}_0, \bar{\sigma}_4$ and $\bar{\sigma}_8$.

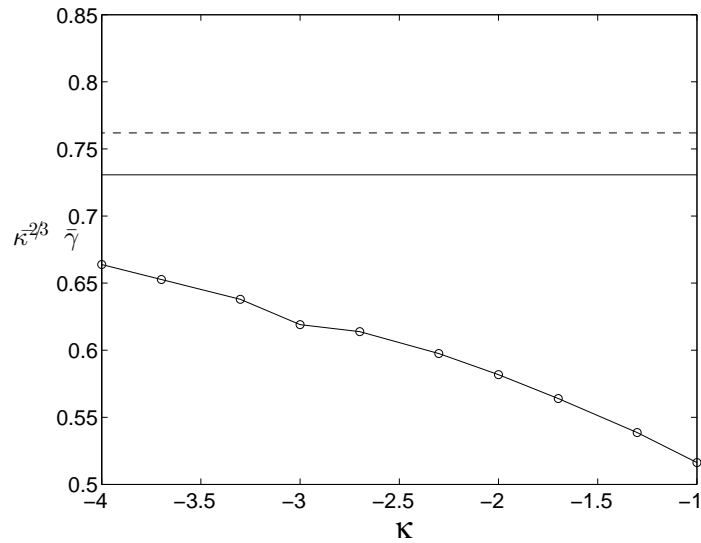
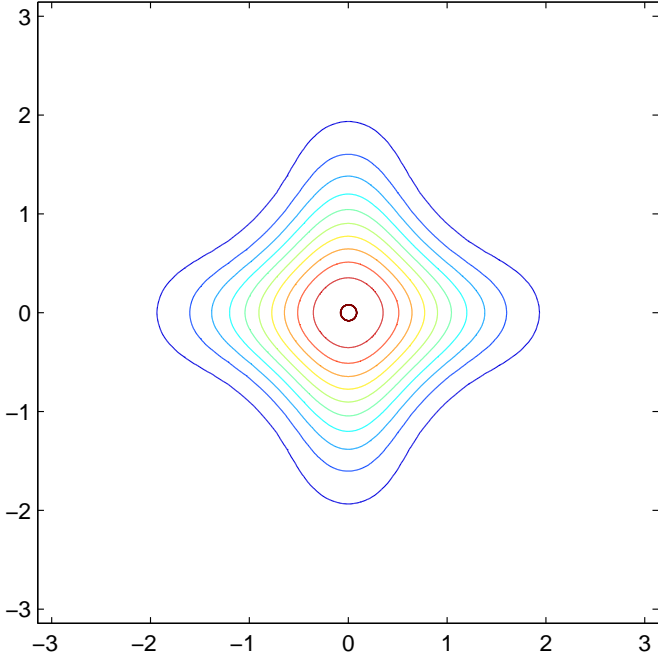


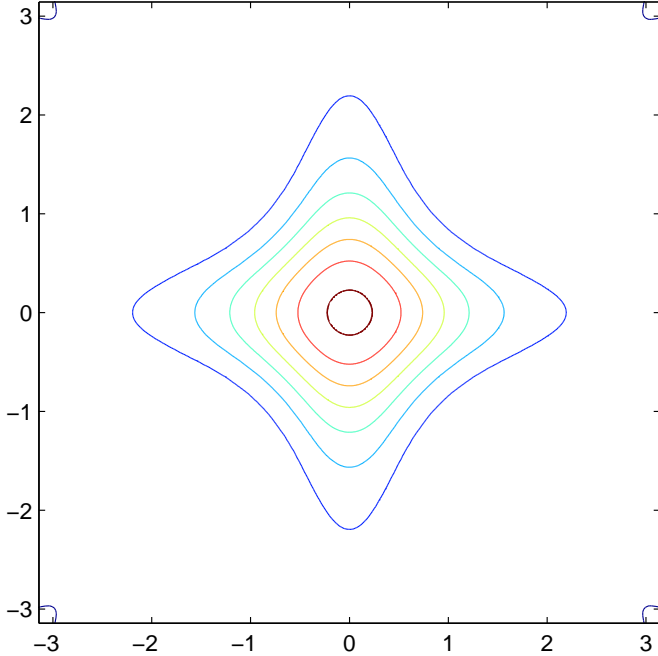
Figure 7.11: Plot of scaled decay rate $\kappa^{-\frac{2}{3}}\bar{\gamma}(\kappa)$ against κ for the no-slip flow $\psi_{no-slip}$ with Neumann boundary condition. Numerical result is given by markers (solid line with circles) and approximations of theoretical results via six-mode truncation are solid and three-mode truncation (dashed).

7.8 Summary

In this chapter, we have given a theoretical basis for our decay rate scaling ($\alpha = 2/3$) obtained in Chapter 3 for the no-slip flow with Neumann boundary condition. Using Fourier series in θ , the evolution of the scalar field of the flow has been analysed near to the corners in terms of the polar co-ordinates (r, θ) . These fields are approximated with three and six mode truncations and displayed in the Cartesian system. As we have noted, the higher truncation gives a more pointed scalar field picture, but the decay rates are almost the same.



(a)



(b)

Figure 7.12: Plots of the scalar distribution of the no-slip flow $\psi_{no-slip}$ with Neumann boundary condition near to the corners in the Cartesian co-ordinate system. Panel (a) shows the approximation of such distribution resulting from (7.7.1), while in (b) it is given by (7.7.2). 232

8

CONNECTION TO MOFFATT EDDIES

8.1 Outline

The seminal work of Moffatt (1964) has been the starting point for a number of works for concerning corner eddies. Moffatt has shown that for a flow near a sharp corner, there exists an infinite sequence of eddies as the corner is approached.

In this chapter, we are interested in making a connection between these eddies and the scaling laws of a flow field driven near such corners. We explore the structure of the flow field and survey the scaling laws for the scalar decay controlled by eddy configurations in the corner regions. The discussion here is based on the work of Moffatt (1964) focusing on the flow near a sharp corner with a semi-angle $\alpha = \pi/4$. We subsequently organise this part of thesis as follows. In Section §8.2 a general framework is provided including the background and a short glance on a Fourier series. This series is used later to simplify the mathematical calculations. In Section §8.3, we discuss the structure of the scalar field as well as corner eddies.

Finally, in Section §8.5 we discuss some aspects of the results that we find.

8.2 Background framework

The purpose of this section is to explore the general structure of Moffatt corner eddies. We describe the nature and the structure of the motion of two-dimensional Stokes flow near the corner. Then we proceed to discover the whole structure of viscous eddies providing an overview on the cases of flows near corners studied by Moffatt (1964).

8.2.1 Motion of fluid

The motion of a fluid which is effectively incompressible and of uniform density ρ is governed by the equation

$$\rho(\partial_t \mathbf{u} + \mathbf{u} \cdot \nabla \mathbf{u}) = \mu \nabla^2 \mathbf{u} - \nabla p; \quad \nabla \cdot \mathbf{u} = 0, \quad (8.2.1)$$

where p is the pressure and ρ is the density of the fluid. In some circumstances, the Reynolds number $Re = |u|l/\nu \ll 1$ is low for $\nu = \mu/\rho$ where l is the typical length scale, μ is the coefficient of the viscosity and ν is the viscosity of the flow, the non-linear term $\mathbf{u} \cdot \nabla \mathbf{u}$ is small, and can be neglected as an approximation. In addition, if the flow is steady, or nearly so that $|\partial \mathbf{u} / \partial t|$ is not appreciably larger than $|\mathbf{u} \cdot \nabla \mathbf{u}|$, the whole inertia force is everywhere small in magnitude compared with either the pressure or viscous force. When the inertia force is negligible

everywhere, the following governing equations for Stokes flow become valid

$$\mu \nabla^2 \mathbf{u} = \nabla p, \quad (8.2.2)$$

$$\nabla \cdot \mathbf{u} = 0. \quad (8.2.3)$$

Assume the motion of the fluid is two-dimensional, so that

$$\begin{aligned} \mathbf{u} &= (u, v, 0) \\ &= \left(\frac{\partial \psi}{\partial y}, -\frac{\partial \psi}{\partial x}, 0 \right) \end{aligned} \quad (8.2.4)$$

and u, v are independent of z . In this case we have

$$\mu (\partial_x^2 + \partial_y^2) \partial_y \psi - \partial_x p = 0, \quad (8.2.5)$$

$$-\mu (\partial_x^2 + \partial_y^2) \partial_x \psi - \partial_y p = 0. \quad (8.2.6)$$

To eliminate the pressure p from the above two equations (8.2.5) and (8.2.6) we have to differentiate (8.2.5) with respect to y and (8.2.6) with respect to x and subtract the two equations to get

$$\mu (\partial_x^2 + \partial_y^2) (\partial_x^2 + \partial_y^2) \psi = 0, \quad (8.2.7)$$

This equation represents the homogeneous biharmonic equation of Stokes flows

$$\mu \nabla^4 \psi = 0. \quad (8.2.8)$$

where $\nabla^4 \equiv \nabla^2 \nabla^2$ is called the Stokes operator. However, Eq. (8.2.8) needs to be supplemented by boundary conditions; e.g., no-slip on specified surfaces. Further

details are found in Moffatt (1964) and Shankar (2007).

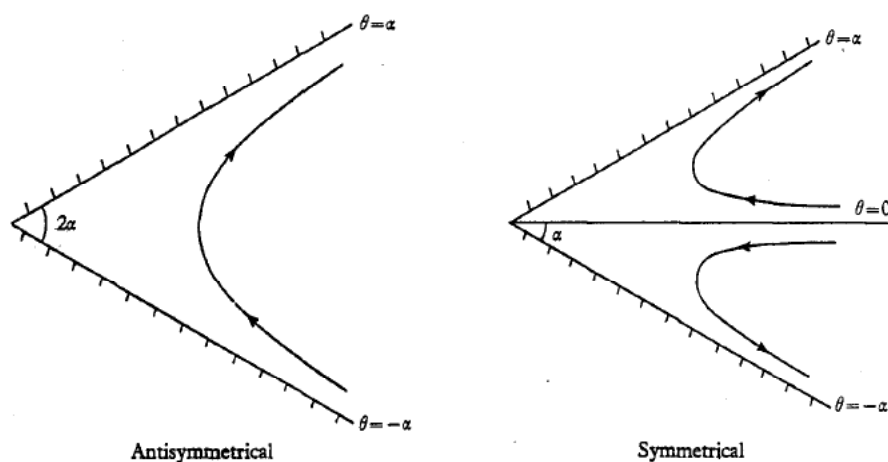


Figure 8.1: Flow in a corner between rigid boundaries, induced by an arbitrary two-dimensional agitation at a large distance (Moffatt, 1964).

8.2.2 Two-dimensional flow near a sharp corner

The Stokes equation (8.2.8) formed above can be solved in a wedge as sketched in Fig. 8.1 where the velocity components in the polar system are given by

$$u_r = \frac{1}{r} \frac{\partial \psi}{\partial \theta}, \quad u_\theta = -\frac{\partial \psi}{\partial r}. \quad (8.2.9)$$

Therefore, the boundary conditions for the Stokes equation (8.2.8) in terms of polar co-ordinates (r, θ) are

$$\frac{\partial \psi}{\partial r} = 0, \quad \frac{1}{r} \frac{\partial \psi}{\partial \theta} = 0 \quad \text{at } \theta = \pm \alpha. \quad (8.2.10)$$

These are no-slip boundary conditions; $u, v = 0$ at both boundaries.

The form of these boundary conditions is such that ψ could be proportional to a

power of r everywhere. In this case, the solution is sought by

$$\psi(r, \theta) = r^\lambda f_\lambda(\theta), \quad (8.2.11)$$

where λ is any number, real or complex called the exponent of the corresponding solution. However, the general function f in (8.2.11) takes the form

$$f_\lambda(\theta) = A \cos \lambda\theta + B \sin \lambda\theta + C \cos(\lambda - 2)\theta + D \sin(\lambda - 2)\theta, \quad (8.2.12)$$

with arbitrary constants A , B , C , and D , to satisfy (8.2.8). It is important to note that if λ and f_λ in (8.2.11) are complex then we need to add a complex conjugate solution, as we will do later in Section §8.3.1. Furthermore, Eqs. (8.2.11) and (8.2.12) satisfy the Stokes equation $\nabla^4\psi = 0$ where

$$\begin{aligned} \nabla^2\psi &= (\partial_x^2 + \partial_y^2)\psi \\ &= \frac{1}{r}\partial_r(r\partial_r\psi) + \frac{1}{r^2}\partial_\theta^2\psi. \end{aligned} \quad (8.2.13)$$

in the polar co-ordinates.

8.2.3 Viscous and resistive eddies near a sharp corner

The structure of the two-dimensional flow has been considered in a detailed study by Moffatt (1964). This structure is considered for a flow of a viscous fluid in the region near a sharp corner. Moffatt studied a number of cases in which, the Stokes approximation for the stream function $\psi(r, \theta)$ satisfies (8.2.8), where (r, θ) are polar co-ordinates with origin at the corner. As we indicated in Section §8.2.2, this equation has the solution (8.2.11) which is relevant to the flow between two

plane boundaries meeting at a sharp corner. The boundaries may be rigid walls on which the fluid velocity is prescribed, or surface on which the stress is prescribed. In this case, locally the flow takes the form (8.2.11) in the polar co-ordinates (r, θ) . In one of the cases studied by Moffatt, the boundary conditions are inhomogeneous and the solutions involve positive integer values of λ . A case of this type, in which one wall moves parallel to itself with constant velocity U , has been described by Taylor (1960). No eddies occur in such a case. In the second case of solutions the motion in the corners is driven by stirring of the fluid at large enough distance from the corner. For example, fluid may be driven into the corner near one of the boundaries and out of the corner near the other. Rayleigh (1920) considered this case firstly and showed that no solution of the form (8.2.11) with integral exponent could satisfy the four homogeneous boundary conditions,

$$\psi = \partial\psi/\partial\theta = 0, \quad \theta = \pm\alpha. \quad (8.2.14)$$

corresponding to zero velocity on two walls inclined at an angle 2α .

Later Dean & Montagnon (1949) showed that the exponent λ is necessarily complex for angles between the planes less than about 146.3° , which was interpreted by Moffatt (1964) as implying the existence of eddies near to the corner. The third case considered by Moffatt describes the flow at large distance from the corner. Again, the boundary conditions are given by (8.2.14). In this case, eddies also occur for angles less than about 146.3° , but the real part of λ is negative to give decay of eddy strength as $r \rightarrow \infty$.

8.2.4 Structure of Moffatt eddies near a sharp corner

One of the categories of solutions considered by Moffatt (1964) and mentioned above describes the flow at small distance from the corner. If two rigid boundaries are fixed at an angle 2α as is sketched in Fig. 8.1, a flow near the corner is simply induced by stirring the distant fluid. Moffatt assumed that in the Stokes regime the stream function can be expanded as

$$\psi = \sum_1^{\infty} A_n r^{\lambda_n} f_{\lambda_n}(\theta). \quad (8.2.15)$$

where A_n are constants and the λ_n are suitably chosen and ordered so that

$$1 < \operatorname{Re}(\lambda_1) < \operatorname{Re}(\lambda_2) < \dots \quad (8.2.16)$$

Clearly the stirring force may produce either an anti-symmetrical or a symmetrical flow pattern near the corner (Fig. 8.1) and the corresponding stream function $\psi(r, \theta)$ is an even or odd function of θ , respectively. In the symmetrical flow, the stress component $(\frac{1}{r})\partial u/\partial\theta$ vanishes on $\theta = 0$, so that the flow between a rigid boundary and a free surface ($\theta = 0$) is determined. If $2\alpha > \pi$, the flow is that round or past the leading edge of a wedge. In the antisymmetric flow, $f_{\lambda}(\theta)$ is even, so that the constants B and D in (8.2.12) vanish producing

$$f_{\lambda}(\theta) = A \cos \lambda\theta + C \cos(\lambda - 2)\theta. \quad (8.2.17)$$

In the case of no-slip boundaries, both velocity components vanish on $\theta = \pm\alpha$ provided $f(\pm\alpha) = f'(\pm\alpha) = 0$, so that

$$A \cos \lambda\alpha + C \cos(\lambda - 2)\alpha = 0, \quad (8.2.18)$$

$$A\lambda \sin \lambda\alpha + C(\lambda - 2) \sin(\lambda - 2)\alpha = 0. \quad (8.2.19)$$

This leads us to obtain the relation

$$\frac{A}{C} = -\frac{\cos(\lambda - 2)\alpha}{\cos \lambda\alpha} = -\frac{(\lambda - 2) \sin(\lambda - 2)\alpha}{\lambda \sin \lambda\alpha}. \quad (8.2.20)$$

Solving these two equations one can obtain

$$\sin 2\lambda\alpha \cos 2\alpha - \cos 2\lambda\alpha \sin 2\alpha = -\lambda \sin 2\alpha + \sin 2\alpha, \quad (8.2.21)$$

which on simplification leads to the equation

$$\sin 2\mu\alpha = -\mu \sin 2\alpha; \quad \mu = \lambda - 1. \quad (8.2.22)$$

As noticed by Dean & Montagnon (1949), when $2\alpha < 2\alpha_1 \simeq 146.3^\circ$; $2\alpha_1$ is the critical angle, Eq. (8.2.22) admits no real solutions, but it does admit complex solutions and we construct the actual, real flow by adding a complex conjugate,

$$\psi = r^\lambda f_\lambda(\theta) + r^{\lambda^*} f_{\lambda^*}^*(\theta). \quad (8.2.23)$$

where λ^* and $f_{\lambda^*}^*$ are complex.

Table 8.1 lists some principal eigenvalues λ corresponding to a range of corner semi-angles α from 1° to 70° quoted from Shankar (2007). It may be noted that

α°	λ
1.000	121.67730+64.47231i
2.000	61.34044+32.22667i
5.000	25.14114+12.86409i
10	13.07948+6.38439i
20	7.05783+3.09537i
30	5.05933+1.95205i
40	4.06743+1.33959i
45	3.73959+1.11902i
50	3.47922+0.93037i
60	3.09414+0.60458i
70	2.82687+0.26170i

Table 8.1: The principal eigenvalue λ corresponding to a corner semi-angle α .

both the real and imaginary parts of λ increase as α decreases. For more details, see Moffatt (1964) and Shankar (2007).

8.2.5 Fourier series

It is well known that the periodic function $f(x)$ of period $2L$ can be represented by a **Fourier Series**

$$f(x) = a_0 + \sum_{n=1}^{\infty} \left(a_n \cos \frac{n\pi x}{L} + b_n \sin \frac{n\pi x}{L} \right), \quad (8.2.24)$$

then the **Fourier Coefficients** satisfy the **Euler Formula**, namely,

$$a_0 = \frac{1}{2L} \int_{-L}^L f(x) dx. \quad (8.2.25)$$

$$a_n = \frac{1}{L} \int_{-L}^L f(x) \cos \frac{n\pi x}{L} dx; \quad n = 1, 2, \dots \quad (8.2.26)$$

$$b_n = \frac{1}{L} \int_{-L}^L f(x) \sin \frac{n\pi x}{L} dx; \quad n = 1, 2, \dots \quad (8.2.27)$$

We shall apply these forms later in Section §8.3.2 to generate and simplify our calculations used to determine the flow near to the corner regions.

8.3 Connection to Moffatt eddies

In this section we aim to connect the mathematical problem that describes the evolution of the scalar field with the structure of Moffatt corner eddies. For this purpose, we analyse the structure of the passive scalar field in terms of polar coordinates (r, θ) . We start by specifying the stream function of the flow in such a system and introducing the full mathematical problem of the evolution of the scalar field. We continue to analyse the diffusivity tensor components D_{ij} described for the averaged scalar field. We then write down the PDEs for solving the averaged scalar fields $\bar{\sigma}(r, \theta, t)$ expanded in Fourier series in θ given in Section §8.2.5.

8.3.1 Specifying the flow

As we have indicated in Section §8.2.2 the Stokes equation of the stream function $\psi(r, \theta)$ in plane polar co-ordinates (r, θ) admits separated solutions of the form (8.2.11). So, if we consider two rigid boundaries fixed at an angle 2α then we can specify (8.2.11) to be

$$\psi(r, \theta) = c(t) r^\lambda f_\lambda(\theta) + c^*(t) r^{\lambda^*} f_\lambda^*(\theta). \quad (8.3.1)$$

where the second term $c^*(t) r^{\lambda^*} f_\lambda^*(\theta)$ on the right-hand side of (8.3.1) is the complex conjugate to the first one. We take $c(t)$ to be random and constant on each time

interval of length τ . For this type of flow, $f_\lambda(\theta)$ is even of the form

$$f_\lambda(\theta) = A \cos \lambda \theta + C \cos(\lambda - 2) \theta. \quad (8.3.2)$$

As we have discussed in Section §8.2.4, under a consideration of no-slip boundaries, both velocity components vanish on $\theta = \pm\alpha$ provided $f(\pm\alpha) = f'(\pm\alpha) = 0$. We choose the values of A and C to normalise the functions f and f' so that

$$\frac{1}{2\alpha} \int_{-\alpha}^{\alpha} f(\theta) f^*(\theta) d\theta = 1. \quad (8.3.3)$$

This is just a choice whereby we can simplify the situation by specifying the values of A and C . In doing so, we define I as

$$I = \frac{1}{2\alpha} \int_{-\alpha}^{\alpha} f(\theta) f^*(\theta) d\theta. \quad (8.3.4)$$

so we can normalise f and f^* , where

$$g(\theta) = f(\theta)/\sqrt{I}, \quad g^*(\theta) = f^*(\theta)/\sqrt{I} \quad (8.3.5)$$

In this case, the function g and g^* will satisfy Eq. (8.3.3). We can now identify the values A and C through the relation (8.2.20) for the eigenvalue problem indicated in Section §8.2.4, where $\lambda \simeq 3.73959 + 1.11902i$ is obtained for $2\alpha = 90^\circ$. For example, choosing $C=1$ and using the relation (8.2.20) we can determine A and then the functions g and g^* are determined based on (8.3.2). This implies that

$$A = 0.1018952588 - 0.7207746771i. \quad (8.3.6)$$

which satisfies Eq. (8.3.3) where g and g^* will be replacing of f and f^* respectively in (8.3.3).

8.3.2 Specifying the components of diffusivity tensor and full mathematical problem

For such a situation, the forms of the velocity components u_r and u_θ with respect to (8.3.1) in general can be written as

$$u_r = (1/r)(\partial\psi/\partial\theta) = c(t) r^{\lambda-1} f'(\theta) + c.c, \quad (8.3.7)$$

$$u_\theta = -(\partial\psi/\partial r) = -c(t)\lambda r^{\lambda-1} f(\theta) + c.c. \quad (8.3.8)$$

where $c(t)$ is a constant on each interval of length τ . Suppose $c = A e^{i\phi}$; ϕ is a random phase that is uniformly distributed from 0 to 2π and A is an amplitude. Therefore, $\langle c^2 \rangle = \langle c^{*2} \rangle = 0$ and $\langle c c^* \rangle = A^2$. Then, the components of the effective diffusive tensor D_{ij} in this case will be found as

$$D_{rr} = \langle u_r^2 \rangle = \mu (2 f' f'^* r^{2\lambda_r-2}), \quad (8.3.9)$$

$$D_{r\theta} = \langle u_r u_\theta \rangle = -\mu (\lambda^* f' f^* + \lambda f'^* f) r^{2\lambda_r-2}, \quad (8.3.10)$$

$$D_{\theta\theta} = \langle u_\theta^2 \rangle = \mu (2 \lambda \lambda^* f f^* r^{2\lambda_r-2}). \quad (8.3.11)$$

where $\lambda_r = Re(\lambda)$ is the real part of λ and $\mu = (\frac{\tau}{2}) A^2$. Again, in the next calculations we will set μ to be 1 and later in Section §8.4.1 will scale it out. Now, the averaged scalar field $\bar{\sigma}$ can be written for $-\alpha \leq \theta \leq \alpha$ as

$$\bar{\sigma}(r, \theta) = \bar{\sigma}_0(r) + \bar{\sigma}_4(r) \cos(\pi\theta/\alpha) + \bar{\sigma}_8(r) \cos(2\pi\theta/\alpha), \quad (8.3.12)$$

in a three-mode truncation, or

$$\bar{\sigma}(r, \theta) = \bar{\sigma}_0(r) + \bar{\sigma}_4(r) \cos(\pi\theta/\alpha) + \bar{\sigma}_8(r) \cos(2\pi\theta/\alpha) + \dots + \bar{\sigma}_{20}(r) \cos(5\pi\theta/\alpha). \quad (8.3.13)$$

in a six-mode truncation based on Fourier series mentioned in Section §8.2.5 with no sine terms as a consequence of the symmetry $\theta \rightarrow -\theta$.

In Section §7.3 we have shown that the averaged scalar field is essentially given by Eq. (7.3.29). Representing this equation in terms of $\bar{\sigma}_0, \bar{\sigma}_4, \dots, \bar{\sigma}_{20}$ can be accommodated by substituting with D_{ij} components determined by (8.3.9), (8.3.10) and (8.3.11).

For the **first** term $\frac{\partial}{\partial r} (D_{rr} \frac{\partial \bar{\sigma}}{\partial r})$ we have from Eq. (8.3.9) that

$$D_{rr} \sim 2r^{2\lambda_r-2} f'(\theta) f'^*(\theta), \quad (8.3.14)$$

Since both D_{rr} and $\frac{\partial \bar{\sigma}}{\partial r}$ are even functions in θ then $(D_{rr} \frac{\partial \bar{\sigma}}{\partial r})$ will be written in terms of even functions,

$$D_{rr} \frac{\partial \bar{\sigma}}{\partial r} = 2r^{2\lambda_r-2} f' f'^* \left(\frac{\partial \bar{\sigma}_0}{\partial r} + \frac{\partial \bar{\sigma}_4}{\partial r} \cos \frac{\pi\theta}{\alpha} + \dots + \frac{\partial \bar{\sigma}_{20}}{\partial r} \cos \frac{5\pi\theta}{\alpha} \right), \quad (8.3.15)$$

and consequently

$$\frac{\partial}{\partial r} \left(D_{rr} \frac{\partial \bar{\sigma}}{\partial r} \right) = \frac{\partial}{\partial r} \left(2r^{2\lambda_r-2} f' f'^* \left(\frac{\partial \bar{\sigma}_0}{\partial r} + \frac{\partial \bar{\sigma}_4}{\partial r} \cos \frac{\pi\theta}{\alpha} + \dots + \frac{\partial \bar{\sigma}_{20}}{\partial r} \cos \frac{5\pi\theta}{\alpha} \right) \right). \quad (8.3.16)$$

This can be written as

$$\begin{aligned}
 \frac{\partial}{\partial r} \left(D_{rr} \frac{\partial \bar{\sigma}}{\partial r} \right) &= \frac{\partial}{\partial r} \left(2 r^{2\lambda_r-2} \frac{\partial \bar{\sigma}_0}{\partial r} \right) f'(\theta) f'^*(\theta) \\
 &+ \frac{\partial}{\partial r} \left(2 r^{2\lambda_r-2} \frac{\partial \bar{\sigma}_4}{\partial r} \right) f'(\theta) f'^*(\theta) \cos(\pi\theta/\alpha) + \dots \\
 &+ \frac{\partial}{\partial r} \left(2 r^{2\lambda_r-2} \frac{\partial \bar{\sigma}_{20}}{\partial r} \right) f'(\theta) f'^*(\theta) \cos(5\pi\theta/\alpha) + \dots \quad (8.3.17)
 \end{aligned}$$

We still proceed with the above term by putting

$$2f'(\theta)f'^*(\theta) = \beta_{00} + \beta_{01} \cos(\pi\theta/\alpha) + \beta_{02} \cos(2\pi\theta/\alpha) + \dots \quad (8.3.18)$$

$$2f'(\theta)f'^*(\theta) \cos(\pi\theta/\alpha) = \beta_{10} + \beta_{11} \cos(\pi\theta/\alpha) + \beta_{12} \cos(2\pi\theta/\alpha) + \dots \quad (8.3.19)$$

$$2f'(\theta)f'^*(\theta) \cos(2\pi\theta/\alpha) = \beta_{20} + \beta_{21} \cos(\pi\theta/\alpha) + \beta_{22} \cos(2\pi\theta/\alpha) + \dots \quad (8.3.20)$$

and so on. However, we now have terms in (7.3.29) of the form

$$\partial_t \bar{\sigma}_0 = \frac{1}{r} \frac{\partial}{\partial r} \left(r^{2\lambda_r-2} (\beta_{00} \partial_r \bar{\sigma}_0 + \beta_{10} \partial_r \bar{\sigma}_4 + \beta_{20} \partial_r \bar{\sigma}_8 + \dots + \beta_{50} \partial_r \bar{\sigma}_{20}) \right) + \dots \quad (8.3.21)$$

where, for example

$$\beta_{00} = 1/(2\alpha) \int_{-\alpha}^{\alpha} 2 f'(\theta) f'^*(\theta) d\theta, \quad (8.3.22)$$

$$\beta_{10} = 1/(2\alpha) \int_{-\alpha}^{\alpha} 2 f'(\theta) f'^*(\theta) \cos(\pi\theta/\alpha) d\theta, \quad (8.3.23)$$

$$\beta_{20} = 1/(2\alpha) \int_{-\alpha}^{\alpha} 2 f'(\theta) f'^*(\theta) \cos(2\pi\theta/\alpha) d\theta, \quad (8.3.24)$$

$$\beta_{30} = 1/(2\alpha) \int_{-\alpha}^{\alpha} 2 f'(\theta) f'^*(\theta) \cos(3\pi\theta/\alpha) d\theta. \quad (8.3.25)$$

also from these D_{rr} terms we obtain

$$\partial_t \bar{\sigma}_4 = \frac{1}{r} \frac{\partial}{\partial r} \left(r^{2\lambda_r - 2} (\beta_{01} \partial_r \bar{\sigma}_0 + \beta_{11} \partial_r \bar{\sigma}_4 + \beta_{21} \partial_r \bar{\sigma}_8 + \dots + \beta_{51} \partial_r \bar{\sigma}_{20}) \right) + \dots \quad (8.3.26)$$

and some coefficients in this case are

$$\beta_{01} = 1/(\alpha) \int_{-\alpha}^{\alpha} 2 f'(\theta) f'^*(\theta) \cos(\pi\theta/\alpha) d\theta, \quad (8.3.27)$$

$$\beta_{11} = 1/(\alpha) \int_{-\alpha}^{\alpha} 2 f'(\theta) f'^*(\theta) \cos(\pi\theta/\alpha) \cos(\pi\theta/\alpha) d\theta, \quad (8.3.28)$$

$$\beta_{21} = 1/(\alpha) \int_{-\alpha}^{\alpha} 2 f'(\theta) f'^*(\theta) \cos(2\pi\theta/\alpha) \cos(\pi\theta/\alpha) d\theta, \quad (8.3.29)$$

$$\beta_{31} = 1/(\alpha) \int_{-\alpha}^{\alpha} 2 f'(\theta) f'^*(\theta) \cos(3\pi\theta/\alpha) \cos(\pi\theta/\alpha) d\theta. \quad (8.3.30)$$

Similarly, for the other terms.

Crucially, the general basic rule to determine the coefficients related to this term

$\frac{\partial}{\partial r} (D_{rr} \frac{\partial \bar{\sigma}}{\partial r})$ can be written as follows

$$\beta_{mn} = \left\{ \begin{array}{ll} \frac{1}{2\alpha} & \text{if } n = 0 \\ \frac{1}{\alpha} & \text{otherwise} \end{array} \right\} \times \int_{-\alpha}^{\alpha} 2 f'(\theta) f'^*(\theta) \cos(m\pi\theta/\alpha) \cos(n\pi\theta/\alpha) d\theta.$$

More specifically,

$$\beta_{mn} = \beta_{nm}; \quad n, m \neq 0, \quad (8.3.31)$$

and

$$\beta_{0n} = 2 \beta_{n0}. \quad (8.3.32)$$

For the **second** term $\frac{1}{r} \frac{\partial}{\partial r} (D_{r\theta} \frac{\partial \bar{\sigma}}{\partial \theta})$, both $D_{r\theta}$ and $\frac{\partial \bar{\sigma}}{\partial \theta}$ are odd functions and hence the Fourier extension of this term will be written in cos functions,

$$D_{r\theta} \frac{\partial \bar{\sigma}}{\partial \theta} = (-r^{2\lambda_r-2}(\lambda^* f' f^* + \lambda f'^* f. \\ (-\pi/\alpha)(\bar{\sigma}_4 \sin(\pi\theta/\alpha) + \dots + 5\bar{\sigma}_{20} \sin(5\pi\theta/\alpha))). \quad (8.3.33)$$

Now, using the operator $\frac{1}{r} \frac{\partial}{\partial r}$ yields that

$$\begin{aligned} \frac{1}{r} \frac{\partial}{\partial r} \left(D_{r\theta} \frac{\partial \bar{\sigma}}{\partial \theta} \right) &= \frac{1}{r} \frac{\partial}{\partial r} \left[r^{2\lambda_r-2} \left(-\frac{\pi}{\alpha} \right) (A_{10} \bar{\sigma}_4 + A_{11} \bar{\sigma}_4 \cos(\pi\theta/\alpha) + \dots + A_{15} \bar{\sigma}_4 \cos(5\pi\theta/\alpha)) \right. \\ &+ r^{2\lambda_r-2} \left(-\frac{2\pi}{\alpha} \right) (A_{20} \bar{\sigma}_8 + A_{21} \bar{\sigma}_8 \cos(\pi\theta/\alpha) + \dots + A_{25} \bar{\sigma}_8 \cos(5\pi\theta/\alpha)) \\ &+ \dots \\ &\left. + r^{2\lambda_r-2} \left(-\frac{5\pi}{\alpha} \right) (A_{50} \bar{\sigma}_{20} + A_{51} \bar{\sigma}_{20} \cos(\pi\theta/\alpha) + \dots + A_{55} \bar{\sigma}_{20} \cos(5\pi\theta/\alpha)) \right]. \end{aligned} \quad (8.3.34)$$

with some A_{mn}

$$A_{10} = 1/(2\alpha) \int_{-\alpha}^{\alpha} -(\lambda^* f' f^* + \lambda f'^* f) \sin(\pi\theta/\alpha) d\theta, \quad (8.3.35)$$

$$A_{11} = 1/(\alpha) \int_{-\alpha}^{\alpha} -(\lambda^* f' f^* + \lambda f'^* f) \sin(\pi\theta/\alpha) \cos(\pi\theta/\alpha) d\theta, \quad (8.3.36)$$

$$A_{14} = 1/(\alpha) \int_{-\alpha}^{\alpha} -(\lambda^* f' f^* + \lambda f'^* f) \sin(\pi\theta/\alpha) \cos(4\pi\theta/\alpha) d\theta, \quad (8.3.37)$$

$$A_{15} = 1/(\alpha) \int_{-\alpha}^{\alpha} -(\lambda^* f' f^* + \lambda f'^* f) \sin(\pi\theta/\alpha) \cos(5\pi\theta/\alpha) d\theta. \quad (8.3.38)$$

and generally

$$A_{mn} = \left\{ \begin{array}{ll} \frac{1}{2\alpha} & \text{if } n = 0 \\ \frac{1}{\alpha} & \text{otherwise} \end{array} \right\} \times \int_{-\alpha}^{\alpha} -(\lambda^* f' f^* + \lambda f'^* f) \sin(m\pi\theta/\alpha) \cos(n\pi\theta/\alpha) d\theta.$$

For example, in this case we get terms in (7.3.29) from $D_{r\theta}$ of the form

$$\partial_t \bar{\sigma}_0 = \dots + \frac{1}{r} \frac{\partial}{\partial r} \left(r^{2\lambda_r - 2} [\gamma_{10} \bar{\sigma}_4 + \gamma_{20} \bar{\sigma}_8 + \dots + \gamma_{50} \bar{\sigma}_{20}] \right) + \dots \quad (8.3.39)$$

$$\partial_t \bar{\sigma}_4 = \dots + \frac{1}{r} \frac{\partial}{\partial r} \left(r^{2\lambda_r - 2} [\gamma_{11} \bar{\sigma}_4 + \gamma_{21} \sigma_8 + \dots + \gamma_{51} \bar{\sigma}_{20}] \right) + \dots \quad (8.3.40)$$

and

$$\partial_t \bar{\sigma}_{20} = \dots + \frac{1}{r} \frac{\partial}{\partial r} \left(r^{2\lambda_r - 2} [\gamma_{15} \bar{\sigma}_4 + \gamma_{25} \bar{\sigma}_8 + \dots + \gamma_{55} \bar{\sigma}_{20}] \right) + \dots \quad (8.3.41)$$

Therefore, the second group of coefficients γ_{mn} is generally given by

$$\gamma_{mn} = \left(\frac{-m\pi}{\alpha} \right) A_{mn}, \quad (8.3.42)$$

This gives that

$$\gamma_{mn} = \left\{ \begin{array}{ll} \frac{1}{2\alpha} & \text{if } n = 0 \\ \frac{1}{\alpha} & \text{otherwise} \end{array} \right\} \times \left(\frac{-m\pi}{\alpha} \right) \int_{-\alpha}^{\alpha} -(\lambda^* f' f^* + \lambda f'^* f) \sin(m\pi\theta/\alpha) \cos(n\pi\theta/\alpha) d\theta.$$

The following are some coefficients γ_{mn} in this case

$$\gamma_{10} = \frac{1}{2\alpha} \left(\frac{\pi}{\alpha} \right) \int_{-\alpha}^{\alpha} (\lambda^* f' f^* + \lambda f'^* f) \sin(\pi\theta/\alpha) d\theta, \quad (8.3.43)$$

$$\gamma_{20} = \frac{1}{2\alpha} \left(\frac{2\pi}{\alpha} \right) \int_{-\alpha}^{\alpha} (\lambda^* f' f^* + \lambda f'^* f) \sin(2\pi\theta/\alpha) d\theta, \quad (8.3.44)$$

$$\gamma_{11} = \frac{1}{\alpha} \left(\frac{\pi}{\alpha} \right) \int_{-\alpha}^{\alpha} (\lambda^* f' f^* + \lambda f'^* f) \sin(\pi\theta/\alpha) \cos(\pi\theta/\alpha) d\theta, \quad (8.3.45)$$

$$\gamma_{21} = \frac{1}{\alpha} \left(\frac{2\pi}{\alpha} \right) \int_{-\alpha}^{\alpha} (\lambda^* f' f^* + \lambda f'^* f) \sin(2\pi\theta/\alpha) \cos(\pi\theta/\alpha) d\theta. \quad (8.3.46)$$

Similarly, for the **third** term $\frac{1}{r} \frac{\partial}{\partial \theta} (D_{r\theta} \frac{\partial \bar{\sigma}}{\partial r})$ where

$$\begin{aligned} D_{r\theta} \frac{\partial \bar{\sigma}}{\partial r} &= -r^{2\lambda_r-2} (\lambda^* f' f^* + \lambda f'^* f) \\ &\times \left(\frac{\partial \bar{\sigma}_0}{\partial r} + \frac{\partial \bar{\sigma}_4}{\partial r} \cos(\pi\theta/\alpha) + \frac{\partial \bar{\sigma}_8}{\partial r} \cos(2\pi\theta/\alpha) + \dots \right). \end{aligned} \quad (8.3.47)$$

This equation collapses to

$$\begin{aligned} D_{r\theta} \frac{\partial \bar{\sigma}}{\partial r} &= r^{2\lambda_r-2} \left(T_{01} \frac{\partial \bar{\sigma}_0}{\partial r} + T_{11} \frac{\partial \bar{\sigma}_4}{\partial r} + \dots \right) \sin(\pi\theta/\alpha) \\ &+ r^{2\lambda_r-2} \left(T_{02} \frac{\partial \bar{\sigma}_0}{\partial r} + T_{12} \frac{\partial \bar{\sigma}_4}{\partial r} + \dots \right) \sin(2\pi\theta/\alpha) \\ &+ \dots \end{aligned} \quad (8.3.48)$$

with

$$T_{01} = \frac{1}{\alpha} \int_{-\alpha}^{\alpha} -(\lambda^* f' f^* + \lambda f'^* f) \sin(\pi\theta/\alpha) d\theta, \quad (8.3.49)$$

$$T_{02} = \frac{1}{\alpha} \int_{-\alpha}^{\alpha} -(\lambda^* f' f^* + \lambda f'^* f) \sin(2\pi\theta/\alpha) d\theta, \quad (8.3.50)$$

and generally

$$T_{mn} = \frac{1}{\alpha} \int_{-\alpha}^{\alpha} -(\lambda^* f' f^* + \lambda f'^* f) \cos(m\pi\theta/\alpha) \sin(n\pi\theta/\alpha) d\theta. \quad (8.3.51)$$

Under the operator $\frac{1}{r} \frac{\partial}{\partial \theta}$ we get even terms of the Fourier series

$$\begin{aligned} \frac{1}{r} \frac{\partial}{\partial \theta} \left(D_{r\theta} \frac{\partial \bar{\sigma}}{\partial r} \right) &= r^{2\lambda_r-3} \left(\frac{\pi}{\alpha} \right) \left(T_{01} \frac{\partial \bar{\sigma}_0}{\partial r} + T_{11} \frac{\partial \bar{\sigma}_4}{\partial r} + \dots \right) \cos(\pi\theta/\alpha) \\ &+ r^{2\lambda_r-3} \left(\frac{2\pi}{\alpha} \right) \left(T_{02} \frac{\partial \bar{\sigma}_0}{\partial r} + T_{12} \frac{\partial \bar{\sigma}_4}{\partial r} + \dots \right) \cos(2\pi\theta/\alpha) \\ &+ \dots \end{aligned} \quad (8.3.52)$$

Consequently, the terms we obtain in this case take the forms

$$\partial_t \bar{\sigma}_4 = \dots + \frac{1}{r} \left(r^{2\lambda_r-2} \left[S_{01} \frac{\partial \bar{\sigma}_0}{\partial r} + S_{11} \frac{\partial \bar{\sigma}_4}{\partial r} + S_{21} \frac{\partial \bar{\sigma}_8}{\partial r} + \dots + S_{51} \frac{\partial \bar{\sigma}_{20}}{\partial r} \right] \right) + \dots \quad (8.3.53)$$

$$\partial_t \bar{\sigma}_8 = \dots + \frac{1}{r} \left(r^{2\lambda_r-2} \left[S_{02} \frac{\partial \bar{\sigma}_0}{\partial r} + S_{12} \frac{\partial \bar{\sigma}_4}{\partial r} + S_{22} \frac{\partial \bar{\sigma}_8}{\partial r} + \dots + S_{52} \frac{\partial \bar{\sigma}_{20}}{\partial r} \right] \right) + \dots \quad (8.3.54)$$

and

$$\partial_t \bar{\sigma}_{20} = \dots + \frac{1}{r} \left(r^{2\lambda_r-2} \left[S_{05} \frac{\partial \bar{\sigma}_0}{\partial r} + S_{15} \frac{\partial \bar{\sigma}_4}{\partial r} + S_{25} \frac{\partial \bar{\sigma}_8}{\partial r} + \dots + S_{55} \frac{\partial \bar{\sigma}_{20}}{\partial r} \right] \right) + \dots \quad (8.3.55)$$

and similarly for the other terms. The coefficients for example S_{01} and S_{02} are defined as

$$S_{01} = \left(\frac{\pi}{\alpha} \right) \left(\frac{1}{\alpha} \right) \int_{-\alpha}^{\alpha} -(\lambda^* f' f^* + \lambda f'^* f) \sin(\pi\theta/\alpha) d\theta, \quad (8.3.56)$$

$$S_{02} = \left(\frac{2\pi}{\alpha} \right) \left(\frac{1}{\alpha} \right) \int_{-\alpha}^{\alpha} -(\lambda^* f' f^* + \lambda f'^* f) \sin(2\pi\theta/\alpha) d\theta. \quad (8.3.57)$$

Thus, the third group of coefficients S_{mn} is given by

$$S_{mn} = \left(\frac{n\pi}{\alpha} \right) \left(\frac{1}{\alpha} \right) \int_{-\alpha}^{\alpha} -(\lambda^* f' f^* + \lambda f'^* f) \cos(m\pi\theta/\alpha) \sin(n\pi\theta/\alpha) d\theta. \quad (8.3.58)$$

Some coefficients S_{mn} for such a case are found as

$$S_{11} = \left(\frac{\pi}{\alpha}\right) \left(\frac{1}{\alpha}\right) \int_{-\alpha}^{\alpha} -(\lambda^* f' f^* + \lambda f'^* f) \cos(\pi\theta/\alpha) \sin(\pi\theta/\alpha) d\theta, \quad (8.3.59)$$

$$S_{21} = \left(\frac{\pi}{\alpha}\right) \left(\frac{1}{\alpha}\right) \int_{-\alpha}^{\alpha} -(\lambda^* f' f^* + \lambda f'^* f) \cos(2\pi\theta/\alpha) \sin(\pi\theta/\alpha) d\theta, \quad (8.3.60)$$

$$S_{12} = \left(\frac{2\pi}{\alpha}\right) \left(\frac{1}{\alpha}\right) \int_{-\alpha}^{\alpha} -(\lambda^* f' f^* + \lambda f'^* f) \cos(\pi\theta/\alpha) \sin(2\pi\theta/\alpha) d\theta, \quad (8.3.61)$$

$$S_{22} = \left(\frac{2\pi}{\alpha}\right) \left(\frac{1}{\alpha}\right) \int_{-\alpha}^{\alpha} -(\lambda^* f' f^* + \lambda f'^* f) \cos(2\pi\theta/\alpha) \sin(2\pi\theta/\alpha) d\theta. \quad (8.3.62)$$

Note that the coefficients γ_{mn} and S_{mn} can be linked together as follows

$$\gamma_{mn} = -S_{nm}; \quad m, n \neq 0, \quad \gamma_{m0} = -\frac{1}{2}S_{0m}. \quad (8.3.63)$$

Finally, for the **fourth** term $\frac{1}{r^2} \frac{\partial}{\partial \theta} (D_{\theta\theta} \frac{\partial \bar{\sigma}}{\partial \theta})$ we have $D_{\theta\theta}$ is an even function in θ while $\frac{\partial \bar{\sigma}}{\partial \theta}$ is an odd function in θ and consequently, the Fourier series for this term $D_{\theta\theta} \frac{\partial \bar{\sigma}}{\partial \theta}$ will be written in sine terms,

$$D_{\theta\theta} \frac{\partial \bar{\sigma}}{\partial \theta} = 2\lambda\lambda^* f f^* \mu r^{2\lambda_r-2} \left(\left(\frac{-\pi}{\alpha}\right) \bar{\sigma}_4 \sin(\pi\theta/\alpha) + \left(\frac{-2\pi}{\alpha}\right) \bar{\sigma}_8 \sin(2\pi\theta/\alpha) + \dots \right), \quad (8.3.64)$$

which gives

$$\begin{aligned} D_{\theta\theta} \frac{\partial \bar{\sigma}}{\partial \theta} &= r^{2\lambda_r-2} (M_{11} \bar{\sigma}_4 + M_{21} \bar{\sigma}_8 + \dots) \sin(\pi\theta/\alpha) \\ &+ r^{2\lambda_r-2} (M_{12} \bar{\sigma}_4 + M_{22} \bar{\sigma}_8 + \dots) \sin(2\pi\theta/\alpha) \\ &+ \dots \end{aligned} \quad (8.3.65)$$

Such coefficients as M_{11} and M_{21} in this case are evaluated by

$$M_{11} = \left(\frac{1}{\alpha}\right) \left(\frac{-\pi}{\alpha}\right) \int_{-\alpha}^{\alpha} 2 \lambda \lambda^* f f^* \sin(\pi\theta/\alpha) \sin(\pi\theta/\alpha) d\theta, \quad (8.3.66)$$

$$M_{21} = \left(\frac{1}{\alpha}\right) \left(\frac{-2\pi}{\alpha}\right) \int_{-\alpha}^{\alpha} 2 \lambda \lambda^* f f^* \sin(2\pi\theta/\alpha) \sin(\pi\theta/\alpha) d\theta. \quad (8.3.67)$$

and generally,

$$M_{mn} = \left(\frac{1}{\alpha}\right) \left(\frac{-m\pi}{\alpha}\right) \int_{-\alpha}^{\alpha} 2 \lambda \lambda^* f f^* \sin(m\pi\theta/\alpha) \sin(n\pi\theta/\alpha) d\theta. \quad (8.3.68)$$

Therefore, applying the full formula $\frac{\partial}{\partial\theta} (D_{\theta\theta} \frac{\partial\bar{\sigma}}{\partial\theta})$,

$$\begin{aligned} \frac{\partial}{\partial\theta} \left(D_{\theta\theta} \frac{\partial\bar{\sigma}}{\partial\theta} \right) &= \frac{\partial}{\partial\theta} \left[r^{2\lambda r-2} (M_{11} \bar{\sigma}_4 + M_{21} \bar{\sigma}_8 + \dots) \sin(\pi\theta/\alpha) \right. \\ &\quad + r^{2\lambda r-2} (M_{12} \bar{\sigma}_4 + M_{22} \bar{\sigma}_8 + \dots) \sin(2\pi\theta/\alpha) \\ &\quad \left. + \dots \right], \end{aligned} \quad (8.3.69)$$

yields that

$$\begin{aligned} \frac{\partial}{\partial\theta} \left(D_{\theta\theta} \frac{\partial\bar{\sigma}}{\partial\theta} \right) &= \frac{\pi}{\alpha} \left[r^{2\lambda r-2} (M_{11} \bar{\sigma}_4 + M_{21} \bar{\sigma}_8 + \dots) \cos(\pi\theta/\alpha) \right] \\ &\quad + \frac{2\pi}{\alpha} \left[r^{2\lambda r-2} (M_{12} \bar{\sigma}_4 + M_{22} \bar{\sigma}_8 + \dots) \cos(2\pi\theta/\alpha) \right] \\ &\quad + \dots \end{aligned} \quad (8.3.70)$$

Hence, in terms of (7.3.29) we have terms from $D_{\theta\theta}$, for example

$$\partial_t \bar{\sigma}_4 = \dots + \frac{1}{r^2} \left(r^{2\lambda r-2} [N_{11} \bar{\sigma}_4 + N_{21} \bar{\sigma}_8 + \dots + N_{51} \bar{\sigma}_{20}] \right) + \dots \quad (8.3.71)$$

$$\partial_t \bar{\sigma}_8 = \dots + \frac{1}{r^2} \left(r^{2\lambda r-2} [N_{12} \bar{\sigma}_4 + N_{22} \bar{\sigma}_8 + \dots + N_{52} \bar{\sigma}_{20}] \right) + \dots \quad (8.3.72)$$

and

$$\partial_t \bar{\sigma}_{20} = \dots + \frac{1}{r^2} \left(r^{2\lambda_r - 2} [N_{15} \bar{\sigma}_4 + N_{25} \bar{\sigma}_8 + \dots + N_{55} \bar{\sigma}_{20}] \right) + \dots \quad (8.3.73)$$

where $N_{11} = \left(\frac{\pi}{\alpha}\right) M_{11}$ and $N_{12} = \left(\frac{2\pi}{\alpha}\right) M_{12}$ and this can be formed with

$$N_{mn} = \left(\frac{n\pi}{\alpha}\right) M_{mn}. \quad (8.3.74)$$

Thus, the fourth group of coefficients N_{mn} for such a specific case can be determined by the form

$$N_{mn} = \left(\frac{1}{\alpha}\right) \left(\frac{-m\pi}{\alpha}\right) \left(\frac{n\pi}{\alpha}\right) \int_{-\alpha}^{\alpha} 2 \lambda \lambda^* f f^* \sin(m\pi\theta/\alpha) \sin(n\pi\theta/\alpha) d\theta, \quad (8.3.75)$$

$$N_{mn} = N_{nm}, \quad m, n = 1, 2, \dots \quad (8.3.76)$$

Here are some coefficients N_{mn} based on (8.3.75):

$$N_{11} = \left(\frac{1}{\alpha}\right) \left(\frac{-\pi}{\alpha}\right) \left(\frac{\pi}{\alpha}\right) \int_{-\alpha}^{\alpha} 2 \lambda \lambda^* f f^* \sin(\pi\theta/\alpha) \sin(\pi\theta/\alpha) d\theta, \quad (8.3.77)$$

$$N_{12} = \left(\frac{1}{\alpha}\right) \left(\frac{-\pi}{\alpha}\right) \left(\frac{2\pi}{\alpha}\right) \int_{-\alpha}^{\alpha} 2 \lambda \lambda^* f f^* \sin(\pi\theta/\alpha) \sin(2\pi\theta/\alpha) d\theta, \quad (8.3.78)$$

$$N_{21} = \left(\frac{1}{\alpha}\right) \left(\frac{-2\pi}{\alpha}\right) \left(\frac{\pi}{\alpha}\right) \int_{-\alpha}^{\alpha} 2 \lambda \lambda^* f f^* \sin(2\pi\theta/\alpha) \sin(\pi\theta/\alpha) d\theta, \quad (8.3.79)$$

$$N_{22} = \left(\frac{1}{\alpha}\right) \left(\frac{-2\pi}{\alpha}\right) \left(\frac{2\pi}{\alpha}\right) \int_{-\alpha}^{\alpha} 2 \lambda \lambda^* f f^* \sin(2\pi\theta/\alpha) \sin(2\pi\theta/\alpha) d\theta. \quad (8.3.80)$$

The other coefficients are determined by a similar way. However, determination of the term $\kappa \left(\frac{1}{r} \frac{\partial}{\partial r} \left(r \frac{\partial \bar{\sigma}}{\partial r} \right) + \frac{1}{r^2} \frac{\partial^2 \bar{\sigma}}{\partial \theta^2} \right)$ yields

$$\begin{aligned}
 \kappa \left(\frac{1}{r} \frac{\partial}{\partial r} \left(r \frac{\partial \bar{\sigma}}{\partial r} \right) \right) &= \frac{\kappa}{r} \frac{\partial}{\partial r} \left(r \frac{\partial \bar{\sigma}_0}{\partial r} \right) + \frac{\kappa}{r} \frac{\partial}{\partial r} \left(r \frac{\partial \bar{\sigma}_4}{\partial r} \right) \cos(\pi\theta/\alpha) \\
 &+ \frac{\kappa}{r} \frac{\partial}{\partial r} \left(r \frac{\partial \bar{\sigma}_8}{\partial r} \right) \cos(2\pi\theta/\alpha) + \frac{\kappa}{r} \frac{\partial}{\partial r} \left(r \frac{\partial \bar{\sigma}_{12}}{\partial r} \right) \cos(3\pi\theta/\alpha) \\
 &+ \frac{\kappa}{r} \frac{\partial}{\partial r} \left(r \frac{\partial \bar{\sigma}_{16}}{\partial r} \right) \cos(4\pi\theta/\alpha) + \frac{\kappa}{r} \frac{\partial}{\partial r} \left(r \frac{\partial \bar{\sigma}_{20}}{\partial r} \right) \cos(5\pi\theta/\alpha)
 \end{aligned} \tag{8.3.81}$$

and

$$\begin{aligned}
 \kappa \left(\frac{1}{r^2} \frac{\partial^2 \bar{\sigma}}{\partial \theta^2} \right) &= - \left(\frac{\pi}{\alpha} \right)^2 \frac{\kappa}{r^2} (\bar{\sigma}_4 \cos(\pi\theta/\alpha) + 4 \bar{\sigma}_8 \cos(2\pi\theta/\alpha) \\
 &+ 9 \bar{\sigma}_{12} \cos(3\pi\theta/\alpha) + 16 \bar{\sigma}_{16} \cos(4\pi\theta/\alpha) \\
 &+ 25 \bar{\sigma}_{20} \cos(5\pi\theta/\alpha)).
 \end{aligned} \tag{8.3.82}$$

Our specific calculations provided above yield the following equations for the essential quantities $\bar{\sigma}_0, \bar{\sigma}_4, \dots$ and $\bar{\sigma}_{20}$:

$$\begin{aligned}
 \frac{\partial \bar{\sigma}_0}{\partial t} &= \beta_{00} (1/r) \frac{\partial}{\partial r} \left(r r^{2\lambda_r-2} \frac{\partial \bar{\sigma}_0}{\partial r} \right) + \beta_{10} (1/r) \frac{\partial}{\partial r} \left(r r^{2\lambda_r-2} \frac{\partial \bar{\sigma}_4}{\partial r} \right) \\
 &+ \beta_{20} (1/r) \frac{\partial}{\partial r} \left(r r^{2\lambda_r-2} \frac{\partial \bar{\sigma}_8}{\partial r} \right) + \dots + \gamma_{10} (1/r) \frac{\partial}{\partial r} (r^{2\lambda_r-2} \bar{\sigma}_4) \\
 &+ \gamma_{20} (1/r) \frac{\partial}{\partial r} (r^{2\lambda_r-2} \bar{\sigma}_8) \\
 &+ \dots + \kappa (1/r) \frac{\partial}{\partial r} \left(r \frac{\partial \bar{\sigma}_0}{\partial r} \right).
 \end{aligned} \tag{8.3.83}$$

$$\begin{aligned}
 \frac{\partial \bar{\sigma}_4}{\partial t} &= \beta_{01} (1/r) \frac{\partial}{\partial r} \left(r r^{2\lambda_r-2} \frac{\partial \bar{\sigma}_0}{\partial r} \right) + \beta_{11} (1/r) \frac{\partial}{\partial r} \left(r r^{2\lambda_r-2} \frac{\partial \bar{\sigma}_4}{\partial r} \right) \\
 &+ \beta_{21} (1/r) \frac{\partial}{\partial r} \left(r r^{2\lambda_r-2} \frac{\partial \bar{\sigma}_8}{\partial r} \right) + \dots + \gamma_{11} (1/r) \frac{\partial}{\partial r} (r^{2\lambda_r-2} \bar{\sigma}_4) \\
 &+ \gamma_{21} (1/r) \frac{\partial}{\partial r} (r^{2\lambda_r-2} \bar{\sigma}_8) + \dots + S_{01} (1/r) \left(r^{2\lambda_r-2} \frac{\partial \bar{\sigma}_0}{\partial r} \right) \\
 &+ S_{11} (1/r) \left(r^{2\lambda_r-2} \frac{\partial \bar{\sigma}_4}{\partial r} \right) + S_{21} (1/r) \left(r^{2\lambda_r-2} \frac{\partial \bar{\sigma}_8}{\partial r} \right) \\
 &+ \dots + N_{11} (1/r^2) (r^{2\lambda_r-2} \bar{\sigma}_4) + N_{21} (1/r^2) (r^{2\lambda_r-2} \bar{\sigma}_8) \\
 &+ \dots + \kappa (1/r) \frac{\partial}{\partial r} \left(r \frac{\partial \bar{\sigma}_4}{\partial r} \right) - (\pi/\alpha)^2 \left(\frac{\kappa}{r^2} \right) \bar{\sigma}_4. \tag{8.3.84}
 \end{aligned}$$

$$\begin{aligned}
 \frac{\partial \bar{\sigma}_8}{\partial t} &= \beta_{02} (1/r) \frac{\partial}{\partial r} \left(r r^{2\lambda_r-2} \frac{\partial \bar{\sigma}_0}{\partial r} \right) + \beta_{12} (1/r) \frac{\partial}{\partial r} \left(r r^{2\lambda_r-2} \frac{\partial \bar{\sigma}_4}{\partial r} \right) \\
 &+ \beta_{22} (1/r) \frac{\partial}{\partial r} \left(r r^{2\lambda_r-2} \frac{\partial \bar{\sigma}_8}{\partial r} \right) + \dots + \gamma_{12} (1/r) \frac{\partial}{\partial r} (r^{2\lambda_r-2} \bar{\sigma}_4) \\
 &+ \gamma_{22} (1/r) \frac{\partial}{\partial r} (r^{2\lambda_r-2} \bar{\sigma}_8) + \dots + S_{02} (1/r) \left(r^{2\lambda_r-2} \frac{\partial \bar{\sigma}_0}{\partial r} \right) \\
 &+ S_{12} (1/r) \left(r^{2\lambda_r-2} \frac{\partial \bar{\sigma}_4}{\partial r} \right) + S_{22} (1/r) \left(r^{2\lambda_r-2} \frac{\partial \bar{\sigma}_8}{\partial r} \right) \\
 &+ \dots + N_{12} (1/r^2) (r^{2\lambda_r-2} \bar{\sigma}_4) + N_{22} (1/r^2) (r^{2\lambda_r-2} \bar{\sigma}_8) \\
 &+ \dots + \kappa (1/r) \frac{\partial}{\partial r} \left(r \frac{\partial \bar{\sigma}_8}{\partial r} \right) - (2\pi/\alpha)^2 \left(\frac{\kappa}{r^2} \right) \bar{\sigma}_8. \tag{8.3.85}
 \end{aligned}$$

Similar calculations are followed for the averages $\bar{\sigma}_{12}$, $\bar{\sigma}_{16}$ and $\bar{\sigma}_{20}$,

$$\begin{aligned}
 \frac{\partial \bar{\sigma}_{12}}{\partial t} &= \beta_{03} (1/r) \frac{\partial}{\partial r} \left(r r^{2\lambda_r-2} \frac{\partial \bar{\sigma}_0}{\partial r} \right) + \beta_{13} (1/r) \frac{\partial}{\partial r} \left(r r^{2\lambda_r-2} \frac{\partial \bar{\sigma}_4}{\partial r} \right) \\
 &+ \beta_{23} (1/r) \frac{\partial}{\partial r} \left(r r^{2\lambda_r-2} \frac{\partial \bar{\sigma}_8}{\partial r} \right) + \dots + \gamma_{13} (1/r) \frac{\partial}{\partial r} \left(r^{2\lambda_r-2} \bar{\sigma}_4 \right) \\
 &+ \gamma_{23} (1/r) \frac{\partial}{\partial r} \left(r^{2\lambda_r-2} \bar{\sigma}_8 \right) + \dots + S_{03} (1/r) \left(r^{2\lambda_r-2} \frac{\partial \bar{\sigma}_0}{\partial r} \right) \\
 &+ S_{13} (1/r) \left(r^{2\lambda_r-2} \frac{\partial \bar{\sigma}_4}{\partial r} \right) + S_{23} (1/r) \left(r^{2\lambda_r-2} \frac{\partial \bar{\sigma}_8}{\partial r} \right) \\
 &+ \dots + N_{13} (1/r^2) \left(r^{2\lambda_r-2} \bar{\sigma}_4 \right) + N_{23} (1/r^2) \left(r^{2\lambda_r-2} \bar{\sigma}_8 \right) \\
 &+ \dots + \kappa (1/r) \frac{\partial}{\partial r} \left(r \frac{\partial \bar{\sigma}_{12}}{\partial r} \right) - (3\pi/\alpha)^2 \left(\frac{\kappa}{r^2} \right) \bar{\sigma}_{12} \tag{8.3.86}
 \end{aligned}$$

$$\begin{aligned}
 \frac{\partial \bar{\sigma}_{16}}{\partial t} &= \beta_{04} (1/r) \frac{\partial}{\partial r} \left(r r^{2\lambda_r-2} \frac{\partial \bar{\sigma}_0}{\partial r} \right) + \beta_{14} (1/r) \frac{\partial}{\partial r} \left(r r^{2\lambda_r-2} \frac{\partial \bar{\sigma}_4}{\partial r} \right) \\
 &+ \beta_{24} (1/r) \frac{\partial}{\partial r} \left(r r^{2\lambda_r-2} \frac{\partial \bar{\sigma}_8}{\partial r} \right) + \dots + \gamma_{14} (1/r) \frac{\partial}{\partial r} \left(r^{2\lambda_r-2} \bar{\sigma}_4 \right) \\
 &+ \gamma_{24} (1/r) \frac{\partial}{\partial r} \left(r^{2\lambda_r-2} \bar{\sigma}_8 \right) + S_{04} (1/r) \left(r^{2\lambda_r-2} \frac{\partial \bar{\sigma}_0}{\partial r} \right) \\
 &+ \dots + S_{14} (1/r) \left(r^{2\lambda_r-2} \frac{\partial \bar{\sigma}_4}{\partial r} \right) + S_{24} (1/r) \left(r^{2\lambda_r-2} \frac{\partial \bar{\sigma}_8}{\partial r} \right) \\
 &+ \dots + N_{14} (1/r^2) \left(r^{2\lambda_r-2} \bar{\sigma}_4 \right) + N_{24} (1/r^2) \left(r^{2\lambda_r-2} \bar{\sigma}_8 \right) \\
 &+ \dots + \kappa (1/r) \frac{\partial}{\partial r} \left(r \frac{\partial \bar{\sigma}_{16}}{\partial r} \right) - (4\pi/\alpha)^2 \left(\frac{\kappa}{r^2} \right) \bar{\sigma}_{16} \tag{8.3.87}
 \end{aligned}$$

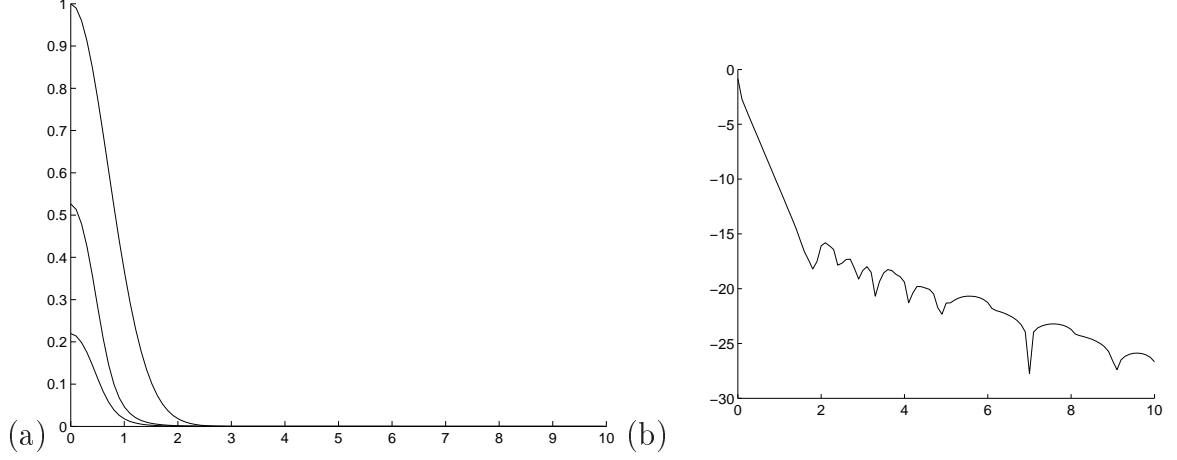


Figure 8.2: Plots of (a) solution profiles of averaged scalar field $\bar{\sigma}(r, t)$ against r for $0 \leq t \leq 2$ for the flow near corner regions of a semi-angle $\alpha = \pi/4$ and $\lambda = 3.73959 + 1.1191i$ with a three-mode truncation resulting from (8.3.12). In (b) $\log \bar{\sigma}(r, t)$ is plotted at $r = 0.45$ against time t ; $0 \leq t \leq 10$ with 201 r -meshpoints between 0 and 10. The fit slope in (b) is 9.06.

$$\begin{aligned}
 \frac{\partial \bar{\sigma}_{20}}{\partial t} &= \beta_{05} (1/r) \frac{\partial}{\partial r} \left(r r^{2\lambda_r-2} \frac{\partial \bar{\sigma}_0}{\partial r} \right) + \beta_{15} (1/r) \frac{\partial}{\partial r} \left(r r^{2\lambda_r-2} \frac{\partial \bar{\sigma}_4}{\partial r} \right) \\
 &+ \beta_{25} (1/r) \frac{\partial}{\partial r} \left(r r^{2\lambda_r-2} \frac{\partial \bar{\sigma}_8}{\partial r} \right) + \dots + \gamma_{15} (1/r) \frac{\partial}{\partial r} \left(r^{2\lambda_r-2} \bar{\sigma}_4 \right) \\
 &+ \gamma_{25} (1/r) \frac{\partial}{\partial r} \left(r^{2\lambda_r-2} \bar{\sigma}_8 \right) + \dots + S_{05} (1/r) \left(r^{2\lambda_r-2} \frac{\partial \bar{\sigma}_0}{\partial r} \right) \\
 &+ S_{15} (1/r) \left(r^{2\lambda_r-2} \frac{\partial \bar{\sigma}_4}{\partial r} \right) + S_{25} (1/r) \left(r^{2\lambda_r-2} \frac{\partial \bar{\sigma}_8}{\partial r} \right) \\
 &+ \dots + N_{15} (1/r^2) \left(r^{2\lambda_r-2} \bar{\sigma}_4 \right) + N_{25} (1/r^2) \left(r^{2\lambda_r-2} \bar{\sigma}_8 \right) \\
 &+ \dots + \kappa (1/r) \frac{\partial}{\partial r} \left(r \frac{\partial \bar{\sigma}_{20}}{\partial r} \right) - (5\pi/\alpha)^2 \left(\frac{\kappa}{r^2} \right) \bar{\sigma}_{20}. \tag{8.3.88}
 \end{aligned}$$

We can rewrite our previous equations in the following form

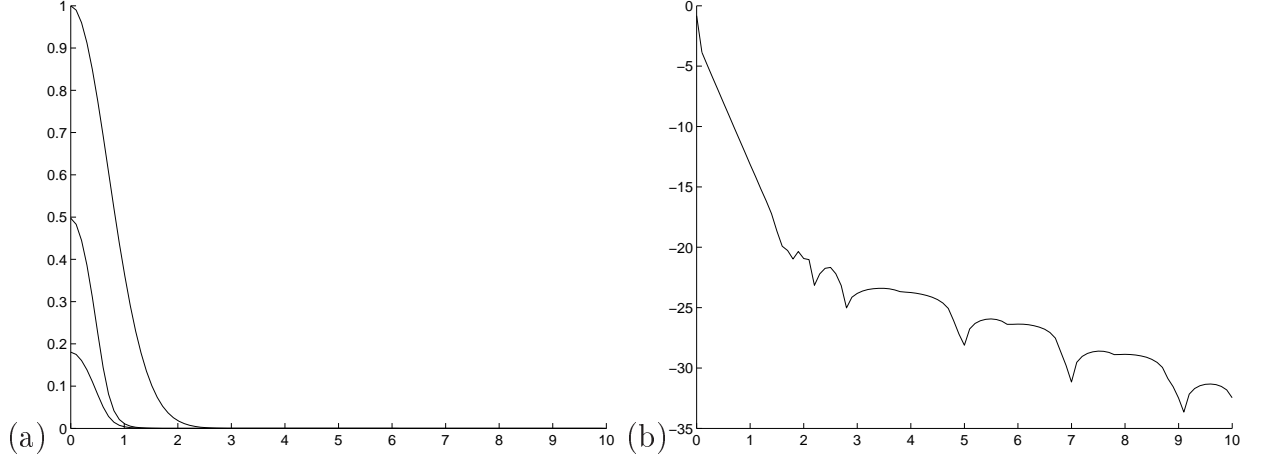


Figure 8.3: Plots of (a) solution profiles of averaged scalar field $\bar{\sigma}(r, t)$ against r for $0 \leq t \leq 2$ for the flow near corner regions of a semi-angle $\alpha = \pi/6$ and $\lambda = 5.05933 + 1.95205i$ with a three-mode truncation resulting from (8.3.12). In (b) $\log \bar{\sigma}(r, t)$ is plotted at $r = 0.45$ against time t ; $0 \leq t \leq 10$ with 201 r -meshpoints between 0 and 10. The fit slope in (b) is 10.24.

$$\begin{aligned}
 \frac{\partial \bar{\sigma}_{4n}}{\partial t} &= \sum_{m=0}^{\infty} \beta_{mn} (\mu/r) \frac{\partial}{\partial r} \left(r^{2\lambda_r-1} \frac{\partial \bar{\sigma}_{4m}}{\partial r} \right) \\
 &+ \sum_{m=1}^{\infty} \gamma_{mn} (\mu/r) \frac{\partial}{\partial r} \left(r^{2\lambda_r-2} \bar{\sigma}_{4m} \right) \\
 &+ \sum_{m=0}^{\infty} S_{mn} \mu r^{2\lambda_r-3} \frac{\partial \bar{\sigma}_{4m}}{\partial r} \\
 &+ \sum_{m=1}^{\infty} N_{mn} \mu r^{2\lambda_r-4} \bar{\sigma}_{4m} \\
 &+ \dots + (\kappa/r) \frac{\partial}{\partial r} \left(r \frac{\partial \bar{\sigma}_{4n}}{\partial r} \right) - (\kappa/r^2) \left(\frac{n\pi}{\alpha} \right)^2 \bar{\sigma}_{4n}. \quad (8.3.89)
 \end{aligned}$$

for $m, n=0,1,2,\dots$

8.4 Numerical solutions and results

Based on the above discussion, in order to solve the equations (8.3.89) for averaged scalar fields we first use **Maple** to calculate all the coefficients β_{mn} , γ_{mn} , S_{mn} and

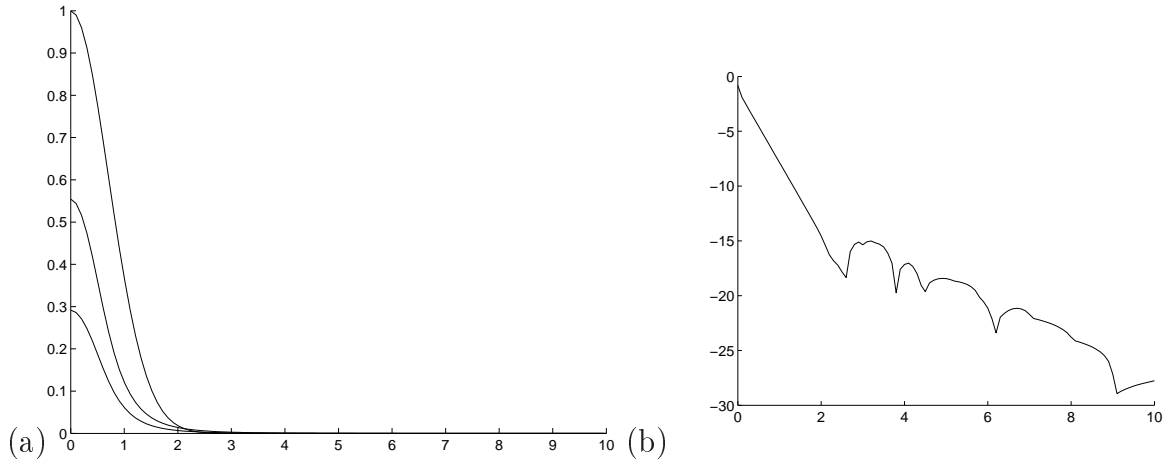


Figure 8.4: Plots of (a) solution profiles of averaged scalar field $\bar{\sigma}(r, t)$ against r for $0 \leq t \leq 2$ for the flow near corner regions of a semi-angle $\alpha = \pi/3$ and corresponding $\lambda = 3.09414 + 0.60458i$ with a three-mode truncation resulting from (8.3.12). In (b) $\log \bar{\sigma}(r, t)$ is plotted at $r = 0.45$ against time t ; $0 \leq t \leq 10$ with 201 r -meshpoints between 0 and 10. The fit slope in (b) is 6.59.

N_{mn} appearing in this equation and required to approximate the averages $\bar{\sigma}_0, \bar{\sigma}_4, \dots, \bar{\sigma}_{20}$. The values of these coefficients are obtained by evaluating the integrations defining the coefficients in the cases of the corner semi-angles $\alpha = \pi/3, \pi/4$, and $\pi/6$ and the corresponding values of λ . These calculations are built based on Eqs. (8.3.2) and (8.3.3). To obtain the solution profiles for the equations (8.3.89) corresponding to $n = 0, 1, 2, 3, 4, 5$, we transfer the values of these coefficients to **Matlab** and use the PDE solver, ‘**pdepe**’ to integrate the equations from (8.3.83) to (8.3.88) or (8.3.89) as we have discussed in the last chapter. Finally, we display these averages in the Cartesian system according to both three and six-mode truncations.

Plots of scalar evolution for the flow near corner region (with $\kappa = 1$ and $\mu = 1$ still) of $\alpha = \pi/4, \pi/6$ and $\pi/3$ with a three-mode truncation (8.3.12) are shown in Figs. 8.2, 8.3 and 8.4, respectively with the corresponding decay rates of the scalar

variance up to time $t = 10$. Note the value of the slope in each case. In panels (b) in these figures the obtained slope is determined based on the data points in each case. For example, in Fig. 8.2 (b), the fit slope is measured based on the points (1.4, -14.88) and (0.2, -4.01) while in Fig. 8.3(b) it is based on (0.2, -5.085) and (1.2, -15.323) and on (1.5, -11.140) and (0.5, -4.550) for the slope in Fig. 8.4(b). Note the complicated behaviour of the scalar in panels (b) at later times in these figures which can be attributed to a numerical error.

Figure 8.5 shows the solution profiles of $\bar{\sigma}_0$, $\bar{\sigma}_4$ and $\bar{\sigma}_8$ with a three-mode truncation resulting from (8.3.12). These profiles correspond to $\alpha = \pi/4$ with $\lambda = 3.73959 + 1.1191i$. See the scale on the vertical axis in each case. The solution profiles of $\bar{\sigma}_0$, $\bar{\sigma}_4, \dots, \bar{\sigma}_{20}$ based on (8.3.89) are shown in Fig. 8.6 and Fig. 8.7 with a six-mode truncation resulting from (8.3.13).

The averaged scalar fields (8.3.89) are displayed in the Cartesian co-ordinate system in Figs. 8.8, 8.9 and 8.10.

8.4.1 Decay of the scalar in the Moffatt problem

In this section we provide calculations to evaluate the decay rate scaling for the flow driven near to the corner. Note that, in the calculations below we put μ back in. However, based on our discussion provided in Section §7.6 the D_{ij} given by (7.2.14), (7.2.15) and (7.2.16) can be now rewritten as

$$D_{ij} = \mu r^{2\lambda_r - 2} F_{ij}(\theta). \quad (8.4.1)$$

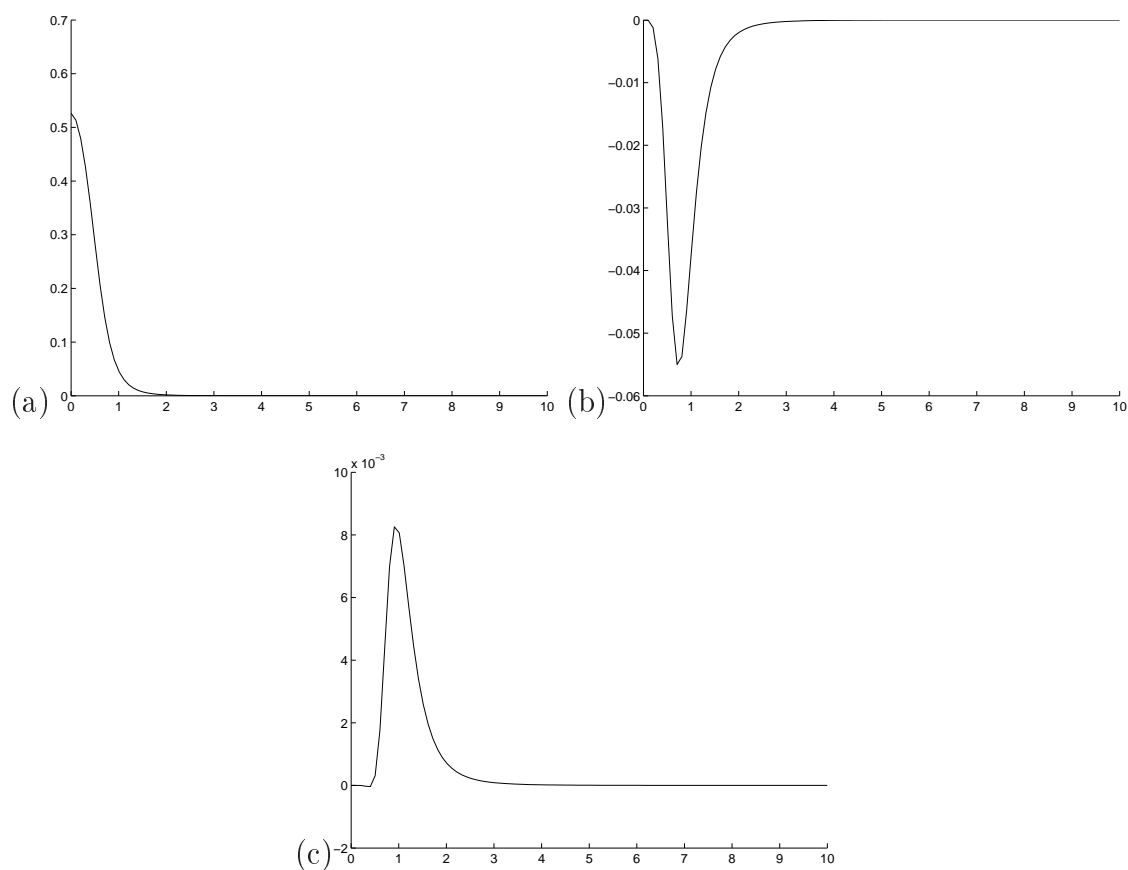


Figure 8.5: Solution profiles based on (8.3.89) with a three-mode truncation resulting from (8.3.12) and computed for averaged scalar field (a) $\bar{\sigma}_0(r, t)$, (b) $\bar{\sigma}_4(r, t)$ and (c) $\bar{\sigma}_8(r, t)$ against r at $t = 0.1$ with $\alpha = \pi/4$ and $\lambda = 3.73959 + 1.1191i$ and 201 r -meshpoints between 0 and 10. The vertical axis is scaled by 10^{-3} in (c).

In this case the evolution of the scalar field is found as

$$\frac{\partial \bar{\sigma}}{\partial t} = \frac{\partial}{\partial x_i} \left(\mu r^{2\lambda_r-2} F_{ij}(\theta) \frac{\partial \bar{\sigma}}{\partial x_j} \right) + \kappa \nabla^2 \bar{\sigma}. \quad (8.4.2)$$

With a general scaling

$$r = a r', \quad x_i = a x'_i, \quad t = b t'. \quad (8.4.3)$$

equation (8.4.2) becomes

$$\left(\frac{1}{b} \right) \frac{\partial \bar{\sigma}}{\partial t'} = \left(\frac{1}{a} \right) \frac{\partial}{\partial x'_i} \left(\mu a^{2\lambda_r-2} r'^{2\lambda_r-2} F_{ij}(\theta) \frac{1}{a} \frac{\partial \bar{\sigma}}{\partial x'_j} \right) + \left(\frac{\kappa}{a^2} \right) \nabla'^2 \bar{\sigma}. \quad (8.4.4)$$

Choosing

$$a^{2\lambda_r-2} = \frac{\kappa}{\mu}, \quad \frac{a^2}{\kappa} \left(\frac{1}{b} \right) = 1, \quad (8.4.5)$$

leads us to get

$$b = \kappa^{-\alpha_D} \mu^{-\zeta}; \quad \alpha_D = (\lambda_r - 2)/(\lambda_r - 1), \quad \zeta = (1/\lambda_r - 1). \quad (8.4.6)$$

Now multiplying both sides of Eq. (8.4.4) by $\left(\frac{a^2}{\kappa} \right)$ and the substitution (8.4.5) transforms Eq. (8.4.4) into a simpler one in terms of (r', θ) ,

$$\frac{\partial \bar{\sigma}}{\partial t'} = \frac{\partial}{\partial x'_i} \left(r'^{2\lambda_r-2} F_{ij}(\theta) \frac{\partial \bar{\sigma}}{\partial x'_j} \right) + \nabla'^2 \bar{\sigma}. \quad (8.4.7)$$

Solving this equation numerically for an exponential decay γ' as an eigenvalue problem with a no-flux boundary condition and $\mu = \kappa = 1$ (as we did in Chapter 7) gives the solution form

$$\bar{\sigma} = e^{-\gamma' t'}, \quad (8.4.8)$$

α	λ	C_D	α_D	ζ
$\pi/6 = 30^\circ$	$5.05933+1.95205i$	10.247	0.7536539281	0.4775229927
$\pi/4 = 45^\circ$	$3.73959+1.1191i$	9.060	0.6349818768	0.3650181231
$\pi/3 = 60^\circ$	$3.09414+0.60458i$	6.598	0.5224770073	0.2463460719

Table 8.2: Corresponding values for the corner angles (2α) based on the three-mode truncation (8.3.12): decay rate slopes C_D , scaling laws α_D and ζ for theoretical decay rate γ given by (8.4.12).

Therefore, we can specify that

$$\gamma' = C_D, \quad t' = \frac{t}{b}, \quad (8.4.9)$$

With these scales, Eq. (8.4.8) can be obtained as

$$\bar{\sigma} = e^{-C_D t/b}, \quad (8.4.10)$$

Substituting with $b = \kappa^{-\alpha_D} \mu^{-\zeta}$ we get the solution (8.4.10) in terms of κ and μ ;

$$\begin{aligned} \bar{\sigma} &\propto e^{-C_D t \kappa^{\alpha_D} \mu^\zeta} \\ &= e^{-\gamma t}. \end{aligned} \quad (8.4.11)$$

where the long-time exponential decay rate is identified with

$$\gamma = C_D \kappa^{\alpha_D} \mu^\zeta; \quad \alpha_D = (\lambda_r - 2)/(\lambda_r - 1), \quad \zeta = (1/\lambda_r - 1). \quad (8.4.12)$$

Our results in last chapter correspond to $\lambda_r = 4$ and $\alpha = 2/3$, but for Moffatt eddies in a right-angled corner we have $\lambda_r \simeq 3.73959$, giving a faster decay, $\alpha \simeq 0.63498$.

Table 8.2 and 8.3 includes corner angles (2α) with the corresponding evaluated

α	λ	C_D	α_D	ζ
$\pi/6 = 30^\circ$	$5.05933+1.95205i$	9.99	0.7536539281	0.4775229927
$\pi/4 = 45^\circ$	$3.73959+1.1191i$	8.259	0.6349818768	0.3650181231
$\pi/3 = 60^\circ$	$3.09414+0.60458i$	5.286	0.5224770073	0.2463460719

Table 8.3: Corresponding values for the corner angles (2α) based on the six-mode truncation (8.3.13): decay rate slopes C_D , scaling laws α_D and ζ for theoretical decay rate γ given by (8.4.12).

values of decay rate slopes C_D , scaling laws α_D and ζ indicated in (8.4.12). The former shows values obtained with the three-mode truncation (8.3.12) whereas for the latter, it is with the six-mode truncation (8.3.13). We expect that the obtained values of slopes would be in good agreement if the truncation used for the approximation were of high modes (we have used the three and six modes in this work). However, with both modes it is clear that the shown slopes increase (decay rate decreases) as the value of α is decreased.

Figures 8.8, 8.9 and 8.10 show scalar field distribution represented in the Cartesian co-ordinate system and corresponding to the corner semi-angles $\alpha = \pi/3, \pi/4$ and $\pi/6$. Both approximations 3-mode (8.3.12) shown in panels (a) and 6-mode (8.3.13) (panels (b)) in these figures provide a good representation. Particularly, for the approximation (8.3.13) shown in panels (b) in these three figures. Similarly to Fig. 7.12, the scalar field distribution expands with a pointy elongated shape along the axes $\theta = \pm\pi/3 = 60^\circ$ and the axis $\theta = \pi$ in Fig. 8.8, along the axes $\theta = \pm\pi/4$ in Fig. 8.9 and along the axes $\theta = \pm\pi/6 = 30^\circ$ and the axis $\theta = \pi/2$ in Fig. 8.10. This elongated expansion appears clearly in Fig. 8.8(b) with a corner angle $2\alpha = 120^\circ$.

8.5 Summary

In light of the discussion introduced in this chapter we can summarise our findings as follows:

Insight into the Moffatt corner problem has been provided, whereby we have specifically analysed the structure of the flow field driven near a corner region. Using the system of polar co-ordinates, averaged scalar fields are approximated by specifying the components of the effective diffusive tensor D_{ij} of the flow in terms of (r, θ) . Our results reveal a diffusivity tensor $D_{ij} \propto r^{2\lambda_r-2}$ with λ_r the real part of λ . This gives a corner boundary layer of scale $x, y = O(\kappa^{1/(2\lambda_r-2)})$ and, from consideration of the time-derivative, the decay rate will be $\gamma = O(\kappa^\alpha)$ with $\alpha = (\lambda_r - 2)/(\lambda_r - 1)$. If the semi-angle α of the corner in (8.2.22) is increased we obtain yet more rapid decay of passive scalars; for example moving to a hexagonal shaped container, the angle β is $\pi/3$ and $\lambda_r \simeq 3.09414$, giving further decrease in the scaling exponent to $\alpha \simeq 0.52248$. If on the other hand the semi-angle is reduced decay is suppressed; for instance for a triangular container, $\beta = \pi/6$, $\lambda_r \simeq 5.05933$ and the decay is much reduced, with $\alpha \simeq 0.75365$.

We have expanded the scalar field $\bar{\sigma}(r, \theta, t)$ using Fourier series in θ , so that the coefficients required for the approximation are obtained. Solution profiles of averaged scalar field are explored with values of slopes that are decreasing gradually as the corner angle (2α) is increased. Moreover, the long-time behaviour characterising the scalar decay has been obtained analytically with an exponential decay $\gamma(\kappa) = C\kappa^\alpha$ confirming our previous result established numerically and theoretically in Part I and Part II of this thesis. The exponent α in this part is determined by the structure of the corner eddies.

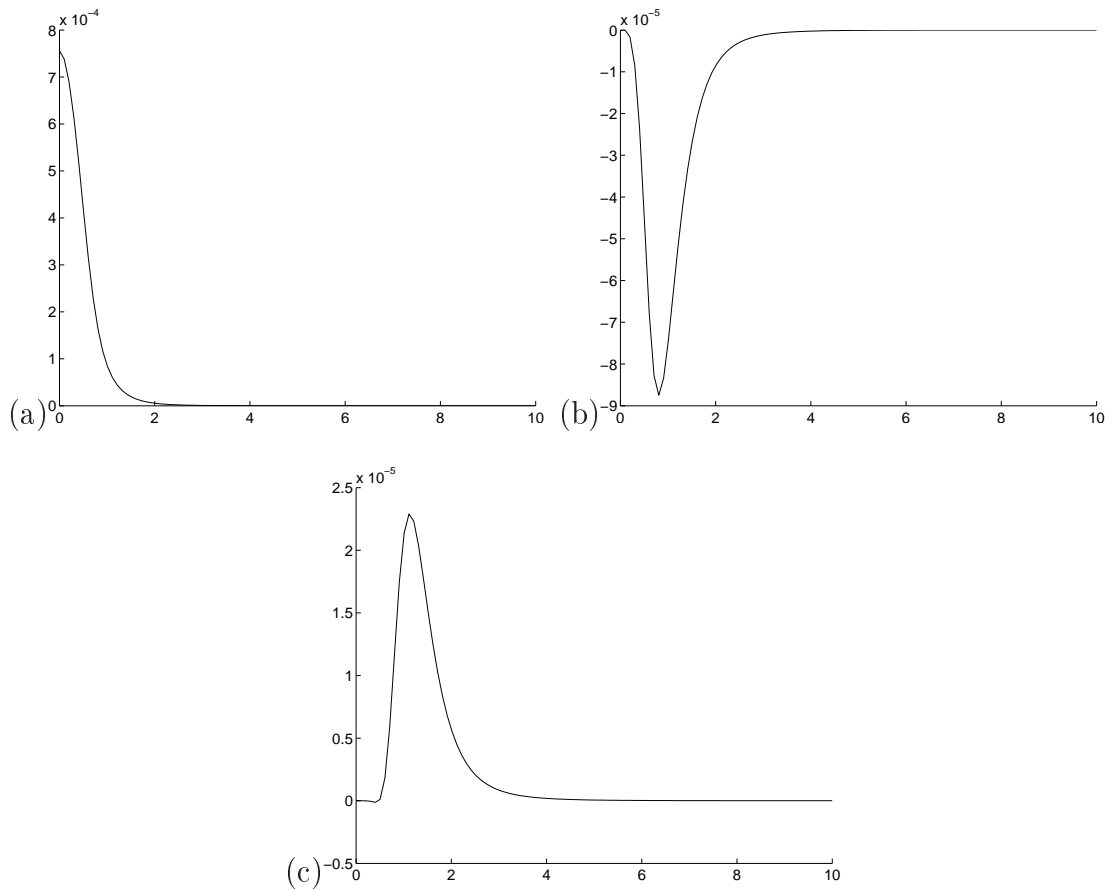


Figure 8.6: Solution profile based on (8.3.89) with a six-mode truncation resulting from (8.3.13) and computed for averaged scalar field (a) $\bar{\sigma}_0(r, t)$, (b) $\bar{\sigma}_4(r, t)$ and (c) $\bar{\sigma}_8(r, t)$ against r at $t = 0.9$ with $\alpha = \pi/4$ and $\lambda = 3.73959 + 1.1191i$ and 201 r -meshpoints between 0 and 10. The vertical axis is scaled by (a) 10^{-4} and (b,c) 10^{-5} .

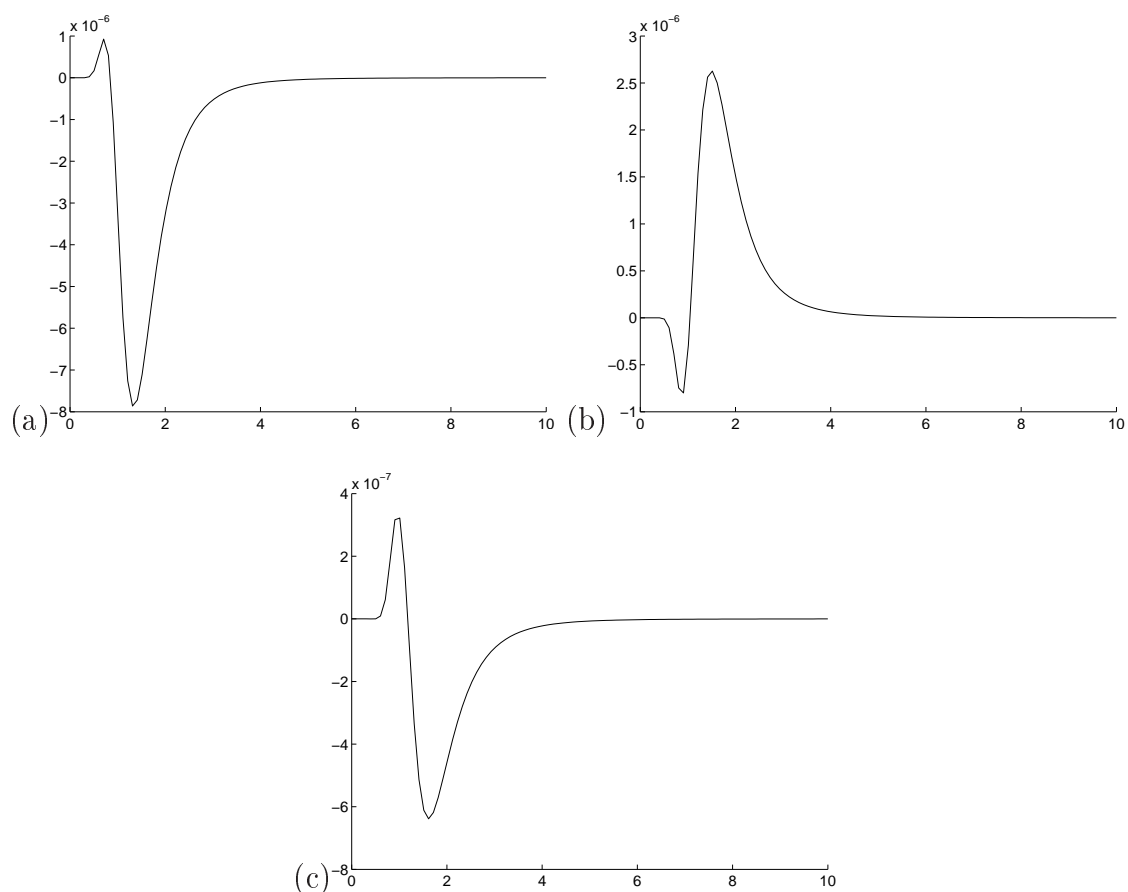
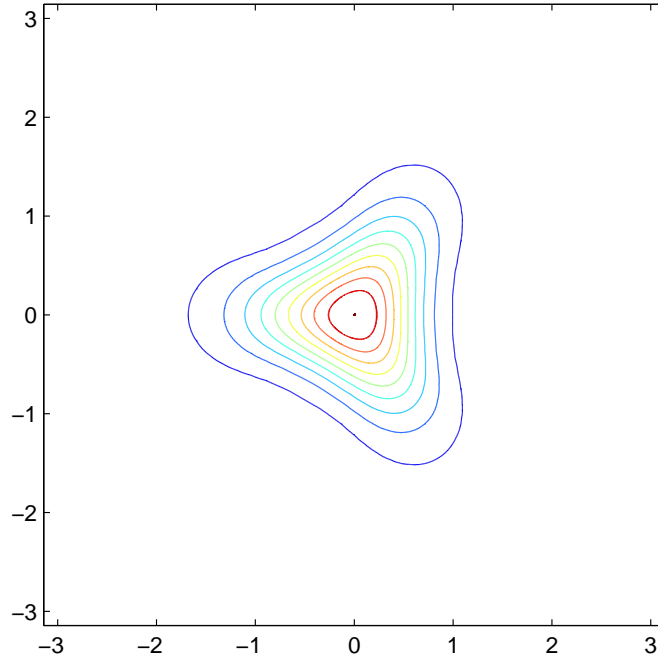
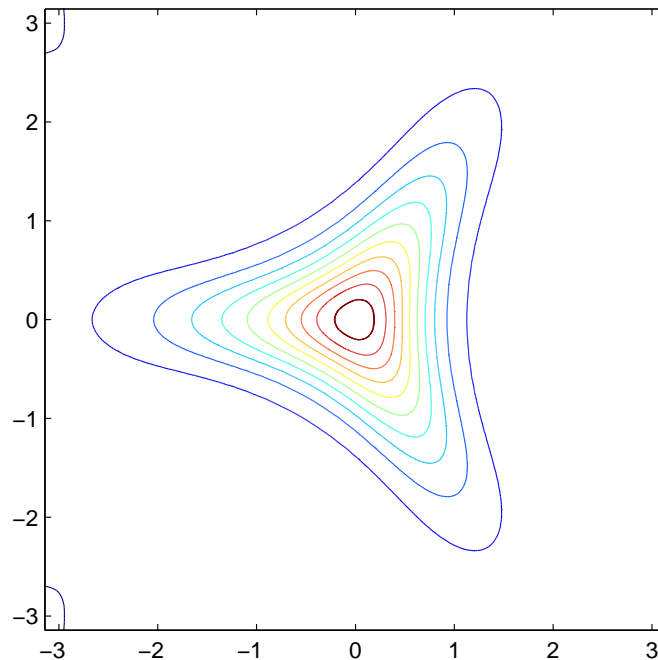


Figure 8.7: Solution profile based on (8.3.89) with a six-mode truncation resulting from (8.3.13) and computed for averaged scalar field (a) $\bar{\sigma}_{12}(r, t)$, (b) $\bar{\sigma}_{16}(r, t)$ and (c) $\bar{\sigma}_{20}(r, t)$ against r at $t = 0.9$ with $\alpha = \pi/4$ and $\lambda = 3.73959 + 1.1191i$ and 201 r -meshpoints between 0 and 10. The vertical axis is scaled by (a,b) 10^{-6} and (c) 10^{-7} .

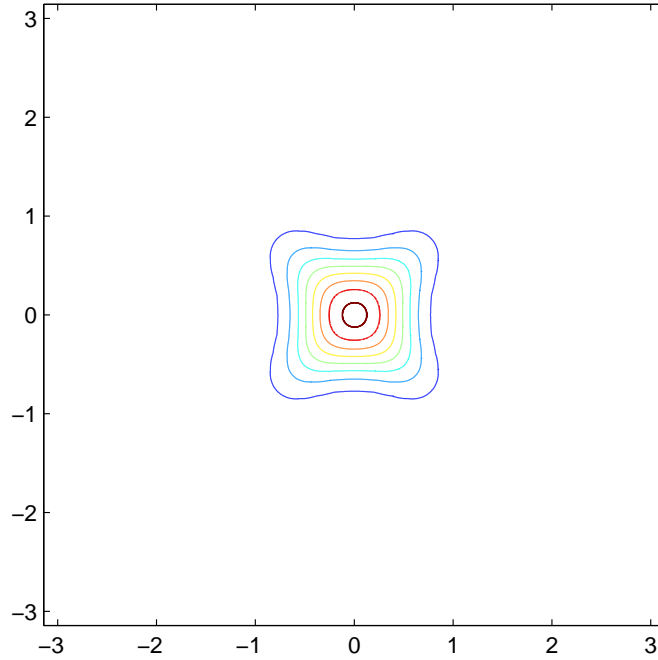


(a)

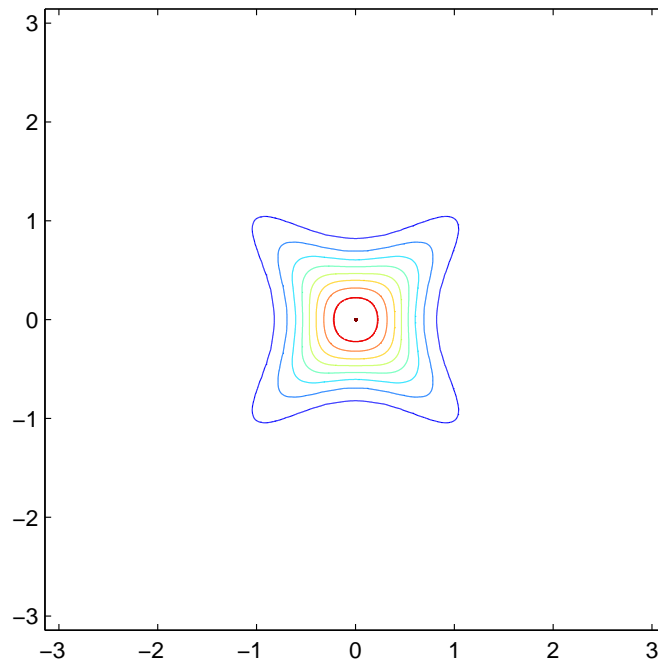


(b)

Figure 8.8: Plots of the scalar distribution of the flow near to the corner of a semi-angle $\alpha = \pi/3$ and $\lambda = 3.09414 + 0.60458i$ in the Cartesian co-ordinate system. Panel (a) shows the approximation of such distribution resulting from (8.3.12), while in (b) it is approximated by (8.3.13). 269

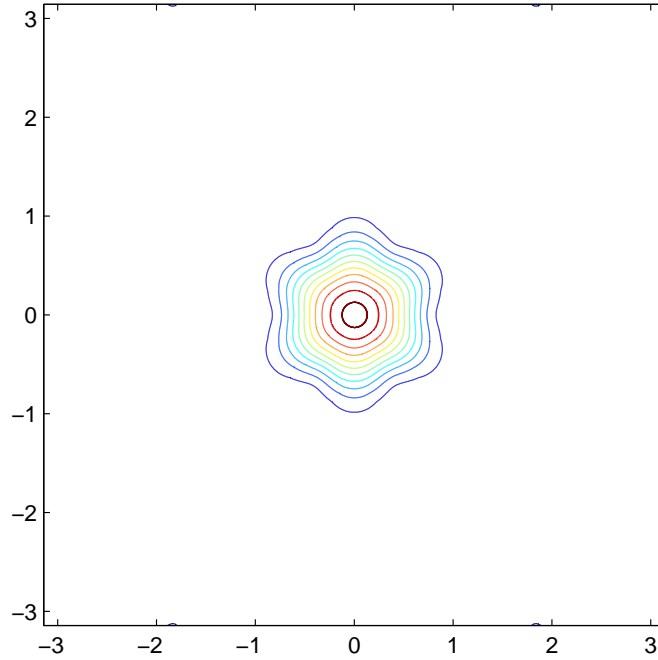


(a)

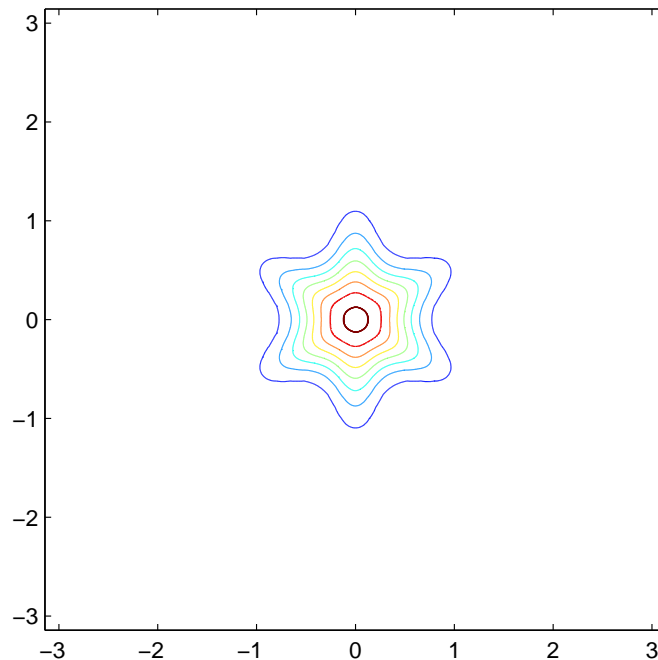


(b)

Figure 8.9: Plots of the scalar distribution of the flow near to the corner of a semi-angle $\alpha = \pi/4$ and $\lambda = 3.73959 + 1.1191i$ in the Cartesian co-ordinate system. Panel (a) shows the approximation of such distribution resulting from (8.3.12), while in (b) it is approximated by (8.3.13). 270



(a)



(b)

Figure 8.10: Plots of the scalar distribution of the flow near to the corner of a semi-angle $\alpha = \pi/6$ and $\lambda = 5.05933 + 1.95205i$ in the Cartesian co-ordinate system. Panel (a) shows the approximation of such distribution resulting from (8.3.12), while in (b) it is approximated by (8.3.13). 271

9

CONCLUSION

9.1 Summary and conclusion

We have investigated the transport of passive scalars in two-dimensional flows with consideration of the long-time decay rate of scalar fields. Our attention focuses on the effect of the boundary conditions for the velocity field of random and time-periodic flows. These flows are considered with both slip and no-slip conditions and the scalar fields with Dirichlet and Neumann boundary conditions.

Chapter 1 shows the importance of mixing of flows. The key concepts and feedback of flows were introduced along with some examples of ‘chaotic advection’.

Building on Chapter 1 and the evident importance of mixing of flows, Chapter 2 includes the main building blocks of this work. Families of flows with slip and no-slip conditions and essential scalar fields have been introduced. A class of symmetries used to impose the boundary conditions on the flows and scalar fields was presented in this chapter. Crucial in our study is the use of symmetries: if the

flows and initial conditions are chosen suitably then evolution under the advection–diffusion equation preserves the Dirichlet or Neumann boundary conditions exactly for the case of slip flow, or approximately in the case of no-slip flow. The numerical scheme used to simulate these flows and scalars was introduced where the passive scalar is simulated using a spectral code.

Chapter 3 includes efficient numerical simulations in the square domain for random flows along with a variety of boundary conditions. This domain was embedded in 2π -periodic space in x and y for these simulations. Our study imposes boundary conditions on the flow and scalar field by means of symmetries which allows a unified approach. We have not pushed κ to extremely low values, preferring to explore a wide range of values and use long runs, but this could be done effectively with the flow fields we have defined. Exact Dirichlet and Neumann boundary conditions were applied for the flows with slip along the boundary. In the case of no-slip flows, these boundary conditions are only imposed approximately as we lose the reflection symmetries about the walls, to be replaced by rotation symmetries. Our results for decay rate exponents α for random flows are summarised in table 6.1 in Chapter 6. These findings confirm previous results, particularly of Lebedev & Turitsyn (2004) and Salman & Haynes (2007), and extend them to consideration of a whole variety of boundary conditions, and square as well as plane layer domains. We have found clear scaling in our numerical results, which led to conjectured values of the scaling exponent α backed up by theoretical discussion. Where there has been an explicit formula for decay rates, $\gamma(\kappa) = C\kappa^\alpha$ with no-slip boundary conditions, we have seen good agreement between our numerical results for a single, long realisation of the random flow and the theoretical values based on an ensemble average in Fig. 6.1(a) and (b).

Chapter 4 focuses on the understanding of the role of corner regions in a square domain, by comparison with the infinite plane layers considered by Lebedev & Turitsyn (2004) and Salman & Haynes (2007). Simulations of random flows in a plane layer domain together with those of time-periodic flows in a square domain have been done. We find that the corners have a largely passive role except in the case of the Neumann boundary condition for a no-slip flow. Here the corner regions act as reservoirs, where the slow motion leads to a slow release of the scalar, controlling the decay of fluctuations in the bulk for small diffusivity κ : the mechanism is the same as that identified for the plane layer boundaries (Lebedev & Turitsyn, 2004), but the time-scale is still slower, leading to an $\alpha = 2/3$ exponent rather than $\alpha = 1/2$, for the flows we have used. Our results for time-periodic flows are summarised in table 4.4 in Chapter 4. These results confirmed those obtained for random flows and indicated that random flows are more effective at transporting scalar.

In order to pave the way for introducing our theoretical developments, Chapter 5 offers supporting theoretical arguments together with essential foundations of the theory of passive scalars in random flows. This theory has further been applied for the flows considered in Chapter 6. Theoretical investigations of the flows were done and the results obtained confirmed those obtained numerically in Part I of this thesis.

Building on our study of flows near corners presented in Chapter 4 and Chapter 6, and for more understanding of the role of the corners, a further investigation of the passive scalar was undertaken in Chapter 7 and Chapter 8. This investigation considers the evolution of the passive scalar field in terms of the polar co-ordinates (r, θ) . We note that in applications the flows in corner regions (in two and three

dimensions) can be rather sensitive to how a fluid flow is driven. For example, if a very viscous fluid motion is driven in a two-dimensional box by means of a periodically oscillating lid, near the corners the flow possesses an infinite sequence of Moffatt or corner eddies (Moffatt, 1964; Shankar, 2007).

Chapter 7 consists of the basic equations written in the polar co-ordinate system. These equations are specifically for investigation of the evolution of the scalar field addressed in Part I and II of this work. A theoretical confirmation for the scaling law $\alpha = 2/3$ in terms of (r, θ) has been obtained for the no-slip flow with Neumann boundary condition. Chapter 8 discusses the structure of a flow driven in a corner region. For a random flow, the average is considered over random corner eddy configurations, assuming that the phases of the constant C in (8.3.1) are uniformly distributed between 0 and 2π . Scalar fields of flows generated in corner regions are expanded using Fourier series in θ and averaged over the polar system. The exponential behaviour $\gamma(\kappa) = C\kappa^\alpha$ obtained in a structure of the corner eddies, crucially confirms our results found numerically and theoretically in Part I and II of this thesis.

9.2 Directions for future work

From the literature reviewed in the thesis, it can be concluded that the investigation of transport of the scalar fields will continue to be a growing area of research, taking into account the nature of the flow, the domain and the approach used. For example, as indicated in this research, the periodic flow is poor in transporting scalar in and out of the corners. This remains to be investigated thoroughly by the study of families of deterministic flows with varying behaviour in the corners

and on the no-slip boundaries. Future work on transport of the scalar can focus on:

- Extending the investigation of the scalar to include three-dimensional models by developing families of flows and investigating scaling laws of these flows. Developing numerical and theoretical predictions in three dimensions seems to be an area for a sensible scientific work.
- Extending the investigation to include structure of scalar fields for flows generated in the polar co-ordinate system, but with expanding the truncation used for approximating the averaged scalar fields to be of high modes. (The truncation levels of the modes currently used in this research are three and six).
- Studying mixing in open flows with a variety of boundary conditions in two and three-dimensional or in more complicated flows (e.g., turbulent).
- Studying mixing and diffusion of reacting chemical in chaotic flows by developing theory of the fast chemical reaction and addressing how these chemicals decay as time advanced. It is also of interest to study mixing process in predator-prey (biological) systems. Modifications that chemical or biological activity introduces in reactive patterns may provide more insights in exploring structures arising in advected reacting tracers in biological systems.

Bibliography

- Aref, H. 1984 Stirring by chaotic advection. *J. Fluid Mech.* **143**, 1–21.
- Aref, H. 2002 The development of chaotic advection. *Phys. Fluids* **14**, 4, 1315–1325
- Aref, H. & Pomphrey, N. 1980 Integrable and chaotic motions of four vortices. *Phys. Lett. A* **78**, 297–300.
- Arnold, V. I. 1965 Sur la topologie des écoulements stationnaires des fluides parfaits. *C. R. Acad. Sci. Paris A*, **261**, 17–20.
- Bajer, K. & Moffatt, H. K. 1990 On a class of steady confined Stokes flows with chaotic streamlines. *J. Fluid Mech.* **212**, 337–363.
- Balmforth, N. J. & Young, W. R. 2003 Diffusion-limited scalar cascades. *J. Fluid Mech.* **482**, 91–100.
- Boffetta, G., De Lillo, F. & Mazzino, A. 2009 Peripheral mixing of passive scalar at small Reynolds number. *J. Fluid Mech.* **624**, 151–158.
- Burghelea, T., Segre, E., Bar-Joseph, I., Groisman, A. & Steinberg, V. 2004 Chaotic flow and efficient mixing in a microchannel with a polymer solution. *Phys. Rev. E* **69**, 066305.
- Burghelea, T., Segre, E. & Steinberg, V. 2004 Mixing by polymers: experimental test of decay regime of mixing. *Phys. Rev. Lett.* **92**, 164501.
- Cerbelli, S., Adrover, A. & Giona, M. 2003 Enhanced diffusion regimes in bounded chaotic flows. *Phys. Lett. A* **312**, 355–362.

- Chaiken, J., Chu, C. K., Tabor, M. & Tan, Q. M. 1987 Lagrangian turbulence and spatial complexity in a stokes flow. *Phys. Fluids* **30**, 687-699.
- Chernykh, A. & Lebedev, V. 2008 Passive scalar structures in peripheral regions of random flows. *JETP Lett.* **87**, 682–685.
- Chertkov, M. & Lebedev, V. 2003a Decay of scalar turbulence revisited. *Phys. Rev. Lett.* **90**, 034501.
- Chertkov, M. & Lebedev, V. 2003b Boundary effects on chaotic advection-diffusion chemical reaction. *Phys. Rev. Lett.* **90**, 034501.
- Chien, W.-L. Rising, H. & Ottino, J. M. 1986 Laminar mixing and chaotic mixing in several cavity flows. *J. Fluid Mech.*, **170**, 355-77
- Dean, W. R. & Montagnon, P. E. 1949 On the steady motion of viscous liquid in a corner. *Proc. Camb. Phil. Soc.* **45**, 389.
- Dombre, T., Frisch, U., Greene, J. M., Hénon, M., Mehr, A. & Soward, A. M. 1986 Chaotic streamlines in the ABC flows. *J. Fluid Mech.* **167**, 353-391.
- El Omari, K. & Le Guer, Y. 2010 Alternate rotating walls for thermal chaotic mixing. *Int. J. Heat Mass Trans.* **53**, 123-134.
- Garcia-Ybarra, P. L. 2009 Near-wall turbulent transport of large-Schmidt-number passive scalars. *Phys. Rev. E* **79**, 067302.
- Giona, M., Adrover, A., Cerbelli, S. & Vitacolonna, V. 2004 Spectral properties and transport mechanisms of partially chaotic bounded flows in the presence of diffusion. *Phys. Rev. Lett.* **92**, 114101.

- Gouillart, E., Dauchot, O., Dubrulle, B., Roux, S. & Thiffeault, J.-L. 2008 Slow decay of concentration variance due to no-slip walls in chaotic mixing. *Phys. Rev. E* **78**, 026211.
- Gouillart, E., Dauchot, O., Thiffeault, J.-L., Roux, S. 2009 Open-flow mixing: Experimental evidence for strange eigenmodes. *Phys. Fluids* **21**, 2, 023603.
- Gouillart, E., Kuncio, N., Dauchot, O., Dubrulle, B., Roux, S. & Thiffeault, J.-L. 2007 Walls inhibit chaotic mixing. *Phys. Rev. Lett.* **99**, 114501.
- Gouillart, E., Thiffeault, J.-L. & Dauchot, O. 2010 Rotation shields chaotic mixing regions from no-slip walls. *Phys. Rev. Lett.* **104**, 204502.
- Haynes, P. H. & Vanneste, J. 2005 What controls the decay of passive scalars in smooth flows? *Phys. Fluids* **17**, 097103.
- Hénon, M. 1966 Sur la topologie des lignes de courant dans un cas particulier. *C. R. hebd. Seanc. Acad. Sci. Paris A* **262**, 312-314,
- Jun, Y. & Steinberg, V. 2010 Mixing of passive tracers in the decay Batchelor regime of a channel flow. *Phys. Fluids* **22**, 123101.
- Lebedev, V. V. & Turitsyn, K.S. 2004 Passive scalar evolution in peripheral regions. *Phys. Rev. E* **69**, 036301.
- Meleshko, V. V. & Aref, H. 1996 A blinking rotlet model for chaotic advection. *Phys. Fluids* **8**, 3215.
- Moffatt, H. K. 1964 Viscous and resistive eddies near a sharp corner. *J. Fluid Mech.* **18**, 1-18.

- Ott, E. & Antonsen, T. M. 1988 Chaotic fluid convection and the fractal nature of passive scalar gradients. *Phys. Rev. Lett.* **25**, 2839–2842.
- Ottino, J. M. 1989 *The kinematics of mixing: Stretching, Chaos, and Transport*. (Cambridge: Cambridge University Press).
- Pierrehumbert, R. T. 1994 Tracer microstructure in the large-eddy dominated regime. *Chaos, Solitons Fractals* **4** 1091–1110.
- Pierrehumbert, R. T. & Yang, H. 1993 Global chaotic mixing on isentropic surfaces. *J. Atmos. Sci.* **50**, 2462–2480.
- Rayleigh, Lord 1920 Steady motion in a corner of a viscous fluid. *Sci. Pap.* **6**, 18
- Salman, H. & Haynes, P. H. 2007 A numerical study of passive scalar evolution in peripheral regions. *Phys. Fluids* **19**, 067101–1.
- Shankar, P. N. 2007 *Slow Viscous Flows*. (London: Imperial College Press).
- Simmonet, C. & Groisman, A. 2005 Chaotic mixing in a steady flow in a microchannel. *Phys. Rev. Lett.* **94**, 134501.
- Skvortsov, A., & Yee, E. 2011 Scaling laws of peripheral mixing of passive scalar in a wall-shear layer. *Phys. Rev. E* **83**, 036303.
- Taylor, G. I. 1960 *Aeronautics and Astronautics*, p. 12, ed. Hoff & Vincenti, Pergamon Press.
- Thiffeault, J.-L., Finn, M. D, Gouillart, E., & Hall, T. 2008 Topology of chaotic mixing patterns. *Chaos* **18**, 033123, arXiv:0804.2520

- Toussaint, V., Carriere, P., Scott, J. & Gence, J.-N. 2000 Spectral decay of a passive scalar in chaotic mixing. *Phys. Fluids* **12**, 50011.
- Turner, M. R., Thuburn, J. & Gilbert, A. D. 2009 The influence of periodic islands in the flow on a scalar tracer in the presence of a steady source. *Phys. Fluids* **21**, 067103.
- Zheligovsky, V. A. 1993 A kinematic magnetic dynamo sustained by a Beltrami flow in a sphere. *Geophys. Astrophys. Fluid Dynamics* **73**, 217-254.